

2017

Optical angular momentum in air core fibers

<https://hdl.handle.net/2144/20841>

Boston University

BOSTON UNIVERSITY
COLLEGE OF ENGINEERING

Dissertation

**OPTICAL ANGULAR MOMENTUM IN AIR CORE
FIBERS**

by

PATRICK C. GREGG

B.S., B.A. , University of Rochester, 2011

Submitted in partial fulfillment of the
requirements for the degree of
Doctor of Philosophy

2017

© 2017 by
PATRICK C. GREGG
All rights reserved

Approved by

First Reader

Siddharth Ramachandran, Ph.D.
Professor of Electrical and Computer Engineering
Professor of Materials Science and Engineering

Second Reader

Alexander V. Sergienko, Ph.D.
Professor of Electrical and Computer Engineering
Professor of Physics

Third Reader

Alice White, Ph.D.
Professor and Chair of Mechanical Engineering
Professor of Materials Science and Engineering
Professor of Physics

Fourth Reader

David O. Caplan, Ph.D.
Senior Staff Member, Lincoln Laboratory
Massachusetts Institute of Technology

Get going, Simon. Just don't be distracted by the what-ifs, should-haves, and if-onlys. The only thing you choose yourself - that -is the truth of your universe.

Kamina (*Tengen Toppa Gurren Lagann*)

Acknowledgments

This thesis would not have been possible without support provided by the Defense Advanced Research Projects Agency (DARPA), the National Science Foundation (NSF), and the Department of Electrical and Computer Engineering at Boston University.

My thanks go to Professor Siddharth Ramachandran for giving me the opportunity to work on this project. He has continually supported me and pushed me to go further, deeper, and better. He has taught me an incredible amount, inside the lab and out, and for this he has my deepest thanks.

This document would not exist without the tireless work of Dr. Poul Kristensen, whose efforts and masterful control of fiber-making black magic have given fiber with which to experiment. Thanks also to Jørgen Olsen for help with fiber fabrication.

My thanks go to my committee members, Professor Sergienko, Professor White, and Dr. Caplan for selflessly volunteering their time and effort in aiding this work.

I would like to thank all of our collaborators who helped to advance different aspects of this work. Thanks especially to Dr. Steve Golowich, who laid much of the foundation for understanding spin-orbit coupling, and who designed the gen2 fiber. Many thanks to Dr. Andrea Rubano for q -plate fabrication, and to Dr. Lorenzo Marrucci, Dr. Mohammad Mirhosseini, Dr. Ebrahim Karimi, and Dr. Robert Boyd for their support with q -plate experiments. Thanks to Dr. Yvonne Kang for her work on OAM EDFA modeling, and to Dr. E.L. Lim, Dr. Yongmin Jung, Dr. Shaif-ul Alam, and Dr. David Richardson for their contributions to the OAM EDFA project. Thanks to Dr. Shankar Pidishety, Muhammad Abdul Khudus, Dr. Balaji Srinivasan, and Dr. Gilberto Brambilla for their work studying OAM fused couplers. Thanks to Kasper Ingerslev, Dr. Michael Galili, Dr. Francesco Da Ros, Hao Hu, Dr. Toshio Morioka, and Dr. Leif Oxenløwe, for their work on the OAM transmission experiments, and for making me feel like a welcome visitor at Denmark Technical

University. Thanks to Dr. Martin Lavery and Dr. Miles Padgett for teaching us about, and generously supplying us with, an OAM mode sorter, and again, to Dr. Mohammad Mirhosseini, for sharing his work on an improved OAM mode sorter. Thanks to Alex Hill, Joe Chapman, and Dr. Paul Kwiat for their help with an OAM entanglement-preservation experiment. Thanks to Dr. Enrico Bellotti and Dr. Roberto Paiella for helpful discussions and generous equipment loans.

Many thanks to all members of the Ramachandran group, past and present. Special thanks to Dr. Nenad Bozinovic, who got me up to speed in the lab, and wrote many of the Labview VIs I would later use or modify. Thanks to Dr. Michael Grogan and Dr. Lars A. Rishøj for being tea-buddies and excellent sounding-boards for new ideas. Thanks to Dr. Paul Steinvurzel for his help in implementing time of flight measurements. Thanks to Asher, Boyin, Du-Ri, Gautam, Jeff, Lu, Roman, Tao, and Yuhao for their continued help, support, and general skullduggery.

Labwork can be stressful, and physical activity outside the lab has kept me from going (more) insane. Thanks to my badminton coach, Pashu, whose knowledge and positivity has taught me many things, on and off-court. Thanks to my training partners: Wei, Kwan, Harris, Eric, Joanne, Aaron, Jeffrey, and Reetik. Thanks to my friends Mindaugas, Zheng, Shige, Daphne, Tim, and Paul, and many others, for countless matches. Thanks to my gym buddy, Mark, for making me wake up at 6AM.

Finally, I would like to thank my family for their endless love and support. Thanks to my parents for supporting me financially through my undergraduate education, and mentally through the present day. Thanks to my grandfather, who always pressed me to think critically. And my endless love and thanks to my fiancée, Wendi, who has supported me for the last 9 years, listened to endless complaining and annoyed ranting, seen me at my worst, and somehow still stays around. You have made me, in many ways, a better person, and I look forward to many more years together.

OPTICAL ANGULAR MOMENTUM IN AIR CORE FIBERS

PATRICK C. GREGG

Boston University, College of Engineering, 2017

Major Professor: Siddharth Ramachandran, Ph.D.
Professor of Electrical and Computer Engineering
Professor of Materials Science and Engineering

ABSTRACT

As data consumption continues to grow, the backbone of the internet, comprising single mode fiber (SMF)-based infrastructure, is fundamentally limited by nonlinear optical effects. One strategy to address this bottleneck, space division multiplexing (SDM), utilizes multiple modes in a single fiber as independent data channels. Orbital Angular Momentum (OAM) carrying modes, which have twisting phase fronts tracing out helices as the beams propagate, have recently received tremendous attention as a means of achieving low-crosstalk digital signal processing (DSP)-free transmission with enhanced capacity. Terabit-scale transmission using 4 OAM modes over 1.1km has been demonstrated, but questions remain - how many OAM modes can fibers support, and how stable is propagation over longer lengths?

In this thesis, we investigate angular momentum carrying modes in a novel class of fibers featuring an air core. We find that high-order OAM states, although arising in degenerate pairs, counter-intuitively resist mode coupling due to OAM conservation, pointing to a unique stability inherent to OAM modes in fibers. We achieve OAM propagation up to 13.4km lengths, and achieve mode purities greater than 15dB at

data-center length scales. We use these fibers to transmit wavelength-division multiplexed data with 25GHz channel spacing, 10 GBaud rates and quadrature-phase-shift keyed modulation formats in 12 modes simultaneously, over 1.2km, and over a large number of wavelengths across the C-band (1530-1565nm). However, transmission over every mode in every channel of the C-band was prevented by the accidental degeneracy of OAM states with undesired modes.

To achieve a larger ensemble of stable modes over a larger wavelength range, we study new fiber designs that avoid this accidental degeneracy problem. We find that the most scalable modal eigenbasis is a set of states that carry non-integer amounts of average OAM, also called spin-orbit coupled modes, in analogy to similar effects observed in atomic physics. We demonstrate excitation and transmission of 24 such modes over device lengths (10m).

The achievement of a record number of uncoupled modes in fibers confirms the viability of angular momentum states as data carriers, and potential applications include links in data centers, high capacity optical amplifiers, and quantum communication links.

Contents

1	Introduction	1
1.1	Higher order fiber modes and their uses	2
1.2	Telecommunications and Datacom	6
1.3	Use of "space" in telecom	8
1.4	Orbital Angular Momentum of light	11
1.5	Thesis Contents and Organization	14
2	Modes of Optical Fibers and Orbital Angular Momentum	17
2.1	Maxwell's Equations and fiber Eigenvalue equations	17
2.1.1	Separation of Variables - Azimuthal Function	20
2.1.2	Separation of Variables - Radial Function	21
2.2	Weak and strong guidance regimes	24
2.2.1	Weak Guidance	25
2.2.2	Polarization-induced degeneracy breaking	26
2.2.3	Strong Guidance	27
2.3	Angular Momentum of Fiber Modes	28
2.4	Summary	32
3	Fiber Mode Coupling	34
3.1	Coupled Mode Theory and Coupled Power Theory	35
3.2	Common Fiber Perturbations	40
3.2.1	Fiber Bends and Shape Deformations - Phase Perturbations	40
3.2.2	Linear Birefringence	41

3.2.3	Twist	42
3.3	Fiber Perturbations and OAM	44
3.4	Crosstalk and Multipath Interference	45
3.5	Summary	47
4	Mode Characterization	49
4.1	Spiral Interference Patterns	51
4.2	Polarization Binning	54
4.3	Symmetry Arguments and Introduction to Ring Method	57
4.4	Swept Wavelength Imaging: Ring Method and S2	61
4.5	Time Domain	65
4.5.1	Theory	65
4.5.2	Measurable Quantities and Practical Limitations	67
4.5.3	Experimental Realization	71
4.6	Output Projection	74
4.7	OAM Mode Sorter	75
4.8	Other Characterization Methods	77
4.9	Summary	78
5	Mode Excitation	80
5.1	In-Fiber Excitation Techniques	80
5.2	Free Space Excitation	81
5.3	Spatial Light Modulators	85
5.4	Liquid Crystal q-plates	101
5.5	Other Excitation Mechanisms	109
5.6	Summary	110
6	OAM in Fibers	112
6.1	The Vortex Fiber	113

6.2	Air Core Fibers: Design Criteria	118
6.3	Generation 1 Air Core Fiber	124
6.4	Air Core Fiber Generation 3 & 4	132
6.5	Air Core Fiber Generation 2	142
6.6	Summary	145
7	Degenerate States and Conservation of OAM	148
7.1	Degenerate States in SMF and the Vortex Fiber	149
7.2	Conservation of OAM	152
7.3	Degenerate States, q-plates, and Twist	155
7.4	OAM Modes, HE/EH Modes, and the Pancharatnam-Berry Phase . .	159
7.5	Summary	163
8	Broken Degeneracy and Long Length OAM State Propagation	165
8.1	Accidental-Degeneracy Induced Coupling	166
8.2	km Length Propagation and Time of Flight	171
8.3	Loop Buildup	174
8.4	Loop Experiment and 13.4km OAM Propagation	180
8.5	Summary	189
9	MIMO-free 12 Mode OAM Transmission	191
9.1	Experimental Setup for 12 Mode Data Transmission	192
9.2	Experimental Results	195
9.3	Limitations	200
9.4	Summary	202
10	Extending the Number of States: Spin-Orbit Coupling Revisited	204
10.1	Spin-Orbit Coupled Mode Excitation	206
10.2	Experimental Results	210

10.3	Limitations	217
10.4	Future Fiber Design Considerations	223
10.5	Summary	224
11	Summary and Outlook	227
11.1	Summary of Results	227
11.2	Outlook	228
11.2.1	OAM in Telecommunications	228
11.2.2	OAM-based Fiber Devices	230
11.2.3	OAM and Nonlinear Optics	231
11.2.4	Quantum Key Distribution and Entanglement Preservation	231
11.3	Conclusion	232
A	Perturbation Theory Derivation of Spin-Orbit Coupled States	234
B	Full Derivation of Angular Momentum of Fiber Modes	237
C	Air Core to Air Core Splice Program	242
D	Publications List	244
	References	248
	Curriculum Vitae	269

List of Tables

6.1	Summary of fabricated gen3 air core fibers. OSE: Outside edge, ISE: Inside edge	133
6.2	Summary of fabricated gen4 air core fibers.	135
6.3	Summary of fabricated gen2 air core fibers.	143
8.1	Summary of experimentally measured mode coupling rates for different OAM modes	188
10.1	Inter-mode-order coupling in gen2 fibers over 50m (in dB).	220

List of Figures

1·1	(a) Fiber optic system capacity and spectral efficiency by year. (b) Spectral efficiency within a single fiber. Star indicates a theoretical nonlinear single-mode limit. Figures with permission from (Essiambre and Tkach, 2012; Essiambre et al., 2010), © IEEE	7
1·2	Estimated energy consumption of broadband internet in Japan. With permission from (Ishii et al., 2015), © IEEE	8
1·3	Overview of classes fibers used for telecommunications. Orange shading: SMF and MMF do not use multiple spatial modes as orthogonal channels; Green shading: Several types of fiber which support and aim to use multiple spatial modes, including multicore fibers, GRIN few-moded MMFs, and sculpted core fibers. Based on a similar figure from (Essiambre and Tkach, 2012)	10
1·4	Intensity (left) and phase (right) distributions for a sample of Laguerre Gauss beams	12
2·1	(a) Schematic illustration of a cross section of a an optical fiber with a ring structure and (b) refractive index profile as a function of the radial coordinate	18

2·2	Schematic representation of the first few guided modes in a few mode fiber, in order of increasing n_{eff} Mode labels for each mode in the scalar picture are on the left, while the labels for each mode in the weakly guiding picture are on the right; both OAM and conventional HE/EH mode labels are listed for clarity. Note that each scalar mode order (blue line) is quadruply degenerate, while each vector mode order (red line) is doubly degenerate	32
3·1	(a) Schematic illustration of a photo-induced fiber grating with period (b) measured transmission spectrum of fiber grating, period $\Lambda \approx 69\mu m$ in Hi980 fiber with intent to excite the $LP_{0,19}$ mode (c) Imaged grating output at resonance	37
3·2	(a) Power transfer predicted by coupled mode theory for different ratios of $\Delta\beta$ to κ (b) Power transfer predicted by coupled power theory . .	39
3·3	Schematic illustration of effective index distribution of OAM modes and the perturbations necessary to couple among them. Inspired by a similar figure in notes presented by Dr. S. Golowich.	44
3·4	Illustration of effective index modulation by applied twist for a sample ($ l = 6$) OAM family. Splitting increases linearly with twist, but at different rates for SOa and SOaa modes due to differing total angular momentum; here exaggerated for illustration purposes.	45
3·5	(a) Experimental schematic: an SMF is spliced to a High-D fiber supporting the $LP_{0,2}$, which can be excited at the splice point. When the High-D fiber is spliced back to SMF, both $LP_{0,1}$ and $LP_{0,2}$ are projected back onto the fundamental mode of SMF, causing MPI (b) Power detected as a function of wavelength. Data courtesy of Boyin Tai.	47

3·6	(a) Experimental image of fiber output. (b) Power detected in gray levels as a function of wavelength for a single pixel	48
4·1	Experimentally measured interference between an OAM state and a Gaussian reference beam under different experimental conditions. (a) $l = 8$ OAM state interfered with tilted Gaussian (b) $l = 8$ state interfered with Gaussian with no defocus (c) $l = 8$ OAM state slightly defocused before interference (d) $l = 8$ state massively defocused (e) $l = 8$ state and reference powers balanced to remove center spot (f) $l = -8$ state and reference (g) $l = 9$ state and reference (h) approximately equal parts $l = 5$ and $l = -5$ and reference	52
4·2	Simulated spiral interference patterns. (a) Pure $l = 8$ OAM state interfered with a Gaussian beam (b-d) Interference between a reference beam and an $l = 8$ OAM state with X crosstalk into $l = -8$, with X printed above each figure (e-g) Interference between a reference beam and an $l = 8$ OAM state with X crosstalk into $l = 7$, with X printed above each figure	53
4·3	Schematic of experimental system for separating circular polarizations	55
4·4	(a) Crescent moon-shaped interference pattern indicative of $\Delta l = 1$ interference pattern, typically due to slight input coupling misalignments. (b) $2l$ bead pattern typical of strong mode coupling in the FUT.	59
4·5	(a) Mode images at different wavelengths showing rotation of interference pattern (b) Azimuthal Fourier series components of interest (c) Mode purity as a function of wavelength	63

4·6	(a) Two-mode fiber in which two modes are both launched and no mode coupling occurs (b) Two-mode fiber in which one mode is launched and a discrete coupling incident occurs at the midpoint of the fiber. Mode coupling is evident with strength, XT, and a delay time corresponding to the position of the perturbation (c) Two mode fiber with weak distributed coupling between modes	66
4·7	(a) Time domain trace on linear scale where several modes intentionally excited simultaneously. Differential group velocities can be determined if the fiber length is known. Ability to independently resolve peaks for each mode reveals stable mode propagation (b) Time domain trace on log scale when only TM_{01} is launched. Peak around 0.5ns from start of trace corresponds to discrete coupling into HE_{11} at fiber input, while shoulder between TM_{01} and arrival time of HE_{21} reveals in-fiber mode coupling	68
4·8	(a) Theoretical power densities as a function of normalized arrival time for particles launched into mode 1 and arriving in mode 1, and particles launched into mode 1 and arriving in mode 2 (b) Theoretical crosstalk, and the crosstalk that would be measured by shoulder integration versus peak integration as a function of mode coupling strength, hz (c) Difference between ‘measured’ and theoretical crosstalk	70
4·9	(a) Time of flight spectrum of $l = 7$ SOa mode after 3.1km of air core fiber measured with picosecond detector (b) Time of flight spectrum, same conditions, measured with the 1GHz detector	74
4·10	(a) Equal parts $l = 7$ and $l = -7$ launched into mode sorter from air core fiber (b) Transformed beam leaving sorter (c) Transformed beam focused by cylindrical lens, yielding spindle-like patterns, one for each l	76

4.11	$l=7$ lens passed through a tilted Wollaston prism, breaking higher order singularity into 7 first order singularities. Credit to Gautam Prabhakar for experimental image	78
5.1	Simplified schematic of experimental system for using SLM in fiber's Fourier plane for mode excitation. Inset: image of light beam between SLM and fiber	87
5.2	(a) Far field pattern of SLM with input Gaussian beam and SLM pattern well aligned (b) and (c) show cases of beam and pattern offset, with a more dramatic offset for (c)	88
5.3	Field in the focal plane of a lens when an OAM state is incident by off-center. Field is both elliptical and clearly brighter on one side than the other, implying undesired OAM coupling in free space	89
5.4	Time domain trace of fiber mode excited with SLM and QWP. Discrete coupling to SO _{aa} from SO _a controllable by QWP angle, coupling from $l = 6$ to $l = 5$ controlled by free space coupling alignment precision	90
5.5	(a) Mode purities as calculated by the Ring method when the fiber is displaced in the focal plane of an $f = 6.25mm$ lens. Circles indicate offset in $+x$, crosses offset in $-x$ (b) Mode purities as a function of source wavelength calculated by Ring method for alignment at 1550nm. Circles indicate calculated mode purities when the wavelength is kept at 1550nm, but the TILT parameter is adjusted as if the source were at those wavelengths. Insets are experimental images from this TILT sweep measurement	92
5.6	Free space diffraction patterns for an ensemble of OAM modes generated by an SLM	93

5·7	(a) Coupling strength into $LG_{3,0}$ of a Gaussian beam multiplied by a spiral phase and modulated by an annular binary transmission aperture; vertical axis is increasing inner radius of the annulus in the downward direction, and horizontal axis is increasing outer radius in the right direction (b) Coupling strength into $LG_{3,1}$ under same conditions (c) Mode purity $LG_{3,1}/LG_{3,0}$ under same conditions. Note a curve (dark red) where $LG_{3,1}$ is suppressed	95
5·8	(a) Near field image of SLM field, showing annular pass-band and fork lines (b) Far field diffraction for $r_{inner} = 20pix$ and $r_{outer} = 300pix$ (negligible effect) (c) $r_{inner} = 20pix$ and $r_{outer} = 100pix$ (d) $r_{inner} = 32pix$ and $r_{outer} = 150pix$ Control of ringing structure is evident . . .	96
5·9	Excitation of (a) $HE_{1,1}$ and (b) $HE_{1,2}$ in air core fiber	97
5·10	Sculpted amplitude distributions for a few OAM states	98
5·11	Image of (a) blank SLM surface illuminated by Gaussian beam (b) SLM surface with a spiral phase pattern and (c) SLM surface with a fork pattern	99
5·12	(a)-(c) Throughput of $q = 1/2$ plate as a function of increasing bias (d) Offset $q = 3$ plate at idea bias (e) Centered $q = 3$ plate at non-idea bias (f) Ideally biased and centered $q = 3$ plate throughput	104
5·13	Sketch of input coupling system with q -plate	105
5·14	(a) Field distribution in focal plane of lens using $q = 1/2$ plate for variety of focal lengths (b) Coupling efficiency versus lens focal length for a fixed z_2 of 16mm, the limit on proximity available in experiment (c) Coupling efficiency as a function of z_2 for a fixed focal length . . .	106
5·15	Schematic of system used to test functionality of $q = 1/2$ plate	107

5.16	(a) Output and (b) output plus reference after propagation through 300m of vortex fiber with 1530nm CW source	108
5.17	Excited mode purities using a $q = 1/2$ plate. Measurement of TE into $LP_{0,2}$ occluded by detector impulse response; cross coupling should be on the same order as that into $l = 0$	109
6.1	(a) Effective index curves for all guided modes in OD110 Vortex Fiber (b) zoom-in of $TM/TM/HE_{21}$ modes, where splitting on the order of 1×10^{-4} is evident (c) Right axis: Field profiles of $HE_{1,1}$ mode in Vortex Fiber plotted with Left axis: index profile (d) Field profiles of $HE_{2,1}$ mode in Vortex Fiber plotted with index profile. Figure based on a similar figure from (Ramachandran et al., 2009)	116
6.2	Field profiles for $l = 2$ mode in Vortex Fiber	117
6.3	(a) Simplified index profile of air core fiber (b) n_{eff} splitting versus inner radius, for constant ring width, and OAM order (c) Metric of spin-orbit coupling in one example fiber versus OAM order (d) Example of radial and azimuthal part of electric field for spin-orbit coupled state, and complete polarization distribution	120
6.4	(a) n_{eff} splitting for a set of air core fibers with ring width $2\mu m$. Number of $m = 2$ modes in each fiber written in purple at right edge of plot. Smaller plots below indicate strength of spin-orbit coupling versus inner radius and mode order for both SOa and SOaa families (b) Same set of plots for air core fibers with ring width $5.25\mu m$. . .	122
6.5	(a) Air core fiber soaks in refractive index matching oil via capillary action (b) Measured refractive index profile of air core fiber plus index matching oil	124

6·6	(a) Imaged cross-section of gen1 air core fiber (b) Zoom-in on core region and adjusted refractive index profile	126
6·7	(a) Imaged cleave with discontinuity across ring region (b) Imaged cleave with unperturbed ring region, but some discontinuity visible in the cladding	126
6·8	Distance between OAM modes and their nearest neighbors as a function of l at 1500nm	128
6·9	(a) Effective index versus wavelength for all $m = 1$ mode orders (b) Effective index versus wavelength for all $m = 2$ mode orders	128
6·10	Mode field distribution versus radius for a subset of OAM modes in the air core fiber	129
6·11	(a) Spiral interference patterns for each of the 12 transmitted OAM states (b) Example of a calculation of MPI (mode purity) versus wavelength; worst case MPI for all modes shown in (c)	129
6·12	Time of flight trace for $l = 8$ (a) SOa and (b) SOaa modes in the gen1 air core fiber.	130
6·13	(a) Time of flight trace for $l = 7$, SOa or SOaa (b) Fiber output after 1km when $l = 7$ is launched, using a narrowband ECL as illumination source. Seven-fold symmetry strongly visible in the right bin	131
6·14	Zoomed-in n_{eff} curves for $l = 7$ and $l = 8$ in gen1 air core fiber	132
6·15	(a) 4- and 8-fold symmetric output when $l = 6$ is launched, indicating accidental-degeneracy induced coupling with $l = 2, m = 2$ (b)4-fold symmetric fiber output when $l = 2$ is launched (c) $l = 3$ launched, $m = 1$ and $m = 2$ modes evident	134
6·16	(a) End facet image of gen3a OSE (b)Refractive index profiles of gen3a and gen3f	135

6·17	(a) Time of flight traces for $l = 5$ and $l = 6$ SOa and SOaa modes in gen3f fiber, offset for vertical clarity. In order of increasing group delay, traces are $l = 5$ SOaa, $l = 5$ SOa, $l = 6$ SOaa, and finally $l = 6$ SOa. Inset: fiber output after 1km (b)-(d) close-ups on each mode group's time of flight trace showing distributed intermodal crosstalk	136
6·18	Time of flight for $l = 6$ in gen4-2B showing mode coupling due to accidental degeneracy	137
6·19	Time of flight for $l = 6$ in gen4-3 showing evolving accidental degeneracy as a function of wavelength. Traces offset for clarity	138
6·20	Time of flight for $l = 0$ in gen4-3. Burst around 20ns is from $m = 1$, burst at 45ns is from $m = 2$	139
6·21	(a) End facet image of gen4-3 (b) Measured transmission loss (c) Effective index versus wavelength. Insets are experimental images after ~ 2 m of fiber propagation at 1550nm, except for leftmost image which is at 1500nm. (d) Group indices and (e) Dispersions for OAM modes of interest over C-band	140
6·22	(a) gen1 air core fiber spliced to SMF at relatively high current; hole collapse evident (b) air core to air core (gen4-3 to gen4-2B) splice at lower current. Guidelines in red to indicate that ring guiding region is tapered slightly but not collapsed	141
6·23	n_{eff} spectrum for all guided modes in gen2-1	143
6·24	Distance in n_{eff} between adjacent modes; for high- l this is SOa-SOaa splitting, while for low- l this splitting is with respect to other mode orders (other $ l $).	144
6·25	Mode fields for $l = 5$ SOa and SOaa states in gen2-1 fiber. Significant difference in radial and azimuthal components indicates SOC	144

6·26	Refractive index profiles for several fabricated air core fibers	146
7·1	In fiber polcon used to switch between spins	149
7·2	In fiber polcon used to switch between $l = 1$ OAM states in the Vortex Fiber	151
7·3	(a) Theoretical predication of OAM content of a bend perturbation with radius 2.8cm. Coefficients rapidly decrease with increasing OAM content (b) Power binning measurement for $l = 7$ SOa. As the pol- con paddles are tuned, negligible coupling between bins is observed (c) Binning measurement for $l = 0$ in SMF for comparison (d) Experi- mentally measured degradation for each l , plotted against a shifted $1/l$ trend line (e) OAM content needed to couple between degenerate states	153
7·4	(a) Binning measurement of $l = 6$ SOaa modes out of gen4-3 fiber as polcon paddles are manipulated (b) Binning measurement of $l = 6$ SOaa modes out of the same gen4-3 fiber, passed through a q -plate and reconverted to $l = 0$ and projected into linear polarizations, thus measuring $HE^{e,o}$ mode content. The fiber is then gently moved around the optical table	154
7·5	(a) Apparatus for inducing twist (b) OAM mode before and after in- duced twist (c) Ring coefficients evolving as the fiber is rotated, in- ducing more twist and apparently coupling between SOa and SOaa states.	156
7·6	(a) In an idea fiber, a single OAM mode is preserved (b) In a long- length, imperfect fiber, coupling between degenerate OAM states oc- curs (c) Precompensation of in-fiber mode coupling by q -plate excita- tion of a superposition of degenerate OAM states	158

7.7	Input beam from an ECL is converted to an SOaa OAM state using a q -plate , and transmitted through 500m of air core fiber. At the output, it is reconverted to an $l = 0$ beam through a second q -plate and coupled into SMF, where it is split by a fiber PBS. Controlling the polcon after the ECL before the first q -plate determines which polarization port the signal arrives at the output. Setting the polcon to minimize power in one port does so at least across C-band, as indicated in (b) and (c)	159
7.8	Polarization distribution of $HE_{3,1}$ and $EH_{1,1}$	160
7.9	Experimental apparatus for measuring geometric-phase induced mode coupling in HE/EH basis	161
7.10	Power in each linear polarization as a function of helix pitch for (a) $HE_{7,1}$ and (b) $EH_{5,1}$	162
7.11	Power in each linear polarization as a function of helix pitch for (a) $HE_{7,1}$ and (b) $EH_{5,1}$	162
8.1	MUX/DEMUX system used to test in-fiber crosstalk by q -plate output coupling	167
8.2	$l = 6$ SOaa (top) and SOa (bottom) states transmitted through a $q = 3$ plate, converting them to $l = 0$ and $l = 12$, respectively. In the farfield (right) these become a spot and a large ring beam. Top far field image attenuated with respect to bottom	168
8.3	Measured powers using q -plate output projection for (a) $l = 6$ SOaa launched and (b) $l = 6$ SOa launched. Difference between curves yields wavelength-dependent crosstalk	169
8.4	Measured powers using q -plate output projection for (a) $l = 6$ SOaa launched and (b) $l = 6$ SOaa launched, with narrowband ECL as source. (c) Measured crosstalk as a function of wavelength	170

8·5	Experimental system for measuring distributed mode coupling by time of flight, and sanity-checking MMF output coupling	172
8·6	(a) Time of flight trace of $l = 6$ SOa after 1200m in gen4-3 fiber, with output coupled into MMF (b) Time of flight trace of the $l = 6$ SOa and $l = 6$ SOaa projected into $l = 6$ SOa.	172
8·7	(a) Time of flight measurement of both $l = 7$ states, excited independently, shown on linear scale (b-d) Time of flight measurements of $l = 5, 6, 7$ on log scale	173
8·8	Simplified loop diagram	174
8·9	First test of fiber-to-fiber coupling using gen4-2B to gen4-3	177
8·10	Time of flight for $l = 7$ SOa coupled into Gen4-2B, which is then free-space coupled, through the reflective port of a plate beamsplitter, into gen4-3. Blip at 2.5ns is due to polarization conversion at beam splitter	178
8·11	Schematic diagram of light source used for loop experiments	180
8·12	Experimental setup for loop experiments	181
8·13	(a) Beam from SLM to pump facet A overlapped with output from facet D (1200m gen4-3) (b) Same but with beam from SLM defocused for illustration, showing the two beams slightly separated	182
8·14	Measured crosstalk for $l = 5$ and $l = 7$. Dashed lines are theoretical crosstalk, for a given h values. Inset mode images become progressively beadier at longer lengths, indicating stronger crosstalk	186
8·15	Measured crosstalk for $l = 6$ in gen3a fiber versus length, with theoretical crosstalk. Insets are experimental fiber outputs passed through a CPBS	187

9.1	Experimental apparatus used for OAM fiber transmission test. WSS: wavelength selective switch, AWG: arbitrary waveform generator, POL: linear polarizer, SLM: spatial light modulator, OBF: optical bandpass filter, OMA: optical modulation analyzer. Insets: comb source optical spectrum and fiber end facet image	193
9.2	Measured BERs as a function of received power for a subset of modes at 1558.5nm, for the case of: launching only pairs of degenerate modes (circles); launching all 4 modes of a given l (diamonds); and launching all modes (squares).	196
9.3	Measured BERs for all OAM modes at three test wavelengths while all OAM modes are simultaneously transmitted. All 34 measurements are below the SD-FEC threshold. Inset: example constellation diagrams.	197
9.4	Measured transmission matrix for system under test. Each column corresponds to an output projection, and each row to a launch condition. Each column is normalized to 0dB in the desired mode with entries denoting crosstalk in dB. $-l$ indicates SOa to SOaa coupling, $\neq l, -l$ indicates contributions from other mode orders, and $\neq l$ indicates total crosstalk.	198
10.1	Increasing waveguide confinement (index step) leads to OAM stability, but eventually to SOC. However, to support a large number of stable vector modes, SOC will almost definitely be encountered	205
10.2	Proposed coupling system for exciting SOC modes in gen2 fiber	208

10·3	(a) Index profile and fiber end facet image (inset) (b) Δn_{eff} between $E_{l,a}$ and its nearest neighbor (c) Polarization distributions for spin-orbit coupled $E_{4,aa}$ (top) and, closer to integer- l , $E_{9,a}$ (bottom) (d) Simulated difference between dominant $ l $ and ensemble average l , quantifying the spin-orbit coupling effect	211
10·4	(a) Excitation and characterization system for “standard” OAM modes in the gen2 fibers (b) time of flight response for $E_{6,aa}$ (c) Output mode image projected into RCP and LCP	212
10·5	(a) Experimental setup for measuring the extent of the SOC effect by output projection (b) Output projection measurement - each column is independently normalized to itself. Blue negative slope diagonal indicates coupling to in-fiber nearest neighbor, black off-diagonals indicate coupling to nearest different mode order, which could be due to imperfect mode excitation or in fiber coupling, and the white, negative slope off-diagonal indicates parasitic input coupling due to the SOC effect (c) Summary of the performance along the three trend lines from (b)	213
10·6	(a) Experimental setup for exciting SOC modes and analyzing beam content (b) Time of flight response for $E_{6,aa}$; note the lack of content in $E_{4,a}$. (c) Free space images of $E_{6,aa}$ after being passed through a CPBS and imaged with an axicon. The laser power has been changed between images to avoid camera saturation	215
10·7	Experimental apparatus for SOC mode output projection experiment	215
10·8	(a) Transmission matrix using SLMs and qplates to excite SOC fiber modes (b) Numerical results corresponding to the diagonals and off-diagonals of interest in (a)	216

10·9	Transmission loss for several different generations of air core fiber and SMF. Sample length specified in the legend.	218
10·10	Time of flight response for $E_{5,a}$ and $E_{5,aa}$ in after 50m of gen2-1. Excitation is performed without a q-plate, ths the parasitic $\Delta l = 2$ content	219
10·11(a)	Time domain response when $E_{9,aa}$ and $E_{9,a}$ are launched and transmitted through 50m of gen2-1 (b) time domain response when $l = 3$ is launched and transmitted through 50m of gen3a	221

List of Abbreviations

A_{Eff}	Effective area
AM	Angular Momentum
AOM	Acousto-Optic Modulator
AR	Anti-Reflection
ASE	Amplified Spontaneous Emission
BER	Bit Error Rate
bps	bits per second
C^2	Cross-Correlated imaging
CPA	Chirped Pulse Amplification
CPBS	Circular Polarization Beam Splitter
CW	Continuous-wave
DBPSK	Differential Binary Phase Shift Keying
DCF	Dispersion Compensating Fiber
DDG	Digital Delay Generator
DEMUX	Demultiplexing
DGD	Differential Group Delay
DMG	Differential Modal Gain
DSP	Digital Signal Processing
ECL	External Cavity Laser
EDFA	Erbium Doped Fiber Amplifier
EOM	Electro-Optic Modulator
FEC	Forward Error Correction
FFT	Fast Fourier Transform
FMF	Few Mode Fiber
FUT	Fiber under test
GRIN	Graded Index
GSA	Gerchberg-Saxton algorithm
GVD	Group Velocity Dispersion
HD-FEC	Hard-Decision Forward Error Correction
HOM	Higher Order Mode
HWP	Half-Wave Plate
ISE	Inside Edge
ITO	Indium Tin Oxide
LED	Light-Emitting Diode
LCP	Left circular polarization

LG	Laguerre Gaussian
LP	Linearly Polarized
LPG	Long-Period Grating
MCVD	Modified Chemical Vapor Deposition
MDM	Mode Division Multiplexing
MIMO	Multiple-Input Multiple-Output
MMF	Multimode fiber
MPI	Multi-path interference
MSE	Mean-Squared Error
MUBs	Mutually Unbiased Bases
MUX	Multiplexing
OAM	Orbital Angular Momentum
OBF	Optical Bandpass Filter
OD	Outer Diameter
OMA	Optical Modulation Analyzer
OOK	On-Off Keying
OSA	Optical Spectrum Analyzer
OSE	Outside Edge
PBS	Polarizing Beam Splitter
PDM	Polarization Division Multiplexing
PM	Polarization Maintaining
PMD	Polarization Mode Dispersion
polcon	Polarization controller
PSF	Point Spread Function
QAM	Quadrature Amplitude Modulation
QPSK	Quadrature Phase Shift Keying
QWP	Quarter-Wave Plate
RCP	Right Circular Polarization
RF	Radio Frequency
RMS	Root-Mean-Square
Rx	receiver
S^2	Spatially and Spectrally resolved imaging
SAM	Spin Angular Momentum
SD-FEC	Soft-Decision Forward Error Correction
SDM	Space Division Multiplexing
SLM	Spatial Light Modulator
SMF	Single Mode Fiber
SNR	Signal to Noise Ratio
SO _a	spin-orbit aligned
SO _{aa}	spin-orbit anti-aligned
SOC	Spin-Orbit Coupled

SPM	Self-Phase Modulation
SPP	Spiral Phase Plate
STED	Stimulated Emission Depletion
TE	Transverse Electric
TM	Transverse Magnetic
Tx	transmitter
VCSEL	vertical cavity surface-emitting laser
VF	Vortex Fiber
VI	Virtual Instrument
WDM	Wavelength Division Multiplexing
WGA	Weak Guidance Approximation

Chapter 1

Introduction

Fools ignore complexity. Pragmatists suffer it. Some can avoid it. Geniuses remove it.

Alan Perlis, *Epigrams on Programming*, 1982.

One of the most common conflicts in engineering and software design is that of simplicity versus complexity. The drive to add more features, more functionality and versatility is often intrinsically competitive with operational simplicity. Moreover, the more moving parts a machine has, the more things that can go wrong. This transcends science into music, arts, and athletics. An example is a service in badminton. On the surface, and at an amateur level, the low serve is one of the simplest shots in sports. However, mastery of the serve at an advanced level is incredibly difficult, and at its core, involves the simplification and near-exact repetition of a single motion to high precision. Typically, the more complicated the server's motion is, the more likely he or she is to fault the serve, but if the serve is too simple, it is predictable and leaves the server open to attack.

In fiber optics, simplicity has proven to be a powerful force. In a circular geometry, standard single mode fiber (SMF) is the simplest waveguide imaginable ¹. Since that advent of low-loss fiber proposed by Kao (Kao and Hockham, 1966) and initially demonstrated by Kapron and collaborators (Kapron et al., 1970), tremendous amounts of SMF have been fabricated. It has been used to send data across

¹By SMF, we mean a piece-wise constant refractive index optical fiber with one guiding region and one cladding region, not fibers which are single mode, but with more complicated refractive index profiles, such as DCF

thousands of kilometers, underground, under water, from nation to nation (Keiser, 2011). It has been used to build high power lasers for machining (Baumeister et al., 2006), in construction of gyroscopes (Burns, 1993), and in temperature and pressure sensors (Hocker, 1979) as well as countless others.

SMF is not without its drawbacks. Its monomode nature implies that it is relatively inefficient at collecting light. As the coupling efficiency is determined by the overlap of an incident light field with the guided mode(s) of a waveguide, SMF is inefficient as a probe for low-light imaging or light collecting applications. Its dispersion is limited by that of the waveguide material, which provides limitations for signal correction in telecommunications, and for nonlinear processes such as four wave mixing (Stolen et al., 1974). Finally, SMF generally requires illumination with a laser diode, as opposed to a less expensive light-emitting diode (LED), because the fiber's size and light-capturing ability is small (Keiser, 2011). To surpass these limitations additional complexity was needed - the complexity of multiple modes.

1.1 Higher order fiber modes and their uses

The word "mode" is used to denote a traveling electromagnetic field with the property that after some propagation distance, the field exactly repeats itself (Snyder and Love, 1983). Mathematically, a mode is a solution to the eigenvalue equations for electric and magnetic fields in a dielectric cylinder, with eigenvalue β , related to the mode's phase velocity by $v_p = \omega/\beta$, for an optical wave of frequency ω .

Typically modes of optical fibers are denoted with a pair of mode indices $\{l, m\}$. l specifies the mode's azimuthal mode number, and denotes the number of times the mode's complex phase circulates around the fiber's transverse plane. m relates the mode's radial mode number and corresponds to the number of zero-crossings along a line in the radial direction between the mode's geometric center and outer edge, plus

one. The first guided mode, often called the "fundamental mode," is conventionally denoted by indices $\{0, 1\}$, when the indices are with respect to Cartesian coordinates in the fiber's transverse plane. Any mode with $l > 0$ or $m > 1$ is denoted a higher order mode (HOM).²

Apart from mode order and propagation vector, modes are classified by a set of properties which may make a specific mode or set of modes attractive for different applications. These include:

- Cutoff wavelength - wavelength below which said mode is guided
- Transverse field distribution. Although specified by $\{l, m\}$, modes of the same modal indices but of different fibers can clearly have significantly different field distributions. For instance, the fundamental mode of single mode fiber is substantially different from the fundamental mode of a ring core fiber due to fiber design (Oh et al., 2005).
- Group velocity $v_g = \frac{d\omega}{d\beta}$, which determines the mode's speed of travel through the fiber
- Group velocity dispersion, $D = -\frac{2\pi c}{\lambda^2} \frac{d^2\beta}{d\omega^2}$, where λ is the optical wavelength and c the speed of light, which determines the relative speeds of different wavelengths through the fiber, and causes pulse broadening. It also plays a critical role in several fiber nonlinear processes, such as four wave mixing (Stolen et al., 1974). Group velocity dispersion is related both to material dispersion and to waveguide dispersion, which is due to the evolution of a mode's field distribution with changing λ .

²Depending on whether the modal representations are scalar or vector in nature, the indices are assigned either in cylindrical coordinates or with respect to Cartesian coordinates. Thus, $l = 0$ in the scalar picture actually refers to $l = 1$ in the vector picture, while $l = 1$ in the scalar picture encompasses both $l = 0$ and $l = 2$ in the vector picture.

- Effective area (A_{eff}), a second-moment calculation of mode size, which contributes to the efficiency of nonlinear processes in fibers (Agrawal, 2008).

Making use of the above properties, HOMs have found a bevy of applications. Due to varying waveguide dispersion, HOMs can have dispersion which varies significantly from that of Silica, suggesting use for dispersion compensation and spectral shaping of broadband pulses (Poole et al., 1994; Ramachandran et al., 2001), manipulation of group index and dispersion for fiber grating devices such as dispersionless bandpass filters (Ramachandran, 2005), as well as nonlinear frequency conversion (Demas et al., 2015b). Modes of appropriate transverse fields have been adapted for advanced microscopy techniques (Yan et al., 2013). The large mode area of certain kinds of HOMs has been utilized for creating more powerful fiber lasers (Nicholson et al., 2010). Phase matched mode conversion has been utilized to enable high quality spectral filtering of atmospheric emission lines, of great significance to terrestrial astronomy (Bland-Hawthorn et al., 2011). It is fair to say that the parameter tunability offered by HOMs has become a rich area of scientific research.

However, one of the key issues for multimode fibers is mode stability. Most of the applications listed above rely on the ability to selectively excite one, or a small number of, HOMs. The possibility of light leaking from one mode to another due to the influence of external perturbations must be accounted for. In the case of SMF power is either transmitted in the fundamental mode, or lost. For many multimoded fibers, intermodal crosstalk is not only possible, but in many cases difficult to avoid. Mode coupling is driven by two quantities - the wave vector mismatch between two modes, and a perturbation with the appropriate symmetry to couple them, as we will see in Chap. 3. HOMs can potentially be stable even in commonly available commercial fibers due to the unlikelihood of perturbations with the correct symmetry to couple neighboring modes, or equivalently, a large wave vector mismatch between

modes likely to be coupled by common perturbations (Ramachandran et al., 2006), but the modal density of states is often such that many authors consider the set of β values to be a continuum (Gloge, 1972; Olshansky, 1975). In a region with many nearly degenerate states, mode coupling at some level is to be expected.

The most common fibers supporting HOMs embrace this mode coupling. Conventional multimode fiber (MMF), which may be considered the complement to SMF, supports hundreds or thousands of modes. With a significantly larger area than SMF, MMF can act as a sort of light bucket, accepting a large percentage of light of nearly any spatial distribution, due to the massive number of spatial modes it supports. Thus, MMFs have found numerous applications in which power capture is desired but spatial mode purity is not essential, such as low-light imaging or light collection for astronomy, where the fiber's light-capturing power is essential (Noordegraaf et al., 2009). In addition, research has shown that mode coupling in MMF can be experimentally determined and, using appropriate wavefront manipulation at the fiber input/output, inverted. This process utilizes mode orthogonality and, in some limited instances (Čižmár and Dholakia, 2011; Čižmár and Dholakia, 2012), it has been shown that MMF can transmit images. However, measurement and computation must be repeated when the fiber is displaced.

MMF comes in two types - step-index MMF, which is simply a larger SMF, and graded index (GRIN) MMF, in which the refractive index profile is tailored to a parabola in order to minimize differential group delay (DGD). Minimization of DGD is necessary in order to use MMF for telecommunications - mode coupling readily occurs within the fiber, but if all the modes travel at the same speed and all of the optical power is recovered, data can be sent in a pseudo-single-mode manner (Freund et al., 2010). This methodology partially utilizes HOMs by employing the greater light-capturing ability of MMF but does not address possibly the most interesting use

of HOMs: their potential use as orthogonal information channels for communications applications where the transmission distance is on the order of 100s of meters to 1000s of kilometers.

1.2 Telecommunications and Datacom

Glass fibers are known to have existed as far back as Egyptian times, but were used exclusively for aesthetic purposes. It was not until the 1950s when bundles of glass were considered for imaging purposes that the idea of adding a non-metallic cladding was introduced by Brian O'Brien and Bram Van Heel, among others (Hecht, 2004). Even until the 1960s, optical fibers had propagation losses on the order of 1000dB/km, limiting their practical applications (Keiser, 2011). Since then, the groundbreaking work by Kao, the invention of the erbium doped fiber amplifier (EDFA) (Mears et al., 1987), and the ensuing implementation of wavelength division multiplexing (WDM) have seen research efforts in fiber optics skyrocket, and fiber usage for data transmission has become near-ubiquitous. Transmission rates have seen a similar meteoric rise, from 10Gbps (Giga bits per second (bps)) in the early 1980s to 10Tbps in the mid-2000s (see Fig. 1.1) Recent hero experiments have demonstrated 101.7 Tbps through a single optical fiber (Qian et al., 2012).

As advanced as current telecommunication systems are, it is projected that even with the use of WDM and advanced modulation formats, which have driven spectral efficiency growth since 2000, there is a fundamental limit to the spectral efficiency achievable within an SMF, limited by instantaneous Kerr Nonlinearities, amplified spontaneous emission (ASE), and chromatic dispersion. In 2010, it was reported that demand for bandwidth was growing at approximately 60% *per year* (Essiambre et al., 2010). The associated energy consumption for a smaller first-world market (Japan), from which this growth can be understood, is shown in Fig. 1.2. Initial

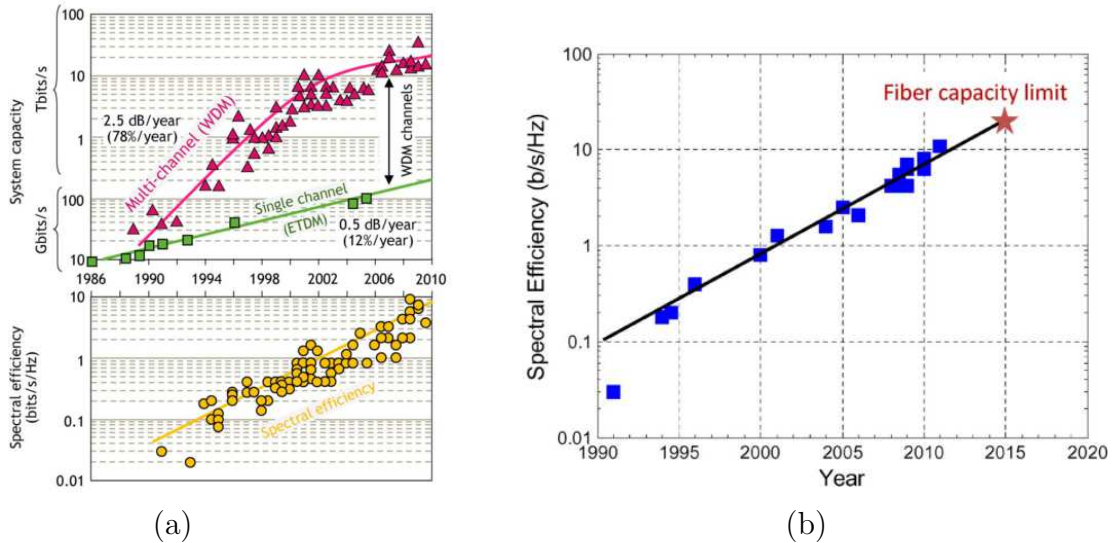


Figure 1-1: (a) Fiber optic system capacity and spectral efficiency by year. (b) Spectral efficiency within a single fiber. Star indicates a theoretical nonlinear single-mode limit. Figures with permission from (Essiambre and Tkach, 2012; Essiambre et al., 2010), © IEEE

growth (2000 ~ 2007) was driven by an increasing number of users, followed by a plateau region in which the number of users had saturated. In recent years traffic has again increased, this time driven by an increase in traffic volume per user, due to users with multiple devices, and higher-bandwidth uses of single devices such as standard and high definition video streaming, peer-to-peer file sharing, etc (Ishii et al., 2015). With demand for bandwidth predicted to increase exponentially, eventually network designers will be forced to deploy new fibers or redesign existing networks.

Similarly, in recent years, the advent of cloud computing has given rise to mammoth data centers for storage of personal and corporate data. Advances in computational density have resulted in a higher demand for chip-to-chip communication requirements, and modern data centers may have hundreds of thousands of cables connecting different racks (Zhang et al., 2012). Data centers of the future are predicted to have link lengths of up to 1-2km for connecting different buildings within

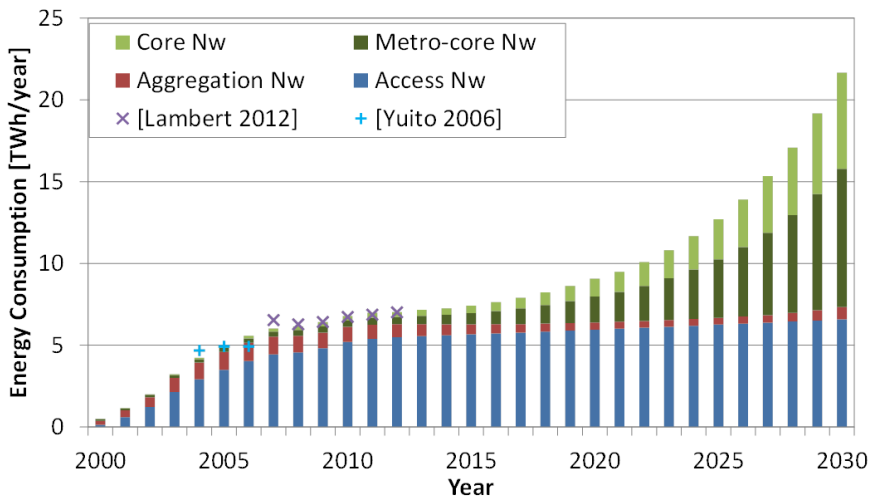


Figure 1.2: Estimated energy consumption of broadband internet in Japan. With permission from (Ishii et al., 2015), © IEEE

a data center campus (Lam et al., 2014), although the majority of links are still expected to be on the order of a few meters to a hundred meters. Thus, end-to-end schemes which could reduce the cable count and thus improve interconnectivity would be extremely beneficial, provided that it is cost effective. Current technology already employs the dimensions of polarization, wavelength, time, and phase (advanced signal processing techniques such as quadrature phase shift keying (QPSK)). Thus usage of another dimension could scale the spectral efficiency of optical fibers, much the same as the introduction of WDM. The clearest remaining dimension is that of space - the utilization of a fiber’s spatial modes.

1.3 Use of ”space” in telecom

Conventional long-haul telecommunications is done with single-mode fiber, wherein mode coupling exists only between the twofold-degenerate polarization modes. Such coupling can either be disentangled with multiple-input multiple-output (MIMO) processing, or largely prevented with the use of polarization maintaining (PM) fibers.

Whereas single mode fiber supports only a single mode with the intent of preventing signal corruption due to intermodal crosstalk, systems using MMF for data transmission assume that crosstalk will occur. Transmission systems utilizing MMF typically employ inexpensive vertical cavity surface-emitting laser (VCSEL)s at the transmitter (Tx) end, and large-area photodiodes at the receiver (Rx) end, and function well so long as the difference in group velocity (DGD) among the modes does not lead to significant distortion. Data transmission rates are limited by the product of fiber length and intermodal dispersion; thus, extremely low differential group velocity dispersion fibers are designed, and have been employed over links of lengths up to a few 100s of meters, at speeds of 10Gbps and 40Gbps (Freund et al., 2010). Recent research efforts have demonstrated 47 Gbps over OM-4 GRIN MMF (Lu et al., 2015).

The possibility of using the spatial modes of a fiber for data transmission, known as space division multiplexing (SDM), has attracted recent attention to a new class of fibers. Dubbed few mode fibers (FMFs), such fibers typically possess anywhere from 2 to 20 or 30 modes (Saridis et al., 2015), and seek to hybridize the advantages of SMF and MMF - that is, to take advantages of properties of HOMs in a controlled fashion. Typically such fibers feature a carefully tailored index profile, either designed to minimize DGD differences among all guided modes, or sculpted to ensure that only modes of a certain type, or with specific desired properties, exist.

An overview of such fibers is presented in Fig. 1.3. Multicore fibers consist of an array of single-mode fiber cores (Saridis et al., 2015). Although both coupled-core and uncoupled-core versions exist, most are designed such that the inter-fiber distance is large enough to prevent evanescent coupling, and each fiber represents an independent spatial channel. Recent results have shown 305 Tbps multiplexed transmission over a 19core fiber (Sakaguchi et al., 2013) and a transmission system including a multicore fiber amplifier (Sakaguchi et al., 2014). Few-mode MMFs are graded index fibers

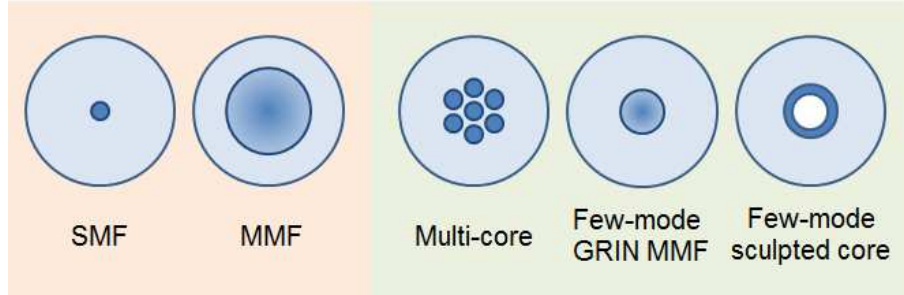


Figure 1.3: Overview of classes fibers used for telecommunications. Orange shading: SMF and MMF do not use multiple spatial modes as orthogonal channels; Green shading: Several types of fiber which support and aim to use multiple spatial modes, including multicore fibers, GRIN few-moded MMFs, and sculpted core fibers. Based on a similar figure from (Essiambre and Tkach, 2012)

which support $6 \sim 30$ modes, which typically exist in degenerate groups for which $2m + l$ is equal to the same integer, and for which the group indices (n_g) of all modes supported by the fiber are nearly identical. MIMO processing is required to disentangle fiber mode coupling and recover data. First iterations of such fibers were designed for 6 modes, with recent fibers supporting up to 15 modes (Grüner-Nielsen et al., 2012; Grüner-Nielsen et al., 2015). Data transmission using 15 spatial modes, requiring 30x30 MIMO was emulated over ~ 23 km using photonic lanterns for multiplexing (MUX) and demultiplexing (DEMUX) (Fontaine et al., 2015). The large-scale MIMO processing used for this experiment required 1800 taps. Given that the computational complexity of MIMO scales super-linearly with the number of channels, this approach will likely see scalability issues in the near future.

Finally, a distinct category of FMFs aims to design fiber in which modes with symmetries likely to couple under common perturbations such as bends are separated from each other in wave vector due to careful sculpting of the refractive index profile, resulting in a potentially large set of modes which are free from intermodal coupling. Such fibers have been used for dispersion compensation (Ramachandran et al., 2001),

large effective area (A_{Eff}) fibers for high-power fiber lasers (Ramachandran et al., 2006), and propagation of optical polarization vortices (Ramachandran et al., 2009). One example is the ring fiber shown in Fig. 1.3. Ring fibers, if well designed, can support many modes with $\{l, m\} = \{L, 1\}$ and no modes with $m > 1$, and which are well separated in effective index (Ramachandran and Kristensen, 2013). Such fibers are the focal point of this thesis, and as we will show, they support orbital angular momentum (OAM) carrying states of light.

1.4 Orbital Angular Momentum of light

Light is known to possess three kinds of longitudinal angular momentum (AM) (Bliokh et al., 2015):

- spin angular momentum (SAM) associated with the rotation of electric and magnetic fields in a circularly polarized beam. Spin takes values of $\pm\hbar$, where a positive helicity denotes left circular polarization (LCP) and a negative helicity right circular polarization (RCP) from the point of view of the source in the ansatz of wave propagation as $kz - \omega t$ (note that negating the wave ansatz or changing the point of view to the receiver flips LCP and RCP). The vector direction of SAM is typically parallel to the direction of propagation.
- An intrinsic orbital angular momentum, carried by beams with helical phase fronts which rotate around the beam center. These beams propagate forward along helical trajectories and contain phase singularities at the beam center. The number of times the beam's phase wraps around the optical axis in one period is referred to as the topological charge, and can take any integer value, positive or negative. The vector direction of this AM is parallel to the direction of propagation. Hereafter this type of AM will be referred to as Orbital Angular Momentum (OAM)

- An extrinsic orbital angular momentum, which arises from beams propagating at a distance from the origin. This kind of AM is not discussed further here.

Each of the different angular momenta are separately observable in a paraxial optical beam. SAM and OAM may be distinguished in the effect each has on a microscopic particle. Spin will cause a charged particle to rotate about the particle's center, while OAM will cause the particle to rotate about the beam axis due to the spatial variation of the electric field (Yao and Padgett, 2011). It was discovered in 1992 that higher-order laguerre gaussian (LG) beams of azimuthal order L carry OAM of $L\hbar$ per photon (Allen et al., 1992). A selection of LG modes is shown in Fig. 1·4 (Siegman, 1986). $L = 0$ corresponds to the well-known Gaussian mode, while modes with $L > 0$ contain a singularity due to an undefined beam phase on axis. We will show in Chap. 2 that $l > 0$ modes in many optical fibers are also OAM states. There has also been recent research on a class of beams which have angular momentum transverse to the direction of propagation, the so-called Photonic Wheel (Aiello et al., 2015). We do not discuss this in detail here.

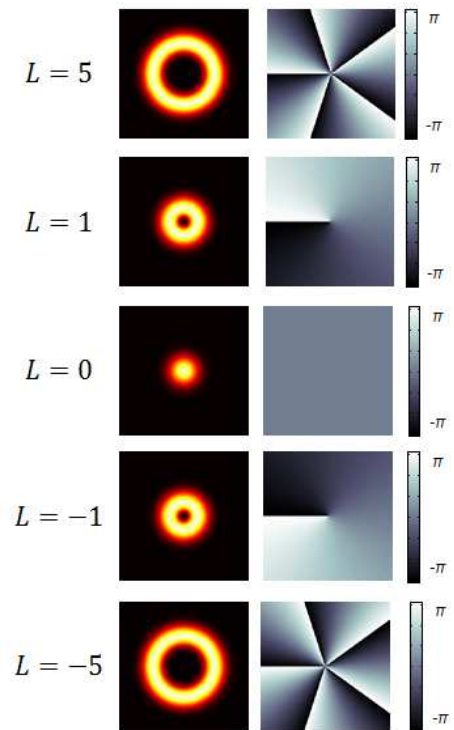


Figure 1·4: Intensity (left) and phase (right) distributions for a sample of Laguerre Gauss beams

Due to the countable infinity of theoretically possible states and the fact that all LG beams are orthogonal, OAM states have received tremendous attention as orthogonal information channels in free space for classical communications (Gibson et al., 2004; Huang et al., 2014) and quantum key distribution (Mair et al., 2001; Vaziri

et al., 2002). Free space data transmission has been demonstrated at Tbps rates over laboratory lengths (Wang et al., 2012), at 400 Gbps over a more practical building-to-building 120m link (Ren et al., 2015), and at a few bps with post-processing required over a city link of 3km across part of Vienna (Krenn et al., 2014). OAM communication in free space has two practical problems: turbulence and diffraction. Turbulence results in beam-wander across the receiver aperture, leading directly to crosstalk between OAM states, whose detection relies on a precise alignment to the optical axis of the receiver (Rodenburg et al., 2012; Malik et al., 2012). Diffraction results in rapid beam expansion, much as with a Gaussian beam, except that the beam waist of a higher order LG beam scales as $\sqrt{2m + l + 1}$, where m is the LG beam's radial index (Siegman, 1986). In experiments described by Vallone *et al*, the authors used an $l = 1$ OAM beam with initial waist $\sim 1cm$ such that the beam expanded minimally over 210m. The use of higher-order states would require larger receiver apertures for similar distances.

Optical fiber addresses both of these issues - turbulence and diffraction do not exist within a fiber by default. OAM states do exist in optical fibers; however, difficulties arise regarding propagation of OAM states. In most fibers, OAM states come in quasi-degenerate mode groups which couple significantly over short propagation distances due to bends and twists, leading to the observation of so-called linearly polarized (LP) modes (Ghatak and Thyagarajan, 1998). Specialty fibers (Ramachandran et al., 2009) have been proposed which break this near-degeneracy; specifically, the $l = \pm 1$ OAM modes have been sent over fiber of roughly 1km in length (Bozinovic et al., 2011; Bozinovic et al., 2012) and WDM-compatible data transmission performed at 1.6Tbps over 1.1km of so-called Vortex fiber (Bozinovic et al., 2013).

However, questions remain about the scalability of OAM modes in optical fiber. Specifically, it is not clear that a fiber can be designed which supports a multitude

(more than 2) OAM modes, in which all the modes are low-crosstalk and low-loss. The problem of input and output coupling multiple modes must be studied, both to determine optimal MUX and DEMUX configurations and to study fiber performance. The intrinsic properties and mode coupling behavior of OAM states must be studied in detail in order to predict system performance. These questions are the focal point of this thesis.

1.5 Thesis Contents and Organization

In this thesis, we study one specific class of FMF - fibers which support OAM carrying states of light. We design and experimentally study a class of air-core optical fiber which supports ensembles of OAM states, examining in detail specifics of fiber design, mode excitation schemes, characterization methods, and intermodal coupling. We show that such fibers have advantages in both shaping of modal density of states and resilience to mode coupling, suggesting applications in datacom, fiber devices, and nonlinear optics.

This document is organized as follows:

Chapters 2 and 3 constitute the theoretical background for this thesis. In Chap. 2, we study the mathematical foundations of fiber vector modes, including comparison of the weak and strong guidance regimes. We also consider the problem of angular momentum in fibers, and show that while fibers carry an integral total angular momentum per photon, they do not necessarily carry an integer OAM. In Chap. 3, we study the problem of fiber mode coupling, and the effects common fiber perturbations may be expected to have on OAM states.

Chap. 4 and Chap. 5 describe the experimental techniques used for the generation and classification of OAM modes, and describe experiments used to test each method. These techniques are then used in the experiments in Chap. 6 through Chap. 8. We

briefly summarize other possible methods not presented in this document.

Chap. 6 discusses in detail the theory behind fibers which support OAM states, and the experimental characterization of 4 generations of air core fiber, fabricated to support OAM states.

Chap. 7 describes experiments performed on high- l states in air core fibers, which show that even though the states are degenerate and in the presence of perturbations, they do not couple over lengths of $\sim 10\text{m}$ or more. We attribute this remarkable stability to the angular momentum needed to cause a transition, and the fact that this becomes increasingly unlikely as l increases.

Chap. 8 describes the study of intermodal coupling between near-degenerate OAM states, and the propagation of OAM states over long lengths. We demonstrate OAM propagation over 13.4km, an order of magnitude greater than previous in-fiber demonstrations of digital signal processing-free OAM transmission.

Chap. 9 describes data transmission experiments using 12 OAM modes simultaneously over a km-length air core fiber at multiple wavelengths. We demonstrate a communications system with a order of magnitude increase in capacity compared with previous OAM efforts.

Chap. 10 describes excitation and projection experiments on spin-orbit coupled angular momentum modes in thin ring fibers. We demonstrate a fiber capable of stably supporting (appx. -20dB of mode purity with respect to in-fiber nearest neighbors and spin-orbit coupled angular momentum pairs) 24 modes over 10m, a length sufficient for fiber devices. We discuss the outlook for fibers capable of supporting a larger ensemble of modes.

Chap. 11 Summarizes the document, and indicates possible directions for future research.

App. A and App. B provide a more thorough derivation for some parts of Chap. 2.

App. C details a splicer program used to splice air core fibers together without collapsing the air hole, by splicing at relatively low current. App. D lists publications resulting from the work related to this project.

Chapter 2

Modes of Optical Fibers and Orbital Angular Momentum

In this chapter, we study the mathematical formulations behind modes in optical fibers. In Sec. 2.1, we begin with Maxwell's equations and proceed to the fiber eigenvalue equation in electric field, \mathbf{E} , and magnetic field, \mathbf{H} . We pay special attention to the process of separation of variables and the ensuing relationships between vector field components. In Sec. 2.2, we study the solutions of the guided electromagnetic fields in regimes of differing refractive index contrast. In Sec. 2.3 we introduce the concept of angular momentum in optical fibers and its quantization, as well as its behavior under differing index contrasts. In no way is this chapter intended to be a complete derivation of the mathematics of fiber modes, as many excellent sources such as (Snyder and Love, 1983) and (Tsao, 1992) already exist. Rather, we aim to highlight the most salient points.

2.1 Maxwell's Equations and fiber Eigenvalue equations

Light propagation in an optical fiber is described by solving Maxwell's equations for a propagating electromagnetic field in a dielectric cylinder. For all discussions, the fiber's longitudinal directions is denoted as the $\hat{\mathbf{z}}$ -axis, while the transverse coordinates are given by (r, ϕ) , as indicated in Figure Fig. 2.1. $n(\mathbf{r})$ denotes the fiber's refractive index profile as a function of transverse coordinates, where $\epsilon = n^2$ is the waveguide's local dielectric constant.

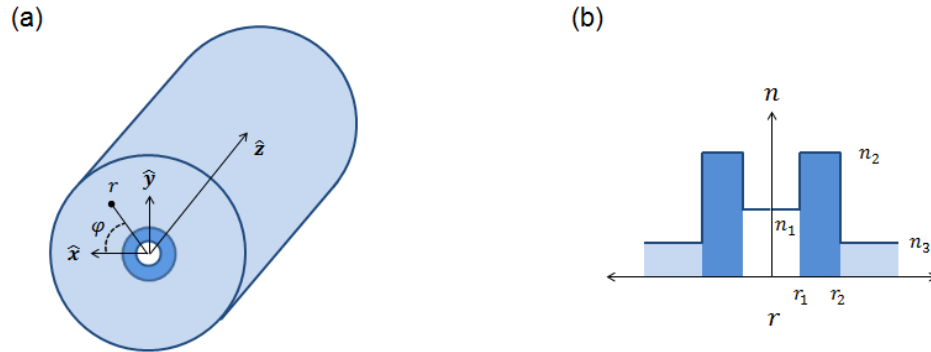


Figure 2.1: (a) Schematic illustration of a cross section of an optical fiber with a ring structure and (b) refractive index profile as a function of the radial coordinate

Maxwell's equations in matter (Jackson, 1999) are given by:

$$\nabla \cdot \mathbf{D} = \rho_f \quad (2.1a)$$

$$\nabla \cdot \mathbf{B} = 0 \quad (2.1b)$$

$$\nabla \times \mathbf{E} = -\frac{\partial \mathbf{B}}{\partial t} \quad (2.1c)$$

$$\nabla \times \mathbf{H} = \mathbf{J}_f + \frac{\partial \mathbf{D}}{\partial t} \quad (2.1d)$$

Here, \mathbf{E} and \mathbf{H} are the electric and magnetic fields, respectively, \mathbf{D} is the displacement field and \mathbf{B} is the magnetic flux density. ρ_f is the free charge density, and \mathbf{J}_f is the free current density. A vector quantity is denoted with bold typeface, although unit vectors are specified with conventional "hats".

The term *mode* is used to designate a propagating electromagnetic field distribution which, after a certain displacement in the \mathbf{z} direction, repeats itself. Thus, we

seek solutions of the form

$$\mathbf{E} = (\mathbf{e}_t + e_z \hat{\mathbf{z}}) e^{i(\beta z - \omega t)} \quad (2.2a)$$

$$\mathbf{H} = (\mathbf{h}_t + h_z \hat{\mathbf{z}}) e^{i(\beta z - \omega t)} \quad (2.2b)$$

Here, the vector fields \mathbf{e}_t and \mathbf{h}_t denote the transverse components of the electric and magnetic fields, while e_z and h_z denote the longitudinal components. The optical frequency is given by ω , while β is called the mode's propagation constant or wave vector, and is also written as $\beta = 2\pi n_{eff}/\lambda$ where n_{eff} is the effective refractive index of the mode. The effective refractive index may be viewed as an average of the refractive indices of the waveguide, weighted by the mode's electric field envelope.

$$n_{eff}^2 \approx \frac{\langle \mathbf{E} | n^2(r) | \mathbf{E} \rangle}{\langle \mathbf{E} | \mathbf{E} \rangle} \quad (2.3)$$

where $\langle a | b \rangle = \int \int dA \mathbf{a}^* \cdot \mathbf{b}$. An electromagnetic field must possess a single, although not necessarily unique, n_{eff} , to be called a mode.

Using the constitutive relations $\mathbf{D} = \epsilon \mathbf{E}$ and $\mathbf{H} = \frac{1}{\mu_0} \mathbf{B}$, and under the approximations $\rho_f = \mathbf{J}_f = 0$ and $\mu(r) = \mu_0$, Maxwell's equations may be rewritten into the vector wave equations (Snyder and Love, 1983):

$$\{\nabla_t^2 + n^2 k^2 - \beta^2\} \{\mathbf{e}_t + e_z \hat{\mathbf{z}}\} = -(\nabla_t + i\beta \hat{\mathbf{z}}) \mathbf{e}_t \cdot \nabla_t \ln(n^2) \quad (2.4a)$$

$$\{\nabla_t^2 + n^2 k^2 - \beta^2\} \{\mathbf{h}_t + h_z \hat{\mathbf{z}}\} = \{(\nabla_t + i\beta \hat{\mathbf{z}}) \times (\mathbf{h}_t + h_z \hat{\mathbf{z}})\} \times \nabla_t \ln(n^2) \quad (2.4b)$$

Here ∇_t^2 is the transverse vector Laplacian, ∇_t the transverse gradient, and $k = 2\pi/\lambda$ is light's wave vector in free space. The vector wave equations are valid for any non-magnetic waveguide geometry. For the case of optical fiber, solution in cylindrical coordinates is most appropriate. Denoting $\mathbf{e}_t = e_r(r, \phi) \hat{\mathbf{r}} + e_\phi(r, \phi) \hat{\boldsymbol{\phi}}$, Eq. (2.4a) can

be rewritten as:

$$\nabla_t^2 e_r - \frac{2}{r^2} \frac{\partial e_\phi}{\partial \phi} + \frac{\partial}{\partial r} \left\{ e_r \frac{d \ln(n^2)}{dr} \right\} - \frac{e_r}{r^2} + \{n^2 k^2 - \beta^2\} e_r = 0 \quad (2.5a)$$

$$\nabla_t^2 e_\phi + \frac{1}{r} \left\{ \frac{d \ln(n^2)}{dr} + \frac{2}{r} \right\} \frac{\partial e_r}{\partial \phi} - \frac{e_\phi}{r^2} + \{n^2 k^2 - \beta^2\} e_\phi = 0 \quad (2.5b)$$

$$\nabla_t^2 e_z + i\beta \frac{d \ln(n^2)}{dr} e_r + \{n^2 k^2 - \beta^2\} e_z = 0 \quad (2.5c)$$

Here ∇_t^2 indicates a transverse scalar Laplacian. The equations for the \mathbf{H} field components are similar and can be obtained from Eq. (2.4b), but are unnecessary for the following discussion, as the comments to follow refer equally to \mathbf{E} and \mathbf{H} . Generally, all three field components of both \mathbf{E} and \mathbf{H} will be nonzero. In regions of constant n the longitudinal component of the electric field, e_z , is analytically solvable, as is h_z , and their full form and relative strengths can be determined by enforcing electromagnetic boundary conditions between different constant-index regions. The rest of the field components can be found by their relations to e_z and h_z through Maxwell's equations. Alternatively, the above set of equations is numerically solvable for a fixed refractive index profile $n(r, \phi)$, although potentially with some difficulty as equations Eq. (2.5a) and Eq. (2.5b) are coupled at all points in space. However; more insight can be gained through a series of operations and approximations.

2.1.1 Separation of Variables - Azimuthal Function

If the refractive index profile is circularly symmetric, $n(r, \phi) = n(r)$, separation of variables can be successfully applied to Eq. (2.5a) - Eq. (2.5c), which results in an index to specify azimuthal mode order (quantum number), hereafter denoted j (Haberman, 2004). The azimuthal functions can be chosen as either cosines and sines (Snyder and Love, 1983), or complex exponentials (Tsao, 1992). Due to rotational symmetry, there are two sets of azimuthal functions corresponding to the same eigenvalue, β . If cosines and sines are chosen, these two sets are referred to as "odd" and "even". If

complex exponentials are chosen, the choice is delineated by a positive or negative j . Thus, the electric field in $(\hat{\mathbf{r}}, \hat{\boldsymbol{\phi}}, \hat{\mathbf{z}})^T$ can be written as:

$$\mathbf{e}_j^e = \begin{pmatrix} i\psi_r(r) \cos(j\phi) \\ i\psi_\phi(r) \sin(j\phi) \\ \psi_z(r) \cos(j\phi) \end{pmatrix} \quad \mathbf{e}_j^o = \begin{pmatrix} -i\psi_r(r) \sin(j\phi) \\ i\psi_\phi(r) \cos(j\phi) \\ -\psi_z(r) \sin(j\phi) \end{pmatrix} \quad j \in (0, 1, 2, \dots, \infty) \quad (2.6)$$

Or

$$\mathbf{e}_j^\pm = \begin{pmatrix} \psi_r(r) e^{\pm ij\phi} \\ \pm i\psi_\phi(r) e^{\pm ij\phi} \\ i\psi_z(r) e^{\pm ij\phi} \end{pmatrix} \quad j \in (0, 1, 2, \dots, \infty) \quad (2.7)$$

ψ_k are purely real functions of only the radial coordinate. Solutions of the type in Eq. (2.6) were commonly used in microwave waveguide theory and were carried over into fiber from that community (Marcuse, 1974), and are more commonly used than equations of type Eq. (2.7). However, both are valid descriptions of the same set of orthonormal modes. As we will shortly show in Sec. 2.3, solutions of the type Eq. (2.7) carry total AM of $j\hbar$ per photon while solutions of the type Eq. (2.6) have exactly zero angular momentum per photon on average.

2.1.2 Separation of Variables - Radial Function

The solutions of Eq. (2.5c) wherever the refractive index profile is constant are Bessel functions of order j , either Bessel functions of the first and second kind, $J_j(\rho)$ and $Y_j(\rho)$, where $n(r) > n_{eff}$, or Modified Bessel functions, $I_j(\rho)$ and $K_j(\rho)$, where $n(r) < n_{eff}$, with $\rho = \sqrt{|k^2 n^2 - \beta^2|} r$. h_z similarly is an identical combination of these functions, but potentially with a different constant prefactor. The entirety of the mode's electromagnetic field can be found by imposing continuity on ψ_z and $n^2 \psi_r$ at refractive index gradients and then by solving the resulting transcendental equation for β , which determines the relative weights of each Bessel function in a region of constant refractive index, and the relative weights of h_z and e_z (Tsao, 1992).

For the special case of $j = 0$, either e_z or h_z can be chosen to be zero, resulting in the so called transverse electric (TE) and transverse magnetic (TM) modes, which have purely azimuthally or purely radially polarized electric fields, respectively. TE and TM modes are non-degenerate. For $|j| > 1$, both e_z and h_z are non-zero. These modes are typically called hybrid modes and designated as either HE or EH modes, but the classification is historically inconsistent. Some authors (Snitzer, 1961) denote a mode as $EH_{j,m}$ if $e_z > h_z$ at some fixed reference point and wavelength, and $HE_{j,m}$ if $h_z > e_z$. Other authors (Alam and Albert, 2013) use the sign of the root of the characteristic equation for β . In most fibers, the notations will be consistent, but in some strongly confining fibers, the notations do not agree (Thomas et al., 2011). We use the former for convenience, comparing at the position of their peak electric field. The HE and EH modes may be viewed as a sum of TE and TM modes, with the EH (HE) modes being more TM (TE)-like. For a fixed $\{j, m\}$, there exist two degenerate HE modes, and two degenerate EH modes, with the two sets being non-degenerate.

Each azimuthal mode order, j , can support multiple radial mode orders, denoted by the radial index, m , where $m - 1$ is the number zero-crossings in the $\hat{\mathbf{z}}$ -component of the Poynting vector. The functional form of \mathbf{E} and \mathbf{H} does not change with m , but rather β changes, giving an apparent change in the mode's radial spatial frequency.

It is useful to consider the shape of the transverse electric field in terms of spatially invariant polarizations, i.e., $\hat{\mathbf{x}}$ and $\hat{\mathbf{y}}$. Using the relations:

$$\hat{\mathbf{r}} = \frac{1}{2} (\hat{\sigma}^+ e^{-i\phi} + \hat{\sigma}^- e^{i\phi}) \quad (2.8a)$$

$$\hat{\phi} = \frac{1}{2i} (\hat{\sigma}^+ e^{-i\phi} - \hat{\sigma}^- e^{i\phi}) \quad (2.8b)$$

with $\hat{\sigma}^\pm \equiv \hat{\mathbf{x}} \pm i\hat{\mathbf{y}}$, one can show that

$$\mathbf{e}_t^\pm = \frac{1}{2} \hat{\sigma}^+ e^{i(\pm j - 1)\phi} (\psi_r \pm \psi_\phi) + \frac{1}{2} \hat{\sigma}^- e^{i(\pm j + 1)\phi} (\psi_r \mp \psi_\phi) \quad (2.9)$$

Note that the helical phase functions have either increased or decreased in order by 1 in the switch from cylindrical polar to cartesian vector coordinates.

The transverse \mathbf{E} field can be obtained from Eq. (2.4a) once the longitudinal field is known. However, it is more useful to gain some insight from an analytical simplification. Using the transformation:

$$\psi_{\pm} = e_r \pm ie_{\phi} = \psi_r \mp \psi_{\phi} \quad (2.10)$$

One finds that the differential equations for ψ_{\pm} are separable (Endean and Allen, 1970). The solutions are Bessel functions of order $j + 1$ for ψ_+ and $j - 1$ for ψ_- . Thus, both the radial and azimuthal parts of the electric field of a given mode order $\{j, m\}$ are composed of Bessel functions of order $j - 1$ and $j + 1$, the relative weights of which are determined by boundary conditions, and are thus tied to the relative weights of e_z and h_z .

$$\psi_r = \frac{\alpha B_{j+1}(r) + \gamma B_{j-1}(r)}{2} \quad (2.11a)$$

$$\psi_{\phi} = \pm \frac{-\alpha B_{j+1}(r) + \gamma B_{j-1}(r)}{2} \quad (2.11b)$$

where B_k is a Bessel function, or linear combination of Bessel functions of the same kind (J and Y, for instance), of order k . Critically, these Bessel functions and prefactors occurring in ψ_r and ψ_{ϕ} are the same. Thus, Eq. (2.9) can be simplified to:

$$\begin{aligned} \mathbf{e}_{\mathbf{t}}^{\pm} = \frac{1}{2} e^{\pm i j \phi} & \left[\delta_{\pm} \left(\gamma \hat{\sigma}^+ e^{-i\phi} B_{j-1}(r) + \alpha \hat{\sigma}^- e^{i\phi} B_{j+1}(r) \right) \right. \\ & \left. + \delta \mp \left(\alpha \hat{\sigma}^+ e^{-i\phi} B_{j+1}(r) + \gamma \hat{\sigma}^- e^{i\phi} B_{j-1}(r) \right) \right] \quad (2.12) \end{aligned}$$

for δ_{\pm} equal to 1 in the + case and 0 in the - case. The two transverse electric fields in Eq. (2.12) are for degenerate fields of a particular $\{j, m\}$; HE and EH modes of

the same $\{j, m\}$ will have different α and γ , with mode orthogonality requiring:

$$\alpha_{j,m}^{HE} \alpha_{j,m}^{EH} + \gamma_{j,m}^{HE} \gamma_{j,m}^{EH} = 0 \quad (2.13)$$

(note that since ψ_r and ψ_ϕ are real, α and γ are as well) This expression for the transverse electric field has been arrived at with no assumptions other than the propagating mode formalism, a non-magnetic fiber, and the choice of the modal basis of Eq. (2.7). The implications of this decomposition will be discussed further in Sec. 2.2 and Sec. 2.3.

2.2 Weak and strong guidance regimes

For simplicity, consider a fiber with a piecewise-constant refractive index profile, as in Fig. 2-1. Fiber modes of this structure can be understood in one of three regimes:

1. The maximum refractive index contrast, Δn , is small enough that it can be completely ignored for the sake of boundary conditions. The solutions in this case are the so-called LP modes.
2. The maximum Δn is large enough that it must be accounted for, but small enough to be accounted for by first-order perturbation theory
3. The maximum Δn is large enough that first order perturbation theory is insufficient to accurately describe the fields.

The modes in case 1 are four-fold degenerate in β due to two-fold degeneracy in rotation and two-fold degeneracy in polarization, with the polarization basis typically chosen as $\hat{\mathbf{x}}$ and $\hat{\mathbf{y}}$ (Ghatak and Thyagarajan, 1998):

$$E_{l,m}^{LP} = \{\hat{\mathbf{x}}/\hat{\mathbf{y}}\} \{\cos(l\phi)/\sin(l\phi)\} F_{l,m}(r) \quad (2.14)$$

These fields can be found from the scalar Helmholtz equation. From the point of view of boundary conditions, this is equivalent to enforcing continuity of ψ_r under the assumption that the refractive index is constant, which is never completely true, although it is potentially a reasonable approximation for some applications. The $d \ln(n^2)/dr$ term in Eq. (2.4a) is also ignored. This case is not further discussed here, except as a stepping stone to case 2.

2.2.1 Weak Guidance

Case 2 is generally referred to as the weak guidance approximation (WGA). It is obtained by taking the solutions of case 1 and accounting for the $d \ln(n^2)/dr$ term in Eq. (2.4a) by first order degenerate perturbation theory (Snyder and Love, 1983). The solutions in this case are two-fold degenerate due to rotational symmetry, but the two-fold polarization degeneracy from case 1 is lifted, although the two sets of modes remain close in n_{eff} . The transverse field descriptions of these modes may be written with either spatially varying linear polarization, or circular polarization, depending on the basis of choice, paralleling the choice of basis in Eq. (2.6) and Eq. (2.7). We choose to work in the circularly polarized basis. The two nearly degenerate sets of modes for $|l| > 1$ are given by (Ramachandran and Kristensen, 2013)

$$V_{l,m}^{\pm} = \hat{\sigma}^{\pm} e^{\pm il\phi} F_{l,m}(r) e^{i\beta_{l,m}^Y z} \quad (2.15)$$

$$W_{l,m}^{\mp} = \hat{\sigma}^{\mp} e^{\pm il\phi} F_{l,m}(r) e^{i\beta_{l,m}^W z} \quad (2.16)$$

As we will show in Sec. 2.3, the helical phase and uniform polarization implies that these modes carry OAM. The modes of Eq. (2.15) have polarization and azimuthal phase of the same handedness, and are referred to as spin-orbit aligned (SOa) OAM modes, while those of Eq. (2.16) are denoted spin-orbit anti-aligned (SOaa) (Ramachandran et al., 2015). We use a lower case ‘a’ for the acronym in hope of avoiding

confusion with Semiconductor Optical Amplifiers. The modes from Eq. (2.15) may be mathematically written as linear combinations of the conventional $HE_{l+1,m}$ even and odd modes, while the modes from Eq. (2.16) may be written as linear combinations of $EH_{l-1,m}$ even and odd modes.

The solutions here are a reduction of Eq. (2.7) in the special case of $\psi_r \approx \psi_\phi$ for spin-orbit aligned modes and $\psi_r \approx -\psi_\phi$ for spin-orbit anti-aligned modes, i.e., $\alpha_{j,m}^{HE} = \gamma_{j,m}^{EH} = 0$. Additionally, note that the azimuthal mode order correspondence is different; $HE_{j,m}$ corresponds to $V_{j-1,1}$ while $EH_{j,m}$ corresponds to $W_{j+1,m}$. Thus, even though these two mode sets are relatively close in β , they actually refer to different mode orders if the modes are labeled in cylindrical coordinates, as the "conventional" HE and EH modes are, reiterating that the mode features in this approximation are described by their transverse fields in a Cartesian coordinate system (as opposed to a cylindrical coordinate system, which is the native coordinate system for the electromagnetic boundary conditions).

For the case of $l = 0$, only two degenerate polarization modes exist for a given m . For $l=1$, the spin-orbit anti-aligned modes do not exist as fiber modes. Rather, their degenerate combination exists as TE and TM modes:

$$TE_{0,m} = \frac{F_{0,m}(r)}{2} \{ \hat{\sigma}^- e^{i\phi} + \hat{\sigma}^+ e^{-i\phi} \} e^{i\beta_{0,m}^{TE}} \quad (2.17a)$$

$$TM_{0,m} = \frac{-iF_{0,m}(r)}{2} \{ \hat{\sigma}^- e^{i\phi} - \hat{\sigma}^+ e^{-i\phi} \} e^{i\beta_{0,m}^{TM}} \quad (2.17b)$$

2.2.2 Polarization-induced degeneracy breaking

The splitting in β , or equivalently in n_{eff} between Eq. (2.15) and Eq. (2.16) can be found from the scalar field profiles. For $|l| > 1$, the splitting is given by (Snyder and Love, 1983):

$$\Delta\beta = \beta_{l,m}^V - \beta_{l,m}^W = l \frac{\Delta}{2\pi} \frac{\lambda}{n_{co}} \int dr F_{l,m}^2(r) f'(r) \quad (2.18)$$

Here $f(r)$ is the shape function of the waveguide, that is, the index profile normalized to the highest refractive index, and Δ is the profile height parameter; thus, $n^2(r) = n_{co}^2 (1 - 2\Delta f(r))$, with n_{co} being the highest refractive index in the guiding region. This equation assumes that $\int r dr F_{l,m}^2 = 1$ [*unitless*] to be dimensionally correct.

For the case of $|l| = 1$, the expression is more complicated, but can be written in terms of the same quantities and their derivatives. Investigation of Eq. (2.18) shows that the splitting in wave vector between the two kinds of modes of a given $\{l, m\}$ is controlled by the amount of field, $F(r)$, at index gradients within the fiber, and also generally increases with l . Thus, the extent to which the SOa and SOaa modes are "nearly degenerate" is controllable with fiber design (Ramachandran et al., 2009) and will be investigated in Chap. 6.

2.2.3 Strong Guidance

In the regime of strong guidance, the refractive index contrast of the fiber is significant enough that it cannot be approximated by first order perturbation theory. The fields are no longer circularly polarized, and instead take a more complicated form in the transverse plane (Ramachandran et al., 2015). This is the case for which Eq. (2.12) is not reducible; that is, $\psi_r \neq \pm \psi_\phi$, or $\alpha_{j,m}^{HE} \neq \gamma_{j,m}^{HE} \neq 0$.

As we will show in Sec. 2.3, these modes do not possess a well-defined orbital angular momentum, although they have a fixed total angular momentum per photon. As such, they are referred to as spin-orbit coupled (SOC) modes (Golowich, 2014). From the point of view of the weakly guided modes, the SOC modes can be approximated using second order perturbation theory, and can be written as a combination of varying amounts of $V_{l,m}^\pm$ and $W_{l-2,m}^\mp$ (see App. A).

2.3 Angular Momentum of Fiber Modes

The fact that light carries angular momentum was known as long ago as 1909, when Poynting demonstrated that a circularly polarized beam of light could cause a piece of birefringent material suspended on a thin wire to rotate about its center (Poynting, 1909). It was not until 1992 that Allen and collaborators proved that an optical beam with a *sole* ϕ dependence of $e^{il\phi}$ carried orbital angular momentum of $l\hbar$ per photon. For paraxial beams in free space, the two quantities are separable (Andrews, 2013). However, there are many cases where the two angular momenta are not separable (Van Enk and Nienhuis, 1994), such as tightly focused (high-NA) free space beams (Bliokh et al., 2010), or interface effects which cause an interaction between spin and orbital angular momenta (Bliokh et al., 2015). The question remains - what does electromagnetic angular momentum look like in optical fibers?

There are two pictures for discussing electromagnetic momentum, the Abraham picture (Abraham, 1909) in which the electromagnetic linear momentum density is written as $p = (\mathbf{E} \times \mathbf{H})/c^2$ and the Minkowski picture (Minkowski, 1908), in which $p = (\mathbf{D} \times \mathbf{B})/c^2$. Recent work (Barnett, 2010) has shown that there is no disagreement between the two pictures, but rather that the Abraham picture corresponds to kinetic momentum and the Minkowski picture to canonical momentum. We use Abraham notation here. The angular momentum density is given by the cross product of position and linear momentum, as in classical mechanics:

$$\mathbf{J} = \mathbf{r} \times (\mathbf{E} \times \mathbf{H})/c^2 \quad (2.19)$$

The total angular momentum flux is the integral of Eq. (2.19) across the cross-section of the fiber. Since \mathbf{E} and \mathbf{H} are time-variant quantities, we consider the time average

of the angular momentum flux:

$$\langle \Phi_{AM} \rangle = \frac{1}{2c^2} \int \int dA r \times \text{Re}(\mathbf{E} \times \mathbf{H}^*) \quad (2.20)$$

Similarly, the time-averaged linear momentum flux is:

$$\langle \Phi_p \rangle = \frac{1}{2c^2} \int \int dA \text{Re}(\mathbf{E} \times \mathbf{H}^*) \quad (2.21)$$

It is tedious but straightforward to show (see App. B) that the only non-vanishing component of $\langle \Phi_{AM} \rangle$ is the $\hat{\mathbf{z}}$ component (due to integration of $\hat{\mathbf{r}}$ and $\hat{\phi}$ over dA), which has the form:

$$\langle \Phi_{AM} \rangle_z = -\frac{1}{2c^2} \int \int dA r \text{Re}(E_r H_z^* - E_z H_r^*) \quad (2.22)$$

The longitudinal field component of \mathbf{H} can be related to the transverse components of \mathbf{E} as (Tsao, 1992):

$$H_z = \frac{1}{i\omega\mu r} \left[\frac{\partial(rE_\phi)}{\partial r} - \frac{\partial E_r}{\partial \phi} \right] \quad (2.23)$$

Further, the radial component of \mathbf{H} can be removed using:

$$i\omega\mu\mathbf{H}_t = [\nabla_t \times (\hat{\mathbf{z}}E_z) + i\beta\hat{\mathbf{z}} \times \mathbf{E}_t] \quad (2.24)$$

leaving

$$\langle \Phi_{AM} \rangle_z = -\frac{1}{2c^2} \int \int dA r \text{Re} \left[\frac{iE_r}{\omega\mu r} \left(\frac{\partial(rE_\phi^*)}{\partial r} - i(\pm j)E_r^* \right) + \frac{E_z}{i\omega\mu} \left(i\beta E_\phi^* - \frac{i(\pm j)}{r} E_z \right) \right] \quad (2.25)$$

Since $|E_z| \ll |\mathbf{E}_t|$ for nearly any reasonable fiber, we drop terms which contain E_z^2 .

To simplify the remaining term containing E_z we substitute using:

$$E_z = \frac{i}{\beta} [\nabla_t \cdot \mathbf{E}_t + (\mathbf{E}_t \cdot \nabla_t) \ln(n^2)] \quad (2.26)$$

Eq. (2.25) can now be simplified as:

$$\langle \Phi_{AM} \rangle_z = -\frac{1}{2c^2} \int \int dA \operatorname{Re} \left[\frac{-(\pm j)}{\omega\mu} (E_r E_r^* + E_\phi E_\phi^*) + \frac{i}{\omega\mu} \left(E_r \frac{\partial(rE_\phi^*)}{\partial r} + E_\phi^* \frac{\partial(rE_r)}{\partial r} \right) + \frac{ir}{\omega\mu} E_\phi^* (\mathbf{E}_t \cdot \nabla_t) \ln(n^2) \right] \quad (2.27)$$

It can be shown by integration by parts (see App. B) that the summation of the middle term and the last term in the integral in Eq. (2.27) is exactly zero. Substituting the modal electric field given by Eq. (2.7), we find that the angular momentum flux is given by:

$$\langle \Phi_{AM} \rangle_z = \frac{1}{2c^2\omega\mu} \int \int dA (\pm j) (\psi_r^2 + \psi_\phi^2) \quad (2.28)$$

Similar to the angular momentum flux, we can integrate the linear momentum density to find the linear momentum flux. Again, $\hat{\mathbf{z}}$ is the only component with a non-zero integration:

$$\langle \Phi_p \rangle_z = \frac{1}{2c^2} \int \int dA \operatorname{Re} (E_r H_\phi^* - E_\phi H_r^*) \quad (2.29)$$

It can be shown using using Green's theorem (App. B), and dropping terms which scale as E_z^2 that the above can be simplified to:

$$\langle \Phi_p \rangle_z = \frac{\beta}{2c^2\omega\mu} \int \int dA \psi_r^2 + \psi_\phi^2 \quad (2.30)$$

The linear momentum flux in the $\hat{\mathbf{z}}$ direction, multiplied by the speed of travel of photons in the waveguide (c/n_{eff}) yields the energy flow. If we consider the ratio of angular momentum flux to energy flux (that is, the ratio of angular momentum to energy), we find that:

$$\begin{aligned} \frac{\langle \Phi_{AM} \rangle_z}{\langle \Phi_p \rangle_z \cdot c/n_{eff}} &= \frac{1}{\beta \cdot c/n_{eff}} \frac{\int \int dA (\pm j) (\psi_r^2 + \psi_\phi^2)}{\int \int dA \psi_r^2 + \psi_\phi^2} \\ &= \frac{\pm j}{\omega} \end{aligned} \quad (2.31)$$

The fiber modes in the basis we have chosen (Eq. (2.7)) evidently carry $j\hbar$ angular momentum per photon, with the direction of the angular momentum parallel to the direction of propagation. However, this derivation does not specify what kind of angular momentum is carried by the mode: OAM or spin. To determine this, we calculate the spin flux density (Kien et al., 2006)

$$\mathbf{J}_S = \epsilon_0 \mathbf{E} \times \mathbf{A} \quad (2.32)$$

where \mathbf{A} is the vector potential. Working in the Coulomb gauge (Jackson, 1999) we can calculate the spin flux as:

$$\langle \Phi_S \rangle = \frac{\epsilon_0}{\omega} \int \int dA \operatorname{Im} [E_r^* E_\phi] \quad (2.33)$$

Again taking the ratio with the energy flow, we find:

$$\frac{\langle \Phi_S \rangle_z}{\langle \Phi_p \rangle_z} = \frac{\pm \int \int dA \psi_r \psi_\phi}{\frac{\omega}{2} \int \int dA \psi_r^2 + \psi_\phi^2} \quad (2.34)$$

It is evident from Eq. (2.34) that the upper bound for the spin flux is $\pm\hbar$ per photon. However, depending on the structure of the waveguide, if ψ_r and ψ_ϕ are sufficiently different, spin can take any value between -1 and 1 .

In the weakly guiding region, $\psi_r \sim \psi_\phi$ for the SOa OAM modes. Evidently these modes carry angular momentum of $\pm j\hbar$ per photon, with spin of $\pm\hbar$ per photon, leaving the remaining $\pm(j-1)\hbar$ per photon for orbital angular momentum, consistent with Eq. (2.15) and the ensuing discussion. Similarly, the SOaa modes carry angular momentum of $\pm j\hbar$ per photon, but with spin of $\mp\hbar$ per photon, implying that they carry OAM of $\pm(j+1)\hbar$ per photon. Thus, the index l used in Eq. (2.15) and Eq. (2.16) can be readily identified as a true orbital angular momentum in the weakly guiding picture. If instead of using the modes as defined in Eq. (2.7), one used the modes defined in Eq. (2.6), or the LP modes in the scalar picture, one would find that the

modes carried zero angular momentum per photon. By investigation of Eq. (2.23) and Eq. (2.22), one notes that the integral in Eq. (2.22) is zero by parity. Alternatively, the angular momentum operators in this system are linear due to parity in ϕ , and the modal basis of Eq. (2.6) is evidently an equal-weight composition of the basis of Eq. (2.7), implying that the ensemble average of OAM would be zero.

We end this section with a table of mode shapes and designations from the LP, HE/EH, and OAM modes in the hope of avoiding confusion in further chapters.

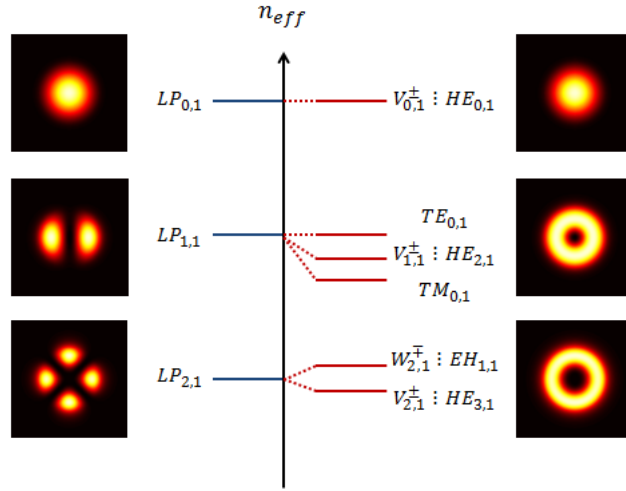


Figure 2-2: Schematic representation of the first few guided modes in a few mode fiber, in order of increasing n_{eff} . Mode labels for each mode in the scalar picture are on the left, while the labels for each mode in the weakly guiding picture are on the right; both OAM and conventional HE/EH mode labels are listed for clarity. Note that each scalar mode order (blue line) is quadruply degenerate, while each vector mode order (red line) is doubly degenerate

2.4 Summary

We have discussed the functional forms of the electromagnetic fields in optical fibers. It has been shown that fiber modes with azimuthal mode order j , where j is assigned in a cylindrical coordinate frame, carry angular momentum of $j\hbar$ per photon. For

weakly guiding waveguides, the modes are readily identifiable as pure OAM states, with SAM either aligned or anti-aligned to the OAM. Conventional HE and EH modes in weakly guiding fibers can be written as linear combinations of degenerate OAM states, but carry 0 angular momentum per photon on average. The separation in β between SOa and SOaa OAM modes is determined by index contrast and electric field overlap with index gradients. The importance of this separation will be discussed in detail in Chap. 3.

For strongly confining waveguides, no such identification is possible, as the modes are not OAM eigenstates, with a non-integer expected value of OAM. This is evident from the mode field structure in the case where the radial and azimuthal components of the electric field become dissimilar, that is, for modes which strongly feel confinement effects in high-contrast fibers. This will provide a design criterion in the coming chapters, when fibers supporting OAM states are discussed.

Chapter 3

Fiber Mode Coupling

The fiber modes discussed in previous section exist in theoretically perfect fibers. Such fibers do not exist in the real world. In practice, there will always be some form of imperfection which affects fiber performance at some level. These imperfections can be separated into two categories: those which are intrinsic to a fiber once it is fabricated such as slight eccentricity, frozen-in birefringence, voids, and longitudinal composition fluctuations, and those which are extrinsic to the fiber, including macroscopic and microscopic bends, twists, and external stress and strain (Marcuse, 1974). Such imperfections can result in loss in single mode fibers (Marcuse, 1982; Petermann, 1976; Bjarklev, 1986), mode-coupling in multimode fibers (Gloge, 1972; Marcuse, 1972; Marcuse, 1975; Olshansky, 1975), and distortion of the guided modes which can compromise large A_{eff} designs for fiber lasers (Fini, 2006).

In addition to parasitic imperfections, controlled perturbations can be induced, typically to excite a specific HOM or set of HOMs. These include long-period gratings, both photoinduced (Vengsarkar et al., 1996) and microbend-induced (Blake et al., 1986), evanescent field couplers (Sorin et al., 1986), and fused fiber couplers (Lai et al., 2007). Fused SMF couplers which rely on perturbative evanescent field coupling are now ubiquitous in research and commercial fiber systems (Sheem and Giallorenzi, 1979). Perturbation-induced mode coupling can be used for sensing applications as well (Burns, 1993).

In this chapter, we briefly review the Coupled Mode and Coupled Power theories.

These theories are well-expounded in other sources (Snyder and Love, 1983; Marcuse, 1974; Chuang, 2009) and we only summarize the main results. We then review two parasitic effects due to mode coupling in coherent communications systems: crosstalk and multi-path interference (MPI), before considering the effects of common fiber perturbations, such as bends, induced birefringence, and twists. Finally, we consider the possible effects of fiber perturbations on OAM carrying fiber modes.

3.1 Coupled Mode Theory and Coupled Power Theory

Coupled mode theory and coupled power theory describe the evolution of an optical field in a waveguide in which the guided modes couple to each other as the fields propagate. Coupled mode theory considers a complex optical field, and accounts for the evolution of the total field (amplitude and phase) while coupled power theory assumes that coupling is incoherent, predicting only the average response of the field amplitude in the coherent case, but at the benefit of a much simplified mathematical form (Marcuse, 1974; Poole, 1988). For the following discussions, we use Marcuse's notation. To formulate coupled mode theory, one can either use ideal modes of a fiber and study their complex amplitude distribution as a function of distance, or use local normal modes, the exact solutions of local waveguides, and study coupling between these modes from segment to segment. We review the former here (Marcuse, 1974).

Suppose that one excites several modes in a fiber, and all propagate in the forward direction with no loss. We write the total optical field as:

$$\mathbf{E}_{total} = \sum_{\mu=1}^N c_{\mu}(z) \mathbf{E}_{\mu} e^{i\beta_{\mu}z} \quad (3.1)$$

Here μ is a mode index, encompassing both radial and azimuthal quantum numbers, N is the total number of modes supported by the fiber, and c_{μ} is the complex weight of the mode μ . The waveguide is perturbed. A perturbation should be classified by a

deformation function, which contains information on its longitudinal behavior, $f(z)$, and a coupling coefficient which describes possible coupling from mode ν to mode μ :

$$\kappa_{\mu\nu} = \frac{\omega\epsilon_0}{4i} \int \int dA \mathbf{E}_\mu^* \cdot \Delta\epsilon(r) \cdot \mathbf{E}_\nu \quad (3.2)$$

Here $\Delta\epsilon = \Delta n^2$ is the local change in dielectric constant provided by the perturbation (i.e. if a hole is cut in the center of the fiber, $\Delta\epsilon$ would be a *circ* function with a negative amplitude and the radius of the hole). $\Delta\epsilon$ could be a scalar (for a bend) or a tensor (for induced birefringence).

Coupled mode theory prescribes a series of coupled amplitude equations to determine the evolution of the mode weights c_μ :

$$\frac{dc_\mu}{dz} = \sum_{\nu=1}^N \kappa_{\mu\nu} f(z) c_\nu(z) e^{i(\beta_\mu - \beta_\nu)z} \quad (3.3)$$

and similarly $\forall\mu$. This results in a set of N coupled differential equations, each of which is dependent on the shape function of the perturbation, $f(z)$.

In the case of very simple shapes such as a grating, in which $f(z)$ is exactly periodic, the equations can be solved directly. Explicitly, for a long period grating:

$$\Delta n = \sigma(z) \left[1 + m \cos\left(\frac{2\pi}{\Lambda} z\right) \right] \quad (3.4)$$

where $\sigma(z)$ describes the spatial envelope of the grating, m is the modulation depth, and Λ is the grating period (Erdogan, 2000). Note that in Eq. (3.3), f is defined with respect to ϵ , but for small deformations $\Delta\epsilon = 2\Delta n$, so Eq. (3.4) is directly usable. Assuming that $\sigma(z)$ is uniform and $m = 1$, $f(z)$ can be directly factored into the complex exponential in Eq. (3.3). If the grating is well designed, $\Delta\beta = \beta_\mu - \beta_\nu - 2\pi/\Lambda \approx 0$ for only one mode, $\nu = s$. Coherent transfer of energy from mode s to mode μ occurs, while the other modes do not see appreciable power due to phase mismatch. If only mode s is excited at the front facet of the waveguide, the power ratio between

modes μ and s is given by (Chuang, 2009):

$$\frac{|c_\mu|^2}{|c_s|^2} = \frac{|\kappa_{\mu s}|^2}{|\Delta\beta|^2 + |\kappa_{\mu s}|^2} \sin^2 \left(z \sqrt{\Delta\beta^2 + \kappa_{\mu s}^2} \right) \quad (3.5)$$

If $\Delta\beta = 0$, total transfer of power can occur, provided that the coupling coefficient is not zero. For a typical photo-induced grating, this means that one can convert between modes of the same azimuthal mode order. For example, Fig. 3-1 shows a fabricated grating converting from the fundamental mode into the $LP_{0,19}$ mode, in this case with conversion of more than 99.99%. For a mirobend grating, this means that the strongest coupling will be between modes with $\Delta l = 1$.

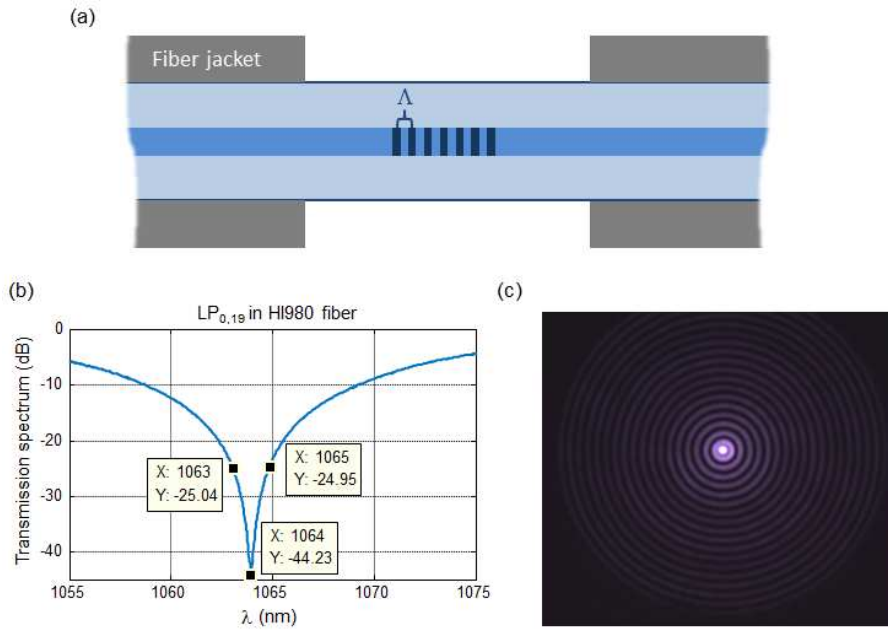


Figure 3-1: (a) Schematic illustration of a photo-induced fiber grating with period (b) measured transmission spectrum of fiber grating, period $\Lambda \approx 69\mu m$ in Hi980 fiber with intent to excite the $LP_{0,19}$ mode (c) Imaged grating output at resonance

However, in the general case, Eq. (3.3) is intractable, or at least computationally intensive to solve. It is more convenient to directly calculate the power in mode μ as

a function of distance (Marcuse, 1974)

$$\frac{dP_\mu}{dz} = \sum_{\nu=1}^N \kappa_{\mu\nu} \langle c_\nu c_\mu^* f(z) \rangle e^{i(\beta_\mu - \beta_\nu)z} + cc. \quad (3.6)$$

where $\langle \rangle$ denotes an ensemble average, and P_μ is the power carried by mode μ . If the mode amplitudes do not appreciably change over the correlation length of the perturbation, that is, if f is a stationary random function with some correlation length L_c over which $c_\mu(z - L_c) \approx c_\mu(z)$, then the coupled power equations, combined with the relationship:

$$\frac{dP_\mu}{dz} = \left\langle \frac{dc_\mu}{dz} c_\mu^* \right\rangle \quad (3.7)$$

can be simplified to:

$$\frac{dP_\mu}{dz} = \sum_{\nu=1}^N h_{\mu\nu} (P_\nu - P_\mu) \quad (3.8)$$

for mode coupling rate

$$h_{\mu\nu} = |\kappa_{\mu\nu}|^2 \langle |F(\beta_\mu - \beta_\nu)|^2 \rangle \quad (3.9)$$

$$= |\kappa_{\mu\nu}|^2 \int_{-\infty}^{\infty} R(u) e^{-i(\beta_\mu - \beta_\nu)u} du \quad (3.10)$$

where $R(u) = \langle f(z)f(z-u) \rangle$, and $R(0) = \sigma^2$, that is, R is the autocorrelation of f and its value at $u = 0$ is the standard deviation. Since h has no spatial dependence Eq. (3.8) is a series of algebraic equations which can be directly solved. In the case of only two modes, where all power is initially launched into mode s , the power transfer between mode s and mode μ is given by (Marcuse, 1974; Kawakami and Ikeda, 1978):

$$\frac{P_\mu}{P_s}(z) = \tanh(h_{\mu s} z) \quad (3.11)$$

The difference between Eq. (3.5) and Eq. (3.9) is coherence. Since the assumptions leading to Eq. (3.9) imply that the mode amplitudes do not change appreciably over

the correlation length of the perturbation, power grows incoherently and tends towards an equilibrium. In the coherent case, return-coupling is permitted. In the case of a grating, for instance, Eq. (3.11) is wildly inappropriate, since the perturbation's correlation length is the length of the grating, over which the modal weights appreciably change. For random perturbations, however, Eq. (3.11) is often appropriate to describe transfer of power.

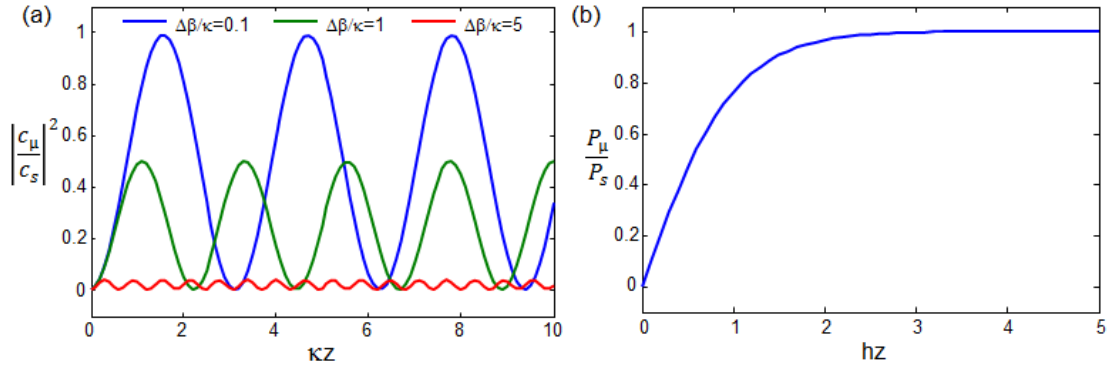


Figure 3.2: (a) Power transfer predicted by coupled mode theory for different ratios of $\Delta\beta$ to κ (b) Power transfer predicted by coupled power theory

Both coupled mode theory and coupled power theory, however, underscore the importance of two intuitive fundamental quantities:

1. Phase matching, that is, the likelihood of a perturbation containing the momentum component $\Delta\beta = \beta_\mu - \beta_\nu$, which, for random perturbations, tends to increase as $\Delta\beta \rightarrow 0$.
2. Perturbation symmetry, manifest in the coupling coefficient, $\kappa_{\mu\nu}$. Even if coupling is phase matched, no coupling is possible if $\kappa_{\mu\nu} = 0$. Thus, consideration of Eq. (3.2) is critical in determining potential sources of and paths for mode coupling.

With these results in hand, we next investigate some random perturbations commonly encountered in optical fibers.

3.2 Common Fiber Perturbations

Unless a perturbation is perfectly periodic, or has some long-range symmetry, the correlation function $R(u)$ will have a maximum value for $u = 0$, and will decay for larger values since a random series of perturbation should, after some distance, lose all correlation with the previous perturbation shape (See Section 4.6 in (Marcuse, 1974)). Eq. (3.9) thus implies that modes which are proximal in β , or equivalently Δn_{eff} , will couple more readily under random perturbations.

In this section, several common types of random perturbations are considered. Their shape functions, $\Delta\epsilon$ (or Δn), are briefly reviewed from literature.

3.2.1 Fiber Bends and Shape Deformations - Phase Perturbations

Bends are likely the most common shape perturbation imaginable. To first order, a bent fiber can be treated as a straight fiber with a phase perturbation (Taylor, 1984), and which can deform lower-order modes in a fiber (Fini, 2006; Fini and Ramachandran, 2007). To second order, bends introduce birefringence (Ulrich et al., 1980), which will be discussed in the next section, as well as elliptical shape deformations.

If a bend is weak enough that birefringence can be ignored, the shape function of the perturbation can be written as (Blake et al., 1987):

$$\Delta\epsilon = e^{i\frac{2\pi n}{\lambda}(1-\chi)r\theta\cos\phi} \quad (3.12)$$

where θ is the local bending angle, n is the refractive index of the core and approximately that of the cladding, $\chi \approx 0.22$ is a factor to account for a stress-induced refractive index change, and (r, ϕ) are transverse coordinates as in Chap. 2. It is

obvious from modeling the bend as a perturbation which is odd in phase, that bends should be able to couple between $l = 0$ and $l = 1$ modes of fibers, and indeed microbend gratings function in such a fashion (Blake et al., 1986)

Eq. (3.12) can be converted into a more useful formula by use of the Jacoby-Anger expansion (Abramowitz and Stegun, 1972):

$$e^{izc\cos\phi} = \sum_{k=-\infty}^{\infty} i^k \alpha_k(z) e^{ik\phi} \quad (3.13)$$

for $z = \frac{2\pi n}{\lambda} (1 - \chi) r\theta$ and $\alpha_k = J_k(z)$ for the bessel function of the first kind of order k , J_k .

The above is evidently an expansion of $\Delta\epsilon$ into OAM orders. Similar formalisms are useful in free-space to predict diffraction from objects with discrete rotational symmetries (Jack et al., 2008). Any general shape deformation can be expressed thus, albeit with different α_k . For instance, an elliptical deformation of the fiber cross-section is a perturbation with predominantly α_2 components (Golowich and Ramachandran, 2005).

3.2.2 Linear Birefringence

Due to the existence of two polarization modes within SMF, the problem of polarization conversion in fibers was widely studied beginning in the late 1980s, since appreciable polarization mode dispersion (PMD) could compromise communications link intensity (Poole, 1988; Kawakami and Ikeda, 1978; Poole et al., 1991).

A single mode optical fiber can be treated as a waveplate, or stack of waveplates (Tsao, 1992). Both intrinsic (added intentionally or unintentionally in fabrication) and extrinsic sources of birefringence exist. The most common extrinsic source is bends, which can induce linear birefringence between the plane of the bend and the plane's normal vector which scales as the curvature of the bend squared (Ulrich et al.,

1980; Smith, 1980). PM fibers are created by adding a significant fabrication birefringence, typically by adding stress rods around the core or by making the fiber elliptical (Rashleigh, 1983). For many PM fibers, the target birefringence $B_{xy} = (n_{eff}^x - n_{eff}^y)$ was on the order of 10^{-4} , with fibers whose birefringence was about 4×10^{-4} showing crosstalk after $1km$ on the order of -20 to $-30dB$, although the exact implementation of the birefringence via stress rods, air holes, etc also partially determines the mode coupling strength (Noda et al., 1986; Kaminow, 1981).

Conventional SMF typically has intrinsic birefringence on the order of $10^{-5} \sim 10^{-6}$, which is still enough to feature PMD over longer fiber links. The solution was to use spun fiber (Barlow et al., 1981), in which the fiber preform is spun as it is drawn. The rotation of the preform results in the local undesired birefringence rotating such that after a few rotations the birefringence is effectively averaged out. Such rotation does not leave torsional stress, unlike a fiber which is drawn and then twisted, to be discussed in Sec. 3.2.3.

One can view linear birefringence as either forcing preferential axes of polarization on the fundamental modes of an SMF, and thus changing the normal modes of the fiber, or as creating an effective waveplate which couples two pre-labeled polarization modes, potentially two circularly polarized modes if the angular momentum basis set for fiber modes is used. Laboratory fiber polarization controllers (polcons) which utilize this effect are readily available (for instance, see Thorlabs catalog item FPC030).

3.2.3 Twist

Extrinsic twist should be considered in two separate regimes: weak and strong twist. Weak twist implies only a rotation of Cartesian coordinates; referring to those rotating axes, it appears that the electric field does not change. Strong twist in SMF results in a circular birefringence $B_c = (n_{eff}^{RCP} - n_{eff}^{LCP})$. The perturbation can be written as

(Ulrich and Simon, 1979):

$$\Delta\epsilon = n_0^4 p_{44} \tau r \begin{pmatrix} 0 & 0 & \sin(\phi) \\ 0 & 0 & -\cos(\phi) \\ \sin(\phi) & -\cos(\phi) & 0 \end{pmatrix} \quad (3.14)$$

where the matrix is in the basis of $(\hat{\mathbf{x}}, \hat{\mathbf{y}}, \hat{\mathbf{z}})$, n_0 is the average refractive index of the fiber, p_{44} is an element of the electrooptic tensor, and $\tau = \frac{2\pi}{\Lambda}$ is the local rotation rate of the fiber over a twist pitch of Λ , and can be positive or negative. In view of circular polarizations, Eq. (3.14) converts:

$$\hat{\sigma}^\pm \rightarrow \mp i e^{\pm i\phi} \hat{\mathbf{z}} \quad (3.15)$$

Thus the longitudinal and transverse fields are coupled.

The circular birefringence induced in SMF is a special case; in general, twist induces a change in n_{eff} according to the total angular momentum, j , carried by a fiber mode (Alexeyev et al., 2008):

$$\Delta\beta_{l,m} = -\frac{\tau p_{44} n_0^2}{2} j \quad (3.16)$$

This splitting breaks the degeneracy between the previously 2-fold degenerate vector modes, and has led to speculation about strongly twisted fibers supporting optical vortices (Alexeyev et al., 2004; Alekseev and Yavorskii, 2005). In a fiber where waveguide design has already broken the degeneracy between SOa and SOaa OAM modes, the application of twist implies that there is no degeneracy among the 4 modes of a given $|l|$. The splitting is directly proportional to both twist rate and total angular momentum, meaning that a particular mode's n_{eff} can be either increased or decreased with the correct handedness of twist, and that if the distribution of twist is random, the expected value of the change is zero.

3.3 Fiber Perturbations and OAM

With the behavior of common perturbations understood, we consider the possible effects of such perturbations on OAM modes of fibers, under the assumption that the weakly guiding approximation is valid. A schematic of the effective index distribution of set of OAM modes and the perturbations of appropriate symmetry to couple among them is shown in Fig. 3-3. $l = 5, 6, 7$ because the fibers to be discussed support these higher order OAM modes. Coupling between adjacent $|l|$ states is enabled by bends.

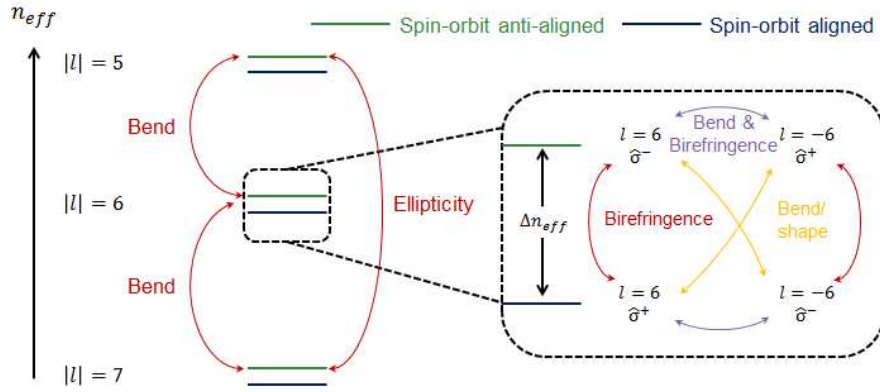


Figure 3-3: Schematic illustration of effective index distribution of OAM modes and the perturbations necessary to couple among them. Inspired by a similar figure in notes presented by Dr. S. Golowich.

Within a family of a given $|l|$, there are several coupling routes of interest. Coupling between $l = 6 \hat{\sigma}^-$ and $l = 6 \hat{\sigma}^+$, for instance, requires a birefringent perturbation to couple spins, the same kind of perturbations under consideration for mode stability in conventional PM fibers. Thus, when designing OAM fibers Chap. 6 we aim to design waveguides where Δn_{eff} between the SOa and SOaa modes of the same family is of the order of 10^{-4} .

Twist, on the other hand, directly modulates the effective index spectrum of the OAM modes, as illustrated in Fig. 3-4. Depending on the handedness of the twist, ei-

ther positive or negative total angular momentum modes will be increased in effective index. It is evident from the schematic that for some critical twist, the $l = 6 \hat{\sigma}^+$ and $l = -6 \hat{\sigma}^+$ states will actually become degenerate. This is experimentally observable, and will be discussed in Chap. 7.

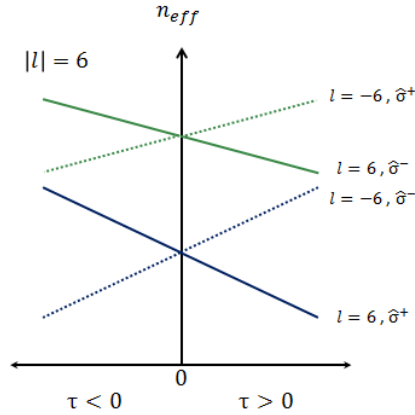


Figure 3-4: Illustration of effective index modulation by applied twist for a sample ($|l| = 6$) OAM family. Splitting increases linearly with twist, but at different rates for SOa and SOaa modes due to differing total angular momentum; here exaggerated for illustration purposes.

We next briefly consider the effect of perturbations on a communications system.

3.4 Crosstalk and Multipath Interference

The quality of a telecommunications system is determined by its data rate and bit error rate (BER), or the probability of transmitting an erroneous bit. Traditionally, high speed optical communications transmitting at 1Gbps required BERs on the order of 10^{-12} , and even lower for higher data rates (Keiser, 2011), although recent advances in coding using forward error correction (FEC) has allowed data transmission with bit error rates as low as 10^{-3} (Sab and Lemaire, 2000; Essiambre et al., 2010).

Mode coupling can be seen to impact the BER in two significant but completely

distinct ways: crosstalk and MPI (Ramachandran et al., 2003; Ramachandran et al., 2005a). Crosstalk is simple to understand as the fraction of power that leaks from one channel or a set of channels into another. If two channels, A and B simultaneously transmit data at the same power and data rate, and 10% of the power from A leaks into B after $1km$, the crosstalk is $-10dB$. For cases of distributed incoherent mode coupling, crosstalk in dB is given by the logarithm of Eq. (3.11).

MPI denotes interference between a desired signal and a weak, possibly delayed, version of the same signal. In the above example, suppose that two identical $1km$ segments of fiber are spliced together, causing another $10dB$ of crosstalk in the second fiber. Thus, a signal at the $-20dB$ level has transitioned from A to B and back again as a weak replica, and will interfere with the original signal. MPI can be coherent or incoherent, depending on source bandwidth and path length difference between the signal and replica (Ramachandran et al., 2003).

Both crosstalk and MPI require a projection to accurately measure (in the above example, the powers of A and B must be independently measurable). In most cases, this projective combining may be unintentional, and can degrade system performance. In Fig. 3-5, an SMF is spliced to a fiber which supports the $LP_{0,2}$ for dispersion compensation. At the splice point, some amount of $LP_{0,1}$ and $LP_{0,2}$ are excited and propagate through the High -D fiber. At the second splice point, both $LP_{0,1}$ and $LP_{0,2}$ are projected back into the guided mode of the SMF but with different phases, given that they have different propagation constants in the High -D fiber. When the total power is measured as a function of wavelength, as oscillation is evident due to MPI and the difference in effective index between $LP_{0,1}$ and $LP_{0,2}$.

Alternatively, MPI can be created by a projective measurement, and used for diagnostic purposes. Two modes ($TE_{0,1}$ and $TM_{0,1}$) are excited in a vortex fiber (to be discussed in Chap. 6) with roughly equal power, the fiber output is filtered into $\hat{\sigma}^+$

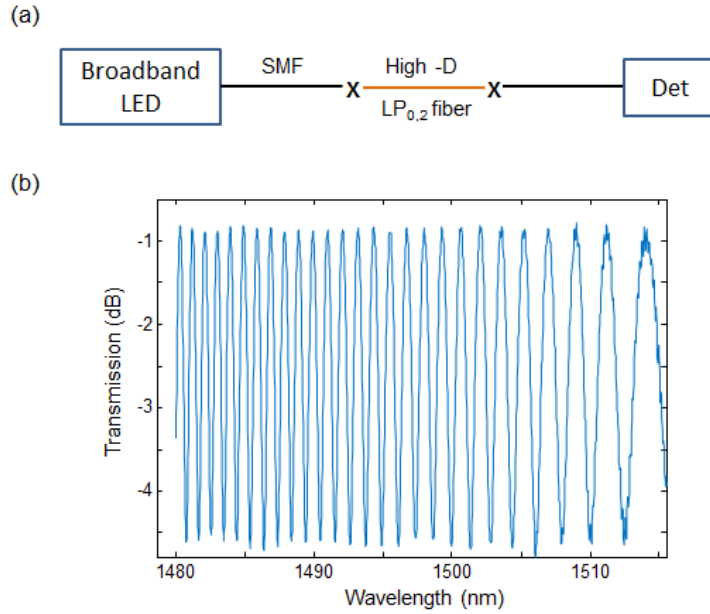


Figure 3.5: (a) Experimental schematic: an SMF is spliced to a High-D fiber supporting the $LP_{0,2}$, which can be excited at the splice point. When the High-D fiber is spliced back to SMF, both $LP_{0,1}$ and $LP_{0,2}$ are projected back onto the fundamental mode of SMF, causing MPI (b) Power detected as a function of wavelength. Data courtesy of Boyin Tai.

and $\hat{\sigma}^-$ and imaged on a camera, and the source wavelength is swept. The intensity value in grey levels at a single pixel is measured as a function of wavelength, and shown in Fig. 3.6. Although each mode is strictly orthogonal and the total power conserved as a function of wavelength, at a single spot interference between the two modes is observed. This empowers interferometric mode purity techniques such as S^2 and C^2 , to be discussed in Chap. 4

3.5 Summary

We have reviewed coupled mode theory and coupled power theory, which underscore the importance of both the spatial symmetry of a perturbation and the difference

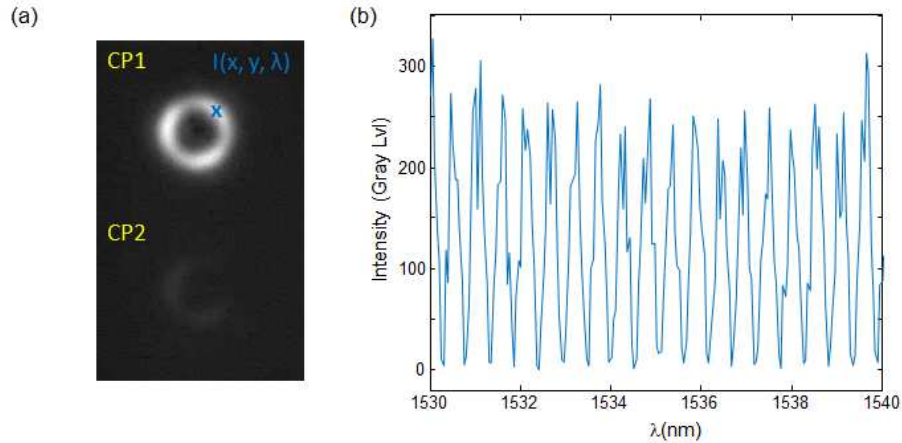


Figure 3-6: (a) Experimental image of fiber output. (b) Power detected in gray levels as a function of wavelength for a single pixel

in effective index (equivalently, β) for mode stability. Birefringent perturbations can couple OAM modes which are nearly-degenerate, underscoring the need for a fiber design in which this near-degeneracy is lifted as much as possible, at least on the order of 10^{-4} in n_{eff} . Bends can couple adjacent OAM mode orders, but as we will see in Chap. 6, these are typically well separated in n_{eff} and resist this coupling.

This concludes the purely theoretical portion of this document. We will next begin to discuss how OAM states can be excited and transmitted over fiber. In Chap. 6 we will discuss fiber design in great detail and in Chap. 5 we will discuss attractive options for state excitation and multiplexing. However, in order to test the fibers we design and fabricate and the excitation mechanisms we propose, methods of determining mode purity must be introduced.

Chapter 4

Mode Characterization

The study of OAM mode characterization, qualitative and quantitative comparisons of fibers supporting OAM modes, and OAM mode excitation are all coupled. To compare different fibers, we need the ability to excite modes in said fibers. To compare different excitation mechanisms, characterization mechanisms are needed. And to test characterization mechanisms, it is of course necessary to have a mode or set of modes in the first place. In order to provide more context for the fibers designed in Chap. 6, in this chapter we describe the theoretical design and experimental results for different mode characterization schemes. Details on how modes are excited are postponed until Chap. 5, but it is assumed for this chapter that methods to selectively excite OAM states exist.

Many modal techniques for determining the modal content emitted by a fiber under test (FUT) exist, and they typically fall into three categories. The first is a computationally intensive modal decomposition via computationally intense algorithms (Brüning et al., 2013). These require the calculation of the guided modes of a fiber, and typically require the measurement of the fiber output in the near field and in the far field. An algorithm then tries to reconstruct the optical near and far fields by varying the complex modal weights and seeking to reduce some cost function such as the mean squared difference between the measured and reconstructed images, or to maximize a correlation function (Shapira et al., 2005). Alternatively a gerchberg-saxton algorithm (GSA) can be used to calculate the full complex amplitude distribution

in the near field, at which point a dot product can be used to calculate the modal weights (Fienup, 1982). These algorithms tend to be slow, and fare poorly when the number of modes is more than 10 or 20 (Brüning et al., 2013). The second category is based on the temporal or frequency response of the fiber under test. As each mode (typically) possesses a unique effective index, sweeping wavelength varies the phases of the modes at the fiber output in a periodic fashion and the wavelength-dependent fluctuations convey information about excited fiber modes. This can be done without a reference beam and is conventionally called spatially and spectrally resolved imaging (S^2) (Nicholson et al., 2008), or with an external reference where it is called cross-correlated imaging (C^2) (Ma et al., 2009). C^2 can be achieved by scanning a delay stage (Tkach and Chraplyvy, 1986) or by scanning a laser’s frequency (Poole, 1989; Gisin et al., 1991), for which a measurement can take on the order of a second (Demas and Ramachandran, 2014). The third category is output projection, where the weight of each mode is (typically sequentially) determined by projection onto SMF via a hologram (Carpenter et al., 2012; Schulze et al., 2013). This method is brute force, generally slow, and requires precise alignment.

In this chapter we describe several methods used to characterize the output of OAM carrying fibers. It is assumed that the modes of interest are weakly guided OAM modes. It is worth noting that several of the methods we discuss are not exclusive, and many can be used in concert. Polarization binning and symmetry arguments (leading to the so-called Ring technique) are outlined, as are swept wavelength techniques such as S^2 imaging. Particular attention is paid to time of flight measurements, which are used throughout the rest of this document to describe discrete and distributed mode coupling. Output projection measurements are performed. Output coupling into an OAM-specific mode sorter is briefly described. We start first with a special, and OAM-specific mode purity metric which has become nearly ubiquitous with OAM

states. It is visually appealing, intuitive, qualitatively deceptive, and quantitatively completely useless.

4.1 Spiral Interference Patterns

A simple method to identify the topological charge of an OAM state is to interfere the phase vortex ($e^{il\phi}$) with an expanded plane wave of the same polarization (Yao and Padgett, 2011). If the vortex beam and an isotropic (no ϕ -dependence) reference wave are spatially centered but tilted with respect to each other, the result is a ‘fork’ interference pattern, as in Fig. 4-1 (a). The topological charge, l , can be determined by counting the number of ‘tines’ on the fork corresponding to a single stem, in this case, 8. The fork points up if the topological charge and the tilt (chosen as along x , $\phi_{tilt} = kx$ for some k) are opposite in sign, and points down if they are of the same sign. If the OAM state and reference beam are coaligned both in space and angle, a spiral pattern instead results. The content of the spiral pattern depends on the relative defocus as the equiphase curves yielding maxima in the interference pattern are given by $l\phi + Rr^2 = 0$, where R is the difference in defocus (spherical wavefront curvature) between the OAM state and the reference beam. Thus, if both beams are collimated the interference fringes are lines pointing radially outward from the beam center and which do not curve Fig. 4-1 (b). If some defocus is introduced to either beam, the interference fringes curve Fig. 4-1 (c-d). The absolute value of the OAM is given by the number of spiral arms, also called parastiches, while the direction of arm curvature depends on the sign of l . Note however that if the OAM state in free space is created by collimating or imaging the output of a fiber, the spiral arm direction can be flipped by physically moving the fiber through the focal plane of the lens, thus changing the sign of the defocus. If two OAM states are added in equal amounts and then interfered with a reference, as in an LP mode, the resulting pattern is star

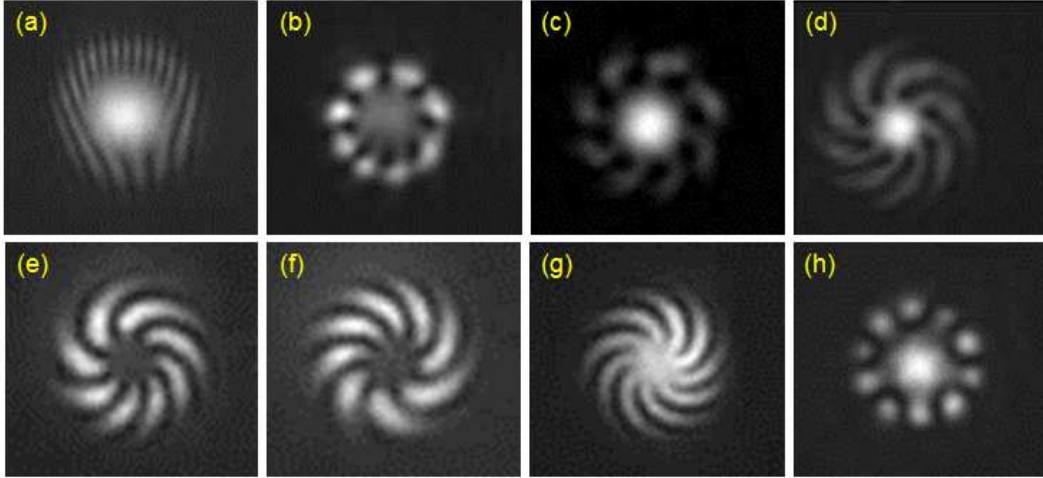


Figure 4.1: Experimentally measured interference between an OAM state and a Gaussian reference beam under different experimental conditions. (a) $l = 8$ OAM state interfered with tilted Gaussian (b) $l = 8$ state interfered with Gaussian with no defocus (c) $l = 8$ OAM state slightly defocused before interference (d) $l = 8$ state massively defocused (e) $l = 8$ state and reference powers balanced to remove center spot (f) $l = -8$ state and reference (g) $l = 9$ state and reference (h) approximately equal parts $l = 5$ and $l = -5$ and reference

shaped and will have no curvature under any defocus, as in Fig. 4.1 (h). Note that Fig. 4.1 (a-e) could readily be achieved with exactly the same input OAM state while only changing the reference beam.

Spiral interference patterns are intuitive and aesthetically pleasing, and as such are typically included in almost any experimental publication on OAM. However, some authors (Courtial et al., 1997; Martinelli et al., 2004; Dashti et al., 2006; Chimento et al., 2012; Brunet et al., 2014b) (among many, many others) use spirals or fork patterns as proof for excitation or existence of pure OAM states. With additional information, this is not an invalid statement, however, spirals yield no quantitative information on mode purity and can be qualitatively deceptive. For instance, consider Fig. 4.2. If the OAM state is predominantly of OAM l with even a slight amount of $-l$, corruption of the spiral pattern is evident as the arms become beady. However, if

the OAM state is predominantly of OAM l and contains a reasonably large amount of OAM $l - 1$, the spiral pattern becomes slightly asymmetric but the arms are still clearly visible. Even in the case of equal power in l and $l - 1$ as in Fig. 4-2 (g), one can still count 8 arms and could conclude, incorrectly that one had an $l = 8$ OAM state. Note that such asymmetric distortions as Fig. 4-2 (f) could also be obtained by

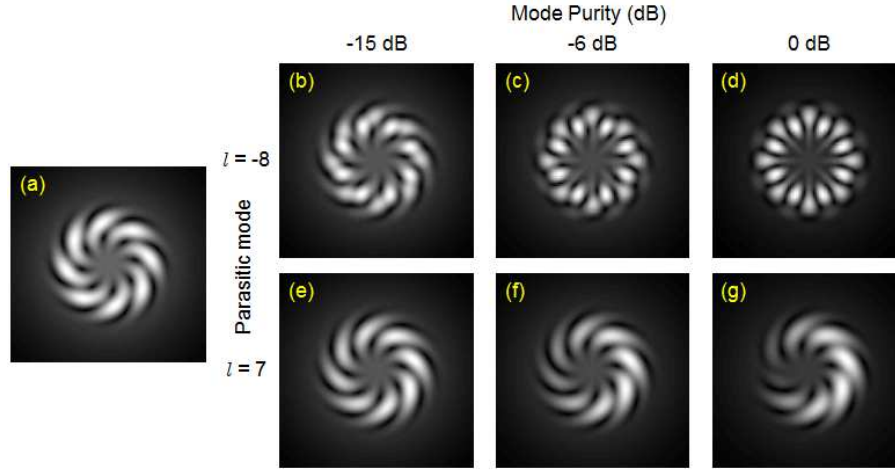


Figure 4-2: Simulated spiral interference patterns. (a) Pure $l = 8$ OAM state interfered with a Gaussian beam (b-d) Interference between a reference beam and an $l = 8$ OAM state with X crosstalk into $l = -8$, with X printed above each figure (e-g) Interference between a reference beam and an $l = 8$ OAM state with X crosstalk into $l = 7$, with X printed above each figure

off-centering the Gaussian reference beam, or having a slightly anisotropic reference beam.

Thus we conclude that while obtaining a spiral pattern is indicative of an OAM state, it is not a robust enough metric to be used for determining mode purity in any sense. If one can be reasonably confident that crosstalk is relatively low, there are cases where performing a spiral interference can yield useful information, such as the Ring method (Sec. 4.3).

4.2 Polarization Binning

Recalling the definition of OAM modes from Chap. 2 (Ramachandran and Kristensen, 2013):

$$V_{l,m}^{\pm} = \hat{\sigma}^{\pm} e^{\pm il\phi} F_{l,m}(r) e^{i\beta_{l,m}^V z} \quad (4.1)$$

$$W_{l,m}^{\mp} = \hat{\sigma}^{\mp} e^{\pm il\phi} F_{l,m}(r) e^{i\beta_{l,m}^W z} \quad (4.2)$$

it is clear that the spatial distributions of the SOa and SOaa OAM modes of the same l within one circular polarization, $\hat{\sigma}^{\pm}$, are complex conjugates of each other. Within the $\hat{\sigma}^+$ projection, for instance, if an OAM mode occurs with an observed $l > 0$ it must by definition be SOa, while $l < 0$ implies SOaa. Critically, this implies that if the fiber supports only radial order $m = 1$, there is only one mode which corresponds to a particular l within $\hat{\sigma}^{\pm}$ (with the exception of $l = 1$, see Eq. (2.17a) and Eq. (2.17b)). For the rest of this chapter we assume that $m = 1$ in all cases.

Let the output field of an optical fiber be written as:

$$\Psi = \sum_{l=0}^{l_{max}} \alpha_l^{\pm} V_l^{\pm} + \sum_{l=0}^{l_{max}} \gamma_l^{\mp} W_l^{\mp} \quad (4.3)$$

where l_{max} is the highest OAM state guided in the fiber under consideration, and α_l and γ_l are complex modal weights. The right and left circularly polarized components of Ψ can be split spatially with a combination of a zero-order quarter-wave plate (QWP) and a polarizing beam splitter (PBS), as in Fig. 4-3. For all experiments in this document, a polarization beam displacing prism is used in lieu of a typical 90-degree polarization splitter such that both polarizations are co-propagating and can be imaged easily. Unless otherwise indicated, PBS refers to this kind of beam splitter. The QWP is set at 45-degrees with respect to the fast and slow axes of the PBS in the following way. Without the QWP in place, put a linear polarizer between the fiber and PBS, and rotate the polarizer axis to minimize intensity in

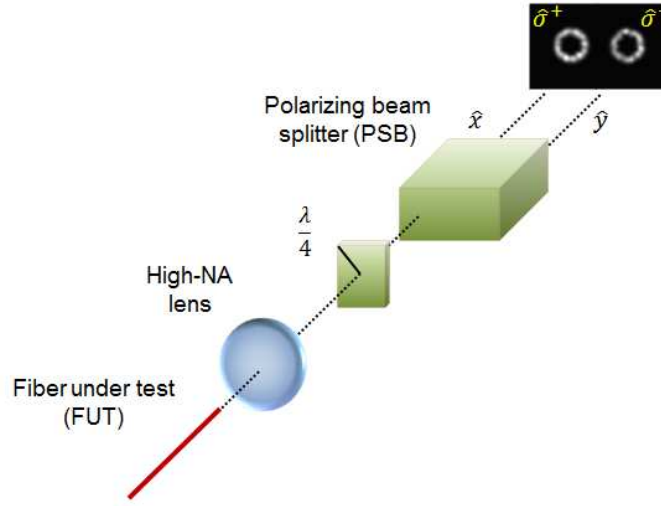


Figure 4-3: Schematic of experimental system for separating circular polarizations

one bin (polarization projection). Then insert the QWP between the linear polarizer and PBS and rotate the QWP until equal power is achieved in each projection. The linear polarizer is then removed. The rotation angle of the PBS is irrelevant so long as the QWP's angle is appropriately selected, but it is typically chosen such that the two beams are horizontally displaced. For such experiments, a high-NA lens, either a short focal length aspheric lens or a microscope objective is needed to reliably capture high-order OAM modes, which diffract rapidly in free space. The fiber facet is imaged onto an InGaAs camera (Allied Vision ‘Goldeye’ series, $30\mu\text{m}$ pixel pitch, 320×256 pixels, 12 bit)

For some cases of interest, comparison of optical powers within each circular polarization bin directly yields information about fiber mode content. For instance, for short fibers (fiber length, $L < 10\text{m}$), which are laid on an optical table in reasonable large coils (radius $\approx 10\text{cm}$), and for which the effective index separation between SOa and SOaa states of the same $|l|$ is of the order of 10^{-4} , we can reasonably assume that the coupling between SOa and SOaa states is negligible, at the -20dB level or

lower. With good input coupling, the presence of other $|l|$ states can be similarly suppressed (see Chap. 5). In this instance, the mode coupling most readily observable is between degenerate states. This can be experimentally confirmed by spiral interference - if power appears in both circular polarization bins, and the observed spirals have the same number of parastiches but with the opposite handedness and reasonably clean quality, we can assume that the dominant mode in each bin is one of the two degenerate states, that is:

$$\Psi^{\hat{\sigma}^+} = \alpha_l^+ V_l^+ = \alpha_l^+ F_l(r) e^{il\phi} \quad (4.4a)$$

$$\Psi^{\hat{\sigma}^-} = \gamma_l^- W_l^- = \gamma_l^- F_l(r) e^{-il\phi} \quad (4.4b)$$

The intensity of the polarization-sorted fiber output is measured by the camera:

$$I^{\hat{\sigma}^+} \propto |\alpha_l^+|^2 F_l^2(r) \quad (4.5a)$$

$$I^{\hat{\sigma}^-} \propto |\gamma_l^-|^2 F_l^2(r) \quad (4.5b)$$

The mode purity of the fiber output is given by $|\alpha_l^+|^2 / |\gamma_l^-|^2$. This can be calculated experimentally by spatial integration over the two polarization bins, since the radial distributions of the intensity are identical:

$$\frac{|\alpha_l^+|^2}{|\gamma_l^-|^2} = \frac{\int dA I^{\hat{\sigma}^+}}{\int dA I^{\hat{\sigma}^-}} \approx \frac{\sum_{(x=j,y=k)} I^{\hat{\sigma}^+}}{\sum_{(x=j,y=k)} I^{\hat{\sigma}^-}} \quad (4.6)$$

where (j, k) indicates a single pixel on the camera, and the sum is taken over a rectangular region containing each separate polarization component. This polarization binning measurement can be used to study mode coupling between degenerate states in fiber (Chap. 7) or to study mode excitation with q -plate s, which can excite arbitrary combinations of a pair of two degenerate fiber OAM states (Chap. 5)

4.3 Symmetry Arguments and Introduction to Ring Method

Much additional information can be obtained from polarization-sorted camera images of the fiber output. Consider the electric field distribution in one of the polarization projections after a fiber of length L :

$$\Psi^{\hat{\sigma}^+} = \sum_{l=0}^{l_{max}} \alpha_l F_l(r) e^{il\phi} e^{i\beta_l^V L} + \sum_{l=0}^{l_{max}} \gamma_l F_l(r) e^{-il\phi} e^{i\beta_l^W L} \quad (4.7)$$

We drop ‘ \pm ’ superscripts for brevity, since a single polarization is assumed. The camera will observe the modulus squared of Eq. (4.7), which could in general have many terms. It is useful to group these for classification. There will be a term of the form:

$$\Psi_{DC} = \sum_{l=0}^{l_{max}} |\alpha_l|^2 F_l^2(r) + |\gamma_l|^2 F_l^2(r) \quad (4.8)$$

which has no ϕ dependence. Consequently, we will call this the ‘DC’ term. The rest will be terms with fixed azimuthal dependences, for instance, $\Psi_{\Delta l}$ for $\Delta l = 1$ is given by:

$$\begin{aligned} \Psi_1 = & \sum_{l=1}^{l_{max}} 2 |\alpha_l \alpha_{l-1}| F_l F_{l-1} \cos [\phi + \arg(\alpha_l \alpha_{l-1}^*) + (\beta_l^V - \beta_{l-1}^V)L] + \\ & \sum_{l=1}^{l_{max}} 2 |\gamma_l \gamma_{l-1}| F_l F_{l-1} \cos [\phi + \arg(\gamma_l \gamma_{l-1}^*) + (\beta_l^W - \beta_{l-1}^W)L] \end{aligned} \quad (4.9)$$

Corresponding terms can be written for $\Delta l = 2, 3, \dots, 2l_{max}$, and higher order terms will include cross terms between SOa and SOaa states. $l = 1$ SOaa is included above as shorthand for a combination of TE and TM. The above suggests a Fourier series in terms of the azimuthal coordinate (Bozinovic et al., 2012).

$$\Psi = \Psi_{DC} + \sum_{\Delta l=1}^{2l_{max}} a_{\Delta l} \cos(\Delta l \phi) + b_{\Delta l} \sin(\Delta l \phi) \quad (4.10)$$

with $a_{\Delta l}$ and $b_{\Delta l}$ to be determined. Note that even though Ψ is by definition positive, two Fourier series coefficients are needed to account for both magnitudes and relative phases. For the case of a total of 6 vector modes ($l_{max} = 1$), this problem has been solved using a linear regression and measured radial mode field distributions, and modal powers and phases can be estimated (Golowich et al., 2013). In the general case for a large l_{max} the problem is less tractable.

The difficulties are twofold. First, multiple modes can contribute to the same Δl terms. For instance, an interference between $l = 6$ and $l = 5$ will contribute a $\Delta l = 1$ term, but interferences between $l = 5$ and $l = 4$, and $l = 6$ and $l = 7$ will as well. The only term which can be written in terms of only two modes is the $\Delta l = 2l_{max}$ term, which necessarily contains interference between l_{max} and $-l_{max}$. Assume that only these two modes, the SOa and SOaa states of l_{max} , exist. There will then be two Fourier series components.:

$$\Psi_{DC} = (|\gamma_{l_{max}}|^2 + |\alpha_{l_{max}}|^2) F_{l_{max}}^2(r) \quad (4.11a)$$

$$\Psi_{2l_{max}} = 2 |\gamma_{l_{max}} \alpha_{l_{max}}| \cos [2l_{max}\phi + \text{arg}(\alpha_{l_{max}} \gamma_{l_{max}}^*) + (\beta_{l_{max}}^V - \beta_{l_{max}}^W)L] \quad (4.11b)$$

Eq. (4.11a) and Eq. (4.11b) are invariant to the permutation $\alpha_{l_{max}} \leftrightarrow \gamma_{l_{max}}^*$, meaning that without either additional polarization projections or *a priori* information about the system, the set of equations is not uniquely solvable.

There are, however, two ways in which an azimuthal Fourier series expansion, and the intuition garnered from that picture, are immensely useful. The first is for *in situ* alignment of a mode excitation scheme. As indicated in Fig. 4-4a, when an input coupling is slightly misaligned the output of the fiber takes on a characteristic crescent moon shape, which is indicative of an interference with a strong $\Delta l = 1$. This is typically a result of slight misalignments in the input coupling system (Chap. 5), and better alignment can be obtained by minimizing the anisotropy by eye. This

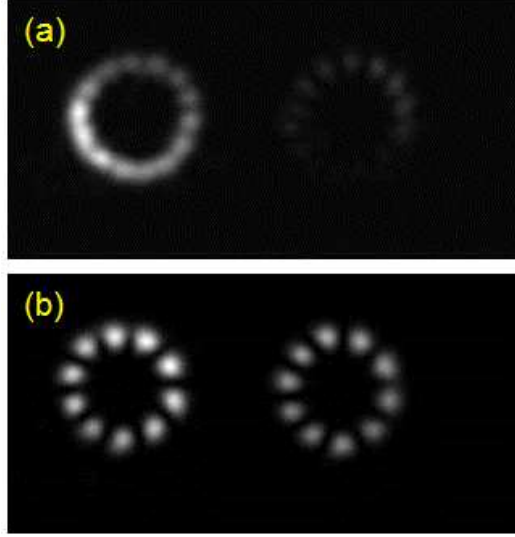


Figure 4-4: (a) Crescent moon-shaped interference pattern indicative of $\Delta l = 1$ interference pattern, typically due to slight input coupling misalignments. (b) $2l$ bead pattern typical of strong mode coupling in the FUT.

provides a useful feedback look for alignment, which can obtain mode purities around $-15dB$ or better. Similarly, if one tries to excite a mode with OAM l and a strong $2l$ component is evident in the fiber output, the cause is typically in-fiber mode coupling, as is the case for $l = 5$ in Fig. 4-4b for one generation of air core fiber. Alternatively, it could be due to poor polarization control following a q -plate used as a free-space OAM generator (Sec. 5.4).

The second useful case is when we can assume that a dominant mode exists, that is, $|\alpha_l| \gg |\alpha_k|, |\gamma_k| \forall k$ if the SOa mode of OAM l is dominant. For the air core fibers under consideration in this document, we may also assume $F_j(r) \approx F_k(r) \equiv F(r) \forall (j, k)$ because of an annular guiding region constraining all modes, including $l = 0$, to have

nearly the same shape, discussed in more detail in Chap. 6. Then:

$$\Psi_{DC} \approx |\alpha_l|^2 F^2(r) \quad (4.12a)$$

$$\begin{aligned} \Psi_{\Delta l=1} \approx & 2 |\alpha_l \alpha_{l-1}| F^2(r) \cos [\phi + \arg(\alpha_l \alpha_{l-1}^*) + (\beta_l^V - \beta_{l-1}^V)L] + \\ & 2 |\alpha_l \alpha_{l+1}| F^2(r) \cos [\phi + \arg(\alpha_l \alpha_{l+1}^*) + (\beta_l^V - \beta_{l+1}^V)L] \end{aligned} \quad (4.12b)$$

⋮

$$\Psi_{\Delta l=2l} \approx 2 |\alpha_l \gamma_l| F^2(r) \cos [2l\phi + \arg(\alpha_l \gamma_l^*) + (\beta_l^V - \beta_l^W)L] \quad (4.12c)$$

⋮

All terms which do not include the dominant mode are assumed small. Eq. (4.12c) is written explicitly because it is often a series component of interest, and is a special case because it can be solved explicitly. Using trigonometric identities, it is clear that:

$$a_{2l} = 2 |\alpha_l \gamma_l| F^2(r) \cos [\arg(\alpha_l \gamma_l^*) + (\beta_l^V - \beta_l^W)L] \quad (4.13a)$$

$$b_{2l} = -2 |\alpha_l \gamma_l| F^2(r) \sin [\arg(\alpha_l \gamma_l^*) + (\beta_l^V - \beta_l^W)L] \quad (4.13b)$$

The product of the modal weights is given by $g_{2l} = \sqrt{a_{2l}^2 + b_{2l}^2} = 2 |\alpha_l \gamma_l| F^2(r)$. The relative mode powers as a function of easily experimentally measurable quantities can then be found by algebraic substitution:

$$\frac{|\gamma_l|^2}{|\alpha_l|^2} = \left(\frac{g_{2l}}{2\Psi_{DC}} \right)^2 \quad (4.14)$$

For other Δl , the Fourier series components still include contributions from 2 parasitic modes, leaving four unknowns (two amplitudes and two phases). Taking

$\Delta l = 1$ as an example:

$$a_1 = 2F^2(r) |\alpha_l| [|\alpha_{l-1}| \cos(\theta_1) + |\alpha_{l+1}| \cos(\theta_2)] \quad (4.15a)$$

$$b_1 = -2F^2(r) |\alpha_l| [|\alpha_{l-1}| \sin(\theta_1) + |\alpha_{l+1}| \sin(\theta_2)] \quad (4.15b)$$

for $\theta_1 = \arg(\alpha_l \alpha_{l-1}^*) + (\beta_l^V - \beta_{l-1}^V)L$ and $\theta_2 = \arg(\alpha_l \alpha_{l+1}^*) + (\beta_l^V - \beta_{l+1}^V)L$. Note that both θ_1 and θ_2 are dependent on the relative phases among three modes. Squaring and summing Eq. (4.15a) and Eq. (4.15b) as earlier will not yield direct information on the relative modal powers involved, due to these relative phases, which could yield falsely high or low mode purity values. To resolve this dilemma, we gain more information by using images at multiple wavelengths, which varies the phase relationship among the modes of interest.

4.4 Swept Wavelength Imaging: Ring Method and S2

Studying fiber modal content by varying the phase relationship among multiple modes has been studied, and has typically been done by sweeping a narrow-band laser or measuring a wide bandwidth of wavelengths at the same time (Nicholson et al., 2008), or by physically scanning a delay stage (Schimpf et al., 2011). We sweep wavelengths using a narrow-band (Bandwidth $< 1pm$) external cavity laser (ECL) (*HP8168F* or New Focus 6528 – *LN*). The wavelength sweep size, $\Delta\lambda$, is determined by the length of fiber under consideration; for lengths of a few meters the ECL is swept over a few *nm* of bandwidth, but for longer lengths the sweep size can be reduced to *1nm* or less. For our case of interest, note that the dependence of the relative modal phases is given by θ_1 and θ_2 , and is broken into two terms, one which depends on fiber length and difference in propagation constant, and one which depends on the relative phase of the modes when they are launched. We assume that the latter is a weak function

of wavelength. Thus:

$$\frac{d\theta_1}{d\lambda} = L \frac{d}{d\lambda} \Delta\beta \quad (4.16)$$

for $\Delta\beta \equiv \beta_l^V - \beta_{l-1}^V$. Taylor expansion of θ_1 to first order yields:

$$\theta_1(\lambda) \approx \theta^0 + (\lambda - \lambda_c) \frac{d\theta_1}{d\lambda} = \theta^0 - (\lambda - \lambda_c) \Delta n_g \frac{2\pi L}{\lambda_c^2} \quad (4.17)$$

where Δn_g is the difference in group index between the two modes interfering, λ_c is the center wavelength of the sweep, and θ^0 is a wavelength-independent phase term. For a $\Delta l = 1$ interference pattern such as the one in Fig. 4-4, this varying phase will cause the crescent moon to rotate as a function of wavelength (see Fig. 4-5 (a)). It will undergo a full rotation when:

$$(\lambda - \lambda_c) = \frac{\lambda_c^2}{\Delta n_g L} \quad (4.18)$$

The Fourier series coefficients can be calculated as a function of wavelength. For mode purity measurements, power in $l + 1$ and $l - 1$ are equally parasitic, so the coefficient $g_1 = \sqrt{a_1^2 + b_1^2}$ is used to estimate the mode purity of the OAM state of topological charge l into any modes with $\Delta l = 1$ by an equation analogous to Eq. (4.14).

Consider an example data set in Fig. 4-5 where an $l = 8$ mode is launched into a first generation air core fiber of length $2m$ and subsequently binned in $\hat{\sigma}^\pm$ components (only one bin is shown as the other polarization bin is near-zero in total intensity). The source wavelength is swept over $\Delta\lambda = 4nm$ with a step size (resolution) of $\delta\lambda = 0.01nm$, and an image is captured at each wavelength. Each image is imported into matlab with the two polarization bins analyzed separately. The center point of each image is first coarsely found by center-of-mass averaging. It is then updated by independently finding 4 points on the bright ring in cardinal directions from the center point, and moving the center point to the geometric center of those four points. This iterates until convergence. The intensity on the ring as a function of angle is

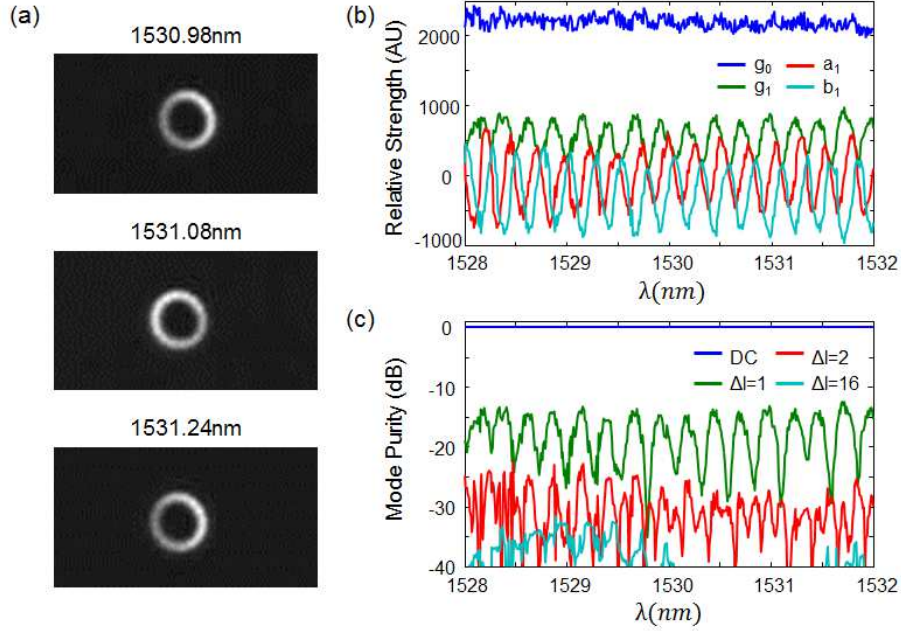


Figure 4-5: (a) Mode images at different wavelengths showing rotation of interference pattern (b) Azimuthal Fourier series components of interest (c) Mode purity as a function of wavelength

then retrieved, and a Fourier series constructed of the ring intensity is calculated (thus the name of ‘Ring’ method) (Bozinovic et al., 2012). A subset of Fourier series coefficients is plotted as a function of wavelength in Fig. 4-5 (b). Oscillation in a_1 and b_1 corresponds to beating between the $l = 8$ mode and the corresponding $l = 7$ and $l = 9$ modes of the same spin and sign of OAM. According to simulation and confirmed by later time domain measurements, the group index separation between $l = 9$ and $l = 8$ is approximately 3.5×10^{-3} , which is nearly identical to the separation in group index between $l = 8$ and $l = 7$, so only one beat frequency is evident. The mode purity is estimated and shown in Fig. 4-5(c) where the mode purity is about -15dB with the strongest parasitic modes being those with $\Delta l = 1$. One could also perform a discrete Fourier transform between wavelength and Δn_g space, analogous to S^2 , in order to back out different oscillation frequencies which contribute to each

term. The resolution available in group index is:

$$\delta(\Delta n_g) = \frac{\lambda_c^2}{LN\delta\lambda} \quad (4.19)$$

for number of wavelengths, N , and δX denoting the resolution of quantity X . This implies that the resolution in the example measurement described above is 3×10^{-4} , with a maximum measurable Δn_g of $N\delta\Delta n_g/2 = 6 \times 10^{-2}$. Resolution of the two different beat frequencies would require $\delta\Delta n_g \approx 10^{-5}$, which would necessitate more than 100,000 measurements at this resolution. At longer fiber lengths, for which the beat frequencies will be effectively larger, this distinction is more useful (Demas and Ramachandran, 2014).

The ring method has several limitations. First, it is dependent on a source or system configuration in which multiple wavelengths can be measured separately or sequentially with the assumption that mode content does not appreciably change. For instance, when using an spatial light modulator (SLM) for input coupling, it is typically advantageous to place a blazed phase grating on the SLM, which imparts an wavelength-sensitive tilt. This can rapidly lead to degradation as a function of wavelength (see Chap. 5). Alternatively, if the in-fiber coupling is strongly wavelength sensitive, for example due to resonant effects as in a grating, the method is inapplicable. Second, it is dependent on a good quality imaging system, as anisotropic aberrations such as astigmatism or coma can artificially degrade the mode purity. For the example above, a high quality 0.4 NA Mitutoyo objective was used for imaging, and care was taken to ensure that the fiber was on-axis while being imaged. However, some corruption is still evident; the images in Fig. 4-5 are slightly egg-shaped, and the b_1 coefficient is not zero mean, implying some constant $\Delta l = 1$ effect. Pixellation could also be a source of error, especially with an InGaAs camera of pixel pitch $30\mu m$, although it would predominantly lead to errors in calculation of higher Δl terms. For

fibers which do not have a ring guiding structure it may not be applicable due to the assumption of identical electric field distributions in the radial direction, and it would need modification for strongly guiding fibers, where the polarizations are not circular.

4.5 Time Domain

In this section, we discuss mode purity measurements made by observing the time of flight spectrum leaving a few-moded fiber. This section is broken into subsections on theory, measurable quantities, experimental realization, and limitations.

4.5.1 Theory

When a pulse of light is incident on a fiber, the spatial distribution of its electric field determines what ensemble of modes is excited at the fiber's input facet (Snyder and Love, 1983). Imagining the pulse as a flux of light particles, this overlap, or explicitly, its absolute value squared, determines the probabilities of the particles being funneled into a given mode. If there is no mode coupling, particles coupled into a mode a will take time $\tau = n_g^a L/c$, where L is the fiber length and c the speed of light in free space, to traverse the fiber. Clearly particles launched into modes with different n_g will arrive at different times, determined by the difference in group index and the fiber length. If all of the times of arrival are separately resolvable, observing the particles arriving as a function of time directly yields information about the input coupling condition.

Similarly, suppose that the light particles are launched into one mode of a fiber containing two modes with different group indices. If particles couple from mode one into mode two somewhere in the fiber, their arrival time will be bound between the arrival times, τ_1 and τ_2 , of light particles launched into either mode and retained there. If there are discrete coupling instances, such as a kink or a grating, the arrival

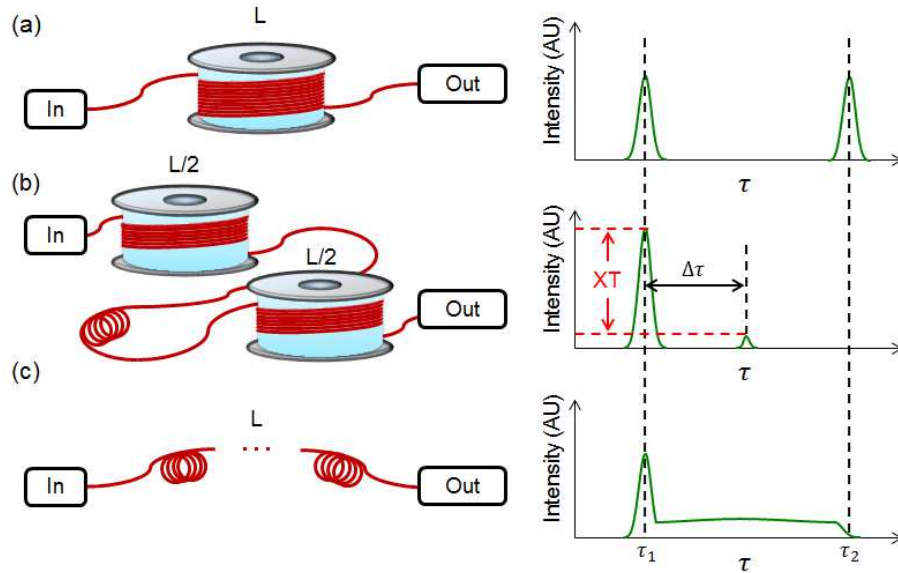


Figure 4-6: (a) Two-mode fiber in which two modes are both launched and no mode coupling occurs (b) Two-mode fiber in which one mode is launched and a discrete coupling incident occurs at the midpoint of the fiber. Mode coupling is evident with strength, XT , and a delay time corresponding to the position of the perturbation (c) Two mode fiber with weak distributed coupling between modes

time of the coupled photons will be localized to a single time, and the ratio of the time differences between that localized time and the arrival times of either mode will correspond to the ratio of the distance between perturbation and fiber end, and fiber beginning and the perturbation. The strength of the coupling can be measured as a ratio between the number of photons in mode 2 and those in mode 1, if only mode 1 is launched. If alternatively there is distributed coupling along the entire length of the fiber, with a small coupling probability h over length dz , then a shoulder will extend between the arrival times of the two modes. h in this instance is exactly the h from coupled power theory discussed in Sec. 3.1 (Kawakami and Ikeda, 1978). These cases are sketched in Fig. 4-6. If $hL \gg 1$ then the time domain response will begin to aggregate around the mean arrival time. These almost mundanely simple ideas can prove incredibly powerful, both in diagnosing input coupling mode purity, and

studying in-fiber mode coupling.

4.5.2 Measurable Quantities and Practical Limitations

Time domain measurements are useful for measuring multiple fiber parameters if a fiber is in a weak coupling regime, and for aligning fiber optic coupling systems in the case where modes are separately resolvable. Consider the case shown in Fig. 4.7(a), in which we excite every mode within an OD110 vortex fiber (Chap. 6) supporting 7 mode families: $HE_{1,1}$, $TE_{0,1}$, $HE_{2,1}$, $TM_{0,1}$, $HE_{1,2}$, $HE_{3,1}$, $EH_{1,1}$, with the $HE_{1,2}$, $HE_{3,1}$, and $EH_{1,1}$ families being nearly degenerate and close to cutoff. The modes are all excited simultaneously by offset coupling an $l = 1$ optical vortex linear polarization. The time domain trace is taken after 300m of fiber propagation (Gregg et al., 2015b). Each peak is clearly defined except for the $LP_{2,1}$ and $LP_{0,2}$ peaks ($HE_{1,2}$, $HE_{3,1}$, and $EH_{1,1}$) which overlap with each other. The differences in group index can be calculated if the fiber length is known. Fig. 4.7(b) shows a time domain trace on log scale of the same fiber but where we attempt to excite only the $TM_{0,1}$ mode with a q -plate (Chap. 5), to which the trace is normalized. The discrete peak around 0.5ns is due to discrete coupling to the fundamental $HE_{1,1}$ modes at the input of the fiber, due to offset coupling, or imperfect mode conversion by the q -plate. The continuous coupling shoulder between the time of flight of a pure $TM_{0,1}$ mode and the time of flight of a pure $HE_{2,1}$ is due to in-fiber coupling, likely due to fiber bend perturbations. Crosstalk between the two modes is given by the integration of the shoulder (on a linear scale) divided by the integration of the peak - in this case, the crosstalk between $TM_{0,1}$ and $HE_{2,1}$ is -15.2dB. Since in-fiber distributed coupling is on the order of a few percent, and the modal dispersions of $HE_{1,1}$ and $TE_{0,1}$ will not result in significant differential pulse broadening over 300m, we recognize the ratio of the peak powers of the time domain responses at the times of flight of $TM_{0,1}$ and $HE_{1,1}$ as the purity of the input coupling, in this case -20dB. This allows time-of-

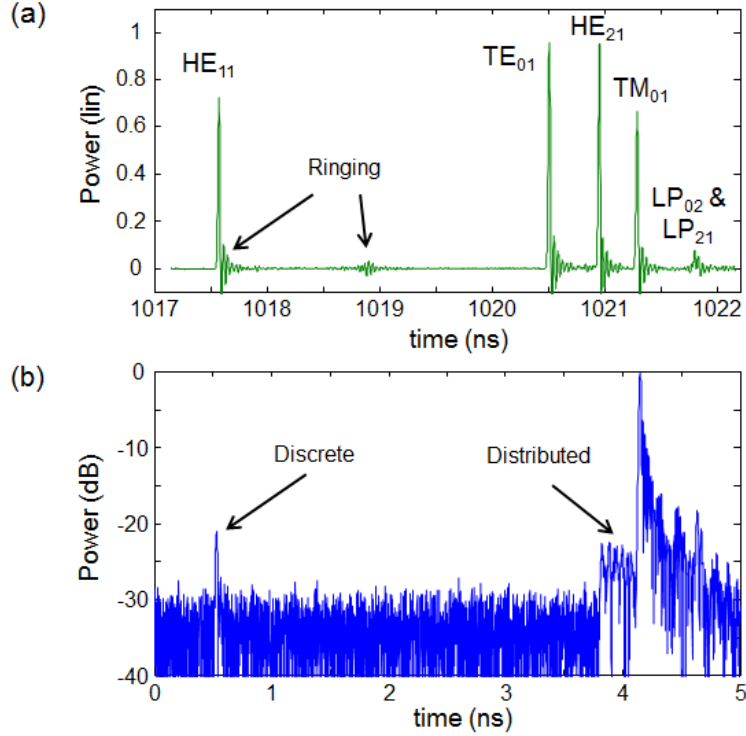


Figure 4-7: (a) Time domain trace on linear scale where several modes intentionally excited simultaneously. Differential group velocities can be determined if the fiber length is known. Ability to independently resolve peaks for each mode reveals stable mode propagation (b) Time domain trace on log scale when only TM_{01} is launched. Peak around 0.5ns from start of trace corresponds to discrete coupling into HE_{11} at fiber input, while shoulder between TM_{01} and arrival time of HE_{21} reveals in-fiber mode coupling

flight to be used as a real time, quantitative alignment technique without the use of complicated components.

In addition to crosstalk, differential group indices, and alignment purity, one could in theory measure dispersion by time of flight by tracking the change in time of arrival, τ , as a function of wavelength.

$$D = \frac{\Delta\tau}{\Delta\lambda} = \frac{1}{c} \frac{dn_g}{d\lambda} \quad (4.20)$$

In practice, the implementation of this is difficult due to electronic trigger signal drift

and environmental effects, which can also vary the time of arrival, especially with the long fiber lengths necessary for a change in time of flight to be visible.

Also evident in Fig. 4.7(a) is electronic ringing due to the upper frequency limit of the fast detector and oscilloscope (details on the equipment used are presented in Sec. 4.5.3). The detected waveform is the convolution of the optical signal and the frequency response of the optoelectronic detector and oscilloscope used. This is responsible for the high frequency temporal content immediately after strong pulses, which takes $\sim 1\text{ns}$ to decay below the -30dB level, as shown in Fig. 4.7(b). This is also responsible for the high frequency burst approximately 1.5ns after the $HE_{1,1}$ pulse in Fig. 4.7(a). These artifacts are visible after pulse propagation in a few meters of SMF, in which case no mode coupling is possible. This restricts the time span in which mode coupling effects can be interrogated, as there must be some measurement dead time after a strong pulse. However, the impulse response is causal, and will not impact time spans preceding a pulse. In this case, if $TM_{0,1}$ is launched, mode coupling to $HE_{2,1}$ can be directly observed. We assume that if $HE_{2,1}$ is launched, mode coupling into $TM_{0,1}$ will happen at the same strength due to reciprocity; however, this is not directly measurable without introducing uncertainty by modeling the impulse response of the detector electronics, inverting the convolution and obtaining an impulse response function in a known single mode case, and de-convolving the $HE_{2,1}$ trace, all while assuming that the detector apparatus is linear (Goodman, 2005).

By integrating over the distributed mode coupling shoulder between the times of arrival of pure modes and comparing with the integration of a main pulse for crosstalk measurement, we implicitly assume that mode coupling within the fiber is a rare phenomenon. Returning to the particle flux view of a pulse in the case of two modes with arrival times τ_1 and τ_2 , any light particles which undergo multiple coupling instances will be bound in arrival time to be within τ_1 and τ_2 , regardless of

which mode they are in when they exit the fiber. Strictly speaking, the measurement can only tell how much power has left the desired mode and become a parasitic signal, either as crosstalk or as MPI. The probabilities of particles launched into mode i and arriving in mode j , $\pi_{i,j}$ are known from theory (Kawakami and Ikeda, 1978), and an example is plotted in Fig. 4-8(a) for the case of $hz = 1$. The concavity in $\pi_{1,2}$ is due to multiple instances of mode coupling, driving the photons towards an arrival time which is the average of τ_1 and τ_2 . As a function of mode coupling rate times length, hz , the difference between theoretical crosstalk, as defined by power in mode 1 versus power in mode 2 when mode 2 only is launched, and crosstalk that would be measured by integrating a time domain trace over the shoulder can be calculated and the approximate difference determined (Fig. 4-8(a) and(b)). In Fig. 4-8(c) below a

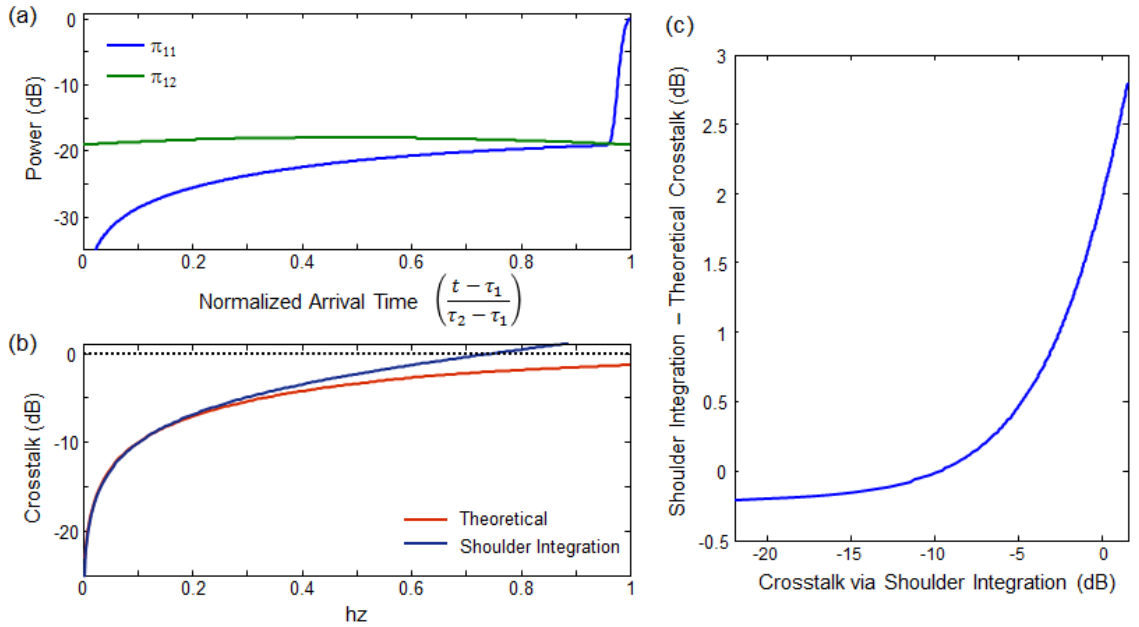


Figure 4-8: (a) Theoretical power densities as a function of normalized arrival time for particles launched into mode 1 and arriving in mode 1, and particles launched into mode 1 and arriving in mode 2 (b) Theoretical crosstalk, and the crosstalk that would be measured by shoulder integration versus peak integration as a function of mode coupling strength, hz (c) Difference between ‘measured’ and theoretical crosstalk

crosstalk of -9.8dB, shoulder integration underestimates the crosstalk by up to 0.2dB due to the portion of the distributed shoulder which is occluded by the finite width of the pure-moded pulse, here assumed a Gaussian for simplicity. For larger measured crosstalk values, the crosstalk is overestimated due to the presence of particles which have experienced intermodal coupling multiple times. This overestimation increases super-linearly with measured crosstalk. Experimentally, one source of uncertainty is the determination of τ_2 , that is the exact point at which the impulse response is dominated by light which has remained in mode 2 versus light which has made an intermodal transition, and can cause measured crosstalk values to vary by ± 0.5 dB.

Time of flight by definition cannot resolve between modes with the same time of flight, such as the degenerate SOa or SOaa OAM states of a given l . It also cannot distinguish between temporal broadening due to severe mode coupling and temporal broadening due to dispersion. To resolve the mode coupling between two modes, we require that temporal broadening due to mode coupling be much larger than that due to dispersion:

$$\Delta n_g \frac{L}{c} \gg D \Delta \lambda L \quad (4.21)$$

where $\Delta \lambda$ is the wavelength bandwidth of the optical pulse and D is the larger of the two modes' group velocity dispersion (GVD). For some low-order mode families in the air core fibers, Eq. (4.21) does not hold, meaning that time domain is inapplicable.

4.5.3 Experimental Realization

Time domain measurements are experimentally realized using a passively modelocked Pritel picosecond pulsed laser, with tunable wavelength between 1530nm and 1560nm, repetition rate 20MHz, measured optical bandwidth of 0.55nm (70GHz at 1550nm), and, assuming a hyperbolic secant pulse envelope with a transform limited pulse, an optical pulse duration ≈ 5 ps. For some measurements, an in-fiber EDFA (Pritel) is

used, but only in the low-gain regime to avoid self-phase modulation (SPM).

Two detectors are used: a New Focus 1611 InGaAs PIN High-speed photoreceiver with specified 3dB bandwidth 30kHz - 1GHz, and a New Focus 1444-50 InGaAs fast detector with ~ 20 ps rise time, hereafter the ‘picosecond’ detector for brevity. The 1GHz detector has an FC-PC ferrule-adapted front window ~ 0.5 mm away from a $100 \mu\text{m}$ diameter photodiode, while the picosecond detector is FC-PC connectorized to a short (~ 10 cm) internal link of $50 \mu\text{m}$ diameter GRIN MMF, which is then epoxy bonded onto a photodiode. Both are electrically connected via SMA cable to the electrical 40GHz detection port of an Agilent 86109A module within an 86100A Agilent Infiniium wide bandwidth oscilloscope, which is triggered from the RF output of the picosecond laser.

When the picosecond detector is used, light must be coupled from the OAM-carrying fiber into a $50\mu\text{m}$ MMF. For high-order OAM states ($l > 5$), the speed of diffraction in free space makes butt-coupling challenging, since the fibers need to be extremely close together to avoid differential loss between high-order and low-order OAM modes. We free-space couple light between the OAM-carrying fibers and the MMF using short-focal length aspheric lenses (typically $f \leq 8$ mm for output coupling from the OAM fiber, and $f \sim 11$ mm for input coupling into the MMF). Coupling is first optimized by observing output power at the end of the MMF and using two alignment mirrors. Afterwards, the signal is relayed to the picosecond detector and observed on an oscilloscope. Mode coupling within the MMF can lead to slight aperturing at the detector, so the input coupling mirrors are slightly aligned to optimize received power into the fast detector. Assuming an optimized-power calibration, this slight adjustment does not appear to introduce or remove artificial crosstalk above the 0.4dB level. If the MMF used to relay the light to the detector module is not GRIN but rather is a step index MMF, mode coupling within the MMF

can be observed in the time of flight spectrum, necessitating the use of GRIN fiber. When using the 1GHz detector, the OAM carrying fiber is inserted into a bare fiber adapter, and pushed into the chamber of the detector until the received signal is maximized.

Time of flight measurements using the two detectors on the same sample of air core fiber are shown in Fig. 4-9, where (a) shows the time of flight spectrum for $l = 7$ SOa after 3.1km of fiber, measured with the picosecond detector and (b) the trace measured with the 1GHz detector. The impulse response function of the 1GHz detector is obviously slower, resulting in a temporally wider response around the main peak, and an apparently higher mode coupling shoulder, since the crosstalk should not change between measurements and is related to a ratio of integrals, not a point-by-point ratio. Finer features are clearly resolvable with the picosecond detector, and the nanosecond detector obfuscates a larger fraction of the distributed coupling shoulder. However, approximating that the slower detector blocks off a fraction of the shoulder given half its width, divided by the total time between SOa and SOaa modes, we can introduce a multiplicative factor to correct this obfuscation. When this is performed, the picosecond detector's trace shows -11.7dB crosstalk, while the 1GHz detector shows -11.6dB, in excellent agreement.

Although the picosecond detector clearly has better resolution, the 1GHz detector is more sensitive to signals with low input powers. When time of flight measurements are made on lossy systems, especially the fiber loop system discussed in Chap. 8, the slower has the advantage of being able to measure smaller features, like locally weak distributed coupling in long-length fibers, while not suffering from a wider impulse response.

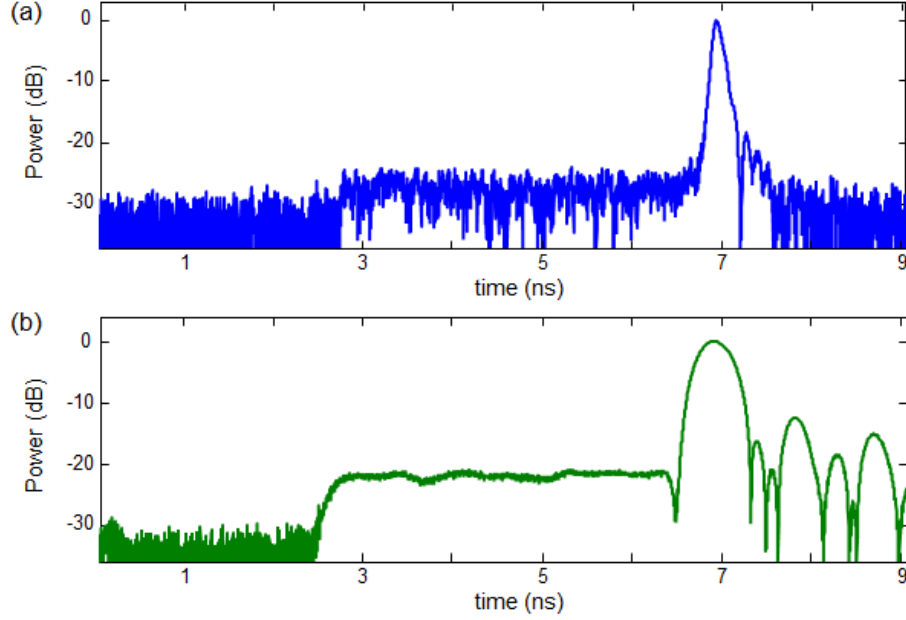


Figure 4-9: (a) Time of flight spectrum of $l = 7$ SOa mode after 3.1km of air core fiber measured with picosecond detector (b) Time of flight spectrum, same conditions, measured with the 1GHz detector

4.6 Output Projection

Another possible measurement for the modal content is to iteratively take mode projections to build up a set of modal weights. With OAM states, this can be done by using an SLM to convert from OAM l to OAM 0 by displaying spiral hologram of topological charge $-l$, and then free space coupling to SMF which acts as a spatial filter passing only $l = 0$ if the fiber is well aligned (Vaziri et al., 2001; Vaziri et al., 2002; Bozinovic et al., 2013). The SLM can then be swept through all values of positive and negative l of interest, and powers measured. For a large set of l free space diffraction and mode conversion will impact measured mode weights, but for a small set of modes like the OAM spectra typically seen from input coupling which contain predominantly $l - 1, l, l + 1$ when l is launched, differential diffraction is a small effect (Siegman, 1986).

Output projection using SLMs and polarizing beam splitters can select one mode

among all fiber modes. Output coupling with q -plates, which convert a linear combination of $\hat{\sigma}^\pm$ to a linear combination of degenerate fiber OAM modes, is useful for directly measuring in-fiber mode conversion between SOa and SOaa states, and will be described in detail with q -plates in Chap. 5. Tolerances on output conversion system alignment parallel those of most of the OAM input coupling systems, and will also be discussed in detail in Chap. 5, but generally both the mode conversion component and the SMF must be aligned at the 10s of nm level to probe states with better than -15dB error, since an offset in the mode converter at fiber output will project OAM l into not only OAM 0, but also into OAM ± 1 ; equivalently it will incorrectly project an OAM $l + 1$ state leaving the fiber into OAM 0 at the -15dB or higher level. Contrarily, it is quite difficult to project OAM l and OAM $-l$ into OAM 0 with the same phase plate regardless of the topological charge of the phase plate, misalignment, etc, meaning that detector-induced crosstalk between SOa and SOaa is unlikely so long as separation into $\hat{\sigma}^+$ and $\hat{\sigma}^-$ can be achieved; experimentally we observe that this can be done to the -25dB level with off-the-shelf components.

Output projection is generally much more difficult to enact experimentally than time of flight or ring measurements, but carries the advantages of very high precision, so long as good alignment is achieved, and simple datapoints, as typically only powers are measured. Output projection can be coupled with time of flight to study distributed mode coupling in fibers; this will be discussed in Chap. 6 and Chap. 8.

4.7 OAM Mode Sorter

Using optical geometric transformations, phase elements can perform coordinate transformations for optical beams (Bryngdahl, 1974). Using a log-polar transformation, the circulating azimuthal phase of an OAM beam can be transformed into a linear phase gradient, that is, a tilt: $l\phi \rightarrow lx$. This is the principle behind the

OAM Mode Sorter proposed by Berkhout and collaborators (Berkhout et al., 2010; Berkhout et al., 2011). The transformation is enacted by two phase elements separated by a wavelength-dependent distance. After the second phase element, the different OAM states have been translated into beams with different tilts and can be separated spatially by using a cylindrical lens. As a consequence of the log-polar transformation, the ring shape is warped into a rectangle which is larger in the x direction, and for which the length in y is determined by the input OAM ring width. The fields in the Fourier plane of the cylindrical lens are then cat's-eye like spots elongated in the y direction.

An OAM beam of equal parts $l = 7$ and $l = -7$ is launched into an air core fiber and transmitted $\sim 2\text{m}$ before being expanded and coupled into the mode sorter, enacted here by two fabricated phase plates, courtesy of Dr. M.P.J. Lavery and Dr. Miles Padgett (Lavery et al., 2012a). The first element acts as optical scissors, cutting the OAM's ring shape along the vertical direction, causing the ring to split upon propagation. The second element halts this unwrapping at a fixed distance away. Images of the sorter input, output, and field through a cylindrical lens is given in Fig. 4-10. The two OAM modes are clearly resolvable as spatially separated spindle patterns.



Figure 4-10: (a) Equal parts $l = 7$ and $l = -7$ launched into mode sorter from air core fiber (b) Transformed beam leaving sorter (c) Transformed beam focused by cylindrical lens, yielding spindle-like patterns, one for each l

Additional features in the Fig. 4-10(c) are visible based on sorter misalignment and

limitations. Since the rings become slightly larger for each l , the unwrapped beam in the plane of the second element become longer and longer in the x direction, eventually clipping the finite aperture and leading to unwanted high-frequency components in the image. Further, the overlap between adjacent l states is large, with neighboring l states having an intensity overlap of about 20%.

Recent improvements have shown a mode sorter capable of sorting more than 50 l states (Lavery et al., 2013), the ability to sort in both radial and azimuthal coordinates (Dudley et al., 2013), and the addition of a fan-out element capable of further separating the spindle patterns, reducing the intensity overlap to about 5% (O’Sullivan et al., 2012), although with a reduction in operating bandwidth to about 4nm at a central wavelength of 749nm (data courtesy of Dr. Mohammad Mirhosseini). The mode sorter appears to be a promising technology for OAM characterization, as well as potentially loss-less MUXing and DEMUXing for optical communications (Lavery et al., 2012b)

4.8 Other Characterization Methods

This discussion is by no means extensive and other means of characterizing the output of OAM fibers exist. Chip-based demultiplexers which function based on the principles of phased array antennas could detect and route different OAM state to different single-moded waveguides (Su et al., 2012). It is well-known in free space that optical vortices with topological charge $N > 1$ are unstable in free space under even weak anisotropic perturbations, and break into N first order ($l = 1$) vortices (Soskin et al., 1997; Freund, 1999; Ricci et al., 2012). This can be exploited by introducing a large astigmatism, through a tilted lens or tilted prism, etc, which breaks up the OAM mode’s singularity into multiple, spatially distinct, first order singularities (Vaity et al., 2013), as shown in Fig. 4-11. $|l|$ can then be observed by the number of

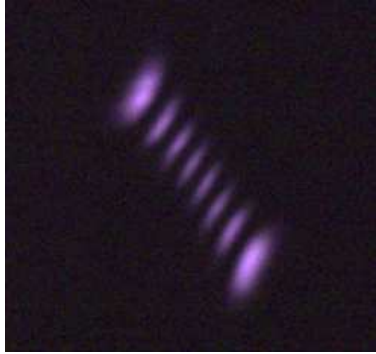


Figure 4-11: $l=7$ lens passed through a tilted Wollaston prism, breaking higher order singularity into 7 first order singularities. Credit to Gautam Prabhakar for experimental image

vortices, while the sign can be inferred from their spatial distribution. A multiplane light converter (Labroille et al., 2014; Genevaux et al., 2015) could losslessly spatially separate the fiber output, assuming that the mode shapes were known *a priori*.

A device leveraging the advantages of waveguides for input/output coupling or characterization of OAM modes, for instance, a photonic lantern (Leon-Saval et al., 2005) or tree of fused couplers (Lai et al., 2007) could utilize phase matching to separate OAM modes of interest. Such research would be of immediate and incalculable use.

4.9 Summary

In this chapter, we have discussed multiple methods for characterizing OAM modes of fibers, predominantly time of flight and ring techniques. Time of flight measurements are generally useful and relatively simple to employ, although there are a range of scenarios in which they do not apply, including very short fibers, and fiber with many modes of similar group index. However, it has the advantage of being agnostic to the spatial shape of the mode in question, able to measure discrete and distributed coupling, and usable *in situ* for alignment for input coupling or fiber splicing. The

problems of OAM characterization and OAM demultiplexing are entangled, and the latter will be discussed more thoroughly in Chap. 11. But, with OAM characterization methods introduced, we may proceed to discussions of launch mechanisms for OAM modes in fibers.

Chapter 5

Mode Excitation

In this chapter, techniques for exciting OAM modes with high purity are discussed. We begin with a brief discussion of in-fiber mechanisms such as tilted long-period gratings (LPGs) and microbend gratings, which are useful for some kinds of OAM-supporting fiber. Most of this chapter is dedicated to two free space techniques - mode excitation with SLMs and q -plates . As we will demonstrate, SLMs have the advantage of being tunable generators of OAM, while q -plates have the advantage of being able to excite arbitrary combinations of degenerate OAM fiber modes of the same l . Both devices have the same disadvantages of demanding precise alignment, and being unable to losslessly combine multiple (non-degenerate) OAM states simultaneously.

5.1 In-Fiber Excitation Techniques

In-fiber OAM excitation techniques typically rely on a phase-matched mode conversion process to go from a fundamental or lower order mode to the desired OAM mode. As in Chap. 3, the perturbation needs to have the appropriate symmetry to excite the OAM mode of choice. Two such controller perturbations are tilted gratings and microbend gratings.

Tilted gratings operate under the same principle as standard fiber LPGs except that the period is written at an angle with respect to the fiber's $\hat{\mathbf{z}}$ axis (Erdogan, 1997; Ivanov et al., 2006; Yan et al., 2015). This tilt while writing induces an asymmetric perturbation from the point of view of light travelling down the fiber, and can result

in cross- l mode coupling, which is maximized when the grating pitch, Λ is given by: $\Lambda = \frac{\lambda}{\Delta n_{eff}}$ where Δn_{eff} is the separation in effective index between the input mode and the desired output mode (Vengsarkar et al., 1996).

A second asymmetric grating is the microbend grating, in which a fiber is compressed in a series of bends with well defined pitch, Λ (Blake et al., 1987). These bends are typically induced by either pressing a mechanical plate with a fixed groove pitch onto the fiber (Blake et al., 1986; Ramachandran et al., 2009) or by periodically inducing lateral stress along the fiber and ‘freezing’ it in with the application of a high current, deforming the fiber (Hwang et al., 1999). Although these gratings are known to induce polarization-dependent resonance splitting (Golowich and Ramachandran, 2005), they have the advantage of being period-tunable, as the mechanical plates can be placed on a rotation stage, which can decrease the period seen by the fiber (Bozinovic et al., 2012).

However, both methods rely on the presence and ability to excite at least one mode in the fiber under test. Traditionally, this is the fundamental $HE_{1,1}$ mode, since it can typically be excited by splicing or butt coupling an SMF to the FUT with additional mode stripping using a fiber taper, if necessary. However, in some of the OAM fibers under consideration in this thesis, the fundamental mode is either difficult to excite purely due to its spatial shape and the presence of $HE_{1,2}$ modes, or unstable due to a small Δn_{eff} with respect to adjacent modes, notably $TE_{0,1}$. In principle gratings could be used to convert among HOMs, but this requires stable excitation of another mode from free space.

5.2 Free Space Excitation

Free space excitation of fiber modes requires the sculpting of an optical field in free space. The weight of mode $\nu = (l, m)$ with spatial and polarization distribution Ψ_ν

excited by a free space optical field Φ incident on the fiber facet is given by:

$$\alpha_\nu = \langle \Phi | \Psi_\nu \rangle \equiv \int \int dA \Phi^* \cdot \Psi_\nu \quad (5.1)$$

Assuming that mode ν is an OAM mode with spatial distribution defined by Eq. (2.15) or Eq. (2.16), and that the incident field can be factored into vector and scalar components, which can be further separated in radial and azimuthal coordinate, $\Phi = \hat{\Phi}\Phi = \hat{\Phi}R(r)G(\phi)$, the overlap can be broken into separate parts:

$$\alpha_\nu = (\hat{\Phi} \cdot \hat{\sigma}_\nu^\pm) \int d\phi e^{il\phi} G^*(\phi) \int r dr R^*(r) F_\nu(r) \quad (5.2)$$

We use $\hat{\sigma}_\nu^\pm$ to denote the sign of the spin of the mode in question, and allow l to be positive or negative. Optimizing mode excitation clearly requires matching three field components: polarization, OAM, and radial field structure, which can be tailored independently in free space. Note that the integral above is in the coordinates of the end facet of the optical fiber, that is, $r = 0$ corresponds to the geometric center of the fiber, around which ϕ is defined. If the input beam and the fiber are misaligned in space, the input field must be redefined in terms of the fiber's coordinate, which will affect the azimuthal component of the overlap integral. Note also that if either the fiber mode or the input field is not separable, either in radial and azimuthal coordinates, or because it has a spatially variant polarization due to tight-focusing (Youngworth and Brown, 2000) or spin-to-OAM conversion (Bliokh et al., 2010), simplification of Eq. (5.1) may not be possible.

The polarization degree of freedom can be manipulated with conventional polarization controllers: free space waveplates, or, if the laser is emitted from an SMF, a fiber-based polarization controller (polcon). The radial and azimuthal parts of the overlap integral require sculpting by optical elements control a beam's spatial distribution; such devices include apertures inside a resonant cavity (Kogelnik and Li,

1966), spiral phase plates (SPPs) (Beijersbergen et al., 1994; Turnbull et al., 1996; Guo et al., 2006), binary phase plates (Davis et al., 2003; Stepniak et al., 2011; Demas et al., 2015a), axicons for radial field re-distribution (McLeod, 1954; Arlt and Dholakia, 2000), or combinations of these (Machavariani et al., 2002). Phase only holograms can be used to tailor optical fields almost arbitrarily (Arlt et al., 1998; Dudley et al., 2012; Bolduc et al., 2013). Computer controlled phase holograms called Spatial Light Modulators (SLMs) will be discussed in detail in the next section (Matsumoto et al., 2008; Ando et al., 2009). There are devices, such as q -plates and s -plates which treat polarization and azimuthal symmetry as one degree of freedom (Marrucci et al., 2006; Beresna et al., 2011). q -plates will be discussed in detail in Sec. 5.4.

With the exception of some mode converters which are fabricated directly onto fiber tips (Kostovski et al., 2014), most mode converters act some distance away from the fiber, and the resultant optical field is either imaged or Fourier transformed onto the fiber facet. Thus, it is useful to review (in extreme brevity) free space beam propagation. This can be cast in terms of Fresnel diffraction (Goodman, 2005) or propagation of Laguerre-Gaussian (LG) beams, both of which are reviewed here.

Assuming a paraxial optical field with spatially uniform distribution of polarization, the evolution of the field shape in free space can be written as a Fresnel integral. This can be generalized to the evolution of a paraxial beam through an optical system described by an ABCD matrix. If an optical field with distribution $U_1(\xi, \eta)$ passes through an optical system described by an ABCD ray matrix to the (x, y) plane, the field distribution in the second plane can be written as (Collins, Jr., 1970):

$$U_2(x, y) = \frac{e^{ikL}}{i\lambda B} e^{i\pi \frac{D}{\lambda B}(x^2+y^2)} \int \int d\xi d\eta U_1(\xi, \eta) e^{i\pi \frac{A}{\lambda B}(\xi^2+\eta^2)} e^{-i\frac{2\pi}{\lambda B}(x\xi+y\eta)} \quad (5.3)$$

Where L is the average path length through the ABCD system, and A , B , and D are elements of the system's ABCD matrix. If the optical system performs an imaging

operation, $B = 0$ (Saleh and Teich, 2007). In the limit $B/A \rightarrow 0$ and using $AD - CB = 1$ (Siegman, 1986):

$$U_2(x, y) = \frac{e^{ikL}}{A} e^{i\pi \frac{C}{\lambda A} (x^2 + y^2)} U_1\left(\frac{x}{M}, \frac{y}{M}\right) \quad (5.4)$$

Where M is the image magnification, given by $M = A$. For a fiber, cylindrical coordinates are more useful, and Eq. (5.3) can be rewritten in terms of a series of Hankel transforms propagating from the (ρ, θ) plane to the (r, ϕ) plane:

$$U_2(x, y) = \frac{e^{ikL}}{i\lambda B} e^{i\pi \frac{D}{\lambda B} r^2} \sum_{n=-\infty}^{\infty} \left[i^{n-1} e^{in\phi} \int \rho d\rho e^{i\pi \frac{A}{\lambda B} (\rho^2)} J_n\left(\frac{2\pi}{\lambda B} r\rho\right) \int d\theta U_1(\rho, \theta) e^{-in\theta} \right] \quad (5.5)$$

It is clear from Eq. (5.5) that the OAM spectrum of U_1 will be maintained as expected; the ABCD matrix framework assumes an isotropic optical system. Eq. (5.3) - Eq. (5.5) are used to simulate field propagation in order to optimize system distances and lens focal lengths. Eq. (5.5) is most intuitive, as it evidently treats different OAM states separately and sums their fields, while Eq. (5.3) is computationally faster, since fast fourier transform (FFT) algorithms are well developed.

Alternatively, beam propagation can be understood through a modal decomposition into the Eigenmodes of free space, which for cylindrical coordinates are the LG beams (Siegman, 1986). The LG beams are given by:

$$u_{l,p}(r, \phi, z) = \frac{c_{lp}}{w(z)} \left[\frac{r\sqrt{2}}{w(z)} \right]^{|l|} e^{-\frac{r^2}{w^2(z)}} L_p^{|l|}\left(\frac{2r^2}{w^2(z)}\right) e^{-ik\frac{r^2}{2R(z)}} e^{il\phi} e^{ikz} e^{i\psi(z)} \quad (5.6)$$

with

$$\begin{aligned}
 w(z) &= w_0 \sqrt{1 + \left(\frac{z}{z_r}\right)^2} \\
 z_r &= \frac{\pi w_0^2}{\lambda} \\
 R(z) &= z \left[1 + \left(\frac{z_r}{z}\right)^2\right] \\
 \psi(z) &= (2p + |l| + 1) \arctan\left(\frac{z}{z_r}\right) \\
 c_{l,p} &= \sqrt{\frac{2l!}{(1 + \delta_{0p}) \pi (l + p)!}}
 \end{aligned}$$

Here $L_p^{|l|}$ is a generalized Laguerre polynomial, w_0 is the beam waist in the focal plane, $\psi(z)$ is the Guoy phase, and z_r the Rayleigh range. The standard Gaussian beam is given by $l = p = 0$. However, for $l > 0, p > 0$, w_0 loses its meaning as a metric for beam spot size. If the spot radius is taken as the standard deviation of the intensity pattern, the true spot radius is instead given by $w = \sqrt{2p + l + 1} w_0$ (Phillips and Andrews, 1983). LG beams are propagation-invariant in free space, meaning that as they propagate, their characteristic sizes will scale as determined by $w(z)$ but they will not change their spatial distribution otherwise. Thus, a free space optical field can be modeled by decomposing it into its $LG_{l,p}$ constituents, propagating them separately, and summing them.

With propagation of higher order modes in free space thus reviewed, we turn to the first of two promising OAM mode converters: programmable SLMs.

5.3 Spatial Light Modulators

Spatial light modulators are programmable holograms which can display near-arbitrary phase patterns and imprint them on an incident optical field, by spatially modulating a liquid crystal film, which locally changes the refractive index of the SLM and thus

manipulates the phase of the incident beam. The SLMs used in these experiments are Hamamatsu LCOS-SLM X10468-08, which have 792x600 pixels of pixel pitch $20\mu m$, a fill factor of 98%, and an operating range of 1000-1550nm. The SLM uses parallel-aligned nematic liquid crystals, such that the device causes no polarization rotation, but only operates on a single polarization, say $\hat{\mathbf{x}}$, with the orthogonal linear polarization ‘seeing’ a blank mirror.

Assuming that the optical field Ψ_{in} is purely $\hat{\mathbf{x}}$ polarized, the near field of the SLM is given by:

$$\Psi_{out} = \Psi_{in} e^{i\Xi(X,Y)} \quad (5.8)$$

where $\Xi(X,Y)$ is the holographic pattern displayed on the SLM, and (X,Y) are SLM coordinates, written in capital letters as a reminder that they are discrete: $(X,Y) = (m,n)\Delta X$; $(m,n) \in \{1,2,\dots,M(N)\}$ for pixel size ΔX and pixel array size (M,N) .

The SLM can be used in two configurations with respect to the FUT: Fourier plane or imaging plane. When in the Fourier plane, the near field of the SLM is allowed to diffract whatever distance between the SLM and the fiber, before it is input coupled with a high-NA lens. The focal length of the lens needed for a given beam size can be approximated by calculating the Gaussian beam width in the lens’ focal plane, and comparing $\sqrt{l+1}w_l$, where w_l is the beam width of a Gaussian beam in the focal plane of the lens and l is the desired OAM order, to the size of the desired fiber mode. Typically, we require focal lengths on of $4 \sim 8$ mm for high- l states.

A schematic diagram of the optical system used with the SLM in the fiber’s Fourier plane is given by Fig. 5.1. A Gaussian beam, whose polarization is controlled by an in-fiber polarization controller to be parallel with the preferential axis of the SLM, impinges on an SLM showing a ‘fork’ hologram of $l = 2$. A fork is a combination of a spiral phase, $il\phi$ and a tilt pattern kx , the far field of which is an OAM mode of

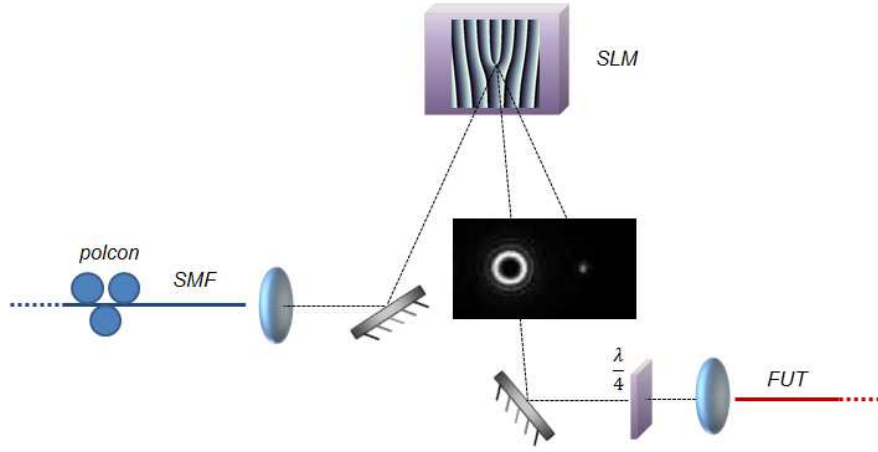


Figure 5-1: Simplified schematic of experimental system for using SLM in fiber's Fourier plane for mode excitation. Inset: image of light beam between SLM and fiber

topological charge l diffracting at an angle determined by the incident angle and k from the SLM. The Gaussian beam will only be converted to the desired OAM mode (or set of modes with the same azimuthal index) with a finite diffraction efficiency, η , determined by the SLM's filling factor, bit depth, finesse (phase quantization) in being able to replicate the phase function, and inability to display a full 0 to $m\pi$ phase pattern, needing instead to display $\text{mod}(\Xi, 2\pi)$ (Goodman, 2005). This results in the appearance of multiple diffraction orders. In the case $k = 0$ these diffraction orders are colinear. For a large enough k , these can be separated in free space. In practice, k does not have to be very large, as the fiber acts as a high-quality spatial filter. The largest possible diffraction angle from the Hamamatsu SLM is 2.5° with typical diffraction angles of $\sim 0.5^\circ$. The SLM is experimentally very easy to align by observing its diffracted beam. The input Gaussian beam should be directed to the SLM's coarse center by use of mirrors, and the far field of that pattern observed. At first, regardless of the OAM desired, a very high topological charge fork pattern, such as $l = 10$ should be displayed. When the center of the fork and the center of the

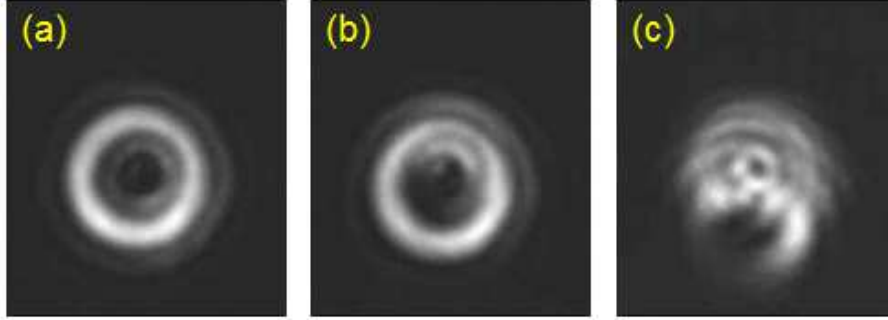


Figure 5.2: (a) Far field pattern of SLM with input Gaussian beam and SLM pattern well aligned (b) and (c) show cases of beam and pattern offset, with a more dramatic offset for (c)

incoming Gaussian beam overlap, the far field pattern should be nearly isotropic as in Fig. 5.2(a). If, however, the beam and pattern are not overlapping on the SLM plane, the far field will show an anisotropic ring shape as in Fig. 5.2(b) and (c). The pattern center may then be moved digitally to single-pixel resolution in order to center it on the incoming beam. A high l should be used for this initial alignment as its effect on the beam is more appreciable due to faster free-space diffraction for larger l .

After the input beam and SLM are centered, the diffracted beam from the SLM is passed through a QWP and into the clear aperture of a high-NA aspheric lens or microscope objective. Two mirrors with tilt control should be between the SLM and fiber. Care must be taken centering the input OAM beam on this lens with low tilt, as if the beam strikes the lens far from center, even if it is not vignetted and even if the input OAM beam is nearly perfect, the focal plane of the lens will feature distortions due to lens aberrations, as in Fig. 5.3. Experimentally this can typically be done by placing an IR card shortly after the lens, and moving the two mirrors such that the beam coming through the lens is both centered and isotropic. Due to the short focal distances involved, placing a camera in this plane involves the use of an imaging system, which is not always practical. However, observing the lens throughput by eye to observe symmetry can typically assure purities on the order of 15dB or better

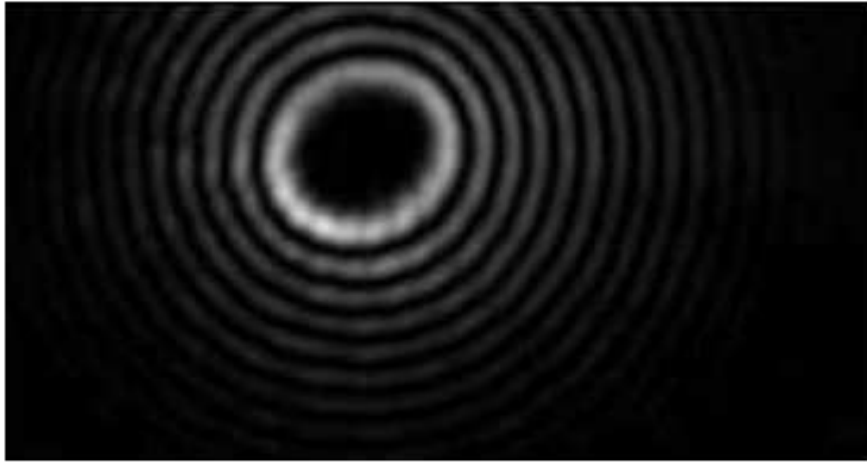


Figure 5-3: Field in the focal plane of a lens when an OAM state is incident by off-center. Field is both elliptical and clearly brighter on one side than the other, implying undesired OAM coupling in free space

and which can be later optimized with better fiber characterization feedback, such as time of flight.

The fiber may then be aligned in the following way. First, reverse-illuminate the fiber from the end which will become the output facet, by butt-coupling that facet with SMF. This will excite a random assortment of predominantly lower-order modes. Using an IR card, manipulate the input facet in the \hat{z} direction such that the reverse-illumination is roughly collimated leaving the coupling lens. Move the fiber in the transverse direction to the lens and roughly center the fiber's output on the SLM pattern, which should visibly enlarge the beam if the SLM has a high- l fork pattern displayed. Adjust the fiber's longitudinal displacement from the lens again to ensure near-collimation. Then, remove the fiber's output facet from the illumination source and image it onto a camera. This alignment will not be enough to ensure good purity, but will be sufficient to act as a starting point, from which the fiber should be moved in the transverse directions to the lens. Alignment is stopped when the imaged output is ring-like and isotropic. Finer adjustment can now be performed by using

the SLM. Typically the pattern center may need to be displaced by a pixel or two, and a spherical wavefront curvature will need to be added to optimize the coupling strength.

Time domain may be used as an *in situ* alignment technique to ensure high-precision alignment. A time domain trace while a fiber is being aligned is shown in Fig. 5-4. $l = 6$ is selected on the SLM, and we try to excite the $l = 6$ SOa mode. Two parasitic features are evident in this trace, one from $l = 6$ SOaa and one from $l = 5$ SOa. Coupling across $l = 6$ mode families may be controlled by tuning the QWP angle. Control of cross- l coupling is determined by free space alignment, and error can come from many sources, including SLM center offset, tilt, and fiber offset. We find that centering the SLM using a camera before the fiber, rough-aligning as described above, and then fine aligning using two mirrors between the SLM and fiber is typically enough to ensure launch purity at the 20dB level. Changing the topological charge

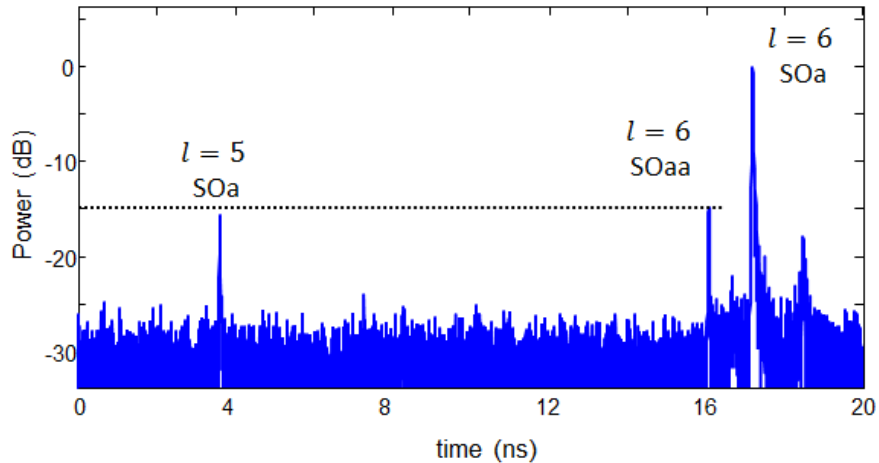


Figure 5-4: Time domain trace of fiber mode excited with SLM and QWP. Discrete coupling to SOaa from SOa controllable by QWP angle, coupling from $l = 6$ to $l = 5$ controlled by free space coupling alignment precision

on the OAM should then result in high purity for OAM states within a Δl of 2 or 3, after which defocus may become an issue and lead to higher crosstalk into other

l modes. It is typically possible to achieve purity of 15dB or better into one OAM mode with an offcenter SLM pattern, using some combination of fiber offset and tilt to counterbalance the error induced on the SLM. However, switching l in this case will quickly yield very poor mode purity. In the process of alignment, it is thus typically helpful to switch the SLM's topological charge a few times to ensure good alignment.

The OAM mode excitation is highly sensitive to fiber position, as shown in Fig. 5-5. Here, the fiber is aligned as well as possible using an $f = 6.25mm$ coupling lens, and the output mode purity is estimated using the Ring method. The fiber is then moved slightly, in $0.5\mu m$ increments, and the mode purity again calculated. Displacing the fiber by as little as $0.5\mu m$ results in a mode purity degradation of 10dB or more.

One disadvantage of using a tilted phase front on the SLM is that the location of the optical field in the lens' focal plane becomes wavelength dependent. The phase pattern on the SLM is written as:

$$\Xi = l\phi + TILT \times X \quad (5.9)$$

The parameter $TILT$ is a phase tilt that is controlled *in situ*, which can also be expressed in terms of an effective grating pitch $\Lambda[mm] = \frac{256}{TILT}$. If we assume that the fiber is in exactly the Fourier plane of the lens, Eq. (5.3) simplifies to a Fourier transform. From the properties of a Fourier transform, a tilt in the space plane will be mapped onto an offset in the Fourier plane (Goodman, 2005). Noting that the kernel of an optical Fourier transform is given by $\frac{2\pi}{\lambda f}$ where f is the focal length of the lens, this coordinate offset in the fiber plane will be given by:

$$x = f \frac{\lambda_0 + \Delta\lambda}{\Lambda} \quad (5.10)$$

where λ_0 is the wavelength at which the system is aligned. Assuming that the system is aligned at the center wavelength, it is clear that there is a wavelength dependent

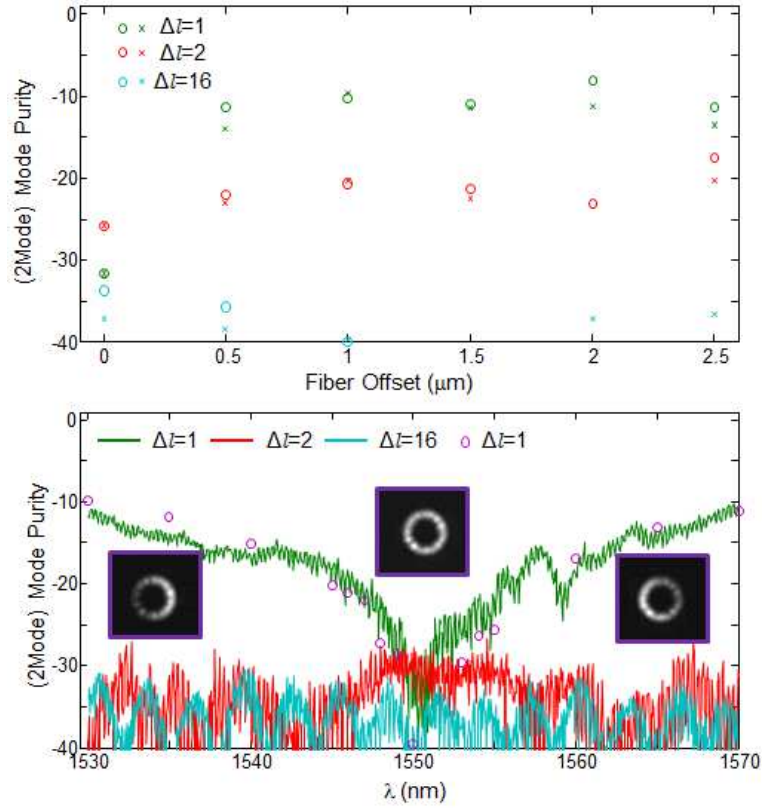


Figure 5-5: (a) Mode purities as calculated by the Ring method when the fiber is displaced in the focal plane of an $f = 6.25\text{mm}$ lens. Circles indicate offset in $+x$, crosses offset in $-x$ (b) Mode purities as a function of source wavelength calculated by Ring method for alignment at 1550nm. Circles indicate calculated mode purities when the wavelength is kept at 1550nm, but the TILT parameter is adjusted as if the source were at those wavelengths. Insets are experimental images from this TILT sweep measurement

offset, $\Delta x = f\Delta\lambda/\Lambda$, which will affect the input coupling. This is shown experimentally in Fig. 5-5(b). The solid traces indicate mode purities from a Ring measurement taken over a wide wavelength range, 1530nm to 1570nm. The mode purity into modes with $\Delta l = 1$ rapidly increases from $\sim -30\text{dB}$ up to worse than -20dB when the wavelength is changed by only 5nm. Instead of changing wavelength, one could also change the *TILT* parameter, and compare the effective offsets in the lens' focal

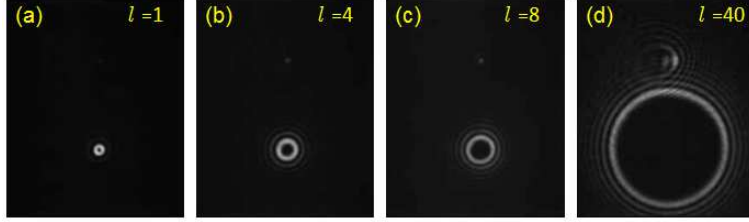


Figure 5-6: Free space diffraction patterns for an ensemble of OAM modes generated by an SLM

plane, we find:

$$\frac{\Delta TILT}{TILT} = \frac{\Delta\lambda}{\lambda_0} \quad (5.11)$$

The wavelength is kept constant at 1550nm but the $TILT$ parameter is changed to achieve the same offset, we find the same deviation in purity (purple circles in Fig. 5-5, where the data is plotted as $\Delta TILT = \Delta\lambda$, which gives finer resolution in fiber position than does our translation state, for which the finest gradation was 500nm. Noting that a 5nm shift in wavelength brings us to approximately -20dB in mode purity, it is evident, using Eq. (5.10) that the fiber needs to be aligned to within 200nm to achieve better than -20dB mode purity. This also places a limit on the operating bandwidth of the system, although for systems implementations across C-band, for instance, two SLMs could be used simultaneously to correct this wavelength dependent offset, much like two parallel gratings are used for chirped pulse amplification (CPA) (Maine et al., 1988).

When the SLM is in the fiber's Fourier plane, the distance between the SLM and fiber should be as short as possible. Far fields from the SLM for various l values are shown in Fig. 5-6, and as expected, higher l states diffract more rapidly. Placing a positive lens on the SLM can alleviate this, but eventually states will be vignettted by the clear aperture of the high-NA focusing lenses, which are typically $< 5mm$. It is also apparent from Fig. 5-6 that as l increases, the number of rings in the far field pattern also increases. This can be understood from LG mode projection. The initial

beam is a near-ideal $LG_{0,0}$ mode, which is then multiplied by a spiral phase front. This will never project perfectly into an $LG_{l,0}$ mode, since $LG_{l,0}$ has no intensity on axis, consequent of its phase singularity. It will instead project into some combination of $LG_{l,p}$ modes, with more and more p needed as l increases, since as l increases, the LG modes tend to become rings which are thinner and have a center-of-mass further away from the origin, with diminishing overlaps with a Gaussian distribution (Siegman, 1986).

To control this ringing effect, we may introduce amplitude-sculpting on the SLM. The simplest method for doing so is by introducing loss, which may be achieved by adding the following checkerboard pattern to the SLM in regions where we desire to lose power (Dudley et al., 2012).

$$\Xi_{loss} = \text{mod}\left(\frac{X + Y}{2}, 2\right) \quad (5.12)$$

Physically, this can be thought of as a combination of gratings in the vertical and horizontal directions, with the most rapid pitch possible, in order to induce significant scattering. Define the SLM's pattern as an annulus of inner radius r_{inner} and outer radius r_{outer} ; the pattern induces high loss for all radial coordinates outside this annulus. The LG projections as a function of these inner and outer radii can be numerically solved; an example for $l = 3$ is plotted in Fig. 5.7. The coupling strength into $LG_{3,0}$ only decreases as the outer radius is shrunk or the inner radius enlarged, but coupling into $LG_{3,1}$ can be minimized for some annular apertures. This becomes more difficult for higher l states as the coupling strength into $LG_{l,0}$ strictly decreases for increasing l . Control of ringing is shown experimentally in Fig. 5.8 for the case of $l = 5$. As the inner and outer boundaries of the annulus are changed, the far field becomes more like a desired ring shape. It should be noted that this does not necessarily improve the coupling efficiency into the fiber; loss at the input facet has

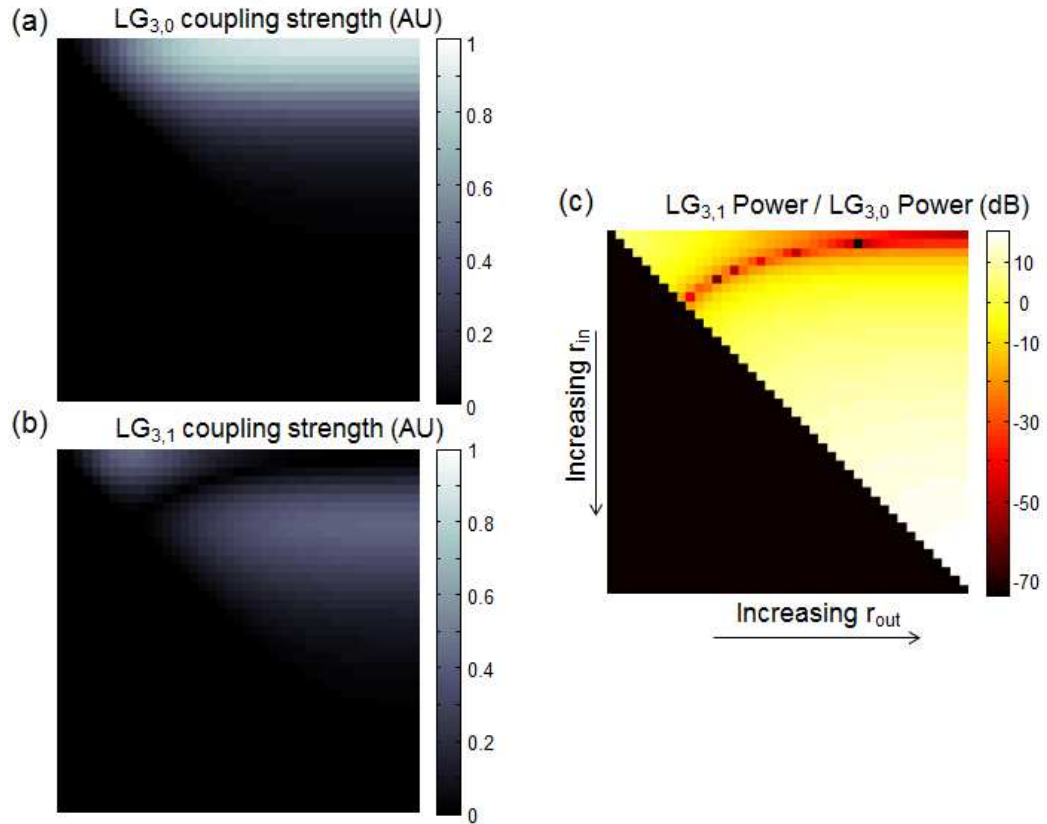


Figure 5-7: (a) Coupling strength into $LG_{3,0}$ of a Gaussian beam multiplied by a spiral phase and modulated by an annular binary transmission aperture; vertical axis is increasing inner radius of the annulus in the downward direction, and horizontal axis is increasing outer radius in the right direction (b) Coupling strength into $LG_{3,1}$ under same conditions (c) Mode purity $LG_{3,1}/LG_{3,0}$ under same conditions. Note a curve (dark red) where $LG_{3,1}$ is suppressed

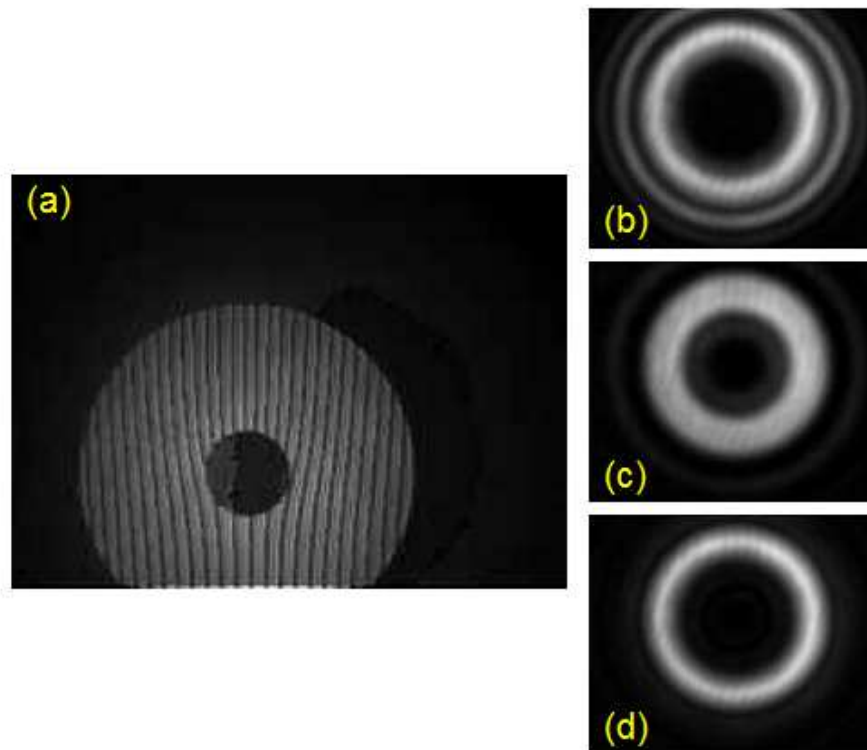


Figure 5-8: (a) Near field image of SLM field, showing annular pass-band and fork lines (b) Far field diffraction for $r_{inner} = 20pix$ and $r_{outer} = 300pix$ (negligible effect) (c) $r_{inner} = 20pix$ and $r_{outer} = 100pix$ (d) $r_{inner} = 32pix$ and $r_{outer} = 150pix$ Control of ringing structure is evident

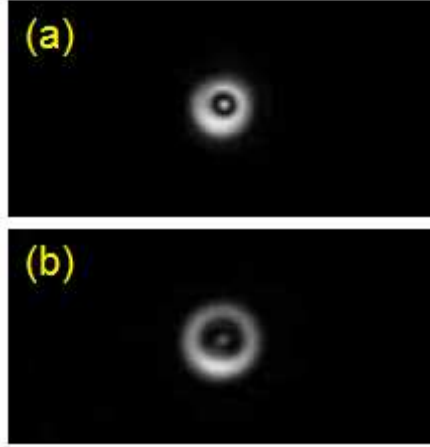


Figure 5-9: Excitation of (a) $HE_{1,1}$ and (b) $HE_{1,2}$ in air core fiber

been traded for loss at the SLM plane. However, this kind of beam sculpting is desired for controlled excitation of $HE_{4,1}$ versus $HE_{4,2}$ modes in fibers which support multiple radial order modes. Fig. 5-9 shows the excitation of $HE_{1,1}$ and $HE_{1,2}$ modes in the first generation air core fiber, enabled by this annular aperturing technique (note that as we will discuss in Chap. 6, the fundamental mode in an air core fiber has a ring shape but no OAM). This technique can be extended to sculpting nearly arbitrary field shapes using more complicated phase masks, which manipulate the full complex amplitude of the beam leaving the SLM (Bolduc et al., 2013). However, more complicate phase patterns will intrinsically result in lower diffraction efficiency and thus higher loss due to finer spatial features.

One intrinsic difficult with using an SLM in the far field is that different mode orders will by default have different mode sizes in the focal plane of the coupling lens, even when the amplitude is sculpted. For exciting a small manifold of OAM states, such as $l = 5, 6, 7$, this is not an issue, but for exciting a wide variety of mode orders, this is problematic. Experimentally, we observe that size-matching the desired OAM mode is crucial for obtaining pure mode coupling. There will always be some tilt or misalignment in the input coupling system which provides an alignment purity

‘noise’. If the input coupling is poor in strength due to the OAM mode being badly mis-sized, the desired mode’s strength will be much closer to this limit imposed by either random defects, or aberrations which are nearly impossible to correct by hand. We observe from time domain that in some cases, we cannot achieve a mode purity of better than $-12 \sim -15\text{dB}$ if the lens and/or beam size are poorly matched to the fiber. This issue can be solved by using an SLM in a multi-pass configuration (Sridharan et al., 2012; Vaity et al., 2014; Gregg et al., 2015a)

A second configuration for an SLM is to use it in the image plane of the FUT, in which case the SLM is typically placed as far away from the fiber as possible to ensure a large magnification. From Eq. (5.4), it is clear that in such a configuration, a spherical phase (lens) should be placed on the SLM to account for the phase accrued in the imaging operation (in imaging a flat surface onto a flat surface, not a sphere onto a sphere) (Goodman, 2005). This configuration is useful as it can provide immediate alignment assistance - the SLM plane can be imaged in either direction (from fiber to input, or input to fiber) and the necessary magnification thus tuned, since the beam sizes can both be defined in terms of pixel radius, and should be about the same. This configuration

can also be useful for differentiating in excitation between $HE_{l,1}$ modes and $HE_{l,2}$ modes by introduce in π phase shift in the appropriate place in the SLM plane. However, this configuration cannot use a tilted grating on the SLM. If the imaging system

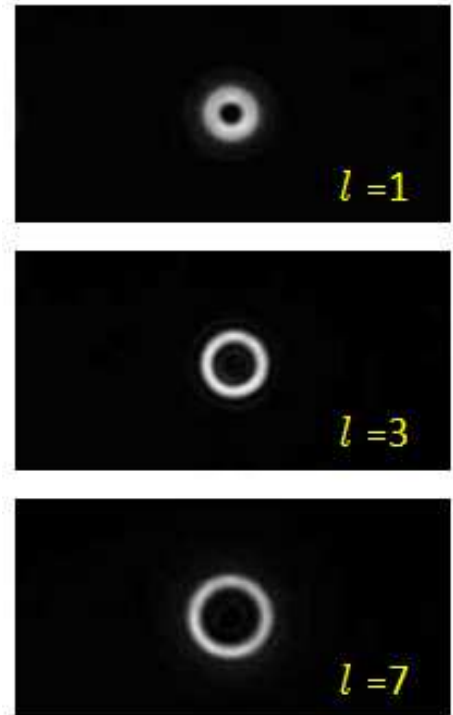


Figure 5-10: Sculpted amplitude distributions for a few OAM states

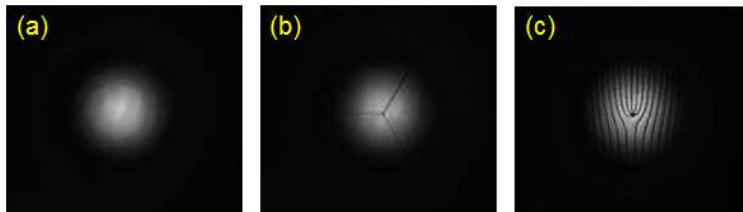


Figure 5.11: Image of (a) blank SLM surface illuminated by Gaussian beam (b) SLM surface with a spiral phase pattern and (c) SLM surface with a fork pattern

has enough clear aperture and is designed intelligently enough that the beam does make it to the fiber facet, the fiber will see a magnified reconstruction of the pattern on the SLM, which now includes a linear phase gradient across the face of the SLM. This is equivalent to trying to input couple an OAM state, and will result in an OAM spectrum with undesired modes. Thus, in an imaging configuration, multiple diffraction orders are not separable in space, although the lens on the SLM may render undesired beams significantly weaker locally.

In (Gregg et al., 2015a) we utilized a two stage SLM excitation system to excite a variety of fiber modes. The input Gaussian beam is collimated as it strikes the first SLM pattern, which contains a helical phase, a tilt, an amplitude mask to excite $LG_{l,0}$ modes of waist w , and a lens of focal length $\sim 1\text{m}$. Light propagates approximately 1m to the second SLM phase plate, thus the first beam is Fourier transformed onto the second SLM plane. The second SLM apertures higher diffraction orders, and contains only a lens, and is imaged into the FUT. The waist from SLM1 was variable, allowing for change in the spot size on SLM2, which varied the coupling efficiency. A phase discontinuity of π at a certain radius is applied on SLM2 to selectively excite first radial order or second radial order modes.

The SLM is controlled by a Labview virtual instrument (VI) which treats the SLM as a monitor. The phase patterns are calculated and summed before being taken modulo 255 (bit depth of the SLM) and displayed. Early versions of this code were

written by Dr. N. Bozinovic, and were expanded and adapted for the work herein. In theory the bit depth of the SLM changes slightly with wavelength, but this leads to negligible loss changes. SLM insertion loss depends on pattern complexity, and is typically on the order of $1 \sim 4$ dB. The SLMs come with pre-calculated calibration patterns meant to account for the fact that the SLM surface can be slightly curved. We find that these patterns do not appreciably change the achievable purity whether they are applied or not; however, if the pattern is applied during alignment and later removed, this can lead to immediate misalignment.

One limitation of SLMs is that they typically cannot modulate light faster than a few tens of Hz. This prevents their application as a dynamic switching element. However, for static alignment, their stability on the order of hours to days in the face of temperature variation and environmental fluctuation can prevent the need for constant realignment.

If zero-order QWPs are used, and the mirrors between the SLM and kept at slight angles, suppression of undesired other polarizations can typically be achieved to -25 to -30dB. The mirrors should be aligned to displace the beam vertically very little (that is, the SLM and the coupling lens/fiber should be mounted such that they are nearly the same height). Then, the QWP should be kept between the second mirror and fiber, as the two mirrors are unlikely to mix the linear polarizations but may induce a phase shift between them, which would scramble circular polarizations.

For input coupling, the fiber is mounted on a fiber V-groove on a Thorlabs nanomax 6-axis stage. We find that although the angular precision is not always necessary to achieve high-purity coupling, these stages tend to be much more stable than the standard 3-axis translation stages, which yields much better long term system stability. For output coupling, any reasonable three-axis stage can be used, although the lens needed to image the fiber must be relatively high-NA due to the

rapid divergence of free space OAM states.

5.4 Liquid Crystal q -plates

Optical systems using SLMs can excite OAM modes in fiber by separately tailoring their polarization and phase. Although this implies the freedom to, within the appropriate system, excite any single OAM mode, it also implies that it may be difficult to excite a controlled superposition of modes efficiently, other than the superposition of SO_a and SO_{aa} of the same l . It is known that for $l = 1$, the degenerate states couple for fiber propagation at 100s of meter, or kilometer length scales (Bozinovic et al., 2013). This was controlled in transmission experiments by making a fiber polcon with loops of OAM carrying fiber, allowing for disentangling of fiber mixing of degenerate states similar to polcons for single mode fiber. However, this unwinding methodology may not be extendable to multiple states simultaneously (in the same fiber), and as we shall see in Chap. 7, high- l states resist this mode coupling completely over short fiber lengths. Thus, it would be beneficial to use a mode converter which has the ability to excite arbitrary controlled superpositions of degenerate OAM states.

Such a functionality is offered by q -plates, which couple spin and orbital angular momentum of free space beams (Marrucci et al., 2006; Marrucci et al., 2011). A q -plate is essentially a spatially variant half-wave plate, wherein the orientation of the fast axis of the half-wave plate, α , varies as a function of azimuthal coordinate, ϕ , and completes q rotations as ϕ goes from 0 to 2π .

$$\alpha(\phi) = q\phi + \alpha_0 \quad (5.13)$$

q can be a positive or negative integer or half-integer, and α_0 is a constant. q -plates can be realized by photo-alignment of liquid crystal cells wedged between indium tin oxide (ITO) substrates (Slussarenko et al., 2011b). An AC bias is applied to the

liquid crystals, causing molecule oscillation into and out of the plane of the q -plate which has the effect of slightly changing the refractive index, thus the birefringence of the q -plate is tunable to arbitrary wavelengths (Slussarenko et al., 2011a).

If a q -plate is biased to half-wave retardance for a given wavelength of operation, it performs the following linear transformation:

$$\mathbf{q} \cdot (A\hat{\sigma}^+ + B\hat{\sigma}^-) = Ae^{i\alpha_0}\hat{\sigma}^-e^{i2q\phi} + Be^{-i\alpha_0}\hat{\sigma}^+e^{-i2q\phi} \quad (5.14)$$

That is, the q -plate flips the spin from plus to minus, or vice versa, and adds OAM of order $2q$. Since half-wave plates (HWPs) will exchange circular polarizations without affecting the sign of the OAM, a q -plate followed by a HWP is effectively a q -plate of charge $-q$ (although the output beam would retain its original polarization. Strictly speaking, a q -plate of charge q followed by an HWP is equivalent to an HWP followed by a q -plate of charge $-q$). Critically, note that $\hat{\sigma}^+$ is exactly converted to the SOaa OAM of topological charge $2q$, while $\hat{\sigma}^-$ is converted to that state's degenerate pair, the SOaa OAM of topological charge $-2q$. Thus, controlling input polarization, with either free space waveplates or fiber polarization controllers, directly controls the superposition of degenerate OAM states excited at the fiber facet. In most cases, the phase term corresponding to α_0 can be safely ignored, as it does not affect the ability of the q -plate ability to excite a controllable OAM superposition. These terms are thus dropped for the rest of this chapter. However, two instances in which this phase term cannot be ignored are discussed in Sec. 7.4 and Sec. 10.1.

All q -plates used in the experiments in this document are provided courtesy of Mr. Andrea Rubano, Dr. Ebrahim Karimi, and Dr. Lorenzo Marrucci. The q -plate can also be biased to be half-wave retardance for a given wavelength by application of an AC voltage of frequency $1 \sim 4\text{kHz}$, which fully converts the input state, or biased to full-wave retardance, leaving the original state intact (Slussarenko et al., 2011a).

For an arbitrary bias, the q -plate will create a superposition of the original state and the converted state as the retardation is between $m\lambda/2$ and $m\lambda$. This is indicated in Fig. 5.12. In Fig. 5.12 (a)-(c) the bias of a $q = 1/2$ plate is increased from its static value for a input wavelength of 1550nm. In the partially biased case in (a) the singularity is off-center due to the superposition of a Gaussian and an $l = 1$ OAM state; note that both spins must be incident upon the q -plate to see this interference, as $\hat{\sigma}^+$ will be converted to $\hat{\sigma}^-$ by the q -plate, and the converted and unconverted beams will not interfere spatially due to orthogonal polarizations. The singularity depth in (b) indicates good conversion to the desired OAM mode, while the clear spot visible in (c) occurs when the q -plate is over-biased to a retardance of λ . (a) demonstrates that for the case of a $q = 1/2$ plate, alignment is achieved iteratively, as both an offset in the center of the beam on the q -plate, and an imperfect q -plate bias setting will yield an off-center, dim singularity. However, for a higher q such as (d)-(e) for $q = 3$, alignment is more straight-forward, as an offset will yield a crescent-moon shape as in (d), and imperfect bias will yield a 6-fold star pattern as in (e), or, in nearly perfect bias, the output beam will look like a bright ring circumscribing a hexagon. A well converted beam is shown in (f).

Although its main utility is in the entangled nature of the spin and OAM degrees of freedom, for the purposes of alignment, those two functions (polarization conversion and OAM conversion) can be treated separately, that is, we can imagine it to be a scalar phase plate with an additional desired property). Thus, the q -plate can be aligned much the same as an SLM regarding centering the plate, and aligning the beam from the q -plate to the fiber, illustrated schematically in Fig. 5.13 for the case of $l = 1$. Much as the SLM required high-fidelity alignment to the pattern center and through the coupling lens, so does the q -plate. We observe that if the q -plate is not centered, one polarization can be well-coupled into the FUT. However, when

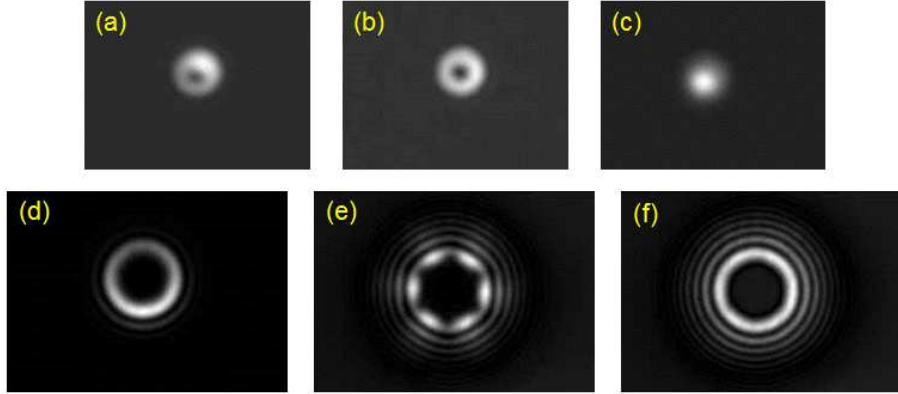


Figure 5-12: (a)-(c) Throughput of $q = 1/2$ plate as a function of increasing bias (d) Offset $q = 3$ plate at idea bias (e) Centered $q = 3$ plate at non-idea bias (f) Ideally biased and centered $q = 3$ plate throughput

the input polarization to the q -plate is changed to the opposing spin, the fiber input coupling will degrade rapidly, even to the point that the $l = 2q$ mode is no longer dominant. Thus, the alignment procedure should be modified as follows. As before, forward illuminate through q -plate and fiber coupling lens, and back-propagate from the FUT to ensure rough alignment and collimation. However, when the output fiber mode is observed, the polarization to the q -plate should be varied between launching one OAM state, and launching a superposition of the two states. The q -plate center and the tilt to the fiber can thus be adjusted iteratively. If the input polarization is set to only excite one OAM state, the alignment tends to coalesce into an equilibrium in which one degenerate OAM state has 20dB or better mode purity, while its degenerate partner has mode purity 10dB or worse. As with the SLM, time of flight is the easiest way to ensure pure coupling, so long as enough fiber is available. However, unlike the SLM, the q -plate lacks the ability to also impose a ‘lens’ on the beam propagating through it, and is thus more sensitive to placement in the optical system, and coupling lenses must be well chosen. Suppose that a collimated beam strikes the q -plate, propagates a distance z_2 between the q -plate and the coupling

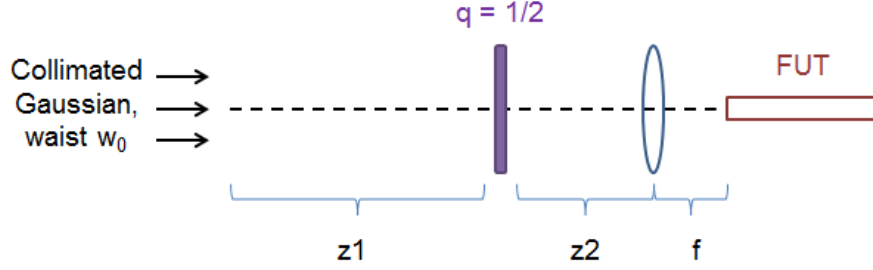


Figure 5-13: Sketch of input coupling system with q -plate

lens of focal length, f , and the focuses down onto the FUT which is exactly in the focal plane of the lens. The ABCD matrix for such a scenario is given by:

$$\begin{pmatrix} 0 & f \\ -\frac{1}{f} & 1 - \frac{z_2}{f} \end{pmatrix} \quad (5.15)$$

Investigation of Eq. (5.5) shows that the field will be an exact Hankel transform of the beam striking the q -plate, although the incident beam has $l = 0$ and the Hankel transform will be order $l = 2q = 1$, with the exception of the spherical phase term outside the integrand. The focal length of the lens will determine the scale of the OAM beam in the plane of the fiber, as shown in Fig. 5-14 (a), where the distribution of the optical field as a function of radius is calculated for multiple lenses and compared with the distribution of the $l = 1$ fiber mode. Fig. 5-14(b) shows the calculated coupling efficiency as a function of coupling lens focal length, with a local maximum of around 1dB at a focal length of 8-10mm. Fig. 5-14(c) shows a decline in coupling efficiency as the q -plate to fiber distance increases, due to the building spherical phase curvature (according to simulations, the absolute value of the field envelope does not change for any point in (c)).

Our full experimental apparatus is sketched in Fig. 5-15. A continuous-wave (CW) laser is passed through an electronic fiber polcon, which can select an arbitrary polarization state at the output of a segment of SMF. The light is collimated and

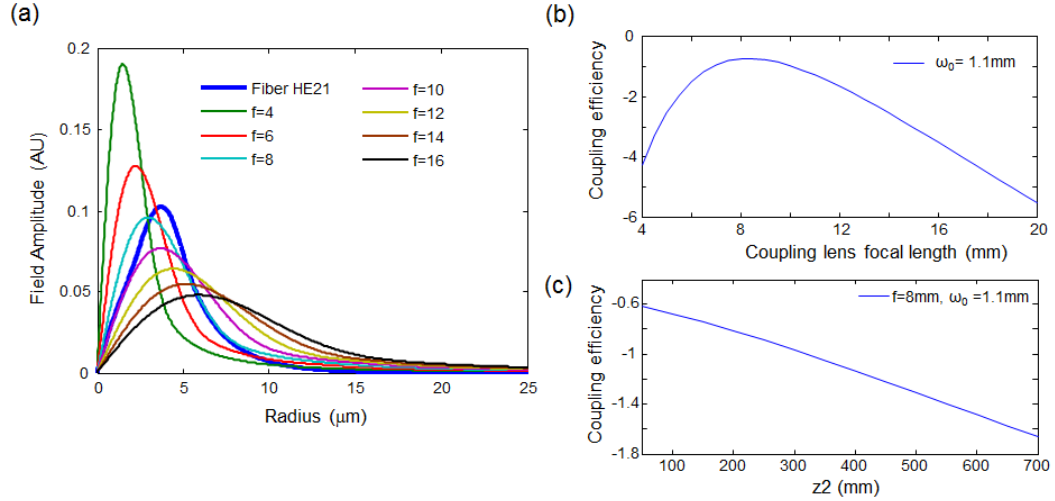


Figure 5-14: (a) Field distribution in focal plane of lens using $q = 1/2$ plate for variety of focal lengths (b) Coupling efficiency versus lens focal length for a fixed z_2 of 16mm, the limit on proximity available in experiment (c) Coupling efficiency as a function of z_2 for a fixed focal length

passed through a q -plate which is biased by a function generator, turning the q -plate ‘on’ or ‘off’. The beam of light is next passed through two QWPs the fast axes of which are either crossed, doing nothing, or parallel, making a HWP. The bias setting determines whether the q -plate converts the Gaussian or not, the QWPs determine whether the SOa $l = 1$ modes or the TE and TM modes, and the input polarization determines which modes within a given set are selected (note that in free space, as given by Eq. (2.17a) and Eq. (2.17b) the TE and TM modes can be written as a linear combination of SOaa $l = 1$ OAM states, although the pure OAM states are by definition not fiber modes as TE and TM are not degenerate). The light is then coupled into OD110 Vortex fiber, which supports $l = 1$ stably at 1530nm, and in which $LP_{0,2}$ and $l = 2$ are nearly degenerate with each other and lossy (Chap. 6). Coupling loss, defined as power before the q -plate minus power after the fiber, after normalizing for in-fiber loss, is 3.1dB for the fundamental mode and 2.4dB for the OAM and TE/TM modes. 1.4dB of loss was insertion loss from the q -plate ,

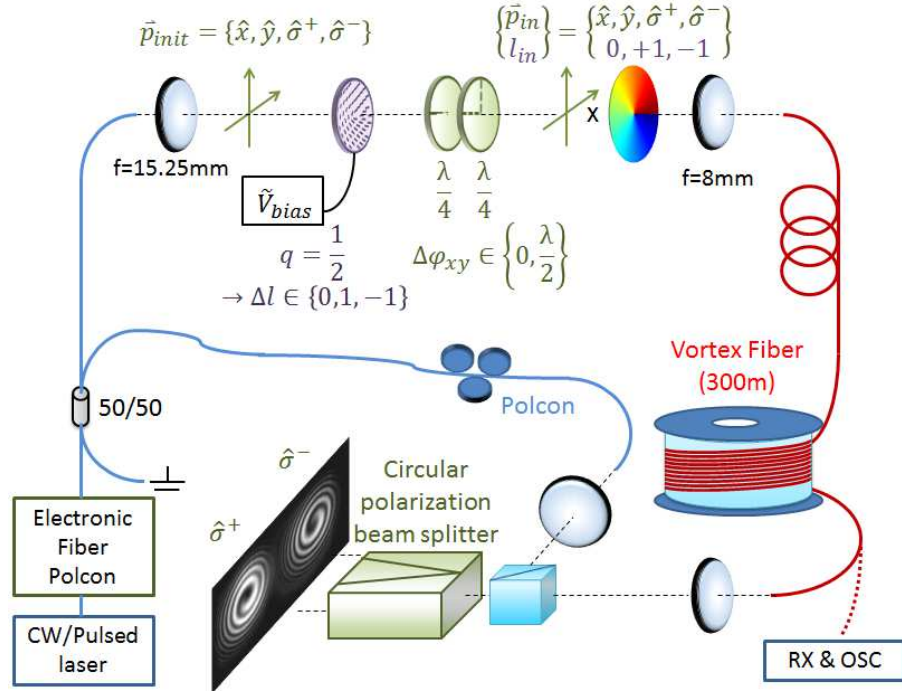


Figure 5.15: Schematic of system used to test functionality of $q = 1/2$ plate

which is not anti-reflection (AR) coated. Coupling is stronger into the higher order modes because the lens was chosen for coupling into the set, resulting in a higher loss into $l = 0$. The states then pass through 300m of vortex fiber, after which they are either sorted by circular polarization, or directed to a fast detector for time of flight measurements. Fiber output images and interference patterns are shown in Fig. 5.16. Only one is shown for $l = 0$ as both modes have identical interference patterns in different bins. As expected, the two OAM modes show bright rings in only one polarization and spirals with one arm and a handedness which matches the polarization orientation. Meanwhile, the TE and TM modes show two rings of roughly equal brightness, and one-armed spiral interference patterns of opposite handedness. Note that the TE constituent OAMs are out of phase by π , while for the TM mode, the arms originate at the same point. Launched mode purities are calculated using time of flight measurements. Since distributed cross-coupling between OAM and

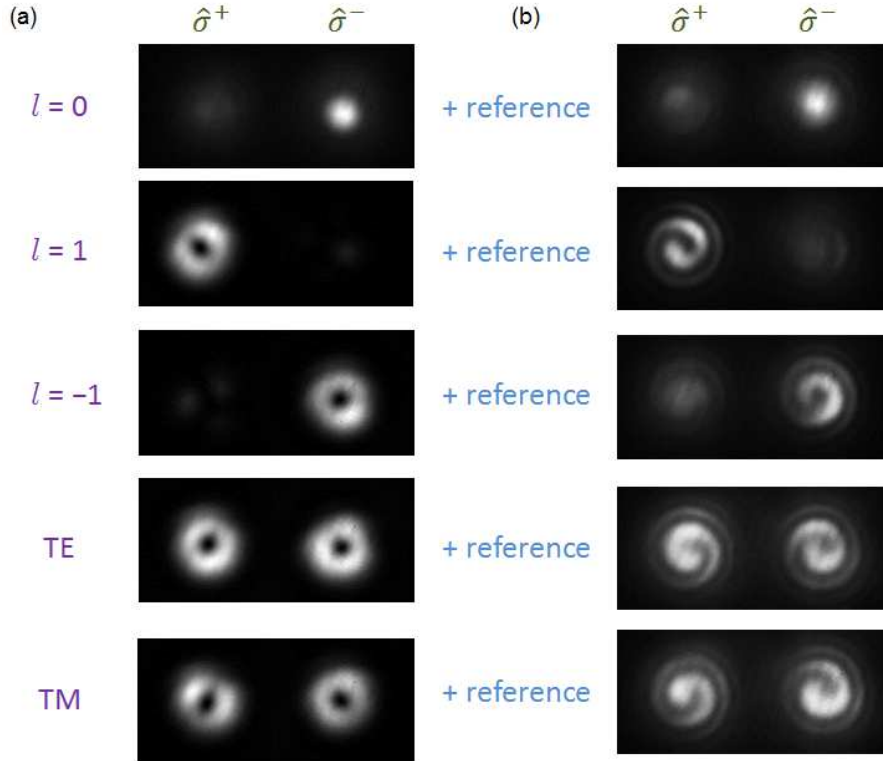


Figure 5-16: (a) Output and (b) output plus reference after propagation through 300m of vortex fiber with 1530nm CW source

TE/TM is on the -15dB level, and distributed cross-coupling between $l = 0$ and $l = 1$ is not observed above the detector noise floor, the input mode purity is calculated as ratios of discrete peaks as described in Sec. 4.5. The results are shown in Fig. 5-17. Discrimination among modes is on the order of 20dB or better, with the exemplary measurement of the power in $LP_{0,2}$ when TE is launched impacted by detector impulse response.

Transitioning from $q = 1/2$ to higher order q -plates, such as $q = 3$ for the $l = 6$ families, mode selectivity remains on the same order of magnitude, although the input coupling efficiency strictly decreases as a function of increasing l for the same fiber. For larger q values, the q plate by itself will excite the SOaa modes if $q > 0$, while a q -plate plus HWP will excite the SOa modes.

Excited\Meas	$l=0$	TE	OAM	TM	LP ₀₂ /LP ₂₁
$l=0$	-	-24.6	-21.0	-24.2	-29.5
TE	-20.4	-	-19.1	-19.1	-13.8*
OAM	-22.9	-22.1	-	-18.8	-19.1
TM	-20.9	-29.9	-19.1	-	18.1

Figure 5.17: Excited mode purities using a $q = 1/2$ plate. Measurement of TE into $LP_{0,2}$ occluded by detector impulse response; cross coupling should be on the same order as that into $l = 0$

Note that the inverse element of a q -plate is a q -plate of the same q , that is,

$$\mathbf{q} \cdot \mathbf{q} \cdot (A\hat{\sigma}^+ + B\hat{\sigma}^-) = (A\hat{\sigma}^+ + B\hat{\sigma}^-) \quad (5.16)$$

Putting a set of degenerate SOaa modes through a negative q -plate of the same $|q|$, for instance, doubles the topological charge imparted:

$$\mathbf{q} \cdot -\mathbf{q} \cdot (A\hat{\sigma}^+ + B\hat{\sigma}^-) = (A\hat{\sigma}^+ e^{i4q\phi} + B\hat{\sigma}^- e^{-i4q\phi}) \quad (5.17)$$

Thus, sending the output of an OAM fiber containing all of the $|l| = 2q$ modes through either a q or $-q$ plate and projecting into SMF provides a method of differentiating SOa and SOaa states with very low measurement crosstalk. This, along with the functionality of q -plates as higher order polarization controllers, will be discussed in depth in Chap. 7

5.5 Other Excitation Mechanisms

There are numerous other strategies for exciting OAM modes, such as on-chip multiplexers (Su et al., 2012; Sun et al., 2014) which typically use a phased-array antenna type structure for emulating the helical phase of an OAM mode. The OAM mode sorter can in theory be applied in the reverse direction, for excitation of collinear OAM beams with negligible loss (Berkhout et al., 2010), although such a system

would require precise free-space optics to match the spindle-like output point spread function (PSF) of the mode sorter. Photonic lanterns (Lai et al., 2007) or fused fiber couplers (Pidishety *et al.*, submitted to CLEO 2016) could be used to excite OAM modes in a phase matched manner. Perhaps one of the most interesting possibilities is the sculpting of multiple modes simultaneously by multi-plane light conversion (Morizur et al., 2010; Labroille et al., 2014), which uses a series of gradual unitary transforms to convert multiple beams with low loss, and has already been demonstrated to be compatible with mode division multiplexing (MDM) (Genevaux et al., 2015). This will be discussed further in Chap. 11

5.6 Summary

We have discussed in detail two methods for exciting OAM modes in fibers: using SLMs to tailor the phase and a QWP to tailor the polarization of the OAM modes, or using q -plates to excite specific linear combinations of degenerate OAM modes using input polarization as a control. Alignment tolerances and procedures are discussed, and the utility of time of flight measurements as an alignment method is reiterated. The ability to excite controlled OAM modes to 20dB or better in mode purity has been demonstrated.

The free space coupling described in this chapter applies only to weakly guided OAM modes in fibers - strongly spin-orbit coupled modes will require additional phase and polarization tailoring not available through the techniques just described (this will be discussed in Chap. 6 and Chap. 11 as research into these modes is still ongoing at the time of writing this document). LP modes could easily be described by the methods described in this chapter, but with binary (0 and π retardance) phase plates which break the SLM into azimuthal segments. SLMs can also be used to excite scalar $LP_{0,m}$ modes in fiber via both imaging and far field configurations (Demas

et al., 2015a), and can be used in single pass or multi-pass, single or multiple beam combinations for a wide variety of beam tailoring options outside the scope of this document (Davis et al., 1999; Maurer et al., 2007; Vasilyeu et al., 2009; Litvin et al., 2015).

With excitation and characterization mechanisms discussed, we turn to the last and more important experimental piece for enabling the transmission and study of OAM states in fibers: the fibers themselves.

Chapter 6

OAM in Fibers

The study of optical vortices in fiber is a relatively recent one. Generation of OAM by stress-induced birefringence (McGloin et al., 1998) and acousto-optic angular momentum transfer (Dashti et al., 2006) were shown, and a large amount of theoretical work describing optical vortices in MMF (Alexeyev and Fadeyeva, 1998), and weakly guiding fibers under a wide variety of perturbations (Alekseev et al., 2002; Alexeyev et al., 2009) (and many more works by the same group of authors) had been demonstrated by the mid-2000s. However, to my knowledge, the first demonstration of propagation of optical vortices in fiber over reasonable length scales (more than a few m) was by Ramachandran *et al* in 2009, while the first demonstration of OAM propagation over lengths of the scale $\sim 1\text{km}$ was not until 2011 (Bozinovic et al., 2011).

The reasons for this delay are twofold. From a more abstract theoretical point of view, authors were interested in obtaining a pure optical vortex which is maintained for arbitrarily long distances, which, given that OAM modes come in degenerate pairs, should be impossible since any perturbation with a nonzero coupling coefficient will eventually couple them. This led to consideration of twisted fibers and twisted elliptical fibers (Alexeyev et al., 2004; Alexeyev and Yavorsky, 2004) with incredibly small and difficult to fabricate twist pitches (well under 1cm) to ensure modal stability by breaking all modal degeneracies. From a conventional ‘fiber’ point of view, if the fiber modes are constructed as LP modes, then a coherent superposition of two LP modes with a fixed phase relationship is necessary to obtain a linearly polarized optical

vortex. LP modes are four-fold degenerate, and can freely couple in the presence of bends and induced polarization birefringence, shape deformation, etc. From that point of view, maintaining an optical vortex under reasonable conditions should be difficult or impossible.

This chapter discusses fibers which support OAM states and polarization vortices. It begins with, to my knowledge, the first fiber to stably support OAM states and polarization vortices over km length scales and in the presence of perturbations, and which is thus denoted the ‘Vortex Fiber.’

All of the fibers in this chapter were fabricated by Dr. Poul Kristensen (OFS Fitel, Denmark), without whose inestimable contributions, both intellectual and experimental, this thesis surely would not exist.

Many of the subsections in this chapter feature field simulations of different waveguide structures. The simulation tool used here, the engine of which was built by Dr. Martin Pedersen (Pedersen et al., 2011), is a finite difference solver which simultaneously finds the coupled H_r and H_ϕ equations as an Eigenvalue problem, then finds H_z using the Magnetic Gauss’ law. As long as $|H_z| \ll |H_r|, |H_\phi|$, due to the relations $H_r \approx -\frac{\beta}{\omega\mu} E_\phi$ and $H_\phi \approx \frac{\beta}{\omega\mu} E_r$ from Eq. (2.24), we can use the \mathbf{H} field as a proxy for the \mathbf{E} field, and specifically, we can use either H_r or H_ϕ in lieu of the mode amplitude in the weakly guided case, $F(r)$.

6.1 The Vortex Fiber

The LP fiber mode solutions are analogous to the solutions one would find solving the time independent Schrödinger equation for a rotationally symmetric 2D quantum well, with the added degree of freedom of polarization (that is, an additional 2-fold

degeneracy in choosing $\hat{\mathbf{x}}$ or $\hat{\mathbf{y}}$ polarization).

$$\left[-\frac{\hbar^2}{2m} \nabla_t^2 + V(r) - E \right] \Psi = 0 \leftrightarrow [\nabla_t^2 + n(r)^2 k^2 - \beta^2] e_t = 0 \quad (6.1)$$

The main insight in (Ramachandran et al., 2005b; Ramachandran et al., 2009) was to invoke the fact that light is not a scalar quantity; that the boundary conditions are not agnostic to polarization, and to leverage this in waveguide design.

Specifically, consider the $l = 1, m = 1$ modes. In the LP picture, these are the four-fold degenerate $LP_{1,1}$ modes, while in the weakly guiding picture, these are the $TE_{0,1}$, $TM_{0,1}$, and the two $l = 1$ SOa OAM modes, or equivalently, the two $HE_{2,1}^{e,o}$ modes. For discussion of the Vortex Fiber, we use HE mode designations, since these were used in the original work. The deviation of each of the vector modes in β from the value predicted by scalar mode theory, β_0 , is given by (Snyder and Love, 1983):

$$\delta\beta_{TE} = 0 \quad (6.2a)$$

$$\delta\beta_{OAM} = \frac{\Delta}{4\pi} \frac{\lambda}{n_{co}} (I_1 - I_2) \quad (6.2b)$$

$$\delta\beta_{TM} = 2 \frac{\Delta}{4\pi} \frac{\lambda}{n_{co}} (I_1 + I_2) \quad (6.2c)$$

with Δ the fiber index profile height parameter, $\Delta = \frac{n_{co}^2 - n_{cl}^2}{2n_{co}^2}$, n_{co} being the maximum refractive index in the guiding region(s) and n_{cl} being the cladding refractive index, with:

$$I_1 = \int r dr F(r) F'(f) f'(f) \quad (6.3a)$$

$$I_2 = l \int dr F^2(r) f'(r) \quad (6.3b)$$

$F(r)$ is the field's radial envelope as in Sec. 2.2, and $f(r)$ is the shape function of the waveguide scaled to 1 at the point of highest refractive index. Note that the TE mode does not have a polarization correction to its β value due to the mode having exactly

zero electric field in the radial direction - thus its behavior is entirely determined by field continuity, making it analogous to a scalar solution. Similarly, the TM mode has the largest correction because its field is entirely radially polarized, thus its behavior is entirely determined by \mathbf{D} field continuity. The HE modes, which have a combination of radial and azimuthal polarization, are between the two extrema.

If the degeneracy among $TE/TM/HE_{2,1}$ is sufficiently lifted, mode coupling among these modes should be significantly reduced due to phase mismatch. Eq. (6.3a) and Eq. (6.3b) imply that the degeneracy can be strongly broken if large values of the electric field and field derivative of the guided mode coincide with large refractive index gradients. Thus, the Vortex Fiber is designed to have a ring-shaped guiding region for the $l = 1$ and TE/TM modes. A central core is retained for ease of coupling from SMF.

The fiber refractive index profile and effective index curves for one realization of the Vortex Fiber (outer diameter (OD)110) is shown in Fig. 6-1(a). As is evident from Fig. 6-1(b), the effective index splitting among the $HE_{2,1}$, TE, and TM modes is on the order of 10^{-4} , which is of comparable order of magnitude to the birefringence induced splitting in PM fibers (Noda et al., 1986). This splitting was confirmed in (Ramachandran et al., 2009) by means of microbend gratings, where it was observed that the resonance wavelengths for TE and $HE_{2,1}$, and $HE_{2,1}$ and TM are split by approximately 100nm, confirming the simulated n_{eff} splitting. Fig. 6-1(c) and (d) show plots of the \mathbf{H} field in the Vortex fiber, obtained by simulation using an experimentally measured index profile. The H_r and H_ϕ components overlap almost perfectly with a relatively small H_z , indicating that the modes are weakly guided, although the $HE_{1,1}$ mode has an atypical Gaussian + ring shape.

The $l = 1$ OAM modes in the vortex fiber have been excited by microbend gratings (Bozinovic et al., 2012) and SLMs, data transmission at Terabit-per-second rates has

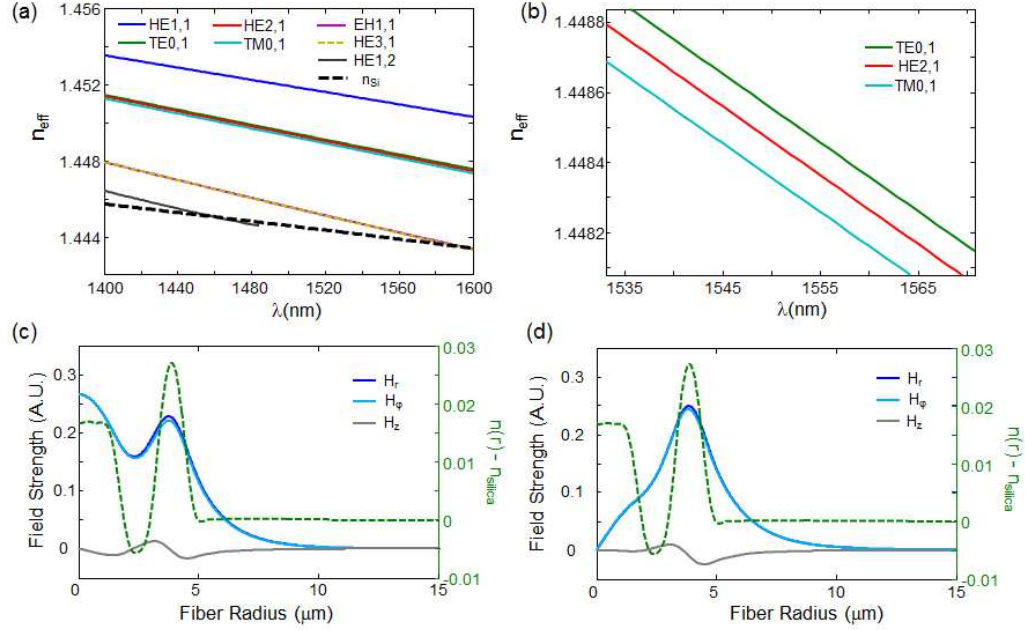


Figure 6.1: (a) Effective index curves for all guided modes in OD110 Vortex Fiber (b) zoom-in of $TM/TM/HE_{21}$ modes, where splitting on the order of 1×10^{-4} is evident (c) Right axis: Field profiles of $HE_{1,1}$ mode in Vortex Fiber plotted with Left axis: index profile (d) Field profiles of $HE_{2,1}$ mode in Vortex Fiber plotted with index profile. Figure based on a similar figure from (Ramachandran et al., 2009)

been demonstrated (Bozinovic et al., 2013), and preliminary experiments have been conducted, suggesting that the Vortex Fiber could be an efficient source for coaligned pump and probe beams for stimulated emission depletion (STED) microscopy (Yan et al., 2013)

However, the Vortex Fiber is designed to support only one set of OAM states, the $l = 1$ SOa modes. Although the splitting between $l = 1$ and TE/TM is 10^{-4} or better at 1550nm, the splitting between the $l = 2$ states at 1550nm is approximately 1×10^{-5} . If the Vortex Fiber is stretched radially to the point that it supports $l = 3$ and $l = 4$, their splitting in effective index will also be on the order of 10^{-5} . This can be qualitatively understood by investigation (and with some aid of hind-sight gained from later considerations in air core fibers). The splitting in β from the scalar

solution for $l > 1$ modes is given by (Snyder and Love, 1983):

$$\delta\beta_{SOa} = \frac{\Delta}{4\pi} \frac{\lambda}{n_{co}} (I_1 - I_2) \quad (6.4a)$$

$$\delta\beta_{SOaa} = \frac{\Delta}{4\pi} \frac{\lambda}{n_{co}} (I_1 + I_2) \quad (6.4b)$$

Equations Eq. (6.4a) and Eq. (6.4b) imply that the splitting between SOa and SOaa modes is therefore only dependent on I_2 , as indicated in Eq. (2.18) but rewritten here:

$$\Delta\beta_l = \beta_{SOa\ l} - \beta_{SOaa\ l} = l \frac{\Delta}{2\pi} \frac{\lambda}{n_{co}} \int dr F^2(r) f'(r)$$

Eq. (2.18) indicates that the splitting depends only on the square of the field distribution and the fiber's index profile. The square of the field is clearly positive definite, but $f'(r)$ can take on positive and negative values, because the refractive index can increase or decrease. If F^2 and f are reflection symmetric about the same point, which is nearly the case for $l = 2$ in the Vortex Fiber, as shown in Fig. 6-2, then the splitting should be zero. This is not exactly true because the mode center-of-

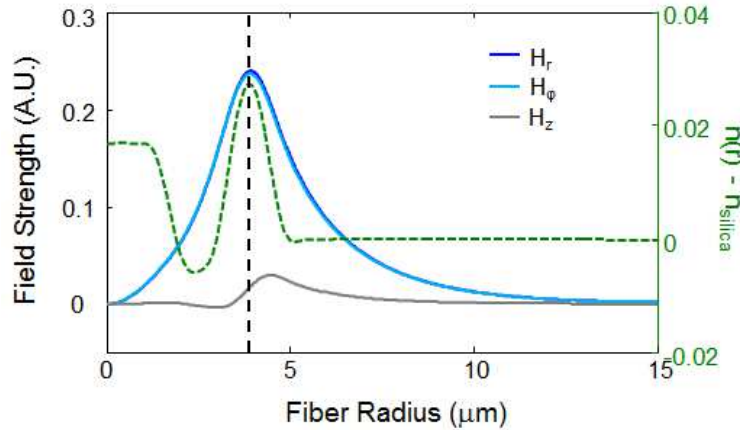


Figure 6-2: Field profiles for $l = 2$ mode in Vortex Fiber

mass changes as a function of mode order and wavelength, and the presence of the high-index core region makes $f(r)$ not reflection symmetric about the ring center. However, the higher l modes in the Vortex Fiber will all be contained mostly in the

ring region, and will feature the same weak splitting. Moreover, the presence of the central core in the Vortex Fiber allows for the presence of multiple radial orders for $l = 0$ (and eventually higher l if the central core becomes large enough), which should be avoided if possible. The removal of the central guiding region, and the insertion of the largest refractive index gradient available for fibers fabricated with modified chemical vapor deposition (MCVD) - that of glass to air- lead to the design and fabrication of a fiber with an air core for supporting OAM states.

6.2 Air Core Fibers: Design Criteria

There are two possible reasons for designing a fiber with an air hole in the center. First, the fiber could be designed to guide light in the air region by creating a photonic bandgap (Bornstein and Croitoru, 1985). These fibers are designed both to avoid undesirable nonlinear effects and to reduce latency, although such fibers can have losses on the order of single dB/m (Temelkuran et al., 2002). Second, the air hole is used to shape the modes, or the modal density of states, which exist in a Ge-doped ring region around the air core (Oh et al., 2005). This class of fibers was proposed and used as tapered mode converters from the fundamental mode in SMF to the $LP_{0,2}$ mode in a HOM dispersion compensating fiber (DCF), or to achieve a monomode fiber with an annulus shaped fundamental mode.

We seek to design a fiber or set of fibers which support OAM modes, featuring large n_{eff} splittings between SOa and SOaa modes of the same l . We know from Sec. 6.1 that a large splitting will be ensured by a large effective index gradient between the ring guiding region and the glass cladding, so as a design parameter, we generally keep that index step as large as possible. In order to obtain a fiber which stably guides an ensemble of OAM states, in addition to designing a fiber with n_{eff} splittings on the order of 10^{-4} as in PM fibers (Noda et al., 1986), we also aim to

design a fiber with the following properties:

- The number of $m = 2$ modes is zero OR
- The number of $m = 2$ modes is small, and none of the $m = 2$ modes feature accidental degeneracy with the OAM modes in the wavelength region of interest (the telecommunications C-band). Ideally this should be robust against fluctuations in air core inner diameter or fiber outer diameter
- The highest order OAM mode has an n_{eff} sufficiently above n_{SiO_2} that it is not cutoff or near cutoff
- The modes are well described by the weakly guiding approximation; that is, they are true OAM modes and not SOC angular momentum modes.

The last point requires some additional comments. As shown in Sec. 2.1, only for weakly-guiding fibers do OAM modes exist. More generally, states with an integral *total* angular momentum exist, with a possibly non-integer breakup of orbital and spin angular momentum. Their electric field distributions for a pair of degenerate angular momentum states are given by Eq. (2.12), rewritten here:

$$\mathbf{e}_{\mathbf{t}}^{\pm} = \frac{1}{2} e^{\pm i j \phi} \left[\delta_{\pm} \left(\gamma \hat{\sigma}^{+} e^{-i \phi} B_{j-1}(r) + \alpha \hat{\sigma}^{-} e^{i \phi} B_{j+1}(r) \right) \right. \\ \left. + \delta_{\mp} \left(\alpha \hat{\sigma}^{+} e^{-i \phi} B_{j+1}(r) + \gamma \hat{\sigma}^{-} e^{i \phi} B_{j-1}(r) \right) \right]$$

Evidently the above is a superposition of two different OAM states of different l , weighted by γ and α . All of the state excitation and characterization techniques discussed in earlier chapters, except for time of flight, will not work for these states to either excite pure modes or determine mode purity so long as γ and α are both nonzero.

A simplified version of the waveguide we simulate is shown in Fig. 6-3(a). The index contrast between ring and cladding, Δn_1 is a free parameter, but for the subset of simulations show in Fig. 6-3 we keep it constant at 0.04, while the cladding is kept at pure Silica and the core kept as air. We vary the inner radius of the fiber while

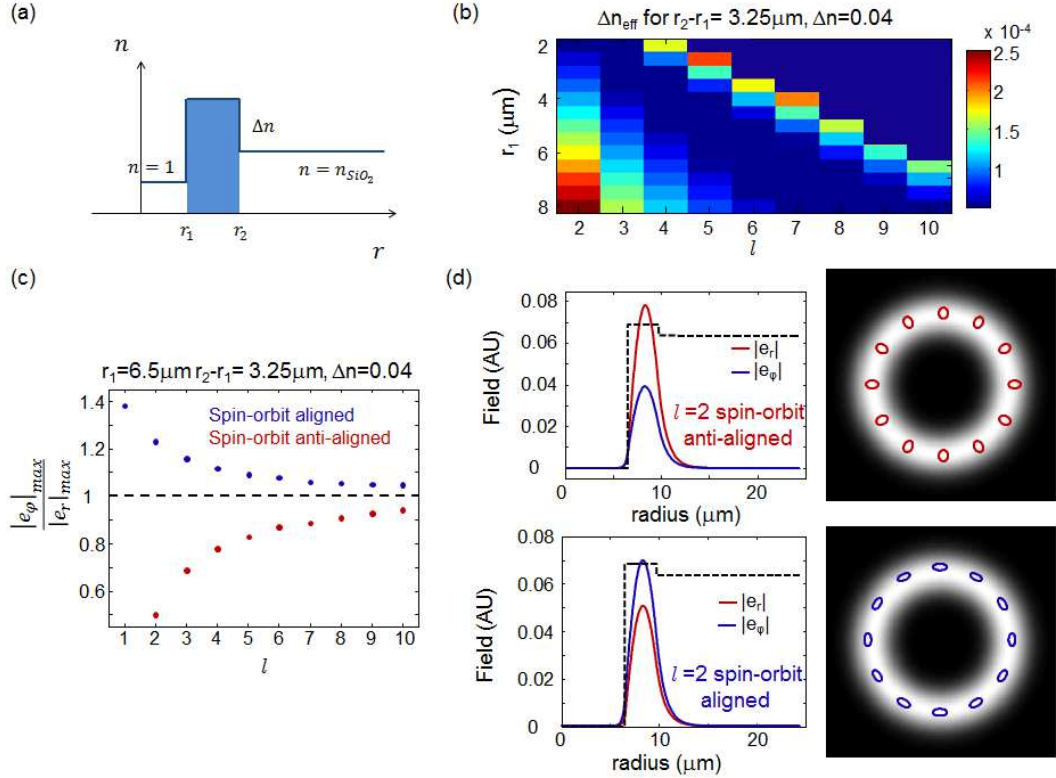


Figure 6-3: (a) Simplified index profile of air core fiber (b) n_{eff} splitting versus inner radius, for constant ring width, and OAM order (c) Metric of spin-orbit coupling in one example fiber versus OAM order (d) Example of radial and azimuthal part of electric field for spin-orbit coupled state, and complete polarization distribution

the ring thickness, $r_2 - r_1$ is kept constant. Δn_{eff} versus azimuthal mode order and inner radius is shown in Fig. 6-3(b). There are two clear regions of high n_{eff} splitting in the parameter space. For waveguides with thin rings relative to the inner radius, there is a large n_{eff} splitting for low- l modes, while for most waveguide designs, there is a smaller band of well-split high- l states. For the latter region, the modes

are OAM states and the n_{eff} splitting is driven by the gradient between the high index ring and the glass cladding. Because this effect happens for modes which come closer and closer to cutoff, in analogy to the radical change in a modal dispersion near to cutoff, we refer to this as the Dispersive Guidance regime. However, the first region features strong SOC, as shown in Fig. 6-3(c). The radial and azimuthal electric field components are nearly identical in shape, due to the strong confinement of the high index region. Thus, as a metric of the strength of SOC, we plot the absolute value of the ratio of the maximum field value of the azimuthal field component, e_ϕ divided by the maximum field value of the radial field component, e_r . In the weak-guidance regime, this is exactly one, which is the tendency for high- l states. Low l states, on the other hand, although they feature large n_{eff} splitting are strongly spin-orbit coupled. An example electric field distribution is shown in Fig. 6-3(d) for the $l = 2$ SOa and SOaa states. The radial and azimuthal field components are clearly different in strength, resulting in a spatially-dependent elliptical polarization, which is pseudo-radial for the SOaa modes and pseudo-azimuthal for the SOa modes. Technically speaking these modes are not OAM states; we retain the SOa and SOaa designations for convenience.

We perform a wide parameter sweep for ring widths varying from $1.5\mu m$ to $5.25\mu m$ in $0.5\mu m$ steps. We find that for very small ring widths, the states are nearly all in the SOC regime, although the number of $m = 2$ modes is typically 0 or at worst 1, as shown in Fig. 6-4(a) (Ramachandran et al., 2015): As the ring size is expanded, there is a greater chance to obtain more OAM states in the Dispersive Guidance regime, but the number of $m = 2$ modes increases as well, as in Fig. 6-4(b). These $m = 2$ modes will be low in n_{eff} , comparable to the desired OAM modes, at which point accidental degeneracy becomes a concern. However, if the ring is made too small, it is often difficult to achieve more than one well-guided OAM mode order; even for a ring

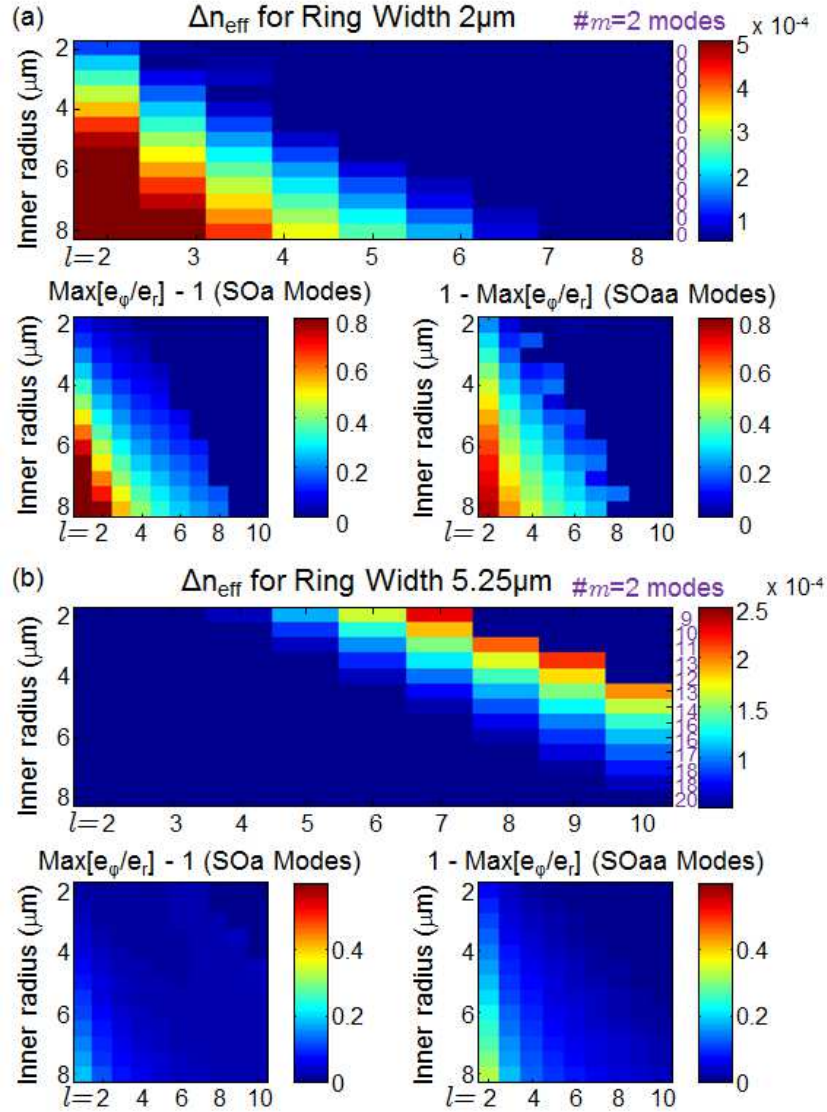


Figure 6-4: (a) n_{eff} splitting for a set of air core fibers with ring width $2\mu\text{m}$. Number of $m = 2$ modes in each fiber written in purple at right edge of plot. Smaller plots below indicate strength of spin-orbit coupling versus inner radius and mode order for both SOa and SOaa families (b) Same set of plots for air core fibers with ring width $5.25\mu\text{m}$

width of $3.25\mu\text{m}$ as in Fig. 6-3 where it appears that three or four designs support 2 OAM families, the highest l is often dangerously close to cutoff, while the lower l may be accidentally degenerate, or nearly accidentally degenerate with an $m = 2$ mode.

The fibers in the next sections are not presented in chronological order. The

first generation of this fiber was designed by Dr. Steve Golowich to support a large number of OAM states which were well separated (on the order of 10^{-4} in effective index) from their nearest neighbors. However, a mistake was made in between the design and the fabrication, leading to an incorrect draw-down ratio used during the draw process. The first air core fiber had a high-index ring larger than was designed; consequently, the index splittings for some of the modes were not large, and several $m > 1$ modes existed. In retrospect, this was a lucky break. The correct fiber, now called generation 2, was fabricated but features strong SOC for most of the guided mode orders, as this was not a design consideration prior to fabrication. The first generation of air core fiber, instead, provided a platform for studying high- l OAM modes, specifically $l = 7, 8, 9$, and strongly informed the design of the third and fourth generation of OAM carrying fibers. Since the first, third, and fourth generation of OAM fibers utilize the Dispersive Guidance regime, they are presented sequentially, and the second generation of fiber is presented last.

As a design compromise between avoiding spin-orbit coupling and still achieving guidance of multiple OAM states, we aim to fabricate a fiber with inner ring radius $3\mu m$, and outer radius $8.23\mu m$, with the goal of stably supporting $l = 5, 6, 7$ OAM modes in the third and fourth generation fibers. Final pre-fabrication simulations are performed using a ‘stretched’ index profile from the gen1 air core fiber, to determine the change in modal density of states when realistic index gradients are added in the ring region. The fiber design is robust to fluctuations of the ring outer diameter by $\pm 0.2\mu m$, but only $\pm 0.1\mu m$ fluctuations in the inner diameter. Due to the demanding draw tolerances, the fiber is drawn from the same preform in ~ 1 km segments for a larger number of possible fiber samples.

6.3 Generation 1 Air Core Fiber

The first generation of fiber was fabricated with an air hole $10\mu m$ in diameter. For this reason, we denote the fiber as ‘gen1’ or ‘Core10’. The fiber is fabricated beginning with a standard MCVD deposition of GeO_2 onto high-purity SiO_2 . After the dopants for the high index ring region are deposited, a small layer of SiO_2 is deposited on the inside of the ring to help with stability during the draw process. The preform is partially collapsed, leaving a smaller air hole in the center. When the fiber is drawn, the hole is pressurized and N gas is flown through the tube. The combination of draw-down ratio and pressure allow control over both the fiber OD and the aspect ratio, defined as the width divided by the radial center-of-mass, of the ring region. The drawn fiber has an OD of approximately $125\mu m$

We measure the index profile of the air core fiber using an interferometric fiber profiler (Interfiber Analysis IFA-100), which illuminates the fiber transverse to its cross-section, and uses the diffraction pattern to infer the index profile. This device

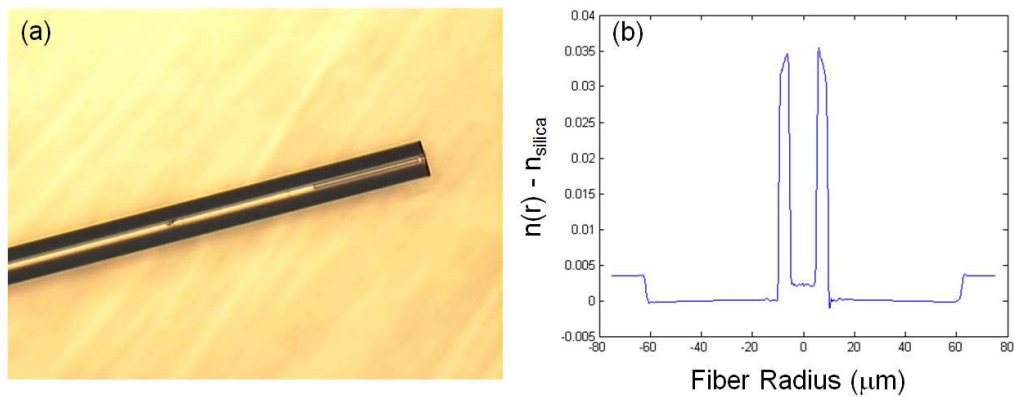


Figure 6.5: (a) Air core fiber soaks in refractive index matching oil via capillary action (b) Measured refractive index profile of air core fiber plus index matching oil

typically is used to measure small refractive index differences, and we find that having it directly measure the glass-air boundary results in substantial rounding errors. We

fill the fiber with index matching oil (Cargille Labs) with refractive index roughly 1.45, the refractive index of silica at the measurement wavelength of 632nm. The fiber is filled by cleaving the end and allowing it to soak in oil overnight via capillary action, as shown in Fig. 6-5(a). The measured refractive index profile of the fiber plus oil is given in Fig. 6-5(b). Evidently a refractive index step of approximately 0.035 has been achieved between guiding region and cladding, although the ring region's index is not constant. The ring is approximately $5\mu m$ thick. The step in refractive index after $62.5\mu m$ in radius is due to immersion of the FUT in oil.

In order to more accurately determine the inner radius of the high-index ring, several air core fiber samples are cleaved and mounted into a sample holder along with several samples of SMF-28e (Corning). The cross-section of the air core fiber is imaged at several magnifications (Fig. 6-6), and the inner radius of the air core fiber (in pixels) is found using Kasa's circle-fitting method (Corral and Lindquist, 1998). The outer radius of the SMF-28e is then found using the same circle fitting method, and the conversion between pixels and μm is achieved by using the documented outer radius of the SMF. We find that the inner radius of the air hole to be $5.1\mu m$.

In the process of cleaving the air core fiber for microscope imaging, several times we noticed a dark line across the high index ring region, as in Fig. 6-7. We interpret this as a shearing effect from the cleave propagating around the fiber in an asymmetric manner. For an ideal cleave, the fiber is clamped and pulled to a desired tension, and a sonic blade is applied to the edge of the cladding with exactly zero angle between the line of the blade and the transverse plane of the fiber. However, if the blade is angled slightly, or if the fiber is mounted improperly such that the blade strikes it at an angle, evidently the cleave will propagate in a plane which is not transverse to the fiber's longitudinal axis. For a solid fiber, this results in a poor cleave angle. However, since the center of this fiber is hollow, the cleave will split

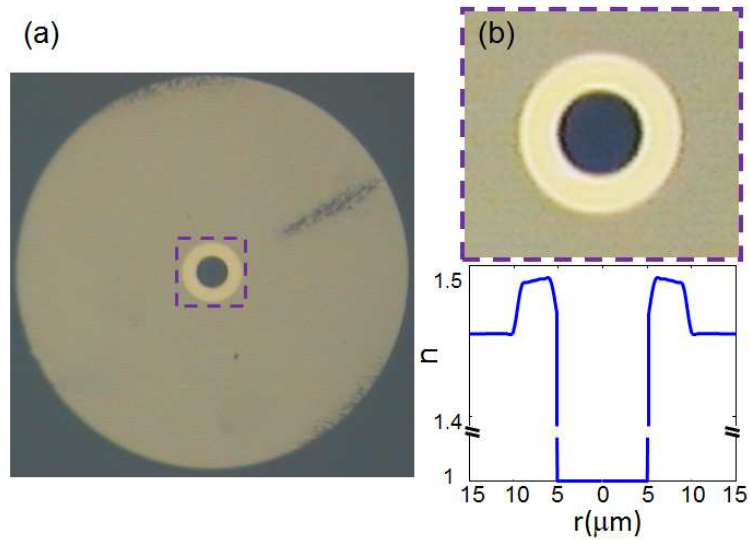


Figure 6-6: (a) Imaged cross-section of gen1 air core fiber (b) Zoom-in on core region and adjusted refractive index profile

into two parts which propagate separately around the air core and combine on the other side. If they are offset in \hat{z} when the two halves recombine, there will be a discontinuity in height on the side of the ring opposite the side struck by the cleaver's blade. Optically, this discontinuity looks like an azimuthally-dependent perturbation and should be avoided if at all possible. This effect becomes progressively worse as the air hole becomes larger, and later fiber-handling experiments with a fiber of air

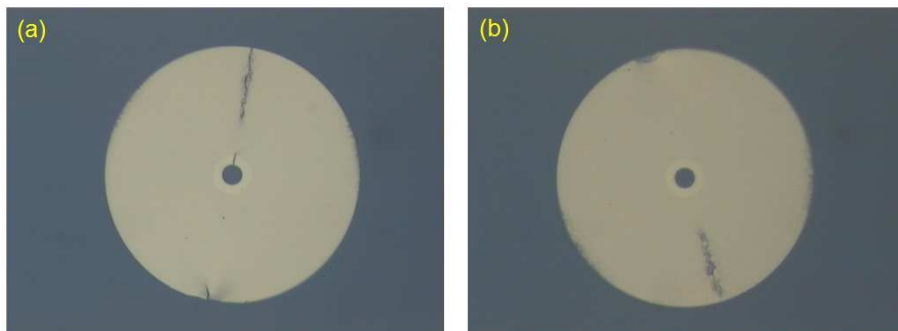


Figure 6-7: (a) Imaged cleave with discontinuity across ring region (b) Imaged cleave with unperturbed ring region, but some discontinuity visible in the cladding

core $25\mu\text{m}$ showed that cleaving was incredibly difficult. For high-precision cleaving, we use a CT-100 Fujikura cleaver, with tension approximately $180g$. The fiber is first stripped with fiber strippers or a razor blade before being wiped down with ethanol and mounted into the cleaver. The cleaver has clamps on both left and right sides of the blade, with the fiber to the right of the blade being discarded after the cleave. We find that ensuring that the right edge extends over its clamp by $\sim 1 - 2\text{cm}$ and then rotating the fiber while tapping the clamp down (but not clamping it) until tapping the clamp onto the fiber does not cause the fiber to jump out of its groove is generally the best way to align the fiber for cleaving; however, a success rate of better than 1 cleave in 4 is unlikely.

With the refractive index profile obtained, we simulate the measured fiber from 1500 to 1600nm. Although the fiber properties are wavelength sensitive, the fiber can be rescaled to achieve the same behavior in any wavelength range of interest. The effective index separation between each OAM mode and its nearest neighbor is shown in Fig. 6.8. For $l > 1$, the nearest neighbor for each SOa mode are the SOaa modes of the same $|l|$, and vice versa, so only one plot is needed for each l . For $l = 1$, the nearest neighbor is TE . For $l = 2 - 4$, the SOa modes are higher in n_{eff} , while for $l > 4$ SOaa have larger n_{eff} . This can be interpreted as the cross-over point in Eq. (6.5), where on one side the air-glass gradient is driving the effective index splitting, while on the other, the large glass-glass gradient drives the splitting. The air core, for these $l > 4$ modes, instead has the effect of a repulsive barrier, forcing the confined field away from the inside edge of the waveguide. We observe that desired n_{eff} splitting has been achieved for $l = 8$ and 9

The effective index curves for all mode orders is shown in Fig. 6.9. The different $m = 1$ OAM families spread out in effective index as mode order increases, with the $l = 0$ and TE modes having comparable n_{eff} splitting to that between TE and $l = 1$,

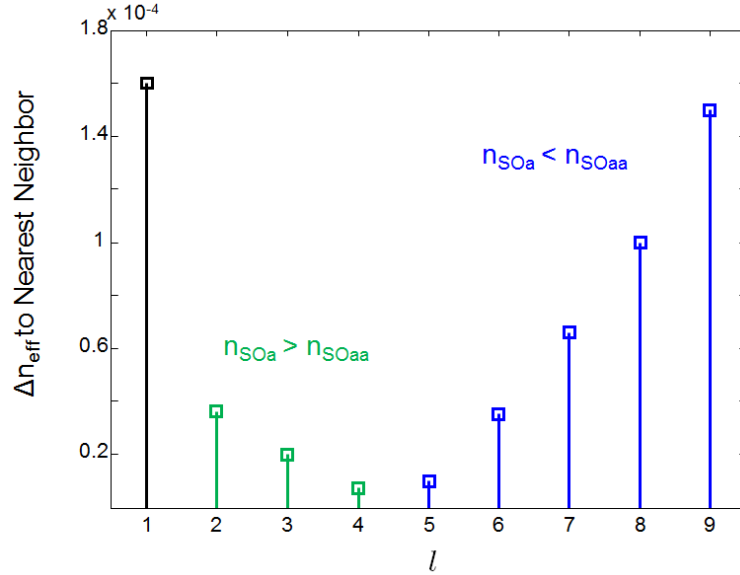


Figure 6-8: Distance between OAM modes and their nearest neighbors as a function of l at 1500nm

while the higher l orders are separated by $\sim 4 \times 10^{-3}$. The fiber supports $m = 2$ modes up to $l = 4$, which are closely bunched at lower effective indices.

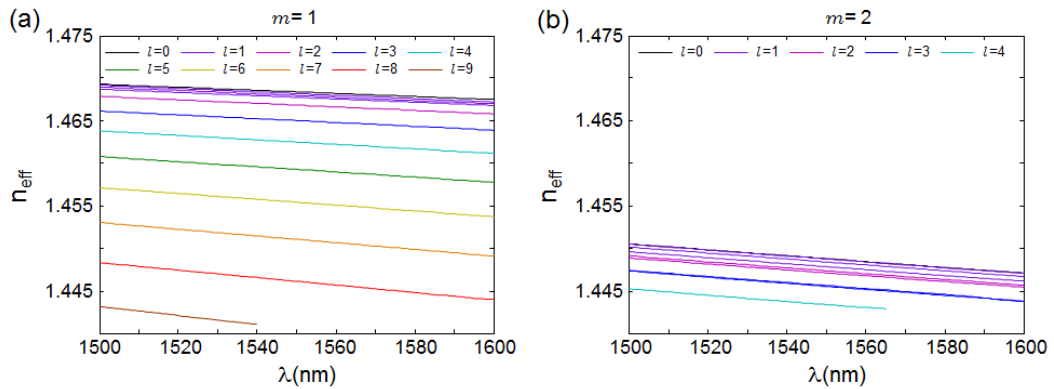


Figure 6-9: (a) Effective index versus wavelength for all $m = 1$ mode orders (b) Effective index versus wavelength for all $m = 2$ mode orders

The mode field distributions are shown in Fig. 6-10. Each $m = 1$ mode is a ring with nearly the same center point and width. The overlap between the radial fields, $\int r dr F_{l1}(r) F_{l2}(r)$, assuming $\int r dr F_l^r(r) = 1$ is 99.9% between $l = 0$ and $l = 3$, 98.6%

between $l = 0$ and $l = 6$, and at worst 93.8% between $l = 0$ and $l = 9$.

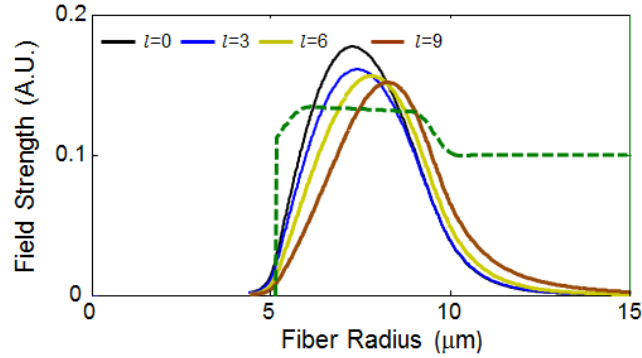


Figure 6-10: Mode field distribution versus radius for a subset of OAM modes in the air core fiber

In order to test the existence and stability of the OAM modes in this fiber, we excite free space OAM states with an SLM, and couple them into the fiber as described in Sec. 5.3. The modes are propagated over 2m of fiber, after which, the output is passed through a circular polarizing beam splitter, and interfered with a Gaussian reference. Each mode obtains a spiral interference pattern as expected, and shown in Fig. 6-11. More quantitatively, we measure the mode purity as a function of

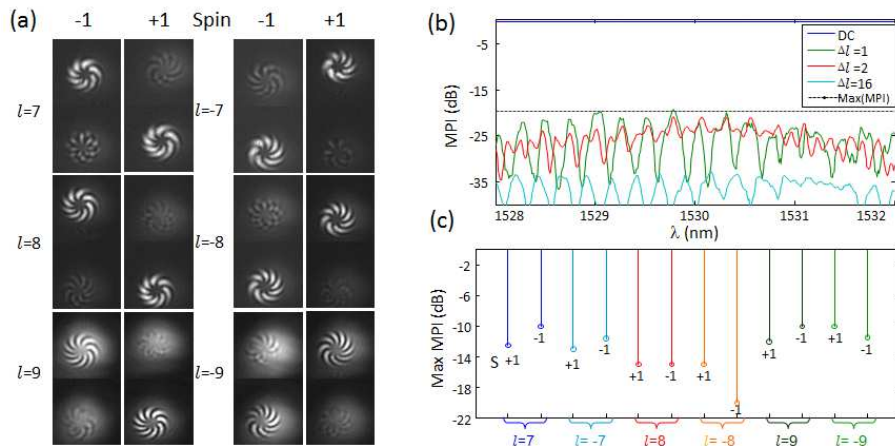


Figure 6-11: (a) Spiral interference patterns for each of the 12 transmitted OAM states (b) Example of a calculation of MPI (mode purity) versus wavelength; worst case MPI for all modes shown in (c)

wavelength using the Ring technique (Sec. 4.3). We find that each mode is at least 10dB pure, with the dominant parasitic modes being $\Delta l = \pm 1$, indicating that the limiting factor was alignment rather than in-fiber coupling. This is, to my knowledge, the first demonstration of the existence and excitation of stable higher order OAM modes in fiber (Gregg et al., 2013). Moreover, over short lengths, it seems that even the degenerate OAM states do not couple to each other - this will be revisited in Chap. 7.

The fiber length is changed to 1km (the longest amount available to us at the time) for time of flight measurements. Results for are shown in Fig. 6-12 for the SOa modes (a) and SOaa modes (b), using the 1GHz detector. The relative delay

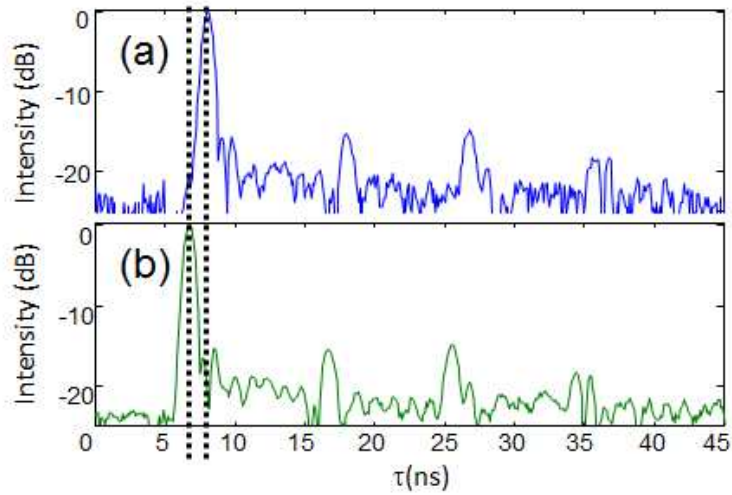


Figure 6-12: Time of flight trace for $l = 8$ (a) SOa and (b) SOaa modes in the gen1 air core fiber.

between the two mode groups is 1.2ns, compared to the theoretical value of 1.1ns. In a standard fiber, these two peaks would not be separately resolvable. Satellite peaks around 17 and 26ns are from the detector’s electrical impulse response.

However, at 1km lengths, $l = 9$ does not propagate due to high loss in the fiber. The loss for $l = 9$ is not directly measured; we find that at 1530nm, the edge of the telecom C-band, $l = 9$ can propagate about 10m, but is not observed at 1550nm,

nor is it observed at longer lengths at 1530nm. Further, propagation of $l = 7$ over 1km yields a large distributed coupling feature, and output mode patterns which have double-ring features, as shown in Fig. 6-13. We postulate that the cause of this

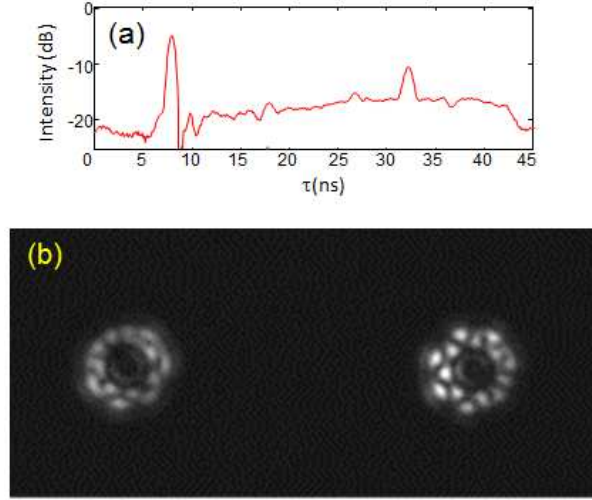


Figure 6-13: (a) Time of flight trace for $l = 7$, SOa or SOaa (b) Fiber output after 1km when $l = 7$ is launched, using a narrowband ECL as illumination source. Seven-fold symmetry strongly visible in the right bin

behavior is a mode-crossing between the $l = 7, m = 1$ mode and the $l = 0, m = 2$, or the $TE_{0,2}$ mode. A zoomed-in view of the n_{eff} curves is shown in Fig. 6-14 $l = 7$ and $l = 8$ are in proximity to several n_{eff} curves for lower-order modes. It is clear from the figure that the $m = 1$ and $m = 2$ mode sets have different dispersions, meaning that intersection between the mode lines is likely at some wavelength. If the measured inner diameter of the air core is slightly incorred, the $l = 8$ modes could be below the set of $m = 2$ lines, while the $l = 7$ modes would be in more danger of being accidentally degenerate with the $l = 0$ and $l = 1$ $m = 2$ modes. It is not infeasible that the inner diameter of the air core fluctuates during the draw, leading to accidental degeneracy at some fiber lengths, which, given that the modes would automatically be phase matched, would lead to mode coupling. The tolerance on

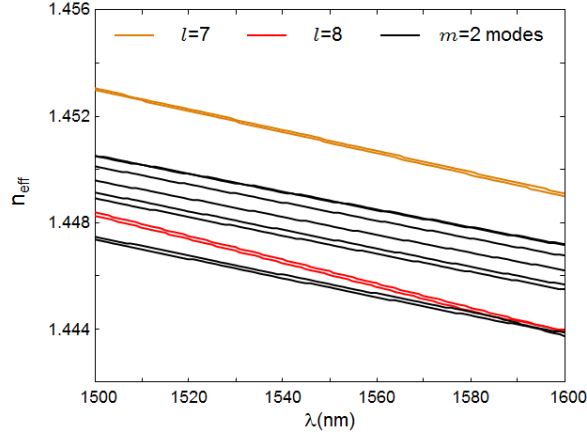


Figure 6.14: Zoomed-in n_{eff} curves for $l = 7$ and $l = 8$ in gen1 air core fiber

inner diameter will be discussed in detail in Sec. 6.2, but according to simulations, a change in inner radius of $0.1\mu m$ is enough to cause a drastic relative shift between the $m = 0$ and $m = 1$ modes.

Thus, the end result for the gen1 fiber is that 4 modes, the $l = 8$ SOa and SOaa modes, are supported for km propagation lengths. This represents a factor of two improvement over the channel capacity of PM fiber. In the next section, we describe how the lessons learned from this first generation of air core fiber led to the design and fabrication of an improved air core fiber for supporting high- l fiber OAM states.

6.4 Air Core Fiber Generation 3 & 4

Six attempts are made to draw the fiber specified at the end of Sec. 6.2, denoted a-f. One trial, b, was found to be very lossy after fabrication and is not included here. Details on the other five samples are found in Table 6.1. Fibers c and d vary drastically over the course of the draw. Fibers e and f are closest to the design specification, while a, although further from the desired inner diameter, is the most stable from a direct comparison of the ends.

Table 6.1: Summary of fabricated gen3 air core fibers. OSE: Outside edge, ISE: Inside edge

Spool	Preform ID	OSE Hole dia (μm)	ISE Hole dia (μm)	Length (m)
A	120607381	5.76	5.46	1365
C	120606381	6.65	9.8	1524
D	120606381	6.5	8.06	1256
E	130402381	5.9	6.08	1450
F	120607381	6.12	5.98	1406

Input coupling with an SLM into a $\sim 1.5\text{m}$ piece of gen3a from the OSE reveals that the $l = 6$ modes run into an accidental degeneracy with $l = 2, m = 2$, as in Fig. 6-15(a), where four-fold and eight-fold rotation symmetry is evident in the output images. Launching instead $l = 2$ shows $l = 4$ symmetry (Fig. 6-15(a)). The SOa states show this behavior from approximately 1530nm to 1590nm, while the SOaa modes show cross-coupling from 1550nm to at least 1605nm, the upper-limit in wavelength accessible for the measurement. $l = 7$ appears to be cutoff in this fiber above 1480nm, according to transmission over a 5m length of the fiber. Gen3a, on the other hand, features no accidental degeneracy of the desired OAM modes in the C-band - no accidental degeneracy is observed for $l = 6$ in a 5m segment from 1440nm to 1590nm. $l = 7$ is guided up to approximately 1500nm, and unfortunately is too lossy to be transmitted over 1km at 1530–1565nm. Gen3f, meanwhile, features intermodal coupling within the first 300m of the OSE as indicated by time domain; when this is cut, Gen3f is found to be stable with respect to $l = 6$ across the C-band, and is functionally identical in transmission to Gen3a. A comparison of the two index profiles is found in Fig. 6-16. The profiles are nearly identical; fiber f is evidently slightly wider, but on the scale measurable by the refractive index profiler, they are difficult to differentiate. Transmission is attempted over 1km for both gen3a and gen3f; time of flight results for gen3f are shown in Fig. 6-17. The peaks for the $l = 5$ states are well separated, as are the peaks for the $l = 6$ states.

Fiber loss is measured by cutback. The $l = 5$ and $l = 6$ states are aligned by time

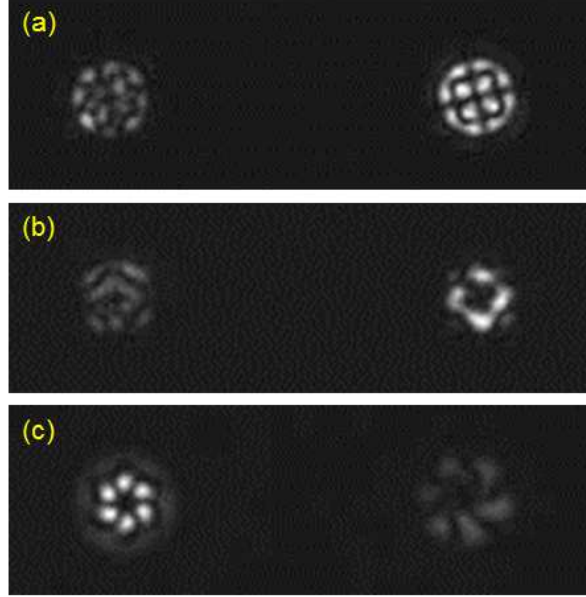


Figure 6.15: (a) 4- and 8-fold symmetric output when $l = 6$ is launched, indicating accidental-degeneracy induced coupling with $l = 2, m = 2$ (b) 4-fold symmetric fiber output when $l = 2$ is launched (c) $l = 3$ launched, $m = 1$ and $m = 2$ modes evident

domain after 1km of fiber, and after mode purities of at least 15dB are confirmed, output power is measured. The fiber is then cleaved after ~ 2 m, and the output power measurement is repeated. Loss is then calculated as 1.9dB/km for the $l = 5$ modes and 2.2dB/km for the $l = 6$ modes, with no differential loss between the SOa and SOaa states measurable.

Fiber handling for gen3 is much the same as gen1. Cleaving should be done with a high-precision cleaver, at a tension of approximately 180g. If the fiber is not held straight while cleaving, a discontinuity is visible across the high-index region.

The gen3 fiber was used for the experiments in Chap. 7 and some of the experiments in Chap. 8. In an attempt to fabricate a fiber which supported 12 OAM states over km lengths, a new version of the fiber was drawn. The only change was an increase in inner diameter of the air hole from $3.0\mu\text{m}$ to $3.05\mu\text{m}$, in an attempt to slightly increase the n_{eff} of the $l = 7$ modes while not affecting the stability of the

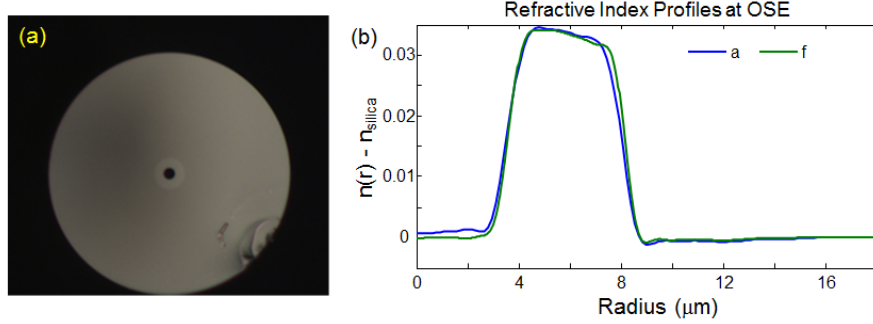


Figure 6.16: (a) End facet image of gen3a OSE (b)Refractive index profiles of gen3a and gen3f

$l = 6$ and $l = 5$ modes. Details on these new fibers, denoted gen4, are found in Table 6.2. To avoid confusion with previous generations of fibers, these are called gen4-X, where X is the spool label in Table 6.2. Fibers gen4-2A and gen4-2B are closest to the design target and appear most stable, while gen4-5 and gen4-6 feature drastic changes across the manufactured fiber.

Table 6.2: Summary of fabricated gen4 air core fibers.

Spool	Preform ID	OSE Hole dia (μm)	ISE Hole dia (μm)	Length (m)
1B	150122281	6.89	6.34	1211
2A	150122281	6.49	6.31	1181
2B	150122281	6.39	6.21	1180
3	150122281	6.78	6.68	1215
4	150122281	5.94	6.23	1966
5	150122281	6.31	5.44	1815
6	150122281	4.12	6.19	1355

Excitation with an SLM is performed on a short length of each fiber pulled from the OSE, except for gen4-5 and gen4-6, and the wavelength is swept looking for accidental degeneracies. Gen4-2A and gen4-2B show accidental degeneracy between $l = 6$ and $l = 2$ from approximately 1530nm to 1590nm. In short lengths of each fiber, $l = 7$ and $l = 5$ are accidental degeneracy free across the measurement range, while $l = 8$ exists up to 1510 \sim 1530nm for the fibers gen4-1B, gen4-2A, gen4-2B, and gen4-3. It is not observed at any wavelength of gen4-4, likely due to the smaller

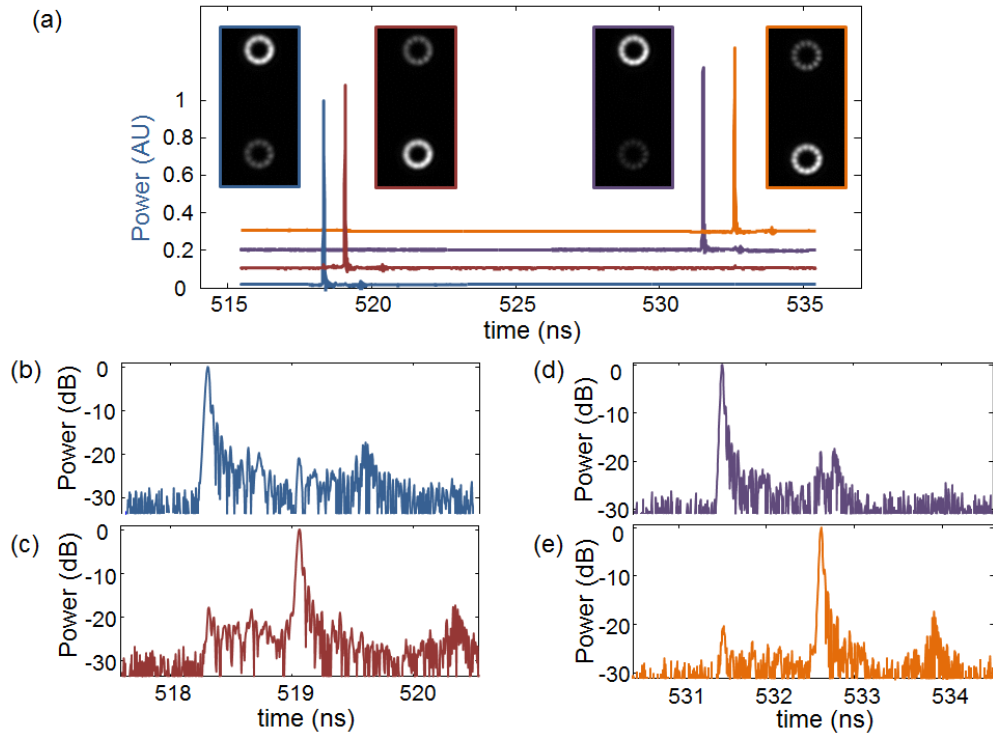


Figure 6-17: (a) Time of flight traces for $l = 5$ and $l = 6$ SOa and SOaa modes in gen3f fiber, offset for vertical clarity. In order of increasing group delay, traces are $l = 5$ SOaa, $l = 5$ SOa, $l = 6$ SOaa, and finally $l = 6$ SOa. Inset: fiber output after 1km (b)-(d) close-ups on each mode group's time of flight trace showing distributed intermodal crosstalk

air hole at the OSE.

Testing is performed at full-spool lengths using either an ECL and observation of fiber output, or a pulsed laser and time domain. $l = 5$ and $l = 7$ are transmitted without accidental degeneracy in each fiber except for gen4-6, which does not support $l = 7$. $l = 6$ is found to exhibit effects of accidental degeneracy in every fiber across C-band, except for gen4-3. An example time of flight measurement for the gen4-2B fiber is shown in Fig. 6-18 when we attempt to excite $l = 6$ SOa and SOaa, by using a q -plate followed by an QWP. If $l = 6$ is well aligned and launched, the large lobes around 15 and 25ns are the only visible features. If the fiber is offset slightly, the

peaks corresponding to $l = 7$, $l = 5$, and $l = 4$ are visible. If no coupling were evident,

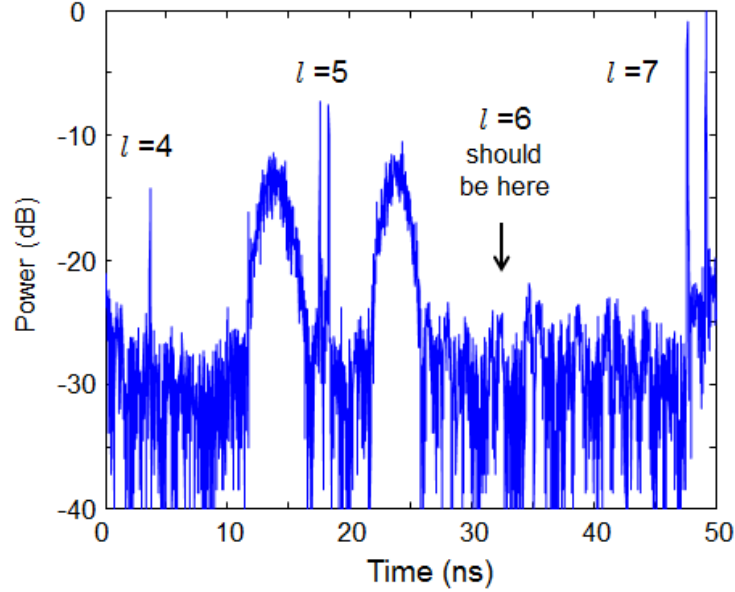


Figure 6-18: Time of flight for $l = 6$ in gen4-2B showing mode coupling due to accidental degeneracy

$l = 6$ should fall almost halfway between $l = 5$ and $l = 7$ in time. Instead there is no strong peak evident, with all of the power being dumped into the large lobes. The difference in time of flight between $l = 6$ and $l = 2, m = 2$, with which $l = 6$ apparently couples, would be 32ns if both were launched purely, the fiber was not distorted, and no mode coupling occurs. If the QWP after the q -plate is removed, or replaced with an HWP such that either the SOa or SOaa are launched independently, both lobes remain, indicating that it is not mode-specific coupling. The separate resolvability of the peaks means that coupling does not occur across the whole length of fiber; if so, one would see only a Gaussian distribution localized around the mean transit time of the two modes (Kawakami and Ikeda, 1978; Poole, 1988).

Gen4-3 provides a window into the evolution of accidental degeneracy induced mode coupling. Both the SOa and SOaa states propagate without issue at 1556nm when both are launched simultaneously, as shown in Fig. 6-19. However, as the

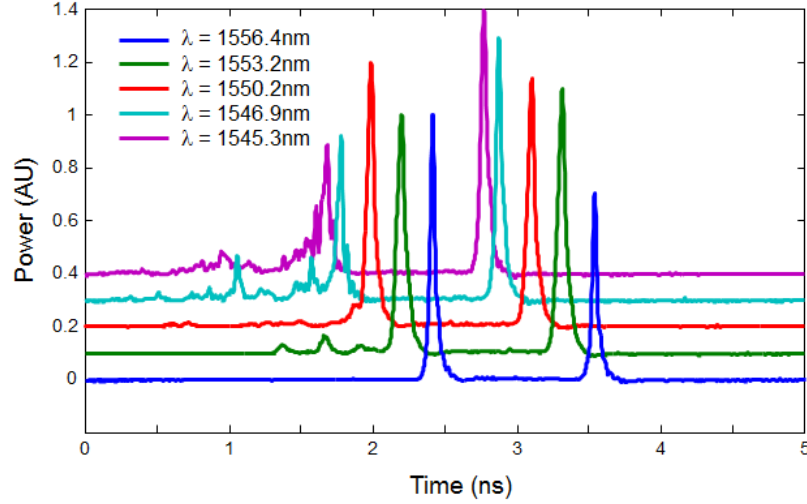


Figure 6-19: Time of flight for $l = 6$ in gen4-3 showing evolving accidental degeneracy as a function of wavelength. Traces offset for clarity

wavelength is decreased, the peak corresponding to the SOaa modes begin to decrease in strength and small features are evident in the times prior to that peak (since the group index for the $l = 2, m = 2$ mode is less than that of $l = 6$, any coupling into that mode will arrive earlier). As the wavelength is further decreased, more mode coupling is evident, as more distributed coupling features can be seen prior to the desired pulse. As the wavelength is further decreased below 1540nm, the $l = 6$ SOa states are corrupted as well.

It is not directly obvious from the above that this accidental degeneracy induced coupling will lead to crosstalk between SOa and SOaa states of the same l . As we will show in Chap. 8, it indeed does lead to debilitating crosstalk between the two sets of modes.

Although there are two radial orders of both $l = 0$ and $l = 1$, there is no immediate reason why these states could not be used as independent information carriers. $l = 0, m = 1$ is separated from the $TE_{0,1}$ mode by 5×10^{-4} in n_{eff} , and the $l = 0, m = 2$ mode is similarly separated from $TE_{0,2}$ by 4×10^{-4} . Further, there is again no

reason in principle why the TE and TM modes could not be used as information channels themselves, as they well separated in n_{eff} from their nearest neighbors, are directly accessible with q -plates, and even feature the advantage that no degenerate state coupling is possible. However, when their time of flight spectrum is measured, distributed coupling between the $l = 0$ and $l = 1$ states is evident, as shown in Fig. 6.20. Despite the large n_{eff} splitting, significant cross-coupling between $l = 0$

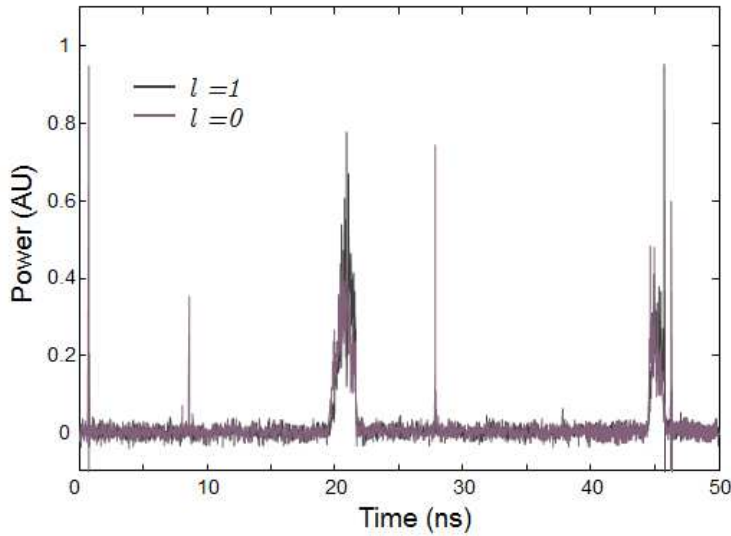


Figure 6.20: Time of flight for $l = 0$ in gen4-3. Burst around 20ns is from $m = 1$, burst at 45ns is from $m = 2$

and $l = 1$ is observed. This will be also revisited in Chap. 8, but we attribute this to the relative likelihood of fiber perturbations - it should be much easier to encounter a perturbation which imparts an OAM perturbation $\Delta l = 1$ such a gentle bend, than one which imparts a transfer of spin.

Loss measurements via cutback are repeated on gen4-3. Loss is measured as 0.8dB/km for $l = 7$ and 1.0dB/km for $l = 5$. This is an exceptionally low loss for a higher order mode in a fiber. We attribute the difference between gen3 and gen4 to a dual-layer polymer coating applied to gen4. Note also that that loss is lower for $l = 7$ than for $l = 5$; we conjecture that this is because the modal field of $l = 7$

encounters the edge between glass and air less, which results in lower scattering loss. The loss measurement is repeated for gen4-1B, and losses of 1.0dB/km and 1.2dB/km are measured for $l = 7$ and $l = 5$, consistent with those measured for gen4-3.

A summary of the relevant properties of gen4-3 is shown in Fig. 6-21. Although only gen4-3 is shown, the other gen4 fibers except for gen4-5 and gen4-6 have very similar n_{eff} , loss, and dispersion characteristics as these properties tend to be slowly varying with respect to small changes in the fabricated waveguide. The only characteristic which varies from waveguide to waveguide is the wavelength of accidental degeneracy, and even this varies along the length of the waveguide, as we will explicitly show in Chap. 8.

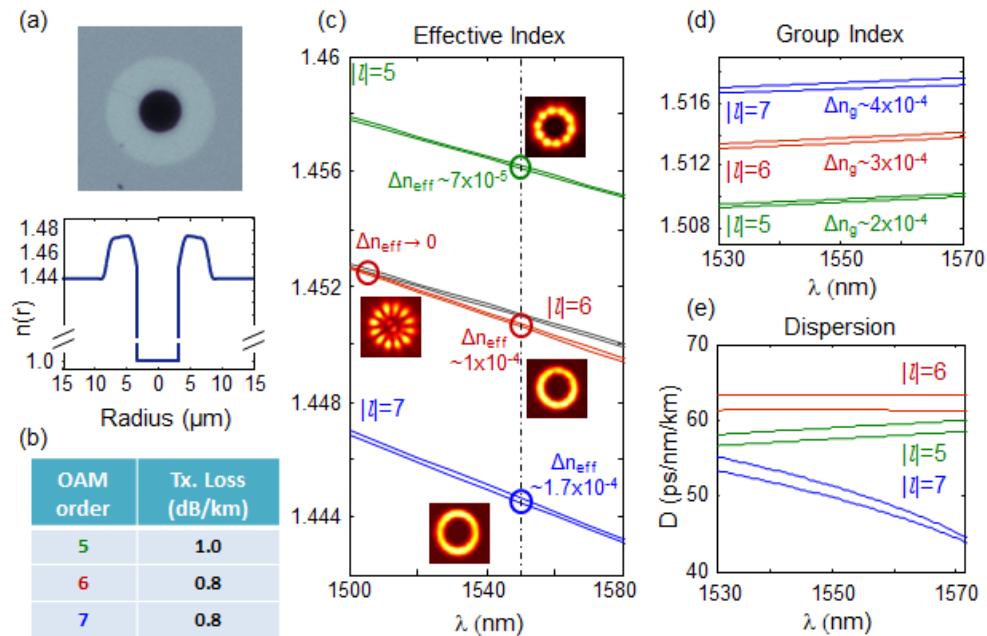


Figure 6-21: (a) End facet image of gen4-3 (b) Measured transmission loss (c) Effective index versus wavelength. Insets are experimental images after $\sim 2\text{m}$ of fiber propagation at 1550nm , except for leftmost image which is at 1500nm . (d) Group indices and (e) Dispersions for OAM modes of interest over C-band

Different sections of air core fiber are spliceable, so long as the current applied

directly to the fiber is kept low. If a high current (15mA or larger in a splicer) is applied to an air core fiber, the air hole will collapse, as shown in Fig. 6·22(a), in which gen1 fiber is spliced with an SMF at currents typical for SMF-SMF splices. If;

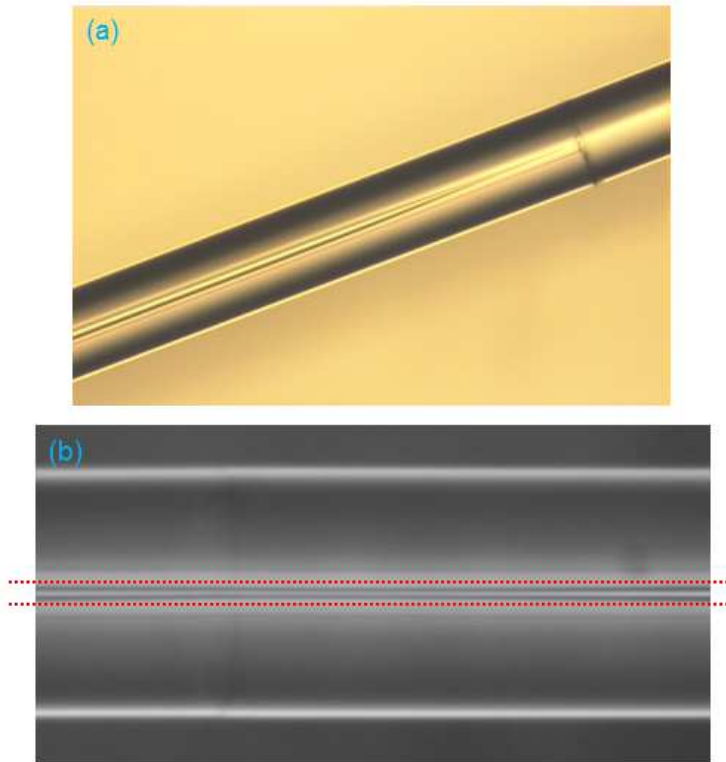


Figure 6·22: (a) gen1 air core fiber spliced to SMF at relatively high current; hole collapse evident (b) air core to air core (gen4-3 to gen4-2B) splice at lower current. Guidelines in red to indicate that ring guiding region is tapered slightly but not collapsed

however, the splice current is kept low, the air core will not collapse. Two air core fibers can be spliced together in this way. Alignment within the splicer is critical, as a misaligned splice will discretely couple power into nearest-neighbor OAM modes. Splices were performed with an Ericsson FSU 995 FA splicer, with a splice program and process detailed in App. C. Crosstalk of -15dB or better and mode-independent loss of 0.2dB can be achieved, but typically several splice attempts are needed. This is

likely due to limited equipment available to us, as high precision splices are possible (see, for instance, high precision splicers offered by OFS or Fujikura/AFL). This enables us to splice together different fiber samples, to study long-distance transport of OAM states.

We close this section with a comment on the use of the air core in the Dispersive Guidance regime. As mentioned in Sec. 6.2, the splitting for these states is driven by the dielectric interface between the ring guiding region and the cladding. One may reasonably ask how the air core itself contributes to the n_{eff} splitting in this case. Simulations indicate that it slightly (by a few percent) *decreases* the desired splitting, since the gradient is opposite in sign to that between ring region and cladding (Eq. (6.5)). Rather, the main function is to alter the density of states, and remove $m = 2$ modes, which could still potentially be done with an all-glass waveguide. The primary advantage of the air core - its massive index gradient, is only utilized in the SOC regime.

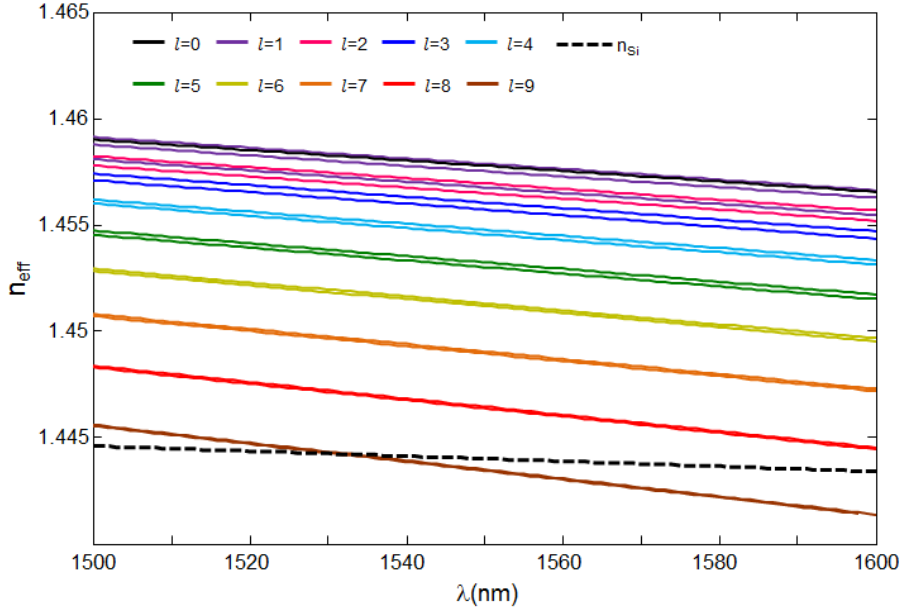
6.5 Air Core Fiber Generation 2

Unlike the fibers in sections Sec. 6.3 and Sec. 6.3, the fiber described in this section generally does not support OAM modes, rather, it supports spin-orbit coupled states. The fiber was designed by Dr. Steve Golowich (Golowich et al., 2012). Fibers were drawn aiming for two different targets, one having an inner radius of $9\mu m$ and one with an inner radius of $12.5\mu m$. The fabricated fibers are detailed in Table 6.3. These fibers should be more stable with respect to fluctuations of the inner radius of the air core, since by design no $m = 2$ modes exist.

The n_{eff} spectrum for gen2-1, calculated using an experimentally measured refractive index profile, is shown in Fig. 6-23. Modes up to $l = 9$ are guided, and large splitting is evident for lower- l modes. The n_{eff} splittings are plotted in Fig. 6-24.

Table 6.3: Summary of fabricated gen2 air core fibers.

Spool	Preform ID	OSE Hole dia (μm)	ISE Hole dia (μm)	Length (m)
1	120606382	9.1	9.3	1211
2	120606382	12.9	12.3	1181
3	120606382	12.4	12.4	1180
4	120302381	9.8	11.7	1215

**Figure 6-23:** n_{eff} spectrum for all guided modes in gen2-1

Lower order modes are affected so strongly by the high-contrast of the air core that they split into other mode orders; for instance, in this fiber, the $TE_{0,1}$ mode is actually *higher* in n_{eff} than the $l = 0$ OAM modes, while the $TM_{0,1}$ mode falls between the $l = 2$ SOa and SOaa states. The splitting generally decreases as a function of mode order, once the mode orders are sufficiently separated as to not cross into each other, as expected from Sec. 6.2.

As expected, even to relatively high mode orders in this fiber, the fields are not scalar. The simulated \mathbf{H} fields for the $l = 5$ SOa and SOaa states are shown in Fig. 6-25. The effect is more pronounced for the SOaa states. The SOaa states have an absolute value of total angular momentum of $l - 1$, and refer to a lower mode order,

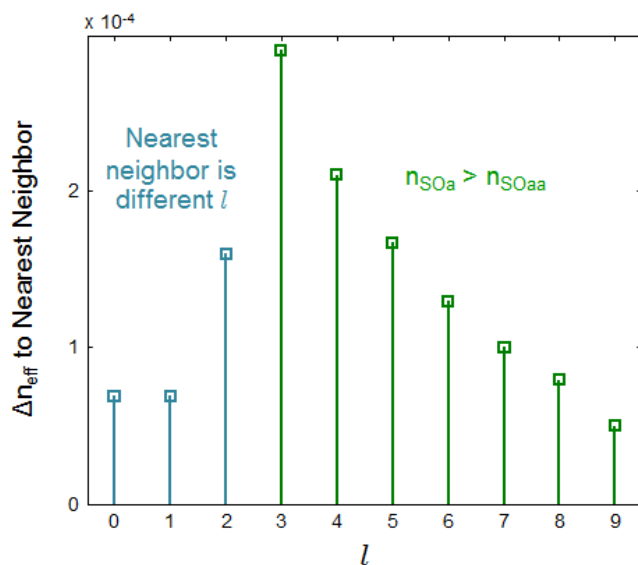


Figure 6-24: Distance in n_{eff} between adjacent modes; for high- l this is SOa-SOaa splitting, while for low- l this splitting is with respect to other mode orders (other $|l|$).

if mode orders are labeled in $(\hat{\mathbf{r}}, \hat{\phi})$. The $l = 5$ SOaa and $l = 3$ SOa states, which are of the same mode (cylindrical) mode order and total angular momentum, have comparable SOC, although the field component becoming stronger (r or ϕ) is different. This is also discernible from Fig. 6-4(a), comparing the SOC for the SOa and SOaa modes, and again reiterates the origin of the modal behavior. Typically, fiber modes are given their mode orders with respect to a Cartesian coordinate frame; i.e. the ‘LP’

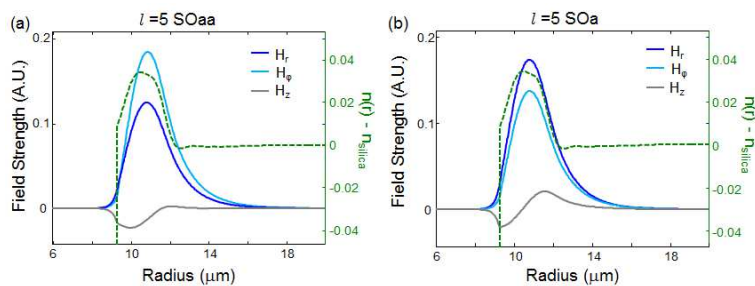


Figure 6-25: Mode fields for $l = 5$ SOa and SOaa states in gen2-1 fiber. Significant different in radial and azimuthal components indicates SOC

modes or the WGA OAM modes refer to coordinate rotations within the (x,y) plane. As the index contrast of the waveguide becomes stronger and the boundary condition difference between $\hat{\mathbf{r}}$ and $\hat{\phi}$ becomes more significant, the mode orders should be applied in the Cylindrical frame as in a metal-clad cylindrical waveguide. The SOC is weakest for the highest-order modes, but so is the n_{eff} splitting. This implies that for truly scaling capacity in air core fibers, the ability to controllably excite the SOC modes is needed. This, along with additional properties of the gen-2 fibers, will be discussed in Chap. 10.

In addition to the creation of the SOC polarization distribution, high-efficiency excitation of a multitude of OAM states with roughly the same ratio of ring width to inner ring diameter, aspect ratio for brevity, is impossible with only one phase element. As described in Sec. 5.2, beams of different l tend to diffract differently, with high- l states tending to have smaller aspect ratios than lower- l states. The low aspect ratio design of this fiber implies that simply converting to an OAM state with a spiral phase plate before input coupling should result in high input coupling loss for low- l modes. Recent work has demonstrated the existence of ‘perfect OAM beams’, which have controllable aspect ratios and are created by two phase plates (Vaity et al., 2014). Alternatively, two axicons can controllably produce a shifted-Gaussian intensity pattern, which could be utilized (Machavariani et al., 2002).

6.6 Summary

Fibers supporting OAM states have been designed and proposed. The design space of air core fibers has been surveyed, and two distinct regions for stable mode guidance have been discussed - the Dispersive Guidance regime in which high- l OAM states are supported with Δn_{eff} increasing as a function of mode order, and the Spin-Orbit Coupled regime, in which many mode orders feature large Δn_{eff} between SOa and

SOaa mode groups, but for which the fiber modes are not OAM states.

Four generations of air core fibers have been fabricated and tested. Gen1 provided a stable platform for $l = 8$ over km lengths, but featured high loss for $l = 9$, accidental degeneracy for $l = 7$, and insufficient splitting for lower- l modes. Gen3a and Gen3f provide a platform for studying $l = 5$ and $l = 6$ across km lengths, with reasonable transmission losses $\sim 2\text{dB/km}$. Gen4-3 supports $l = 5$ and $l = 7$, and partially supports $l = 6$ over C-band, while 4 other fibers from Gen4 support $l = 5$ and $l = 7$ across C-band, with mode loss $\sim 0.8\text{dB/km}$ for $l = 7$ and 1.0dB/km for $l = 5$. Gen2 provides a multitude of states which are well separated from their nearest neighbors in n_{eff} but which are spin-orbit coupled.

Several index profiles of air core fibers are given in Fig. 6-26. It is interesting to

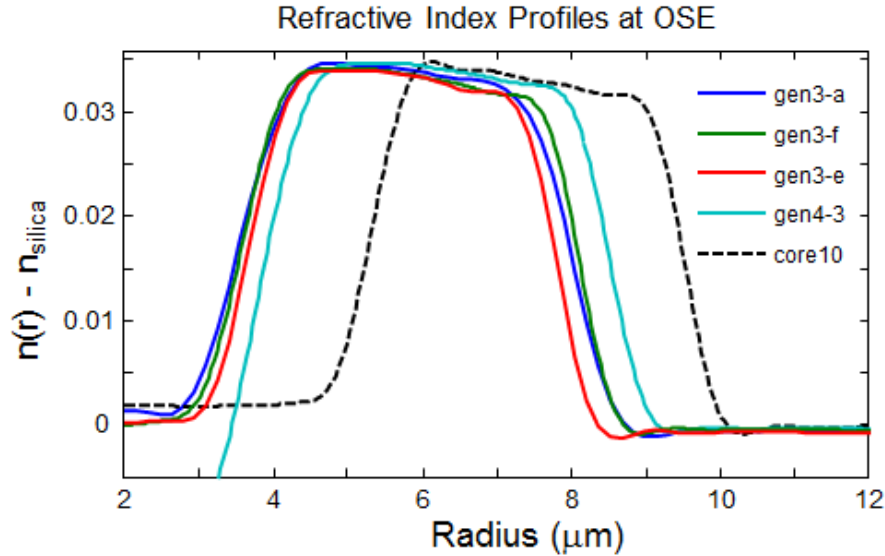


Figure 6-26: Refractive index profiles for several fabricated air core fibers

observe the differences between gen3-a and gen3-f, which were successful in avoiding accidental degeneracy of $l = 6$, with that of gen3-e, which was not. Fiber gen3-e is only slightly thinner, approximately $0.25\mu\text{m}$ with respect to the other two, yet

this shift is sufficient to vary the n_{eff} curves enough to cause accidental degeneracy. Although this fluctuation could feasibly be improved with more iterations to the draw process, it also underscores the utility of the SOC fiber design, assuming that the SOC states can be successfully excited. Gen4-3 and core10 are included in the figure for reference. Both fibers have comparable ring sizes and suppress SOC - indicating that so long as the mode fields have space in which to expand they will tend to avoid the sharp index gradient at the air-glass edge, and will not be SOC.

In parallel to the research outlined in this document, research has been performed on OAM in fibers by the group of Dr. Sophie LaRochelle. An inverse parabolic fiber was designed to support low order OAM states (Ung et al., 2014), and at least two iterations of low aspect ratio air core fibers were fabricated and tested (Brunet et al., 2014a; Brunet et al., 2014b). However, in testing a fiber which was claimed to support 36 states, the effects of spin orbit coupling were ignored, and modes were transmitted only over 85cm. Thus, we consider the investigation of these kinds of fibers an unsolved problem, although one which is beginning to attract more attention.

Having demonstrated fibers which support OAM states, we next study the properties of OAM-carrying modes in these fibers, specifically, their mode coupling properties regarding coupling between degenerate (Chap. 7) and nearly-degenerate (Chap. 8) modes.

Chapter 7

Degenerate States and Conservation of OAM

It is well known that degenerate eigenmodes of many systems tend to couple strongly due to inherent phase-matching, which is the operating principle of fiber gratings (Erdogan, 1997) and of nearly all coherent nonlinear processes (Agrawal, 2008). The degenerate polarization modes of SMF, for instance, couple readily, as anyone who has worked with SMF can attest. Polarization stability was only attained by disrupting the rotation symmetry of the fiber by inducing a large birefringence, either by deforming the core or by adding stress rods as in Panda fiber (Noda et al., 1986), which broke the degeneracy between the polarization modes on the order of 10^{-4} in n_{eff} . Modern PM fibers (such as Corning PM1550) are specified to maintain polarization to -30dB or better after 100m based on this principle.

One might expect, then, to observe coupling between degenerate OAM states over even short lengths of air core fiber. For high- l states, one would be wrong. In this chapter, we discuss the curious perturbation resistance of high- l OAM states to bend perturbations, as realized by a conventional polarization controller (polcon). We show that mode stability generally increases with mode order, and attribute this stability to conservation of OAM - like a top which becomes more stable to external perturbations as it spins faster, OAM states in air core fibers become more stable against the influence of external perturbations as their angular momenta become larger. Over longer lengths, coupling between degenerate OAM states is observed.

We postulate that this is an effect of distributed fiber twist, and show that it can be precompensated, across a wide wavelength range, by using q -plates for mode excitation.

7.1 Degenerate States in SMF and the Vortex Fiber

It is well known that bend-induced birefringence causes polarization mode coupling in SMF (Ulrich et al., 1980; Barlow et al., 1981). The coupling itself is a second-order stress effect, where the induced stress is proportional to the square of curvature of the bend, or inversely proportional to the square of the radius of the bend (in SMF, first order effects have no effect due to parity). This effect can be utilized to make a polarization controller (polcon). If SMF is wrapped tightly in a circular bend, some amount of birefringence is induced for the polarizations in-plane and out-of-plane with respect to the bend. A length of uniformly bend SMF bent is essentially a waveplate of some retardance. In free space, a series of QWP, HWP, and QWP can enact any polarization mapping on the Poincare sphere (Saleh and Teich, 2007). Thus, three such fiber bends, with approximate retardances $\lambda/4$, $\lambda/2$, and $\lambda/4$, are used, with the ability to rotate the bends with respect to each other, to make a polcon (see, for instance, Thorlabs FPC030). In practice, the lengths within the bend are never equivalent to quarter and half-wave retardance, but near-arbitrary polarization transformations are still possible.

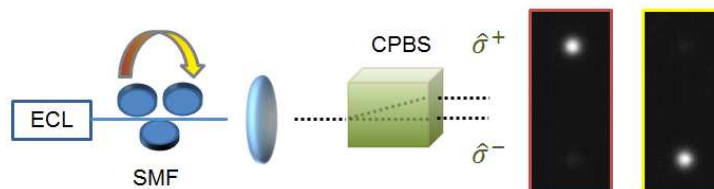


Figure 7-1: In fiber polcon used to switch between spins

The behavior of the polcon on SMF can be understood from the alternative point

of view of the circular polarization states as ideal modes, instead of the linear states as local normal modes. In Fig. 7.1, tuning an in-fiber polcon is used to switch between $\hat{\sigma}^+$ and $\hat{\sigma}^-$. In that picture, the local birefringence causes phase-matched mode coupling between $\hat{\sigma}^+$ and $\hat{\sigma}^-$. Specifically, if we assume that the local perturbation has slow and fast axes x and y , and can be modeled as:

$$\Delta n = \begin{pmatrix} \delta n & 0 \\ 0 & -\delta n \end{pmatrix} \quad (7.1)$$

Which, from the point of view of $\hat{\mathbf{x}}$ and $\hat{\mathbf{y}}$ implies:

$$n_{eff,x} = n_{eff,0} + \langle \hat{\mathbf{x}} | \Delta n | \hat{\mathbf{x}} \rangle = n_{eff,0} + \delta n \quad (7.2a)$$

$$n_{eff,y} = n_{eff,0} + \langle \hat{\mathbf{y}} | \Delta n | \hat{\mathbf{y}} \rangle = n_{eff,0} - \delta n \quad (7.2b)$$

Where the inner product implies both a conjugate vector dot product and an integration over all space; mode envelopes as a function of r are assumed identical and are assumed to be normalized to 1 under inner product with themselves. From the point of view of $\hat{\sigma}^+$ and $\hat{\sigma}^-$ implies that the coupling coefficient between them is:

$$\kappa_\sigma = \langle \hat{\sigma}^+ | \Delta n | \hat{\sigma}^- \rangle = \delta n \quad (7.3)$$

In view of this perturbation, the $\hat{\mathbf{x}}$ and $\hat{\mathbf{y}}$ fields are unchanged, but pick up an additional propagating phase. Their superpositions, the $\hat{\sigma}^+$ and $\hat{\sigma}^-$ states, are no longer modes in the perturbed fiber, or equivalently, feature mode coupling between them.

Recently, it has been shown that using the same polcon can induce mixing between the degenerate $l = 1$ OAM states in Vortex Fiber (Bozinovic et al., 2012; Bozinovic et al., 2013). This is indicated schematically in Fig. 7.2. Clearly the above analysis is inadequate to describe this case, since if the simplistic model of Eq. (7.1) is applied to the $l = 1$ OAM states, the mode coupling coefficient is zero by azimuthal symmetry.

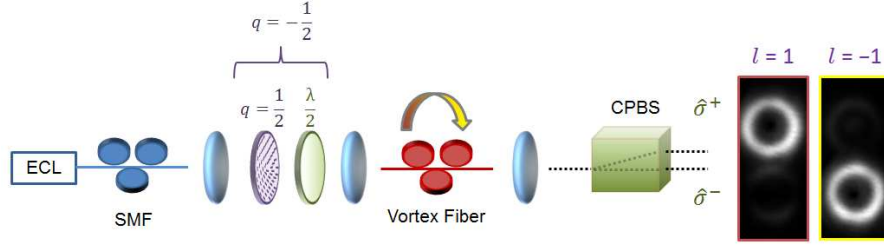


Figure 7.2: In fiber polcon used to switch between $l = 1$ OAM states in the Vortex Fiber

$$\kappa_{l=1} = \langle \hat{\sigma}^+ e^{il\phi} | \Delta n | \hat{\sigma}^- e^{-il\phi} \rangle = \delta n \langle e^{il\phi} | e^{-il\phi} \rangle = 0 \quad (7.4)$$

Much as $\hat{\sigma}^+$ and $\hat{\sigma}^-$ have an alternate representation as combinations of $\hat{\mathbf{x}}$ and $\hat{\mathbf{y}}$, the OAM modes have an equivalent representation in the HE (and EH for $l > 1$) modes. The alternative basis for the $l = 1$ OAM modes are the $HE_{2,1}^{e,o}$ vector modes, with:

$$V^\pm = HE_{2,1}^e \pm iHE_{2,1}^o \quad (7.5)$$

and

$$HE_{2,1}^e = F_1(r) [\hat{\mathbf{x}} \cos(l\phi) - \hat{\mathbf{y}} \sin(l\phi)] \quad (7.6a)$$

$$HE_{2,1}^o = F_1(r) [\hat{\mathbf{x}} \sin(l\phi) + \hat{\mathbf{y}} \cos(l\phi)] \quad (7.6b)$$

The correction to the effective indices of the HE modes is also zero by parity, unlike the case of $\hat{\mathbf{x}}$ and $\hat{\mathbf{y}}$ in SMF. Rigorously, the dominant sources of stress in the fiber should have an x or x^2 dependences, where x is the coordinate in which the fiber is deflected (Ulrich et al., 1980). The former does nothing in SMF or here in the Vortex Fiber by parity, and the latter is a second-order dependence. A more probable description is that the polcon can be approximated as a tensoral polarization perturbation, as in Eq. (7.1), in conjunction with a tilted phase front.

$$\Delta n = e^{ipx} \begin{pmatrix} \delta n & 0 \\ 0 & -\delta n \end{pmatrix} \quad (7.7)$$

Where p depends on the bend angle and fiber material parameters, as in Eq. (3.12). As noted in Chap. 5, a tilted beam incident from free space can excite an OAM spectrum centered around a desired l , thus, it is reasonable to posit that a ‘tilt’ in the fiber could cause similar mode coupling, which might be expected in any event since the OAM modes are degenerate. After any reasonable length of Vortex Fiber, the OAM modes are observed to be in a superposition of degenerate modes, even if only one is launched. Thus, controlled perturbations to switch between the degenerate states is not only beneficial, but necessary, if the two $l = 1$ OAM modes are to be used as MIMO-free data channels.

7.2 Conservation of OAM

Given that the OAM modes coupled under both controlled and distributed perturbations in the Vortex Fiber, it was curious to observe that in the air core fiber, after 5m or 10m of fiber propagation, the degenerate OAM states do not show significant crosstalk. The polcon experiment was repeated with air core gen3a fiber inserted into a fiber polcon, as in Fig. 7-2 except with air core fiber instead of Vortex Fiber and an SLM as excitation instead of a q -plate, in a 2-4-2 loop configuration, bend radius 2.8cm. The output is imaged onto a camera after passing through a circular polarization beam splitter (CPBS), as in Fig. 7-3(b). A series of images is saved as the polcon paddles are tuned, and the power within each circular polarization bin is measured at each orientation. We define a degradation factor, α , indicating the maximum crosstalk. For high l states, as the $l = 7$ SOa state in (b), degradation factors are typically $< 10\%$. For comparison, the $l = 0$ mode in SMF, for the same series of bends, $\alpha \cong 1$. Measurements for all OAM states for which SOa to SOaa coupling is suppressed is shown in Fig. 7-3(d). Thus we find that for high- l states in air core fibers, OAM is truly a conserved quantity even in the presence of anisotropic

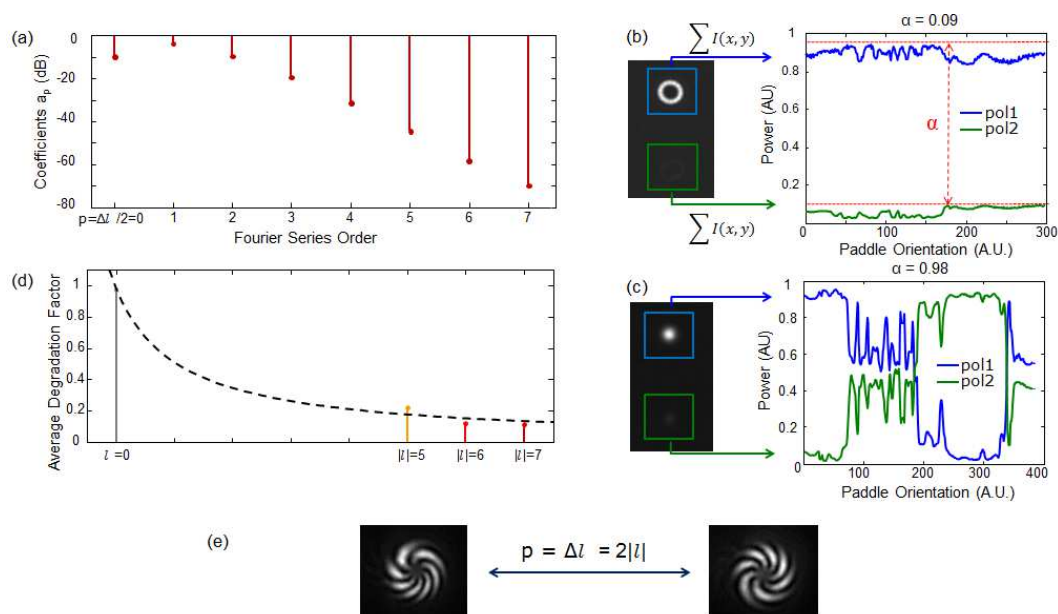


Figure 7-3: (a) Theoretical prediction of OAM content of a bend perturbation with radius 2.8cm. Coefficients rapidly decrease with increasing OAM content (b) Power binning measurement for $l = 7$ SOa. As the polcon paddles are tuned, negligible coupling between bins is observed (c) Binning measurement for $l = 0$ in SMF for comparison (d) Experimentally measured degradation for each l , plotted against a shifted $1/l$ trend line (e) OAM content needed to couple between degenerate states

perturbations. The OAM decomposition (that is, the azimuthal Fourier series, as in Eq. (3.13)) of a 2.8cm bend is shown in Fig. 7-3(a). The coefficients rapidly decrease with increasing Δl . Assuming that the bends transfer spin angular momentum, the OAM transition needed to couple between degenerate states is $\Delta l = 2l$ (Fig. 7-3(e)), which becomes increasingly difficult as the OAM order increases. Like a spinning top or bicycle wheel which becomes more difficult to perturb with increasing angular velocity, these states become more stable with increasing OAM. This finding is counter-intuitive for two reasons. First, the states are degenerate and do not couple, indicating a paucity of perturbations with the necessary OAM transition. Second, in many systems, the lowest order eigenstate is the most stable, and the opposite is true

here.

Implicit in the above discussion is the fact that OAM modes are stable against gentle motions of the air core fiber on a lab table, or coiling the fiber in bends at least a few cm in diameter. The same cannot be said of the HE modes of the same order. As shown in Fig. 7-3, when an $l = 6$ SOaa mode in gen4-3 is imaged into $\hat{\sigma}^+$ and $\hat{\sigma}^-$ bins, and polcon paddles are turned, negligible mode coupling between degenerate states occurs. The same fiber's output is then passed through a q -plate and a (linear) PBS, which then measures HE^e and HE^o in separate bins. As the fiber is gently moved around the optical table, sloshing between bins is evident, suggesting that the HE modes of the same mode order are themselves not stable. Thus, the

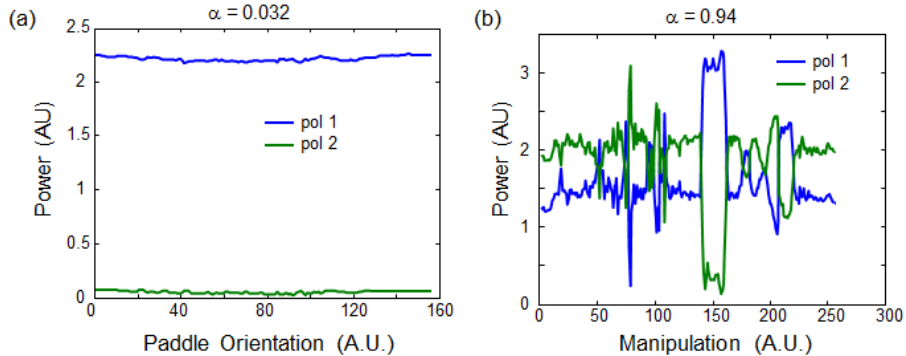


Figure 7-4: (a) Binning measurement of $l = 6$ SOaa modes out of gen4-3 fiber as polcon paddles are manipulated (b) Binning measurement of $l = 6$ SOaa modes out of the same gen4-3 fiber, passed through a q -plate and reconverted to $l = 0$ and projected into linear polarizations, thus measuring $HE^{e,o}$ mode content. The fiber is then gently moved around the optical table

effect measured in Fig. 7-3 is characteristic only of the higher order OAM modes, not of the higher order vector modes.

We conjecture that this can simply be understood from the point of view of simple rotations (discussed below) or from geometric effects (see Sec. 7.4). Suppose that the fiber is rotated such that adjacent sections see a differential rotation, modeled as

$\phi \rightarrow \phi + \phi_0$. Evidently, the OAM modes will acquire a phase shift from this counter-clockwise rotation:

$$V^\pm \propto \hat{\sigma}^\pm e^{\pm il\phi} \rightarrow e^{i(l+1)\phi_0} V^\pm \quad (7.8)$$

Note that the phase shift goes as $l+1$ and not l because the circular polarizations also acquire a phase shift upon rotation. Only SOa modes are shown, but clearly the effect is similar for SOaa modes. This phase shift gels well with previous research indicating that twist induces an angular momentum-dependent birefringence (Alexeyev et al., 2008). The HE modes are not simply expressed in terms of a phase shift; Eq. (7.6a) Eq. (7.6b) are modified by $\phi \rightarrow \phi + \phi_0$. Under this rotation, the modes transform to:

$$HE^e \rightarrow \cos(l\phi_0)HE^e - \sin(l\phi_0)HE^o \quad (7.9a)$$

$$HE^o \rightarrow \cos(l\phi_0)HE^o + \sin(l\phi_0)HE^e \quad (7.9b)$$

The EH modes, although not written, show similar behavior. For a given rotation, as l increases, the vector modes will actually become less stable, and will couple more freely. Thus, it may be not only convenient, but appropriate, when describing higher order modes in weakly guiding fibers, to use the OAM basis rather than the HE basis, due both to its physical intuition and the states' resistance to common perturbations. Further, the perturbation resistance of these modes could be advantageous for applications requiring high purity over short distances, such as chip-to-chip or chip-to-rack communications, or fiber sensing.

7.3 Degenerate States, q-plates, and Twist

Over long propagation lengths, light can encounter myriad perturbation symmetries due to imperfections in the draw process, or twists and microbends. We observe that for fibers of length 50m or greater, the degenerate OAM states are typically mixed.

Cutback results from 50m down to 10m did not yield conclusive results on the beat length of the degenerate states. At this moment, the exact coupling mechanism is not known.

We suspect that the main culprit is distributed twist. As described in Sec. 3.3, twist can modulate the effective indices of each OAM mode according to the total angular momentum. We use the experimental apparatus in Fig. 7-5(a) to study induced twist in air core fibers. One of the $l = 6$ SOaa modes is excited in gen3a fiber using a q -plate and propagated for ~ 2 m. The fiber is then clamped, strongly enough to prevent the fiber from moving, but weakly enough that SOa to SOaa coupling is not observed. The fiber is then clamped again into a Newport F-AM-FC bare fiber adapter with the fiber ferrule removed, which is then mounted onto a motorized rotation stage. The fiber fed through the clamp is clamped again on a Thorlabs HFF001 clamp, after which it is imaged through a CPBS. The apparatus is designed

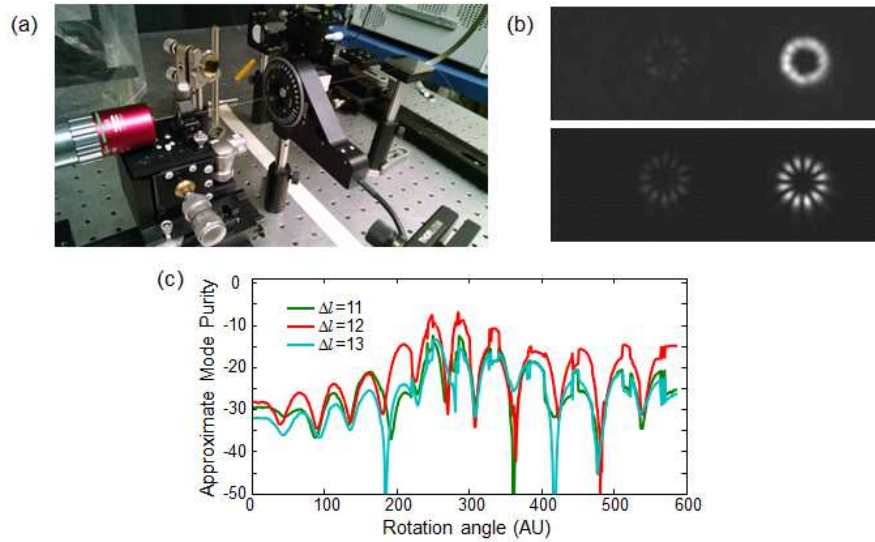


Figure 7-5: (a) Apparatus for inducing twist (b) OAM mode before and after induced twist (c) Ring coefficients evolving as the fiber is rotated, inducing more twist and apparently coupling between SOa and SOaa states.

to controllably induce twist. If the twist is induced in the middle of the fiber, there

will be equal and opposite twists imposed on either side of the rotation point; thus the end must be twisted. However, if the fiber end facet is directly mounted into the rotation mount, the fiber will move unstably around, and off of, the camera, as the fiber mount is not well-centered enough on the center of symmetry of the rotation stage. This apparatus is used to controllably induce twist between the first clamp and the rotation stage; the final HFF001 clamp has an adjustable groove size, and is used to prevent the fiber end facet from moving (the fiber is free to rotate between the rotation stage and the output clamp). For the experimental data below, the distance between rotation stage and first clamp is 8cm.

One OAM mode is launched, as in Fig. 7-5(b), top. The fiber is twisted, and after a certain amount of twist, approximately 270° in this case, the smooth ring gives way to an LP-like constellation of beads, indicating interference between l and $-l$, and thus mode coupling between SOaa and SOa. When the fiber is rotated the same amount in the opposite direction (-270°), no such mode coupling is observed. However, when the other SOaa state is launched, LP-like mode coupling is observed at -270° and no mode coupling is observed at 270° . Coefficients for the ring method for one rotation sweep from $90^\circ - 450^\circ$ are shown in Fig. 7-5, indicating that the mode coupling appears periodic with angle. Wavelength was swept, and it was found that the ring coefficients did not change appreciably over 40 to 50nm.

The results from this experiment in the end were inconclusive; no statistically significant trends were observed as a function of twist length, and experiments still remain to be performed. However, it is evident from these preliminary measurements that twist has the potential to couple across a $\Delta l = 12$, and may thus lead to coupling between the degenerate states in the presence of intrinsic or external birefringence.

However, any mode coupling between degenerate states can be compensated with a q -plate of appropriate charge, over some wavelength range. As illustrated in Fig. 7-6,

any fiber coupling between any two degenerate OAM states can be seen as a linear transformation in the 2-mode subspace of those OAM states. If the fiber is written

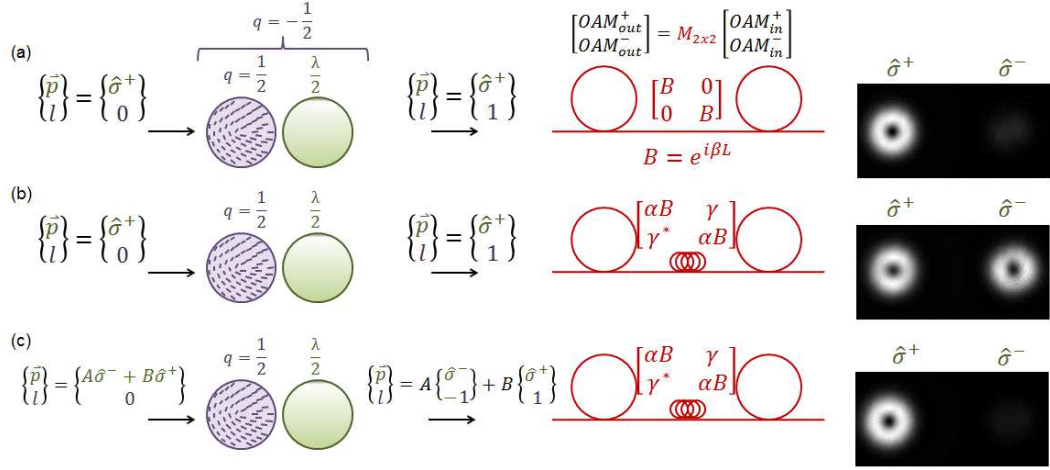


Figure 7-6: (a) In an idea fiber, a single OAM mode is preserved (b) In a long-length, imperfect fiber, coupling between degenerate OAM states occurs (c) Precompensation of in-fiber mode coupling by q -plate excitation of a superposition of degenerate OAM states

as a 2×2 matrix in the basis of degenerate OAM states, in the presence of mode coupling, the matrix is non-diagonal. However, by launching into the fiber a controlled superposition of the two OAM states, enabled by illuminating the q -plate with a some combination of $\hat{\sigma}^+$ and $\hat{\sigma}^-$, one can make the transmission matrix between input circular (or linear) polarization and output OAM states diagonal. A second q -plate (or other mode converter) at the fiber output can thus diagonalize the transmission matrix between input and output polarizations. This is shown explicitly in Fig. 7-7, in which a polcon prior to the q -plate used to excite modes in the air core fiber determines in which polarization port light leaves the system, as measured by an HP optical multimeter. The effect is wideband, with at least 17dB of suppression across the C-band. The extinction of 17dB could be limited by several factors; cross- l detection can be observed at this level due to imperfections in alignment of the input or output coupling systems, and due to different degenerate state mixing in the fiber,

there is no reason to presume that the input polarization which unwinds the fiber perturbation matrix for $l = 6$ is the same as that which unwinds $l = 5$. The optimal bias point of each q -plate is itself a function of wavelength, and some small amount of light could remain in $l = 0$ for the entire measurement.

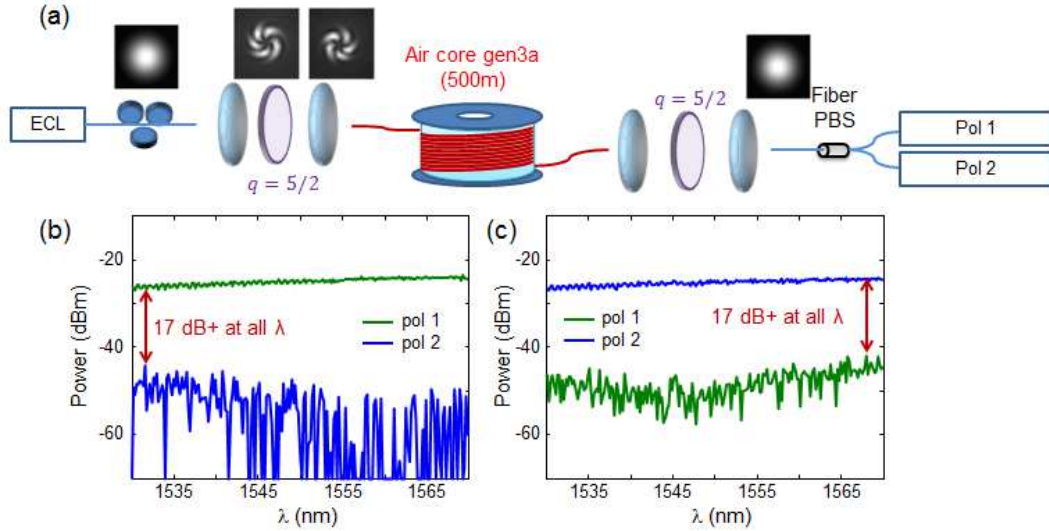


Figure 7.7: Input beam from an ECL is converted to an SOaa OAM state using a q -plate, and transmitted through 500m of air core fiber. At the output, it is reconverted to an $l = 0$ beam through a second q -plate and coupled into SMF, where it is split by a fiber PBS. Controlling the polcon after the ECL before the first q -plate determines which polarization port the signal arrives at the output. Setting the polcon to minimize power in one port does so at least across C-band, as indicated in (b) and (c)

7.4 OAM Modes, HE/EH Modes, and the Pancharatnam-Berry Phase

It is well known that even in the absence of linear or circular birefringence a polarization rotation can be observed in SMF due to geometric effects when the fiber's trajectory is not restricted to a plane (Pancharatnam-Berry phase) (Chiao and Wu, 1986; Tomita and Chiao, 1986; Berry, 1987). The exact polarization rotation de-

pends on how the fiber is arranged in three dimensions (Wassmann and Ankiewicz, 1998). When a fiber is bent into a two-dimensional curve and a linear polarization is launched, the angle of the linear polarization with respect to the normal vector of the plane containing the curve is constant. Any continuous curve through three-dimensional space can be broken into components, each of which is contained entirely in one plane, but for which adjacent planes may be rotated with respect to each other. In three dimensions, the polarization will rotate according to the integrated torsion of the curve (Ross, 1984):

$$\theta_p = \theta_0 - \int_0^P \tau(s) ds \quad (7.10)$$

where we measure the polarization at point P , θ_j is the angle of the linear polarization with respect to the input binormal of the fiber (i.e. a reference vector) at point j , τ is the torsion, and s denotes arc length. Even if the fiber endpoints are fixed, torsion may be induced by bending the fiber in three dimensional space. It is even possible to make a polarization controller with this effect (Han et al., 2015).

The OAM modes themselves are rotation invariant. However, their linear combinations, i.e. the HE and EH modes, are not, as indicated in Sec. 7.2. Moreover, the EH and HE modes of the same $|l|$ have different rotation symmetry, corresponding to their total angular momentum rather than their OAM. The $HE_{3,1}$ mode is 3-fold

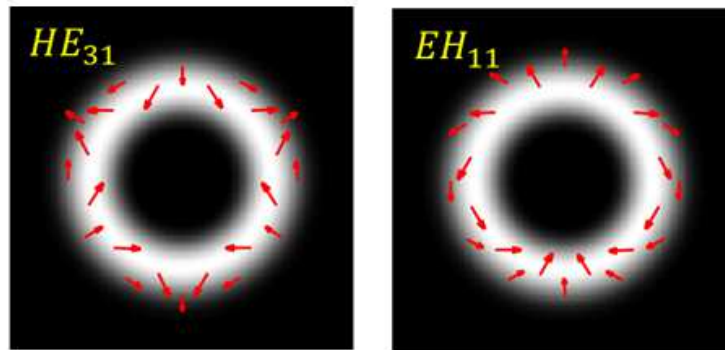


Figure 7.8: Polarization distribution of $HE_{3,1}$ and $EH_{1,1}$

rotationally symmetric, requiring a rotation of 120 degrees to maintain its orientation. The $EH_{1,1}$ mode, on the other hand, requires a rotation of 180 degrees, as does the fundamental mode of an SMF. We thus make the empirical assertion that the sensitivity to such geometric phases should increase as j .

We test this using the apparatus in Fig. 7-9. The fiber is laid out on the table except for a part approximately 50cm in length, which is lifted off the table and wrapped onto a single coil, suspended by a rod. The ends of this coil are laid on the table with enough slack that they can move freely. The ends of the coil are then moved apart in controlled 5mm steps, inducing a linearly increasing torsion in the single-coil helix. At the input of the fiber, a polcon and a q -plate are used to excite a

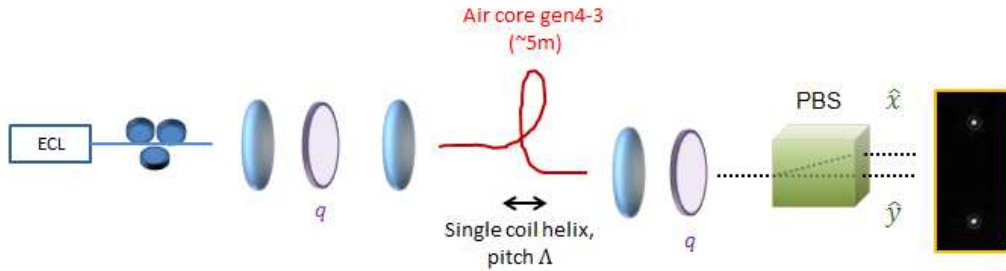


Figure 7-9: Experimental apparatus for measuring geometric-phase induced mode coupling in HE/EH basis

single HE or EH mode. At the output, a second q -plate is used to project the HE or EH mode back into an $l = 0$ mode with spatially invariant polarization, after which the beam is passed through a polarizing beam splitter and imaged with a camera. The images are binned and the relative powers in \hat{x} and \hat{y} thus computed. In this manner, the geometric effect experienced by the OAM modes is mapped back onto a simple polarization rotation. Experimentally, it is difficult to return exactly to the same initial conditions. However, the steps are repeatable, and we compare periodicity from measurement to measurement.

Data for $EH_{5,1}$ and $HE_{7,1}$ are shown in Fig. 7-10. The last data point in the

$EH_{5,1}$ is spurious due to the fiber slipping, otherwise a clear periodicity is evident. Measurements were repeated three times due to uncertainty in the “helix” and the

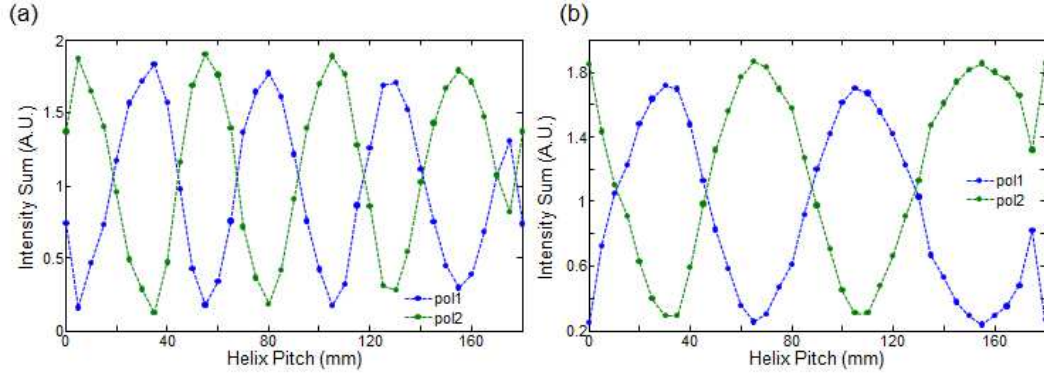


Figure 7-10: Power in each linear polarization as a function of helix pitch for (a) $HE_{7,1}$ and (b) $EH_{5,1}$

periods calculated and averaged. The ratio of the periods of $EH_{5,1}$ to $HE_{7,1}$ is 0.69, while $5/7 \approx 0.71$, indicating good agreement with the expected result.

The measurement is repeated using OD105 Vortex fiber, with the $HE_{2,1}$ modes and the same experimental apparatus, although we note that the exact shape of the helix has likely changed, since the fiber sample has been swapped out. The pitch, shown in Fig. 7-11 (a), is much reduced from that of $l = 6$. An interesting comparison

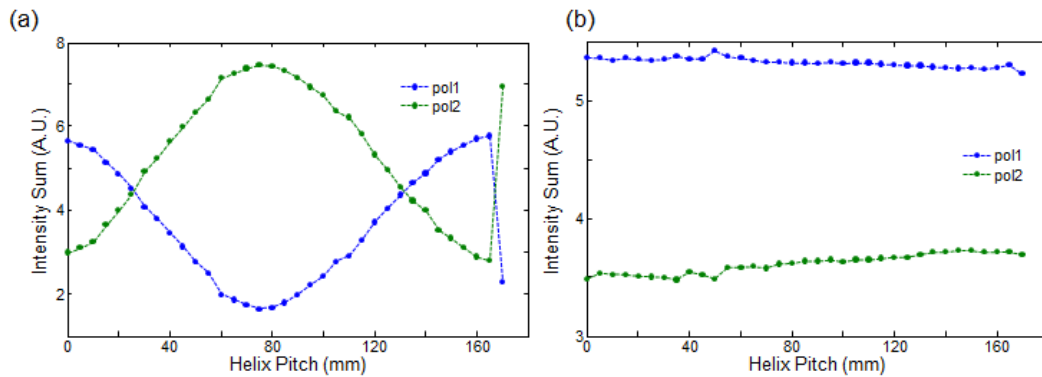


Figure 7-11: Power in each linear polarization as a function of helix pitch for (a) $HE_{7,1}$ and (b) $EH_{5,1}$

is with TE/TM, shown in Fig. 7-11 (b). Because the modes are symmetric, they are

unaffected by the geometric phase and no polarization cross-coupling is observed. (However, as a caveat, we note that the TE and TM modes are not degenerate; if this result is due to some other strange mode coupling effect between degenerate states, we expect it to be much reduced for the largely dephased TE and TM modes).

This behavior helps to explain the results of Fig. 7-4, in which the powers in EH/HE were seen to vary strongly while the powers in their constituent OAM modes were relatively stable. Indeed, when the stability experiment is repeated using a pol-con, we observe similar mode stability from both HE/EH modes and OAM modes of high- l . This indicates that there may be some hope for a true polarization maintaining fiber, if the fiber can be constrained to lie in one plane.

The fact that the rotation scales with j suggests a possible use for OAM modes + q -plates to be used as a fiber sensor, as the high- l modes will by default be j times more sensitive than SMF. Additionally, the ability to launch multiple modes, which will have controllably different responses, simultaneously suggests a reduction in ambiguity. This will be discussed more in Sec. 11.2.

7.5 Summary

We have demonstrated in this chapter that high- l OAM states resist common perturbations over short length scales, even though the modes come in degenerate pairs. Not only does this open the possibility of using each state independently over short length without the need for pre- or post-compensation, but it also implies that there is, innately, a difference between the OAM and EH/HE basis sets for higher order modes in weakly-guiding fibers, since the EH/HE modes are themselves not stable to simple fiber rotations and experimentally are observed to couple freely in the presence of even relatively faint perturbations. We expect that this stability in the face of common perturbations will be advantageous for OAM in applications desiring short

length transmission without digital signal processing (DSP), such as short-reach communications inside data centers (Zhang et al., 2012).

We have shown that although degenerate state mixing does occur for fiber transmission at the hundreds of m to km lengths, q -plates can be used to pre-compensate this mode coupling, and such compensation is relatively wideband, with one polcon setting able to pre-compensate for the entire C-band.

It would be interesting to study the stability properties of OAM states across a wide range of l . Behavior for $l = 0$ and $l = 1$ are well known (Bozinovic et al., 2012; Gregg et al., 2015a), and recent research on OAM polarization mode dispersion in 1.1km of an inverse-parabolic fiber seems to indicate that $l = 2$ also couples in the presence of common perturbations (Wang et al., 2015). To my knowledge, the space between $l = 2$ and $l = 5$ remains unexplored. Given the rapid decay in bend azimuthal Fourier series coefficients in Fig. 7.3, it may be the case that a wide array of OAM states are stable against such perturbations, but we have also seen in air core fibers accidental-degeneracy induced coupling between states which have $\Delta l = 4$ (gen3e, and gen4) and $\Delta l = 7$ (gen1), so it may be that only for $l \geq 4, 5$ that this stability truly occurs. Further, it is unknown how this concept will extend to the SOC states. Likely such stability will be equivalent or even slightly better, since the states now exist in an OAM superposition, and coupling should be driven by interactions between the lower l components, which now have modal weights less than unity. This; however, remains to be tested.

Chapter 8

Broken Degeneracy and Long Length OAM State Propagation

The main argument behind the introduction of stress rods into PM fiber (Varnham et al., 1983; Tsao, 1992), and the design of a fiber with high refractive index contrast (Ramachandran et al., 2005b), is the breaking of modal degeneracy to introduce stability for the modes in question, either the polarization modes of SMF or the azimuthal mode order $L = 1$ vector modes.

However, according to coupled mode theory, mode coupling between even phase mis-matched states can and does still occur (Marcuse, 1974). The polarization stability in PM fibers is well known, and depending on the type and fabrication quality can be -30dB or better per 100m (Noda et al., 1986) (or see, for instance, Corning Panda PM 1550). The $l = 1$ OAM mode stability versus TE and TM modes is estimated as -10dB after 1km (Bozinovic et al., 2013), which was enough for Tbps communications using FEC. Experimentally, a sharp enough bend can induce visible coupling between high- l SOa and SOaa OAM states even over a bend a few cm in length, although the bend diameter needed to observe such coupling is less than 1cm.

In this chapter we study distributed mode coupling between SOa and SOaa OAM states over long lengths of fiber. Note that the symmetry arguments discussed in Chap. 7 *do not* apply here for high- l states; for a given l , there exists a pair of non-degenerate states $V^+ \propto \hat{\sigma}^+ e^{il\phi}$ and $W^- \propto \hat{\sigma}^- e^{il\phi}$ such that coupling between them

only requires a birefringent perturbation which couples spins:

$$\langle \hat{\sigma}^- | \Delta n | \hat{\sigma}^+ \rangle \neq 0 \quad (8.1)$$

Such perturbations are known and expected in SMF, and will occur over long lengths of air core fiber. For low- l states for which $\Delta l = 2l$ is small, it may be the case that coupling between V^+ and W^+ may be preferred over the birefringent perturbation needed to coupling V^+ and W^- . This is a possible subject for future work.

In Sec. 8.1, we discuss coupling from SOa to SOaa which, instead of being enabled by birefringent perturbations, is enabled by accidental degeneracy with a lower l OAM family. The remainder of the chapter discusses distributed coupling between adjacent modes of the same l . In Sec. 8.2, time domain and time domain + q -plate output projection measurements are performed on air core links ≈ 1 km in length. Sec. 8.3 describes preliminary experiments leading to the OAM loop experiment, which is discussed in detail in Sec. 8.4, and in which distributed mode coupling is measured at multiple fiber lengths and a comparison is made with coupled power theory in a two-moded fiber. It is found that OAM modes follow the expected hyperbolic tangent power transfer behavior, and that relatively small changes in Δn_{eff} can lead to large changes in mode coupling coefficient. We compare our results on recent work studying distributed mode coupling between adjacent LP mode families, and find that for similar splittings, OAM modes perform at least an order of magnitude better in resisting mode coupling.

8.1 Accidental-Degeneracy Induced Coupling

As discussed in Sec. 6.4, gen4-3 of the air core fiber features accidental degeneracy across only part of the C-band, with higher wavelengths featuring stable propagation of SOa and SOaa $l = 6$ modes, while lower wavelengths feature output symmetries

indicative of $l = 2, m = 2$ modes, and according to simulations, these mode families are proximal in n_{eff} . Here, we study the level at which this coupling influences the intermodal crosstalk between $l = 6$ SOa and SOaa; at some point, for instance, perhaps only single-coupling events between $l = 6$ and $l = 2$ will be likely, resulting only in loss. Alternatively, if multiple-coupling instances are possible, both crosstalk and MPI are possible, with both impairing any system relying on modal stability.

We study this coupling with the apparatus in Fig. 8-1. OAM states of $l = 6$ are launched, either by a $q = 3$ plate for SOaa states, or a $q = 3$ plate followed by an HWP for SOa states. As previously described, a q -plate followed by an HWP

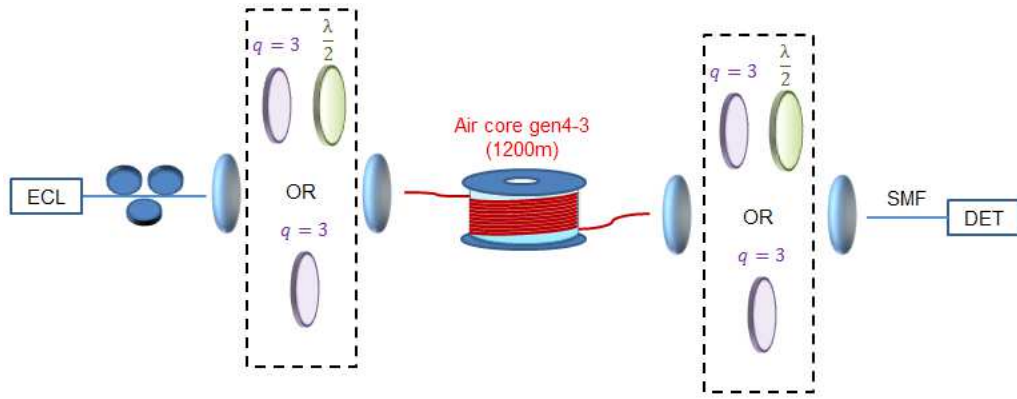


Figure 8-1: MUX/DEMUX system used to test in-fiber crosstalk by q -plate output coupling

is essentially a q -plate with charge of $-q$, so $q = -3$ will be used for brevity for this combination. The states are propagated through 1200m of gen3-4 fiber, after which they are passed through either a $q = 3$ or $q = -3$ plate and coupled into SMF. When the SOaa states are launched by a $q = 3$ plate, using a $q = 3$ plate at the output measures power retained into SOaa states, while deMUXing with a $q = -3$ plate measures power coupled into the SOa states. The output coupling loss is approximately 5.8dB, with 1.5dB lost in transmission through the q -plate and 4.3dB lost in SMF input coupling. We expect that the resolution between power in

SOa and SOaa will be excellent, since one mode set will be sent to the fiber as $l = 0$ states, and one as $l = 12$ states, which will have a miniscule overlap integral. Fig. 8·2 shows the effect of transmitting an $l = 6$ SOaa (top) and SOa (bottom) state, after 1.1km fiber propagation in gen3f, through a $q = 3$ plate, which down-converts the SOaa states to $l = 0$ while up-converting the SOa states to $l = 12$. This is especially evident in the far-field, where the $l = 0$ beam has evolved into a spot, while $l = 12$ is clearly a ring. Some light in the center is evident due to crosstalk in the FUT;

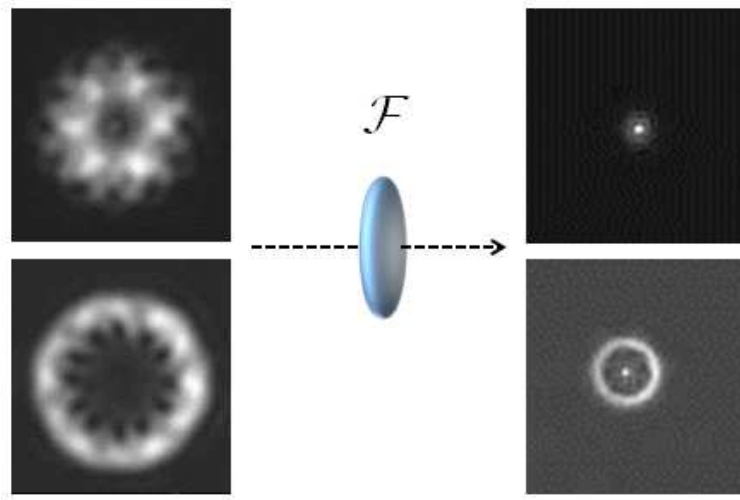


Figure 8·2: $l = 6$ SOaa (top) and SOa (bottom) states transmitted through a $q = 3$ plate, converting them to $l = 0$ and $l = 12$, respectively. In the farfield (right) these become a spot and a large ring beam. Top far field image attenuated with respect to bottom

however, note that the even though the spot is bright crosstalk is not necessarily severe, since the power in the parasitic modes has now been condensed into a small spot while the power in the desired modes is now spread out into a larger ring.

When performing input coupling, the limiting factors determining how much parasitic SOaa is excited when intending to launch SOa are the precision of the HWP used, which is typically -22 to -25dB, and the amount of polarization scrambling off of theoretically polarization insensitive components, such as mirrors. In this out-

put coupling setup, the q -plate is placed before two coupling mirrors, removing this uncertainty.

The Pritel pulsed laser ($\Delta\lambda \approx 0.5\text{nm}$) is swept across C-band, and $l = 6$ SOa and SOaa are launched. For each launch condition, output projections with a $q = 3$ and $q = -3$ plate are performed, thus giving crosstalk for each mode set at each wavelength. The measured powers are plotted in Fig. 8-3. As is evident from Fig. 8-3

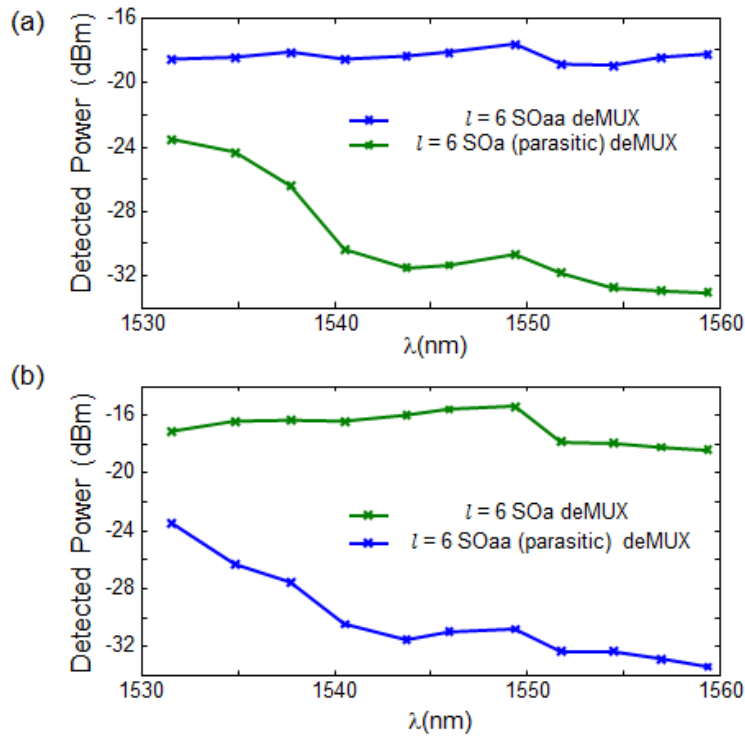


Figure 8-3: Measured powers using q -plate output projection for (a) $l = 6$ SOaa launched and (b) $l = 6$ SOa launched. Difference between curves yields wavelength-dependent crosstalk

both the SOa and SOaa modes deteriorate as the wavelength is decreased, especially for wavelengths shorter than 1540nm. Evidently, in this range coupling between the two mode sets aided by accidental degeneracy is possible, and $l = 6$ SOaa appears to be more strongly affected, as would be expected from time domain Sec. 6.4. Measured crosstalks at longer wavelengths agrees quantitatively with that measured by time of

flight, lending credence to both measurements.

The measurement in Fig. 8·3 is incoherent in nature, given the wide bandwidth of the laser source. The measurement is repeated using a narrowband ECL. Wavelength is swept across 1nm in 100steps for seven wavelengths across the C-band, using the same MUX/deMUX setup as above. Data is shown in Fig. 8·4(a) when $l = 6$ SOa is launched and (b) when $l = 6$ SOaa is launched. Not only the crosstalk but evidently the MPI in the parasitic mode increases as the wavelength is decreased.

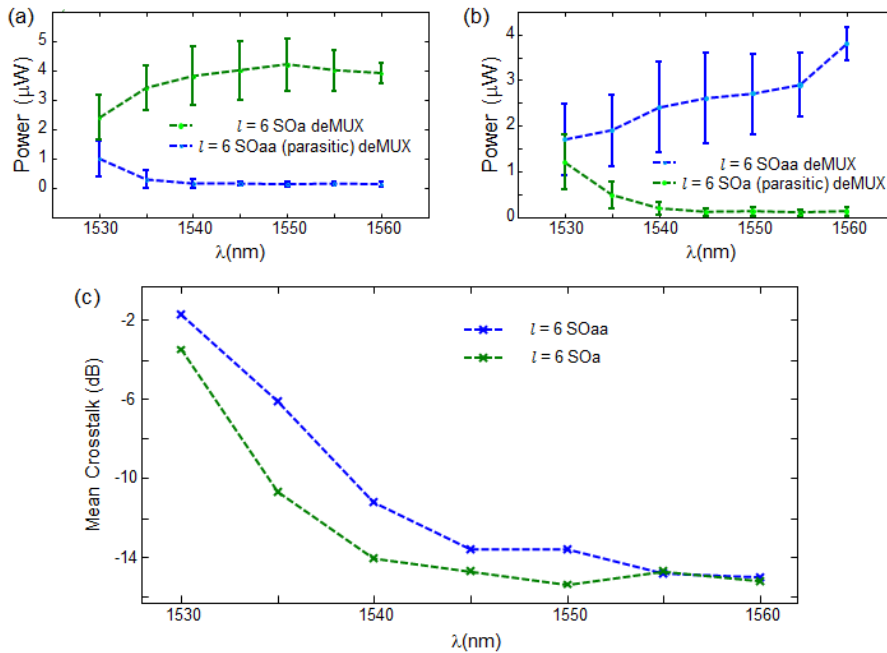


Figure 8·4: Measured powers using q -plate output projection for (a) $l = 6$ SOaa launched and (b) $l = 6$ SOaa launched, with narrowband ECL as source. (c) Measured crosstalk as a function of wavelength

The only other component which could directly lead to wavelength-sensitive crosstalk is the HWP used to make the $q = -3$ element. The HWP used is a zero-order HWP from Thorlabs, which previous (and later) measurements confirm does not contribute to crosstalk above the -20dB level across the C-band.

Thus, we conclude that operating in this regime will be extremely detrimental from a communications point of view. It is unclear whether the coupling is a two-

step process, aided by two different accidental degeneracies, or a three-step process aided by one:

$$l = 6 \text{ SOa} \rightarrow l = 2 \text{ SOa} \rightarrow l = 6 \text{ SOaa} \quad (8.2)$$

Or

$$l = 6 \text{ SOa} \rightarrow l = 2 \text{ SOa} \rightarrow l = 2 \text{ SOaa} \rightarrow l = 6 \text{ SOaa} \quad (8.3)$$

This could likely be tested using output coupling of $l = 2$ on short lengths of fiber. Regardless of the exact transition, it is evident that coupling among all $l = 6$ states has occurred.

It may be the case that this regime has other applications we have not considered. If the fiber strongly couples the photons, one could imagine it as a black box out of which, if $l = 6 \text{ SOa}$ is inserted, one of eight ($l = 6 \text{ SOa} \times 2$, $l = 6 \text{ SOaa} \times 2$, and then the four $l = 2 \text{ } m = 2$ states) emerge with some probability. This could have application to quantum entanglement experiments, or more prosaically, if the coupling is sufficiently random, random number generation.

8.2 km Length Propagation and Time of Flight

We use time of flight to study distributed coupling over long-length fibers. Given the equipment available to us, to study distributed coupling between SOa and SOaa states, which are typically separated in group index by $2 \sim 4 \times 10^{-4}$, fibers of at least 50m are needed. As sample system diagram is shown in Fig. 8-5. At the fiber output, for most measurements, we couple into an MMF which is patched into a fast detector. This results in traces such as Fig. 8-6(a), when the $l = 6 \text{ SOa}$ mode is launched. We have hereto assumed that the distributed in the $\sim 1\text{ns}$ preceding the main peak is entirely in the $l = 6 \text{ SOaa}$ mode set. We confirm this by using the second output setup in Fig. 8-5 where the fiber output is passed through a $q = 3$ or $q = -3$ plate and then coupled into SMF, revealing separately the time signatures of the SOa and

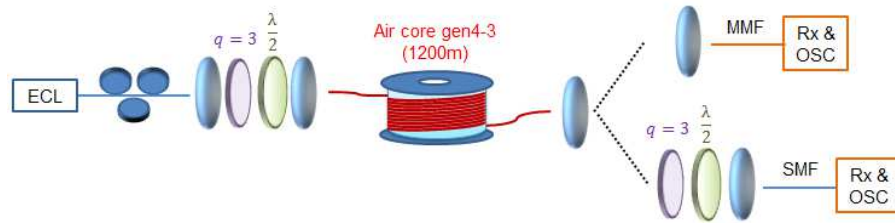


Figure 8.5: Experimental system for measuring distributed mode coupling by time of flight, and sanity-checking MMF output coupling

SOaa modes. As expected, the mode coupling shoulder is, to the resolution of the measurement, entirely in the parasitic mode group.

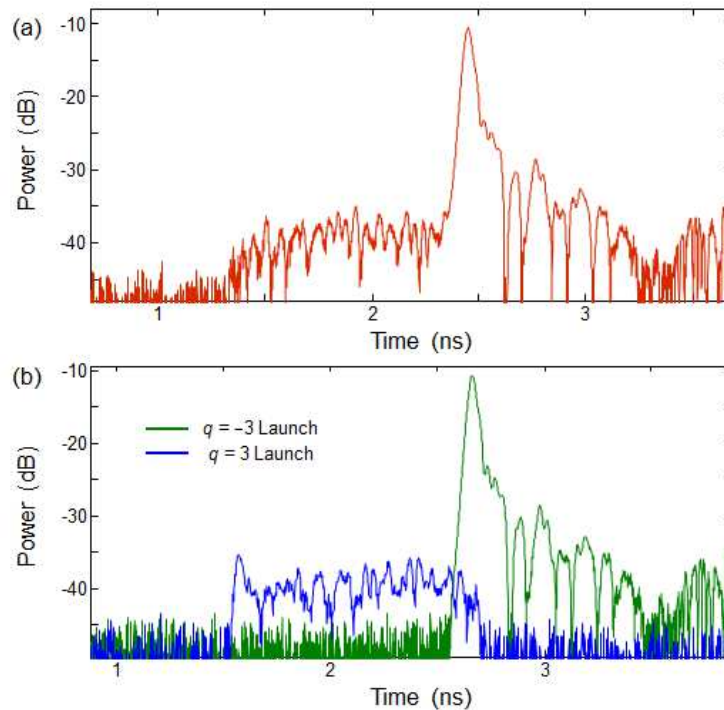


Figure 8.6: (a) Time of flight trace of $l = 6$ SOa after 1200m in gen4-3 fiber, with output coupled into MMF (b) Time of flight trace of the $l = 6$ SOa and $l = 6$ SOaa projected into $l = 6$ SOa.

Time of flight traces are measured for the $l = 5, 6, 7$ modes in gen4-3 (at 1555nm, where $l = 6$ is stable), and shown in Fig. 8.7. Dashed lines and corresponding y-axis label indicates strength of local intermodal coupling, while integration over

the shoulder (red) divided by integration over the peak (green) yields the crosstalk numbers given in red. Measured crosstalk values are comparable for $l = 6$ and $l = 7$,

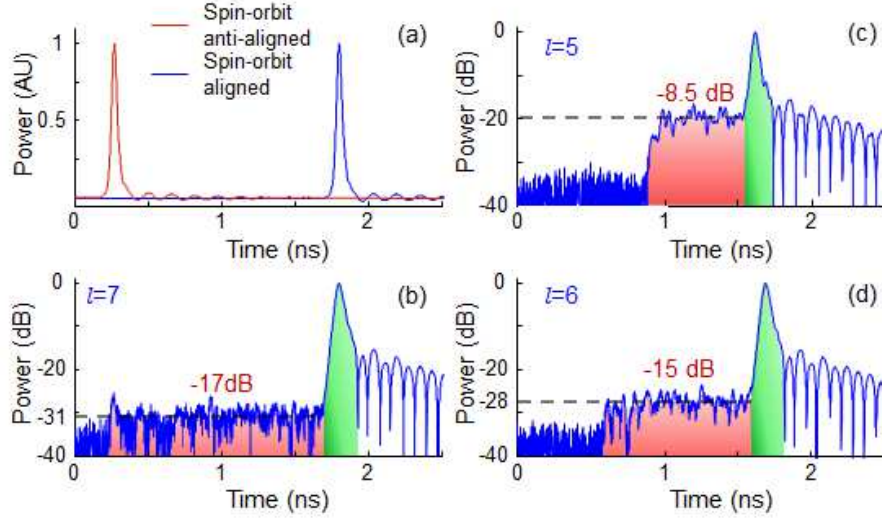


Figure 8-7: (a) Time of flight measurement of both $l = 7$ states, excited independently, shown on linear scale (b-d) Time of flight measurements of $l = 5, 6, 7$ on log scale

the effective indices of which are, according to simulation, 1×10^{-4} and 1.7×10^{-4} . $l = 5$ on the other hand is significantly worse, despite having an n_{eff} separation of 7×10^{-5} , seemingly comparable to $l = 6$. This underscores the dependence of intermodal coupling on phase mismatch between modes - typically the functional dependence on phase mismatch in coupled mode or coupled power theory, given by R in Eq. (3.10), is assumed to be strongly peaked around $\Delta\beta = 0$, meaning that power transfer could, and apparently does, rapidly increase as the phase mismatch is decreased. Unfortunately, the group index separation of $l = 4$ in this fiber is insufficient to resolve between mode-coupling induced broadening and dispersive broadening. The same is true for $l = 3$ and $l = 2$, so time domain measurements in a more heavily-coupled regime are not possible. Short length experiments, however, nearly always show a strong LP-like output for $l = 4$, which has a simulated n_{eff} splitting of approximately

2×10^{-5} .

It would be useful to develop a model to predict the intermodal coupling between OAM modes at arbitrary lengths, which by necessity must include mode coupling measurements at multiple data points. Furthermore, given the large amount of air core fiber (albeit in $\sim 1\text{km}$ pieces) fabricated, it is possible for us to test OAM propagation at length scales $\sim 10\text{km}$; to my knowledge, OAM propagation over more than 1.1km in fiber has yet to be demonstrated, and questions still remain about OAM scalability. We realize this long-length propagation by using a recirculating loop experiment, akin to the classical telecom experiments used to test trans-oceanic length cables (Bergano and Davidson, 1995). Before this experiment can be performed, several practical lead-up tasks required investigation.

8.3 Loop Buildup

A simplified schematic for the loop experiment is shown in Fig. 8.8. A pump beam (red

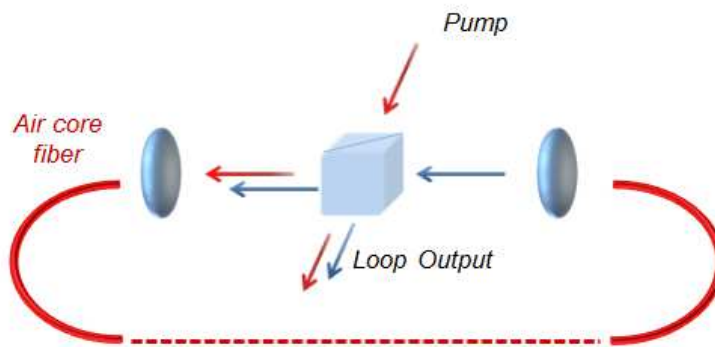


Figure 8.8: Simplified loop diagram

arrow) enters the loop through an input/output coupling element, here represented with a beam splitter. The part of the pump which is coupled into the loop traverses the fiber loop and is emitted from the loop fiber's output facet (blue arrow) and fed back into the coupling element. It is either re-coupled into the loop for further round

trips, or output coupled for diagnosis.

For traditional loop experiments in SMF, in-fiber acousto-optic modulators (AOMs) were typically as the coupling element, as they were low-loss ways of both rapidly input/output coupling, and could also be varied in time such that a near-arbitrary number of round trips could occur before detection. This is impossible for air core fibers, as in-fiber AOMs do not exist, and free-space ones are slow for large beams, and tend to distort the beam passed through them unless collimation is near-perfect. The last point is critical, since beam distortion will immediately yield crosstalk in our case. A previous HOM loop experiment circumvented this issue by building long (60km) loops and using a free-space beam chopper with frequency $\sim 100\text{kHz}$ (Sleiffer et al., 2013). For our experiments, we are thus restricted to using a standard 3dB splitter for the input/output coupling element. The pump OAM beam is created using an SLM and a QWP.

To perform the loop experiment, several things have to be tested.

- Free-space coupling from air core fiber to air core fiber. Coupling from free space to fiber was discussed in Chap. 5, but coupling from fiber to fiber may be more difficult due to the precision needed for mounting angle, cleave angle, fiber position, lens position, etc.
- Components must be tested for polarization scrambling, especially the beam splitter used for input/output coupling. It would also be preferable to couple fiber-to-fiber without using mirrors. Silver or gold mirrors at large angles of incidence can cause polarization scrambling between $\hat{\sigma}^+$ and $\hat{\sigma}^-$ due to differences in Fresnel reflection coefficients between \mathbf{s} and \mathbf{p} polarized light (Saleh and Teich, 2007); even small differences at slight incidence angles could eventually become significant due to being in the loop, and thus experienced multiple times.

- A splice program (as described in Chap. 6 and App. C) must be developed for low-loss, low crosstalk splicing.
- The use of a 3dB splitter as opposed to an AOM poses an additional problem - the loop pump will pass through the beam splitter with only 3dB of loss. Meanwhile, the beam emitted from the loop after one round trip has suffered 6dB in beam splitter loss, in addition to input coupling, fiber transmission, and splice loss, meaning that the loop pump will be significantly stronger than the loop output. These two beams must be separated before the Rx.
- A pulsed source with acceptable repetition rate must be engineered. The Pritel picosecond pulsed laser used for all time domain measurements to this point has a repetition rate of 20MHz. This inter-pulse duration of 50ns is insufficient for longer fiber lengths, as the growing delay between time of arrival of different modes implies that the time signatures of different pulses may overlap, preventing analysis.

Free space fiber-to-fiber coupling is first attempted with the fibers a minimal distance apart, as in Fig. 8-9. The fibers are mounted onto two translation stages along with two $f \sim 4.5mm$ lenses, and the two stages are directly butted together. Gen4-2B is illuminated with $l = 7$ from an SLM, which is checked for alignment with time of flight, before the end facet is placed into the groove of one of the translation stages. Throughput is first optimized for power, then for output symmetry on a camera. Gen4-3 is the ‘receiving’ fiber, as it stably supports $l = 6$ for the wavelength used (1555nm); thus, imperfections in the coupling will be more resolvable than if $l = 6$ strongly coupled to lower l modes under the influence of accidental degeneracy. Better than 20dB extinction of undesired l states is achieved, with a fiber-fiber coupling loss of $\sim 0.5dB$. The same fiber alignment stably couples both $l = 5$ and $l = 7$. Thus, fiber-fiber coupling without mirrors is in principle possible.

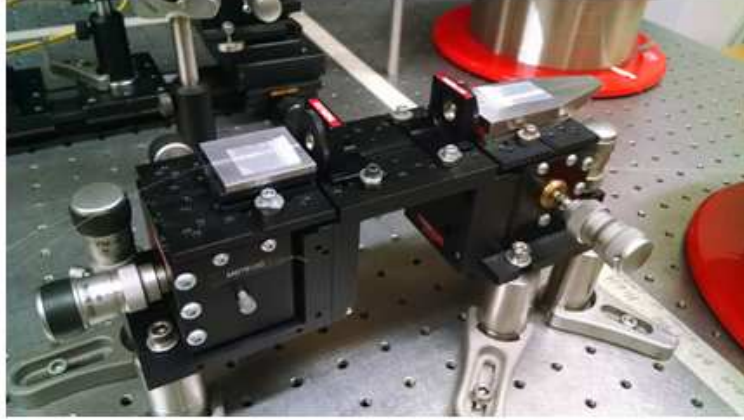


Figure 8.9: First test of fiber-to-fiber coupling using gen4-2B to gen4-3

However, when the translation stages are separated by approximately 80cm, low-crosstalk coupling is no longer possible. Crosstalk is measured as -13dB for $l = 7$. Further, the coupling losses are 1.2dB for $l = 5$ and 3.0dB for $l = 7$, implying that diffraction is beginning to play a role in loss. Introduction of two mirrors between the stages reduces crosstalk to -22dB or less, with coupling loss 2.2dB for both $l = 5$ and $l = 7$.

From the above two measurements, we infer that the larger the fiber-fiber distance, the larger the loss will be, as might be expected from diffraction theory (note that this only constitutes a $4F$ system if the distance between the lenses is $2F$). We also infer that control in addition to the lateral/vertical displacement of the fibers is necessary. The two lenses also need to be centered with respect to each other, else significant crosstalk can occur. For the loop experiment, we mount both lenses on x-y translation mounts, giving an additional alignment degree of freedom.

The beam splitter is an especially important component for this loop, as it has the potential to induce significant crosstalk between the SOa and SOaa OAM states by means of discrete polarization scrambling. Standard non-polarizing beam splitters such as Thorlabs BS015 (or similar from Edmund or Newport) only maintain

polarization at the few percent level, and testing our lab revealed that transmission through the beam splitter preserves circular polarizations to about -18dB, while using the beam splitter in reflection mode preserves circular polarizations to only -10dB.

We are fortunate in this case, because Tholabs also makes a wedged plate (BSW06, dielectric coating) beam splitter, which generally does no better at maintaining polarizations, but for which the coating is optimal around 1550nm. In-lab testing reveals that in both reflection and transmission the plate beam splitter preserves circular polarizations to $-21 \sim -22$ dB, with the reflected case being slightly worse. Fig. 8-10 shows a time of flight trace for fiber-fiber coupling with a plate beam splitter operated in reflection between the fibers. Discrete polarization conversion is evident above the distributed coupling shoulder from in-fiber, but is at least 20dB down. For the loop

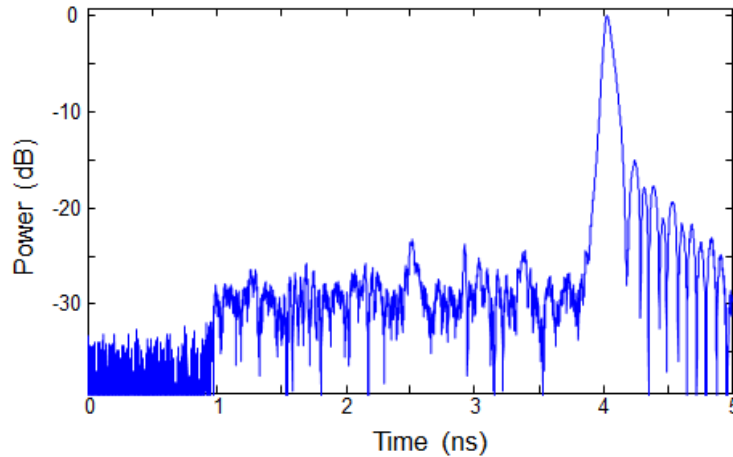


Figure 8-10: Time of flight for $l = 7$ SOa coupled into Gen4-2B, which is then free-space coupled, through the reflective port of a plate beam-splitter, into gen4-3. Blip at 2.5ns is due to polarization conversion at beam splitter

experiment, we use a transmission mode to retain the beam inside the loop; thus, parasitic polarization conversion can only happen once since polarization conversion while leaving the loop is irrelevant.

To solve the beam overlap leaving the loop, a free-space AOM is used (Isomet

1205C-1). If a single pulse is incident on the loop, the part of the pulse which propagates around the loop and the parasitic part which simply passes through the beam splitter will be well separated in time, with the round trip time being approximately $5\mu\text{s}$ per km of fiber. The beam leaving the loop is passed through a 1:4 telescope to shrink the beam size, and is coupled into the AOM. The AOM is set to diffract the beam for all times except for those when a parasitic pulse is incident, at which point the AOM is biased for zero deflection. The rise and fall time of the AOM is approximately 200ns, sufficient for separating desired loop output from undesired parasitic pulses. The diffracted beam from the AOM is coupled into an MMF and fed into a fast detector. The AOM diffraction efficiency plus MMF insertion loss is approximately 4dB for $l = 5$ and $l = 7$.

The light source used in these experiments is diagrammed in Fig. 8-11. The RF output of picosecond laser is amplified and triggers a digital delay generator (DDG). The trigger signal is down-sampled, amplified, and then applied to an electro-optic modulator (EOM) (Thorlabs 10GHz $LiNbO_3$) which is biased to a null setting, blocking all pulses when no voltage is applied. The laser repetition rate is thus down-sampled by a factor between 10 and 200 depending on the fiber loop length, such that only one or a few pulses are in the loop at a given time, and their temporal responses are well separated from each other, and well separated upon reaching the detector from the train of parasitic pulses which do not enter the loop. The insertion loss of the EOM is 3.2dB, while the extinction ratio is approximately 25dB. The output pulse train then passes through a 99/1 coupler, where the 1% tap is sent to the wide bandwidth oscilloscope as a trigger signal. In some cases for longer fiber lengths, an EDFA is used to boost the peak powers of the pulses such that multiple round trips through the loop are visible. However, the EDFA has a minimum average power setting, below which the amplifier pump is electronically shut off to suppress ASE.

The down-sampled pulse train is far below this minimum average power limit due to losing a large number of pulses. To ‘trick’ the amplifier into working, an ECL with average power 3mW is combined with the pulse train through an in-fiber PBS. The two signals then pass through a polcon which aligns the pulse train’s polarization with the SLM used in our free space coupling system (Fig. 8-12). Thus, the amplified CW beam can be directed to a beam dump in free space. We do observe randomly polarized ASE after the EDFA in free space; this is reduced by using a bandpass filter before the AOM after the loop. The bandpass filter contributes an additional 3dB to the system loss. The EDFA is operated in a low-gain regime to avoid the onset of SPM in either the SMF leading to the input coupling system, or in the FUT. The EDFA itself contains a few meters of gain fiber and SMF, limiting the peak powers available.

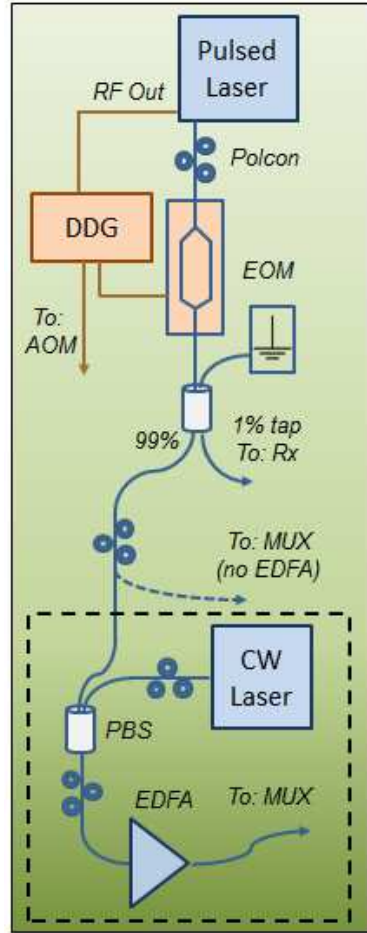


Figure 8-11: Schematic diagram of light source used for loop experiments

8.4 Loop Experiment and 13.4km OAM Propagation

All fibers from gen4 other than gen4-5 and gen4-6 are used for the loop experiment. Details on gen4-3 are listed in Fig. 6-21, and are similar for all other fibers used in terms of Δn_{eff} , Δn_g , and loss. The fibers stably guide $l = 5$ and $l = 7$, but $l = 6$ is lost to accidental degeneracy. We have four samples of length 1.2km, and one sample

of 1.9km, allowing loop lengths of up to 6.7km. After the longest loop is measured, gen4-2A is cutback by 600m, allowing for a shorter-length data point.

The experimental setup is shown in Fig. 8-12. Light from the source described

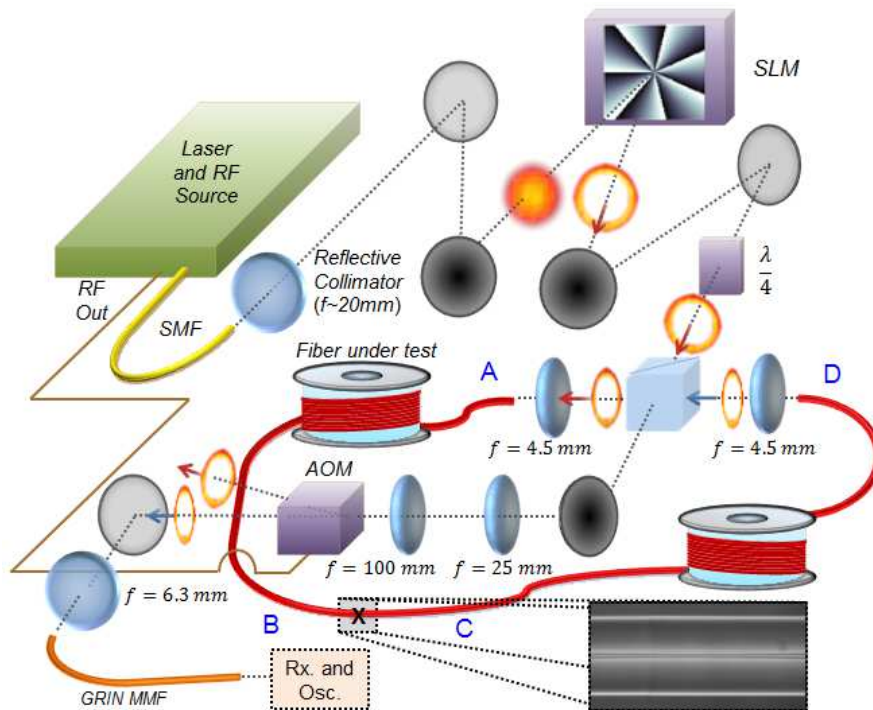


Figure 8-12: Experimental setup for loop experiments

in Fig. 8-11 is collimated and converted into an OAM mode by an SLM and QWP. The fibers are aligned in two distinct segments. Segment C-D is illuminated from facet C, using a second SLM. Once good ($< -20dB$) mode purity has been observed via time domain, the coupling from D to A is optimized, and observed at facet B. Optimization from D to A involves aligning both the two fibers and the coupling lenses - this is done first by eye and by IR card to ensure that the beam emitted from D is collimated and strikes the coupling lens for A at the center, and then observing that the focusing beam is always roughly centered on the lens' optical axis. Finer tuning is then performed while observing the output field and time of flight spectrum from B. The ability to change the excited state illuminating facet A is crucial; often,

for a given l , coupling between D and A can be optimized, but only for that state; that is, some combination of different offsets and aberrations leads to decent mode purity even though the beam may be offset on some elements, especially for $l = 7$, which is the highest l guided in these fibers at 1550nm. Iterating through the desired states while aligning ensures a more accurate alignment. Coupling loss from D to A is measured as 1.2dB. Input coupling from the SLM to facet A is then optimized

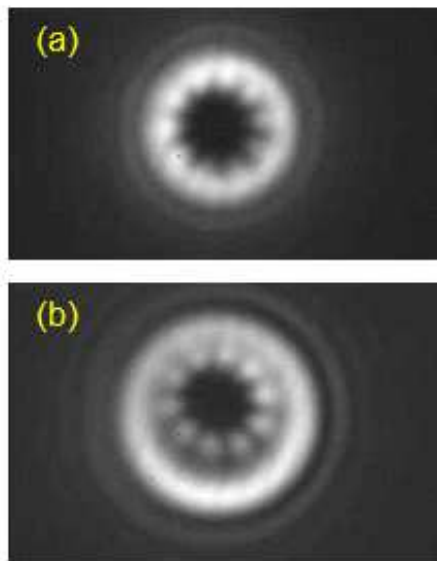


Figure 8-13: (a) Beam from SLM to pump facet A overlapped with output from facet D (1200m gen4-3) (b) Same but with beam from SLM defocused for illustration, showing the two beams slightly separated

using two guiding mirrors and observing the output from B; the fiber is not touched again. Note that coupling from D to A could not be optimized just by input coupling into facet A and observing the output from D, as the first round trip will always be significantly stronger than the second, resulting from coupling from D to A. Moreover, when the system is well-aligned, the output from facet D and the pump beam from the SLM, as observed at the loop output, are well aligned in space as in Fig. 8-13(a). Finally, the loop is closed by splicing facets B and C while observing the time of flight from the loop output. The average measured splice loss is 0.2dB with crosstalk -15dB

or better.

Measurements are taken at several loop lengths between 1.2km and 6.7km, and crosstalk is measured by time of flight for both $l = 5$ and $l = 7$. Since the EOM used to select pulses only has 25dB of extinction, there are parasitic pulses which are emitted from the EOM and pass through the beamsplitter, thus arriving at the detector 28dB suppressed from the beam pumping the loop. For comparison, for $l = 7$, we are interested in measuring distributed coupling features approximately 30dB suppressed from $l = 7$'s main peak, which itself is 6dB of beam splitter loss and approximately 6dB of input coupling loss suppressed from the loop pump. To avoid encountering these parasitic pulses within the time of flight region of interest, the fiber is cut back by a few cm when necessary, since doing so changes the arrival time of the features of interest while it does not change the time of arrival of the parasitic features.

For loops of 3.1km length or less, the Newfocus 1444-50 picosecond detector is used due to its time resolution. For loops of 3.1km and longer, the Newfocus 1611 1GHz photoreceiver is used, due to its superior sensitivity. Note that not only does the pulse become weaker, but it broadens due to dispersion, which makes it appear weaker in peak power to a detector capable of resolving the pulse. Even a significantly broadened picosecond pulse appears as a Dirac delta to a detector with resolution of only 1GHz. The two detectors agree on the measured crosstalk at 3.1km to within 0.5dB so long as the calculation for the 1GHz detector includes a multiplicative factor to make up for the occlusion of part of the mode coupling shoulder due to the slower impulse response for the main peak. This multiplicative factor becomes less and less significant as the fiber length increases.

For first round trips, integration as described in Sec. 4.5 and illustrated in Fig. 8-7 is sufficient to yield accurate crosstalk values. For second round trips at longer lengths,

although the fiber can be cutback slightly to avoid parasitic peaks, those peaks have impulse responses of their own which, for the 1GHz detector, take almost 40ns to completely die out. Given that the repetition rate of the laser was initially 50ns, the entire timespan is thus filled with this ringing noise. In this case, the root-mean-square (RMS) strength of the mode coupling shoulder is determined. Distributed coupling is then approximated as this RMS value multiplied by the shoulder width. Supposing the detector is linear; that is, the electrical receiver measured by the oscilloscope is $E = E_{loop} + E_p$, where E_p is the parasitic signal from the ringing noise of the parasitic pulses. If (a, b) denotes the interval in time over which cross-coupling can be observed, and (b, c) denotes the interval of the main (unconverted) pulse, then:

$$XT_{meas} = \frac{\int_a^b E}{\int_b^c E} \simeq XT_{ideal} + \frac{\int_a^b E_{pump} dt}{\int_b^c E_{loop} dt} \quad (8.4a)$$

$$XT_{ideal} = \frac{\int_a^b E_{loop} dt}{\int_b^c E_{loop} dt} \quad (8.4b)$$

$$XT_{RMS} = \frac{\sqrt{\langle E_{loop}^2 \rangle} \times (b - a)}{\int_b^c E_{loop} dt} \quad (8.4c)$$

Where $\langle Y \rangle$ denotes an ensemble average of quantity Y . The RMS value of the measured trace is given by

$$E_{RMS} = \sqrt{\langle E_{loop}^2 + 2E_{loop}E_{pump} + E_{pump}^2 \rangle} \quad (8.5)$$

The middle term in Eq. (8.5) is zero. E_{loop} is a positive, slowly varying quantity in the region of the cross-coupling shoulder so long as it is above the noise floor. If, in the region of the cross-coupling shoulder, we subtract the mean of the pump trace from both the combined and pump traces, E_{pump} is evidently zero-mean and sinusoidally variant, with an amplitude changing slowly on the scale of its oscillations. Thus, we

make the approximation that:

$$\langle E_{loop}E_{pump} \rangle \approx 0 \quad (8.6)$$

Then:

$$\langle E_{loop}^2 \rangle = E_{RMS}^2 - \langle E_{pump}^2 \rangle \quad (8.7)$$

Both quantities on the RHS of Eq. (8.7) are independently obtainable from subsequent measurements of the time of flight with the loop open and then with the loop blocked (measuring only the parasitic pump). The RMS crosstalk can then be calculated directly. The RMS method and integration method are performed on a first round trip of at 5.5km loop - the measured crosstalks are -10.8dB with the background subtraction and -9.8dB for the RMS method, indicating good agreement.

The out-of-fiber losses in this system are significant. The addition of an EOM, 3dB splitter, and an AOM introduce approximately 10dB of loss, on top of ≈ 6 dB of coupling loss for $l = 7$, higher than optimal since the lenses and fiber positions were optimized for fiber-fiber coupling instead of free-space to fiber coupling. The relatively poor extinction of the EOM and lack of an in-fiber AOM also restrict measurement capabilities, since the parasitic signals become more and more comparable to the features of interest. Note that it is harder to measure crosstalk for stable OAM states, since the mode coupling shoulder is relatively weaker, and more comparable to discrete parasitic effects. Ultimately these imperfections and external losses dictate that we only successfully observe 2 round trips for most fiber lengths (at 2.4km we observe round trip 3, but at a power level too weak to calculate crosstalk). SMF loops have the luxury of including an EDFA within the loop itself to negate loop loss, which we cannot (yet!) do for these fibers.

Measured crosstalks are plotted in Fig. 8-14 for $l = 5$ and $l = 7$. The crosstalks follow well a hyperbolic tangent, as expected from coupled power theory (Kawakami

and Ikeda, 1978). Based on the data, we find that the mode coupling rates are approximately $h = 1.4 \times 10^{-1}/km$ for $l = 5$ and $h = 1.7 \times 10^{-2}/km$, based on minimization of mean-squared error (MSE) between the theoretical crosstalk and the measured crosstalk. The latter value is comparable to measured values in elliptical core PM fibers (Noda et al., 1986). After transmission over 13.4km, the $l = 7$ OAM states are pure to approximately -7.2dB. The states are $> 10dB$ pure at 5.5km, and at 2km, a distance relevant for large-scale data centers (Lam et al., 2014), they are 15dB pure. The crosstalk is measured at several points across the C-band for a loop length of

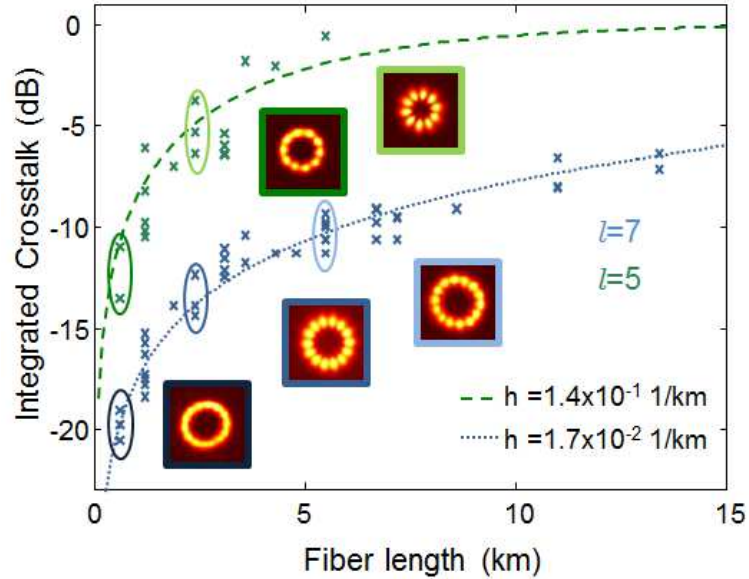


Figure 8-14: Measured crosstalk for $l = 5$ and $l = 7$. Dashed lines are theoretical crosstalk, for a given h values. Inset mode images become progressively beadier at longer lengths, indicating stronger crosstalk

5.5km, and fluctuates by only 0.5dB across that wavelength range, confirming that the crosstalk is wavelength agnostic. This measurement is, however, an incoherent one and will not reveal information about MPI (Ramachandran et al., 2003). We find more than an order of magnitude difference in mode coupling rate between $l = 7$ and $l = 5$, despite the Δn_{eff} being different by only a factor of ~ 2 .

Due to accidental degeneracy in most of the gen4 fibers, $l = 6$ cannot be measured at a multitude of lengths. However, when gen4-2A was cutback, it was found that $l = 6$ propagates in one half of the fiber, meaning that two data points - one at 600m and one at 1200m, can be obtained. Considering only those two point, $l = 6$ should have a mode coupling rate of $h \approx 4 \times 10^{-2}/km$, more comparable to $l = 7$ than $l = 5$, as results over 1.2km shown in Fig. 8·7 seem to suggest. During unrelated measurements, gen3a was cut back in 50m segments from 1000m to 500m, with time domain being taken at each length. This cutback yields several more data points, which are plotted in Fig. 8·15. The n_{eff} splitting for $l = 6$ in gen3a is 1.1×10^{-4} , comparable to that in the gen4 fibers. The experimental data suggest a mode coupling rate of $h \approx 4.1 \times 10^{-2}$, again similar to that found in the gen4 fibers. A summary of

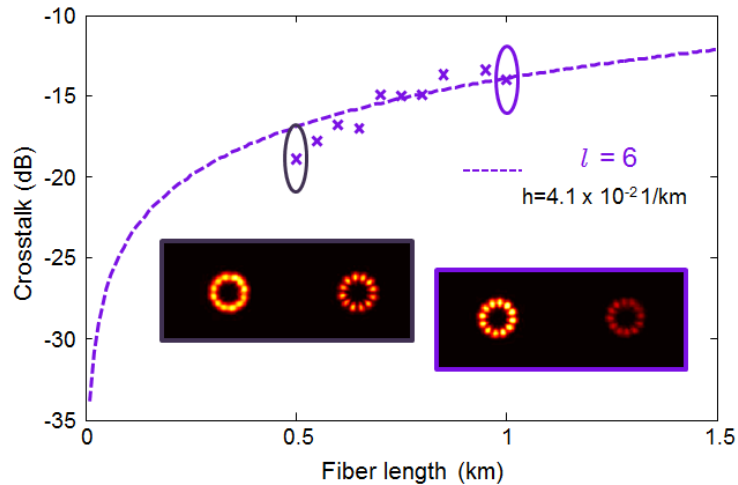


Figure 8·15: Measured crosstalk for $l = 6$ in gen3a fiber versus length, with theoretical crosstalk. Insets are experimental fiber outputs passed through a CPBS

the n_{eff} splittings and associated mode coupling rates is given in Table 8.1. These data points provide ‘benchmarks’ from which the crosstalk of a given mode of a known effective index splitting can be predicted for a given fiber length. Although there are only three data points, it appears that the change in h per change in n_{eff} is more

significant between $l = 5$ and $l = 6$ than between $l = 6$ and $l = 7$. Given that phase matched coupling is nonlinearly stronger than phase mismatched coupling, and that many authors model the phase mismatch dependence as a Gaussian centered at $\Delta\beta = 0$, this is believable (Bjarklev, 1986).

Table 8.1: Summary of experimentally measured mode coupling rates for different OAM modes

l	Δn_{eff}	$h(1/km)$
5	7×10^{-5}	1.4×10^{-1}
6	1.1×10^{-4}	4.1×10^{-2}
7	1.7×10^{-4}	1.7×10^{-2}

Recent measurements have studied similar mode coupling between adjacent LP mode families (Maruyama et al., 2015). Despite comparable spooling tensions ($\sim 0.45\text{N}$ used in these experiments), the OAM states are an order of magnitude or greater more stable for comparable Δn_{eff} . Although the smallest spooling tension in (Maruyama et al., 2015) is 0.7N , the mode coupling should scale approximately linearly with applied force (Tsubokawa et al., 1988), meaning that extrapolation from the data in that paper by a factor of two is reasonable. We attribute this stability to the larger probability of perturbations, such as slight bends, containing the $\Delta l = 1$ OAM component needed to couple between $LP_{0,1}$ and $LP_{1,1}$, compared with the birefringent perturbations necessary to couple spins.

We also find over the course of the measurement that the crosstalk for $l = 5$ is strongly sensitive to spooling tensions. Spooling at high tension can cause crosstalk in a single spool to degrade from about -10dB to -3dB or worse. On the contrary, the crosstalk for $l = 7$ does not change for similar changes in spooling tensions. Both states become worse when the spooling tension is too low, as this tends to lead to slippage during the spooling process, which can cause microbends. This also gels with observations in (Maruyama et al., 2015), which indicate that mode coupling is a

strong function of spooling tension if the effective index separation between nearest-neighbor modes is below a certain level.

8.5 Summary

We have shown, by means of a circulating loop experiment enabled by a large Δn_{eff} between adjacent OAM states and an extremely low ($0.8\text{dB}/\text{km}$) loss, OAM state propagation over 13.4km. Three OAM states have been measured, and their mode coupling rates determined by time of flight measurements. The $l = 7$ modes, featuring a Δn_{eff} of 1.7×10^{-4} are found to have mode coupling properties comparable to elliptical core fibers.

It is at this point worth commenting on the outlook of these fibers to long-haul communications. A splitting of 1.7×10^{-4} is quite large, without transitioning into the SOC regime. Although the refractive index of the ring guiding region can be further increased, in practice to about 0.05 above the index of Silica, it will be difficult to significantly increase the refractive index splitting of the OAM modes in the weak guidance regime. Supposing that one wanted to transmit data over classical long haul links of 26km (Keiser, 2011), the crosstalk for these $l = 7$ modes would be about -4dB. To obtain even 10dB purity at these lengths would require a mode coupling rate a quarter of what we measure. Given that the stability as a function of n_{eff} is not linear, it may take a significantly larger splitting than currently obtained to achieve such a low mode coupling rate. These fibers will be hard pressed to obtain intermodal crosstalk comparable with, for instance, uncoupled multi-core fibers (Saridis et al., 2015). Further, although the loss of 0.8dB is incredibly low for a higher-order mode in a fiber, it is still a factor of four larger than that in SMF. Some of this loss may be due to fabrication imperfections, but fibers with higher Germanium concentrations will intrinsically feature higher losses (Lines, 1984). It is thus unlikely that air core

fibers will ever see implementation in long-haul communications, even presuming that SDM is implemented in some form.

However, a recent class of so-called ‘Mega’ data centers has recently arisen, driven by the omnipresence of cloud computing (Zhang et al., 2012) which feature a myriad of both short (few m) and long (1-2km) links, and for which the additional system complexity and energy consumption of telecom DSP is undesirable. Provided that a simple way of exciting multiple OAM modes simultaneously, such as a tree of fused fiber couplers, can be developed, OAM could make a significant impact on such systems, both in terms of energy consumption and in terms of on-chip or rack-to-rack fiber footprint.

One additional measurement that should be made regarding intermodal OAM stability is a study of lower order OAM modes with comparable Δn_{eff} s. It may be the case that for a low l mode such as $l = 2$, significantly higher Δn_{eff} is required to obtain intermodal stability, since a transition of $\Delta l = 4$ is not impossible with a gentle bend, and may even be more likely than a birefringence-induced spin transition.

Chapter 9

MIMO-free 12 Mode OAM Transmission

The performance of OAM modes in “real” systems is little-studied. Most OAM transmission experiments are either performed at lab scale (meters) or were data-free. Several authors have erroneously studied “OAM transmission” in fibers not designed to support OAM states (Wang et al., 2016), thus ignoring any advantage that may be gained by fruitfully employing OAM modes. Transmission of true OAM modes has been demonstrated using up to 4 modes at km -length scales both in an entirely MIMO-free manner, where degenerate mode coupling was unwound using an fiber polcon (Bozinovic et al., 2013), and using degenerate mode group (2×2) MIMO (Nejad et al., 2016).

Our target is the transmission of multiple OAM modes simultaneously, using QPSK or a higher order modulation format. Although traditional optical communication systems have strict limits on BERs- for instance, Gigabit Ethernet requires a BER of 10^{-12} or less, the advent of FEC coding has allowed a more relaxed threshold at the cost of a system overhead which decreases the data rate (Hamming, 1950; Freeman, 2007; Chang et al., 2011). Two common FEC protocols are hard-decision forward error correction (HD-FEC) and soft-decision forward error correction (SD-FEC). The required BER for HD-FEC is 3.8×10^{-3} with an overhead of 7%, while the required BER for SD-FEC is 2.4×10^{-2} with an overhead of 20% (Yu et al., 2011; Cho et al., 2012; Dong et al., 2016). We require OAM transmission with BERs under the SD-FEC limit at minimum.

Based on the results from Chapters 6-9, we have the building blocks necessary to perform a transmission test of multiple higher order OAM modes simultaneously. In this chapter we describe experiments, in collaboration with Denmark Technical University (DTU), studying data transmission on $|l| = 5, 6, 7$. We perform data transmission using 10 GBaud QPSK on a 25 GHz-spaced frequency comb containing 60 wavelength channels over 1.2km. We find that, at three test wavelengths, all modes not affected by accidental degeneracy may be sent simultaneously with BERs below the soft FEC limit. This experiment is, to my knowledge, the first transfer data on more than 4 distinct spatial modes without MIMO. Our limitations are accidental degeneracy, which prevent the transmission of $l = 6$ at some wavelengths, drift and imperfection in input coupling, and potentially difference in degenerate state coupling across the source bandwidth, which limits the mode extinction available with our q -plates. Our experiments underscore the critical need for an efficient, low-crosstalk, stable MUX, if OAM transmission in fibers is ever to become practically feasible.

9.1 Experimental Setup for 12 Mode Data Transmission

The experimental setup is outlined in Fig. 9-1. A frequency comb with 60 WDM channels, spanning from 1550nm to 1562nm with 25GHz spacing, is generated using a 1544nm CW source which is phase and intensity modulated for sideband generation. This is amplified and passed through highly nonlinear fiber to broaden the optical spectrum. The comb is spectrally flattened and split into even and odd channels using a wavelength selective switch (WSS). In most experiments, the odd and even channels are separately modulated with 10 GBd QPSK signals and combined using a 3dB PM coupler as shown in Fig. 9-1. For some experiments they are instead modulated with 10GBd differential binary phase shift keying (DBPSK), using an intensity modulator biased at the null point. DBPSK is used instead of on-off keying

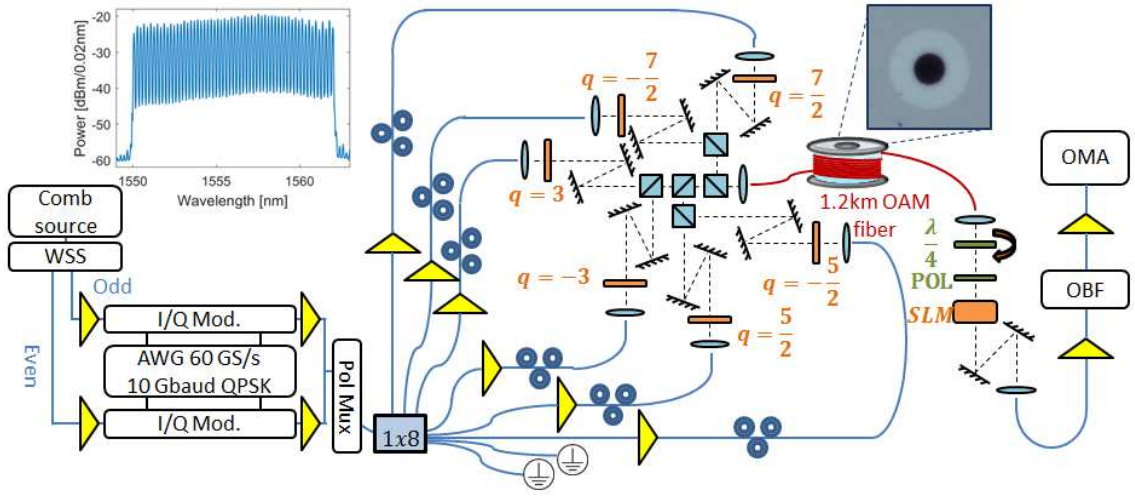


Figure 9-1: Experimental apparatus used for OAM fiber transmission test. WSS: wavelength selective switch, AWG: arbitrary waveform generator, POL: linear polarizer, SLM: spatial light modulator, OBF: optical bandpass filter, OMA: optical modulation analyzer. Insets: comb source optical spectrum and fiber end facet image

(OOK) due to an increase in receiver sensitivity of 3dB (Weber, 1978). Difficulties in source preparation prevented us from considering 16-QAM, or other higher complexity modulation formats.

The signal is split in a 1×8 coupler. Two outputs are discarded, while the other 6 outputs are independently amplified for use as data channels for the 12 OAM modes. Each of the 6 amplified outputs of the 1×8 coupler is passed through a polarization controller and collimated using a reflective collimator (Thorlabs RC04APC-P01). Each path is directed through a q -plate, creating a combination of degenerate states. The specific linear combination is adjusted, using the preceding polcon, such that the degenerate state mixing in the fiber is unwound and each data stream leaves the fiber as a pure OAM state (see Sec. 5.4). With two modes each in the SOa and SOaa sets for $|l| = 5, 6, 7$, we excite 12 modes in total. The states are made collinear using a system of 3dB splitters, and coupled into the fiber under test with an $f = 8\text{mm}$ aspheric lens. Although the current system design cannot increase the link capacity

over simply using 12 SMFs in tandem, since it doubles the number of channels by decreasing the signal to noise ratio (SNR) of each channel, it suffices to test the transmission properties of the air core fiber. The signals are transmitted through 1.2km of gen4-3 fiber. The fiber output is collimated and passed through a CPBS before being directed to an SLM. The combination of CPBS and SLM project one of the desired modes into an $l = 0$ free space mode. This is coupled to an output SMF, such that only one data stream is read at a time. Thereafter, the desired WDM channel is selected using a tunable optical bandpass filter (OBF), and is sent to an optical modulation analyzer (OMA), which handles detection and error counting for QPSK. For DBPSK, the output of the OBF is sent to a delay line interferometer with a delay of one bit, converting the phase difference to an amplitude modulation and enabling direct detection (Xu et al., 2004).

The inputs are independently amplified to account for differential loss. The $l = 7$ channels have one less 3dB beam splitter in path than the $l = 5$ and $l = 6$ channels, and will thus have lower loss. Even if the number of beam splitters were equal for all channels, there would be slight differences in size mismatch between the different l states, and it would be difficult to position the q -plates equally distant from the fiber coupling lens (where a difference in distance between plate and lens would result in a differential loss from differing phase curvature; see Sec. 5.4). The amplifiers are tuned to equalize detected power in each mode.

The system is aligned using a tunable repetition rate pulsed laser by measuring the time of flight response and optimizing for mode purity. The output projection is aligned in steps - first the projection is set for the desired mode and all input data streams except for the desired mode are blocked. The output coupling mirrors and SLM settings are aligned to optimize power coupled into the output SMF. After this, the desired input data stream and the data stream of the same $|l|$ are blocked and all

others, already aligned at the input by time domain, are unblocked. The SLM pattern at the output is then shifted by a few pixels to minimize total detected (parasitic) power.

The polarization of each arm is aligned by temporarily removing one input to the polarization MUX and adjusting polarization such that the output projection into one degenerate state is minimized across the frequency comb. We observe that it is not always possible to achieve a strong suppression of degenerate states across the frequency comb, which may be due either to imperfect mode coupling, or more likely to in-fiber mode coupling (Wang et al., 2015). Transmission of $l = 6$ SOaa is lost around 1550nm due to the presence of accidental degeneracy. We attribute this to the occurrence of MPI: light couples from $l = 6$ to a lower order mode, with which $l = 6$ is accidentally degenerate, before coupling back to the channel, corrupting the datastream.

9.2 Experimental Results

Using a DBPSK modulation format, we may map out the detected BER as a function of input power. We consider several cases of interest:

- Only the two degenerate modes, of a given mode order, are sent and the rest are blocked
- Only the four modes of the same $|l|$ are sent simultaneously; the rest are blocked
- All modes are sent at the same time

Each of these cases is shown for the $l = 5, 6, 7$ SOa modes at a representative wavelength of $\lambda = 1558.5nm$ in Fig. 9.2. As can be seen, when only the two degenerate modes are sent, the mode orders are nearly identical and error-free transmission is achieved for all of the modes considered. When all 12 modes are sent, the channels

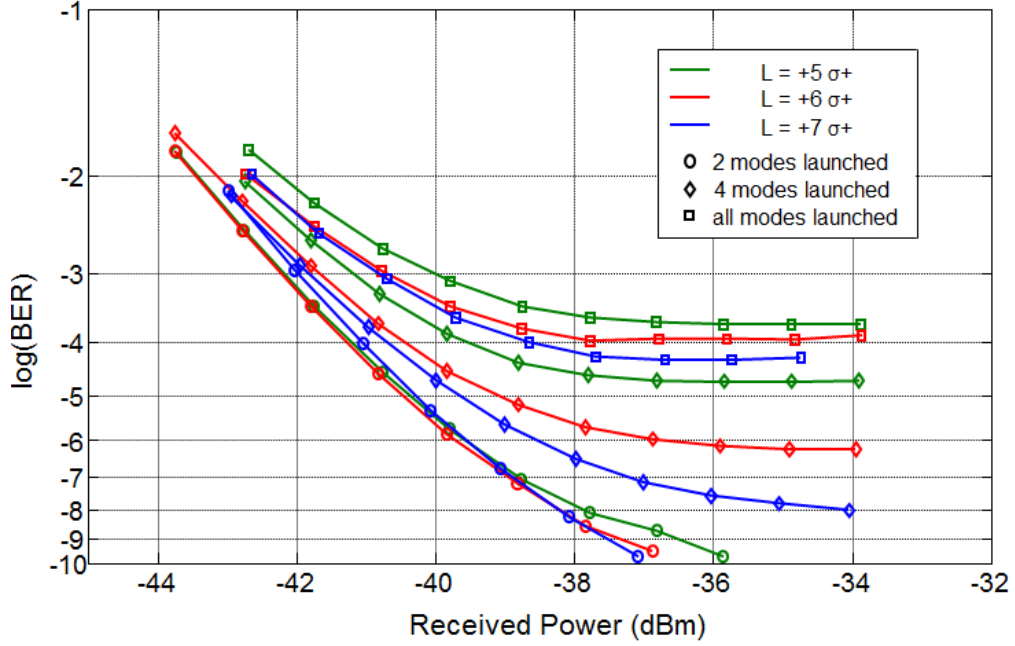


Figure 9-2: Measured BERs as a function of received power for a subset of modes at 1558.5nm, for the case of: launching only pairs of degenerate modes (circles); launching all 4 modes of a given l (diamonds); and launching all modes (squares).

are again markedly similar to each other, plateauing as the received power increases due to mode coupling. However, when the 4 mode case is considered, the channels are markedly different, with the $l = 7$ SOa modes almost achieving error-free communication, plateauing around a BER of 10^{-8} . $l = 5$ is significantly worse, with a BER plateau around 10^{-5} , while $l = 6$ falls between the two. This directly correlates with the n_{eff} splitting as a function of mode order, as might be expected, since this should be the dominant source of crosstalk in the 4 mode case (input coupling crosstalk due to polarization scrambling from the beam splitters expected to be -20dB or less in each case). The mode orders being similarly bad in the 12 mode case suggests that inter- l crosstalk from the MUX or DEMUX is the dominant source of error. However, the plateau region for $l = 5$ should always be higher in BER than those for $l = 6$ and $l = 7$, since the contribution to MPI from in-fiber crosstalk is higher.

For QPSK transmission, BERs are measured at three test wavelengths: 1550nm, 1556nm, and 1562nm, corresponding to the comb's shortest, center, and longest wavelength, respectively. Measured BERs with constellation diagrams inset are shown in

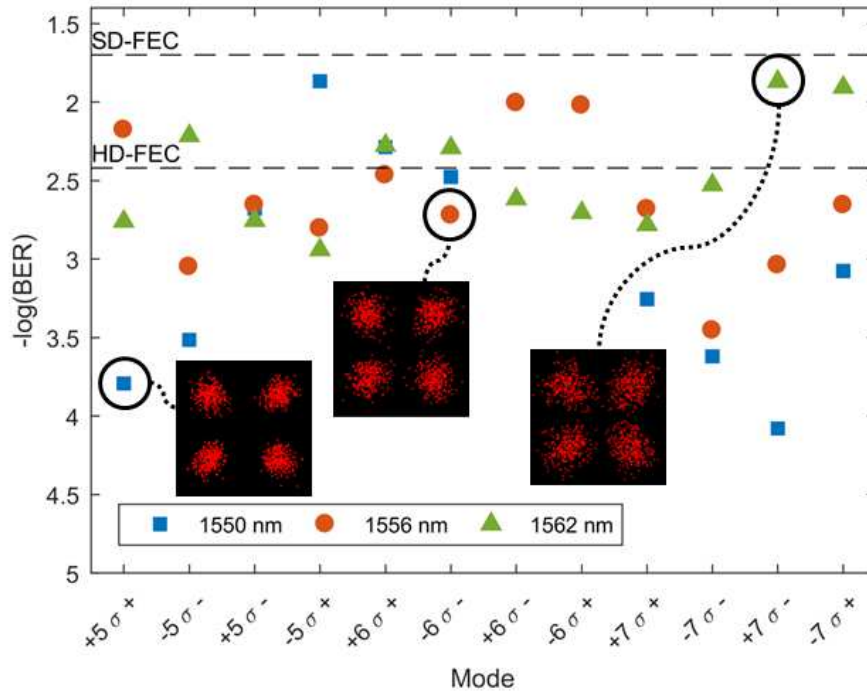


Figure 9-3: Measured BERs for all OAM modes at three test wavelengths while all OAM modes are simultaneously transmitted. All 34 measurements are below the SD-FEC threshold. Inset: example constellation diagrams.

Fig. 9-3. The measurements are performed with the fiber loaded with 60 WDM channels and all 12 modes. The $l = 6$ SOaa modes experience accidental degeneracy in the vicinity of 1550nm, as MPI corrupts the channel un-recoverably, meaning that only 10 modes are measured at this wavelength. All 34 measurements are below the SD-FEC limit, while 24 of the 34 are below HD-FEC. Pessimistically assuming that all 30 WDM channels between 1550nm and 1556nm support only 10 modes, while the 30 longer wavelength channels support 12, the demonstrated system has an aggregate capacity of 10.56 Tbit/s after the 20% SD-FEC overhead has been subtracted for

all modes. The demonstrated spectral efficiency is thus 7.04bit/s/Hz. Had we not been limited by accidental degeneracy, and with a comb source extending across the C-band, our system would have a potential capacity of 33.6 Tbit/s. The spectral efficiency would instead have been 7.7bit/s/Hz.

System performance is limited by intermodal crosstalk, which has two contributions: in-fiber mode coupling and misalignment or imperfections in the MUX or DEMUX. The *in-situ* transmission matrix of the fiber under test is shown in Fig. 9-4. Intermodal crosstalk is shown to vary between $-10.3dB$ and $-17.1dB$ depending on

Launched mode(s)	$\neq l$	-10.8	-10.3	-11.2	-10.6	-11.3	-11.8
	$\neq l, -l$	-15.1	-10.8	-12.8	-14.6	-14.8	-13.0
	$-l$	-12.8	-14.7	-16.0	-12.8	-14.0	-17.1
		+5	+6	+7	-5	-6	-7
		Detected mode (l)					

Figure 9-4: Measured transmission matrix for system under test. Each column corresponds to an output projection, and each row to a launch condition. Each column is normalized to 0dB in the desired mode with entries denoting crosstalk in dB. $-l$ indicates SOa to SOaa coupling, $\neq l, -l$ indicates contributions from other mode orders, and $\neq l$ indicates total crosstalk.

the mode. Each column corresponds to an output projection setting, while each row indicates which modes are launched and thus contribute to crosstalk at the receiver. The strongest parasitic contribution for $|l| = 5$ is in-fiber crosstalk between the $|l| = 5$ SOa and SOaa modes ($-12.8dB$) because this mode group has the smallest Δn_{eff} . $|l| = 6$ and $|l| = 7$ are mainly limited by crosstalk from different l orders. Since the splitting between the OAM mode of order l and that of order $l + 1$ is an order of magnitude or more larger than the splitting between modes of the same $|l|$, we expect

in-fiber mode coupling between adjacent OAM mode order to be negligible over 1km as in Chap. 8 (Maruyama et al., 2015). Thus, we conclude that such crosstalk is a direct result of imperfections in the free space MUX or DEMUX.

Over the course of these experiments, significant drifting of the MUX and DEMUX are observed as a function of time, limiting the number of measurements which could be made before the system required realignment. For a true transmission test, the fiber should not be perturbed or moved between channel measurements. This is the primary reason we measure only 3 wavelength channels as opposed to all 60; we do not expect to see significant variation among nearby wavelength channels. As part of the alignment, we observed the optical frequency comb transmitted through the system on an optical spectrum analyzer (OSA). We observe that the degenerate-mode-coupling unwinding performed by the polcons + q -plates does vary across the frequency comb. We are better able to control degenerate state mixing with $l = 7$ compared to $l = 5$, as might be expected from Chap. 7. However, we note that the experimental data shown here includes both endpoints of the comb, which should be the worst case(s), since the polcon is optimized for the whole comb.

Although all measured BERs are below the SD-FEC limit, there is no clear trend as to which are below HD-FEC as opposed to SD-FEC. Generally, the $l = 7$ modes are better than the $l = 5$ and $l = 6$ modes, as might be expected from the highest l mode and the mode order with the largest Δn_{eff} . However, two of the $l = 7$ modes at 1562nm are almost above the SD-FEC limit. On average, the $l = 6$ modes actually have *higher* BERs than the $l = 5$ modes, which may be a consequence of the fact that they have two nearest-neighbor OAM mode orders carrying data (as opposed to $l = 5$, which effectively has one neighbor, since $l = 4$ is not used as a data carrier). This may again be indicative of poor input coupling.

9.3 Limitations

In the process of performing these experiments, we were limited by the piezo stage which held the input end of the fiber under test, and potentially some of the mirrors on the input side as well. The fiber input coupling was observed to drift on the time scale of tens of minutes, which prevented intense characterization of WDM data transmission. In the lab at BU, we use a 6-axis stage from Thorlabs (MAX600 series), which we find to be time-stable on the order of half a day, (after the system has been realigned once or twice). The 3-axis piezo used for these experiments was insufficient for the time necessary to take data for 60 WDM channels \times 12 spatial modes = 720 data streams. This difficulty underscores the need for a stable, low-crosstalk MUX and DEMUX.

However, even presuming that the stage and mirrors had been perfectly stable, consider the case of an OAM mode like $l = 6$ which has two adjacent mode orders in l . In such a case, it can be difficult to achieve parasitic mode suppression, as evidenced by time of flight measurements, to better than -20 to -25dB. Assume -20dB as an order of magnitude approximation. Both $l = 7$ and $l = 5$ will leak into $l = 6$ at this level, meaning that the signal leaving the fiber in $l = 6$ will only be -17dB pure, from equal weight contributions at the -20dB level from both $l = 5$ and $l = 7$. We have no reason to assume that the mode selectivity at the fiber output, projecting back into SMF should be any purer. Thus, when we launch all modes simultaneously, we expect similar crosstalk from $l = 5$ and $l = 7$ into the $l = 6$ datastream at the point of coupling into SMF, for a purity of -14dB, assuming negligible differential loss. In addition, we expect in-fiber crosstalk between $l = 6$ SOa and SOaa to occur at the -15dB level or so, meaning that if we consider the $l = 6$ SOa mode, the total MPI is only on the order of -11.5 to -12dB if the MUX and DEMUX have selectivity -20dB. This number is of the same order of magnitude as those in the transmission matrix

in Fig. 9-4.

We have observed over the course of experiments that using the polcons to unwind degenerate state coupling may have some limited bandwidth. Suppose that this effect is due to in-fiber properties as opposed to input coupling imperfections, such as differential input coupling loss between degenerate states, a symmetry-breaking effect which could prevent the polcon + q -plate from spanning the higher order OAM Poincare sphere (Padgett and Courtial, 1999). In this case, the only solution is to use 2×2 MIMO to unwind channel-dependent degenerate state coupling. Although this adds to the complexity of the receiver, it also allows for a greater diversity of possible MUX devices, as the state-tuning functionality of the q -plate is no longer useful.

All of these considerations inform the design of a MUX or DEMUX device for OAM states. Such a device should be selective in OAM order by -25dB at absolute minimum to get all states below the hard FEC limit for QPSK (higher selectivity would be preferable as it might allow for the possible use of higher dimensional modulation formats, with more stringent SNR requirements). An alternative would be to design the OAM fibers with the strategy of using every other OAM order and leaving an "OAM guardband". However, given that weakly guided OAM states well split in n_{eff} themselves tend to come in bands or groups, this would constitute a significant design sacrifice. Our MUX must also be WDM-compatible, and either polarization insensitive, or designed to launch circularly polarized OAM beams. At current, there is no known technology this author is aware of which meets these requirements. Photonics lanterns (Huang et al., 2015) and evanescent fiber couplers (Pidishety et al., 2016) may become promising candidates, and the performance of multi-plate light converters (Morizur et al., 2010) with OAM modes remains to be validated.

Investigation of the WDM-compatibility of our system was limited by the EDFA gain bandwidth on the long wavelength side. On the short wavelength side, our

12 mode transmission was limited by accidental degeneracy, which is the poltergeist haunting the stability of high- l OAM modes in the weakly guided regime, especially since the vector splitting between OAM modes is a slowly varying function of wavelength. Although improvements in air core fiber fabrication have enabled long-length transmission of OAM modes in the presence of parasitic lower- l , $m = 2$ modes, their existence represents a serious challenge to fabrication of air core fibers on a large scale, and to developing fibers supporting a larger ensemble of OAM states. To truly scale capacity by an order of magnitude or more above what has already been shown, accessing the spin-orbit coupled regime will be necessary.

9.4 Summary

Data transmission utilizing MDM falls under two schools of thought - either the transmission fiber is designed such that mode coupling during transmission is minimized as with the OAM fibers discussed herein and with multicore fibers, or the fiber is designed such that the group indices of all modes of interest are matched, as in traditional MMF, and mode coupling is unwound using $N \times N$ MIMO DSP (Grüner-Nielsen et al., 2012).

Here we have demonstrated a system capable of a 6-fold improvement over previous OAM transmission results in overall capacity (10.56 Tbit/s compared to 1.6 Tbit/s) and a 4-fold improvement in spectral efficiency (7.04 bit/s/Hz compared to 1.6 bit/s/Hz) (Bozinovic et al., 2013). With the full C-band, and using an improved fiber with no accidental degeneracy, the improvements would be even more significant (33.6Tbit/s and 7.7bit/s/Hz). However, a more meaningful comparison for the long-term outlook of OAM in fibers is with SMF and other MIMO-free MDM strategies. The record result for transmission capacity in SMF, to my knowledge is 101.7 Tb/s, achieved by using both the C and L-bands, using orthogonal frequency divi-

sion multiplexing and 128-ary quadrature amplitude modulation (QAM) (Qian et al., 2012). This result had a spectral efficiency of 11 bit/s/Hz. Our system could surpass this spectral efficiency by increasing the modulation format to only 8-QAM, or by increasing the baud rate from 10GHz to 20GHz, which should be possible with a more intelligent MUX.

As of the writing of this document, the highest capacity achieved without higher order MIMO (i.e., results can include a conventional 2×2 MIMO for polarization division multiplexing (PDM)) is 2.15 Pb/s, using a 22 core single mode multi-core fiber, with 399 25GHz spaced WDM channels and 24.5 GBaud 64 QAM, achieving a spectral efficiency of 215.6 bits/s/Hz (Puttnam et al., 2015). This represents a significant increase over our results. Higher order modulation formats and an excessively large frequency comb aside, the fiber demonstrated by Puttnam et al contains 44 spatial modes (including polarization diversity), which is more than 3 times the number of modes demonstrated in this chapter.

However, this result, as with many of the early multi-core fiber results, does not utilize “space” in the sense that none of the spatial channels within the fiber overlap. The best case for total aggregate capacity should include both multi-core and multi-mode strategies (Soma et al., 2015; Igarashi et al., 2016). Indeed, the current record holder for spectral efficiency (as of ECOC 2016) employs both of these strategies (Soma et al., 2016). This will be discussed in more detail in Chap. 11. OAM modes remain the only known and verified way to access the design space of n_{eff} without the use of heavy MIMO processing.

Chapter 10

Extending the Number of States: Spin-Orbit Coupling Revisited

The motivation for moving from the Vortex Fiber to the air core fibers was to increase the number of stably supported OAM modes. As a consequence, high- l OAM modes were studied and found to have several desired properties. However, experiments to this point have focused on fibers which have an OAM guide-band, that is, a segment of OAM states that are supported with higher states cut-off and lower states unstable. This is fundamentally inefficient, as it discards large portions of the possible state space in n_{eff} . A fiber which stably supports a wide array of modes populating the available contrast in refractive index is the ultimate goal.

Outside of OAM modes, an alternative strategy for breaking modal degeneracy is to use elliptical core, or otherwise PM fibers (Wang and LaRochelle, 2015; Li et al., 2016). These fibers require moderate ellipticities (1.4) to achieve a modest number of modes (8), and work has not addressed the possibility of accidental degeneracy, which may prove problematic to scaling this class of fiber. However, in such fibers, all modal degeneracies are removed, eliminating the necessity for q -plates or 2×2 MIMO. This class of fibers is still in its infancy and may receive more attention in the coming years.

Given the discussions of Chap. 6, it seems that to reach the point of many (more than 20) well-supported states in a circularly symmetric fiber while avoiding accidental degeneracy with $m = 2$ modes, which limited the experiments in Chap. 8 and

Chap. 9, one will need to access the Spin-Orbit Coupled regime. To support more modes, a larger mode volume is needed. To break the ‘LP’ degeneracy, stronger confinement is needed (Fig. 10-1) In this chapter, we excite SOC Angular Momentum

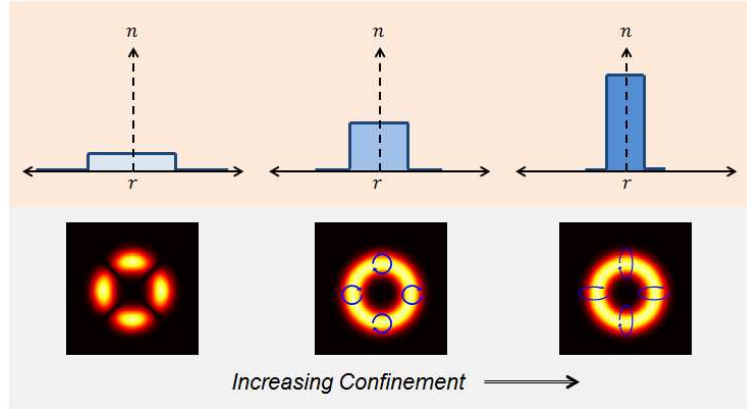


Figure 10-1: Increasing waveguide confinement (index step) leads to OAM stability, but eventually to SOC. However, to support a large number of stable vector modes, SOC will almost definitely be encountered

modes by using a combination of a q -plate and an SLM. Excitation purity and intermodal crosstalk will be measured by time of flight and output projection into all guided fiber modes. We find that we can controllably excite and stably transmit 24 modes over 10m of gen2 fiber, an improvement in mode count by a factor of 2 over the gen4 fibers. This is the first demonstration of controlled excitation of such SOC fiber modes, to our knowledge, and the first time that such a large stable mode count has been demonstrated. The spin-to-orbit coupling effect observed in these fibers is similar to that found in nanofibers and high NA focusing in free space (Bliokh et al., 2015; Shahraam Afshar et al., 2012). However, we also find that the fibers in gen2 are incredibly lossy, potentially due both to the larger air core and a strong water absorption, and that intermodal $\Delta l = 1$ coupling between adjacent mode orders is much stronger than expected. This points towards future work with these fibers, both in reducing the transmission loss and understanding the origin of the increased

intermodal coupling.

10.1 Spin-Orbit Coupled Mode Excitation

As discussed briefly in Chap. 5, standard methods of exciting OAM states will not excite pure SOC modes. Insight into exciting these modes can be gained by returning to Eq. (2.12). We have seen in simulations that the shapes of the radial and azimuthal components of the electric field, ψ_r and ψ_ϕ , are nearly identical. We see the effect of the SOC as a difference in peak value, rather than shape of either field, in contrast to higher order modes in standard ‘top-hat’ fibers where the field envelope of the radial and azimuthal components of the mode can differ significantly (Thomas et al., 2011; Israelsen et al., 2014; Rishøj et al., 2016). We can thus make the approximation that $B_{j+1} \approx B_{j-1} \equiv F_j(r)$.

There are two intelligent choices for mode designation schemes. We could denote the modes according to the absolute value of their total angular momentum, j , and its sign. For instance:

$$AV_j^+ = N_j e^{ij\phi} F_j(r) [\gamma_j^V \hat{\sigma}^+ e^{-i\phi} + \alpha_j^V \hat{\sigma}^- e^{i\phi}] e^{i\beta_{V,j}z} \quad (10.1a)$$

$$AV_j^- = N_j e^{-ij\phi} F_j(r) [\alpha_j^V \hat{\sigma}^+ e^{-i\phi} + \gamma_j^V \hat{\sigma}^- e^{i\phi}] e^{i\beta_{V,j}z} \quad (10.1b)$$

$$AW_j^+ = N_j e^{ij\phi} F_j(r) [\gamma_j^W \hat{\sigma}^+ e^{-i\phi} + \alpha_j^W \hat{\sigma}^- e^{i\phi}] e^{i\beta_{W,j}z} \quad (10.1c)$$

$$AW_j^- = N_j e^{-ij\phi} F_j(r) [\alpha_j^W \hat{\sigma}^+ e^{-i\phi} + \gamma_j^W \hat{\sigma}^- e^{i\phi}] e^{i\beta_{W,j}z} \quad (10.1d)$$

Where we use V and W in analogy to the weakly guided OAM modes, N is a normalization factor, and F_j does not depend on whether the mode is SOa or SOaa, and radial subscripts are dropped as the fiber of interest support only $m = 1$. This way of writing the modes has the advantage of underscoring the underlying physics of the the SOC modes, but contains an unnecessary number of free variables, since α_j^V and α_j^W are related by Eq. (2.13).

Alternatively, we could denote these SOC modes as $E_{l,A}$ and $E_{l,AA}$:

$$E_{l,a} = N_{l+1}F_{l+1}(r) [A_{l+1}\hat{\sigma}^+ e^{il\phi} + B_{l+1}\hat{\sigma}^- e^{i(l+2)\phi}] e^{i\beta_{l,a}z} \quad (10.2a)$$

$$E_{-l,a} = N_{l+1}F_{l+1}(r) [A_{l+1}\hat{\sigma}^- e^{-il\phi} + B_{l+1}\hat{\sigma}^+ e^{-i(l+2)\phi}] e^{i\beta_{l,a}z} \quad (10.2b)$$

$$E_{l,aa} = N_{l-1}F_{l-1}(r) [A_{l-1}\hat{\sigma}^- e^{il\phi} - B_{l-1}\hat{\sigma}^+ e^{i(l-2)\phi}] e^{i\beta_{l,aa}z} \quad (10.2c)$$

$$E_{-l,aa} = N_{l-1}F_{l-1}(r) [A_{l-1}\hat{\sigma}^+ e^{-il\phi} - B_{l-1}\hat{\sigma}^- e^{-i(l-2)\phi}] e^{i\beta_{l,aa}z} \quad (10.2d)$$

Here l is the SOC mode's dominant component, where $|A_j| \gg |B_j|$, and a and aa are short for “aligned” and “anti-aligned” and are kept in analogy to the weakly guiding OAM modes, since these modes are still *predominantly* spin-orbit aligned or anti-aligned. The negative sign in Eq. (10.2c) and Eq. (10.2d) is necessary to ensure A and B are real, as discussed in Sec. 2.1.2. Here, $A_j \neq B_j$; the two coefficients being equal implies that they are *TE* or *TM* which is impossible for a finite-cladding fiber (Snyder and Love, 1983). The advantage of the second form is its similarity to the weakly guided OAM states as well as the convenience of fewer parameters. The disadvantage is in mode order bookkeeping, as Eq. (10.2a) has three different subscripts to keep track of. We use the form in Eq. (10.2a) - Eq. (10.2d) for the remainder of the chapter. We can calculate the expectation value of the OAM-per-photon for a spin-orbit aligned mode as:

$$\langle l \rangle = A_{l+1}^2 \times l + B_{l+1}^2 \times (l + 2) \quad (10.3)$$

And similarly for the anti-aligned modes. The degree to which the modes are coupled is directly indicated by the ratio of A to B . In the weak guidance approximation, $B_j = 0 \forall j$, and $E_{l,a}$ and $E_{l,aa}$ correspond exactly to OAM states.

Most of the methods described in Chap. 5 rely on making a single OAM state with uniform polarization. For instance, an SLM and QWP can create $l = 5$, $\hat{\sigma}^+$, which is sufficient to excite the $l = 5$ mode in gen3 or gen4. However, in this case, such

excitation will excite both $E_{5,a}$ and $E_{3,aa}$ to varying degrees, and there is no way for a single uniformly polarized OAM state to excite only one mode in the SOC regime. Two SLMs which independently tailor two OAM beams, which are then stitched together with a PBS before being passed through a QWP could in principle be used to tailor these SOC states (Maurer et al., 2007), but this would require high-precision path-length matching.

Instead, we utilize the spin-to-orbit conversion effect of q -plates. The basic experimental system is sketched in Fig. 10.2. To excite SOC modes, an SLM creates a

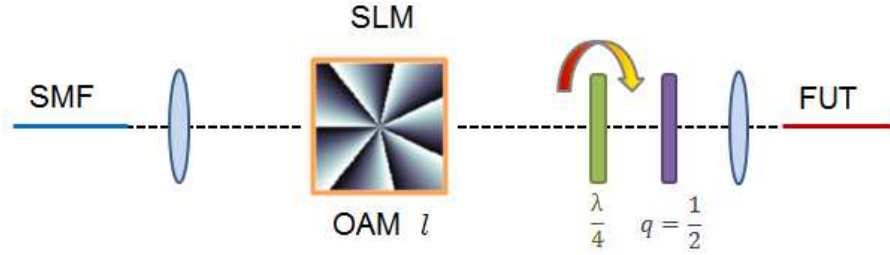


Figure 10.2: Proposed coupling system for exciting SOC modes in gen2 fiber

free-space OAM state of topological charge l which is linearly polarized. This beam is sent through a QWP at angle θ_0 with respect to the incident beam's polarization, and is then sent through a $q = 1/2$ plate. The free space beam immediately after passing through the q -plate can be written as (see Eq. (5.14)):

$$\Psi = NG_l(r) \left\{ \hat{\sigma}^+ e^{i(l-1)\phi} e^{i(\alpha_0 + \theta_0)} [\cos(\theta_0) + \sin(\theta_0)] + \hat{\sigma}^- e^{i(l+1)\phi} e^{-i(\alpha_0 + \theta_0)} [\cos(\theta_0) - \sin(\theta_0)] \right\} \quad (10.4)$$

i.e.

$$\Psi = NG_l(r) \left\{ \xi \hat{\sigma}^+ e^{i(l-1)\phi} + \eta \hat{\sigma}^- e^{i(l+1)\phi} \right\} \quad (10.5)$$

for

$$\xi = e^{i(\alpha_0 + \theta_0)} [\cos(\theta_0) + \sin(\theta_0)] \quad (10.6a)$$

$$\eta = e^{-i(\alpha_0 + \theta_0)} [\cos(\theta_0) - \sin(\theta_0)] \quad (10.6b)$$

The angle θ_0 controls the weights of the $l - 1$ and $l + 1$ components in the free space beam, but it also induces a phase difference between the two components, in addition to the phase shift imparted by the q -plate if it is mounted at a non-zero angle with respect to the horizontal ($\alpha_0 \neq 0$). The input coupling crosstalk suppression between two modes of the same j will be determined entirely by the ability to match ξ and η to a given A, B . The ratio of power coupled into an anti-aligned mode of a given j , compared to the power coupled into an aligned mode of the same j , is:

$$\frac{P_{aa,j}}{P_{a,j}} = \left| \frac{A_j \xi - B_j \eta}{A_j \eta + B_j \xi} \right|^2 \quad (10.7)$$

Any dephasing between ξ and η clearly could prevent the ratio in Eq. (10.7) from going to zero (or infinity). We solve this issue by realizing the $q = 1/2$ plate by using a $q = -1/2$ plate followed by a half-wave plate. The half-wave plate induces an angle-dependent phase shift between $\hat{\sigma}^-$ and $\hat{\sigma}^+$ which can be used to make ξ and η purely real. However, we note that the angle of the HWP is also a function of mode order, and must be carefully adjusted *in-situ*.

This phase-compensation could also be performed by rotating the q -plate, although this would require centering the q -plate perfectly on the center of the rotation mount, which is practically challenging. We also note that phase compensation could be required for other reasons:

- There is no guarantee that the fiber under test will be exactly in the focal plane of the input coupling lens. Thus, the two free space OAM modes may experience different Guoy phases as they are focused by the coupling lens (Saleh and Teich,

2007). Although the OAM superposition created in Fig. 10.2 is a propagating mode of the fiber under test, it is *not* a propagating mode of free space.

- As the two different free space OAM states diffract at different speeds, they may encounter different radial positions on the coupling lens, and thus pick up slightly different phases due to the different glass thickness. Moreover, the quality of the lens (aberrations or lack thereof) will change as a function of radius, with Seidel aberrations tending to be worse near the lens edge (Wyant and Creath, 1992).

A possible additional complication is that the two constituent beams will originally have identical ring-shapes, but this may not be true in the fiber plane, i.e., if the coupling lens Fourier Transforms the free space beam, the two states will map to slightly different sizes, thus changing their relative weights after input coupling. This can be compensated with QWP setting. The best method for alignment is thus *in-situ* characterization, preferably with time of flight.

The radial envelope, G_j , may be controlled with a lens or axicon on the SLM. Using a combination of SLM and q -plates the beam leaving the q -plate can be a radius of size scaled to match the fiber modes, and of relative weight and sign between the OAM superposition controlled by rotating a QWP and a HWP.

10.2 Experimental Results

We have 4 fibers in gen2 which should support a bevy of stable modes. For reasons discussed in Sec. 10.3 gen2-1 was the most successful fiber, and results presented in this section are from gen2-1.

The details of gen2-1 are reviewed in Fig. 10.3. Modes below dominant $l = 3$ have nearest neighbors which are different mode orders, due to the strong vector splitting. Modes of order $l = 4$ and higher have nearest neighbors of the same dominant $|l|$.

Lower order modes, due to higher overlap with the air glass interface, more strongly display the spin-orbit coupling effect, as indicated in Fig. 10-3 (d). For a given dominant $|l|$, the SOaa mode features stronger SOC than the SOa mode, due to being of a lower vector order.

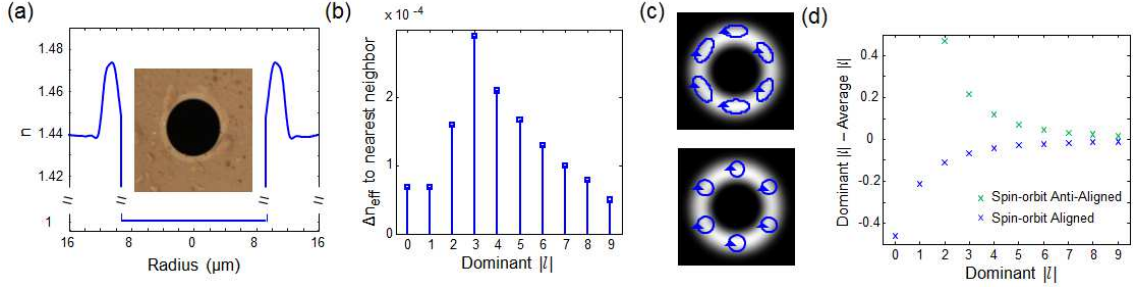


Figure 10-3: (a) Index profile and fiber end facet image (inset) (b) Δn_{eff} between $E_{l,a}$ and its nearest neighbor (c) Polarization distributions for spin-orbit coupled $E_{4,aa}$ (top) and, closer to integer- l , $E_{9,a}$ (bottom) (d) Simulated difference between dominant $|l|$ and ensemble average l , quantifying the spin-orbit coupling effect

First, we attempt coupling without a q -plate, which should excite a combination of modes of the same j . Using the system in Fig. 10-4, we excite modes in gen2 using an SLM and QWP only and measure the time of flight response after 10m, such that contributions from in-fiber mode coupling should be minimized. $E_{6,aa}$ is shown in Fig. 10-4 (b) as a representative example. A strong parasitic peak at -11.6dB relative to the desired mode appears in the time bin corresponding to $E_{4,a}$ (i.e. the SOa mode of the same j which shares an OAM component). When the fiber mode is imaged, we observe power in both $\hat{\sigma}^-$ and $\hat{\sigma}^+$ polarization bins, although the power in $\hat{\sigma}^+$ is considerably weaker than that in $\hat{\sigma}^-$.

We quantitatively study the level of SOC in gen2-1 by performing output projection measurements on one of each of the degenerate mode sets, as indicated in Fig. 10-5. Although only one SLM is illustrated schematically, we use two in series to mitigate differential input coupling loss across all mode orders, due to the large set

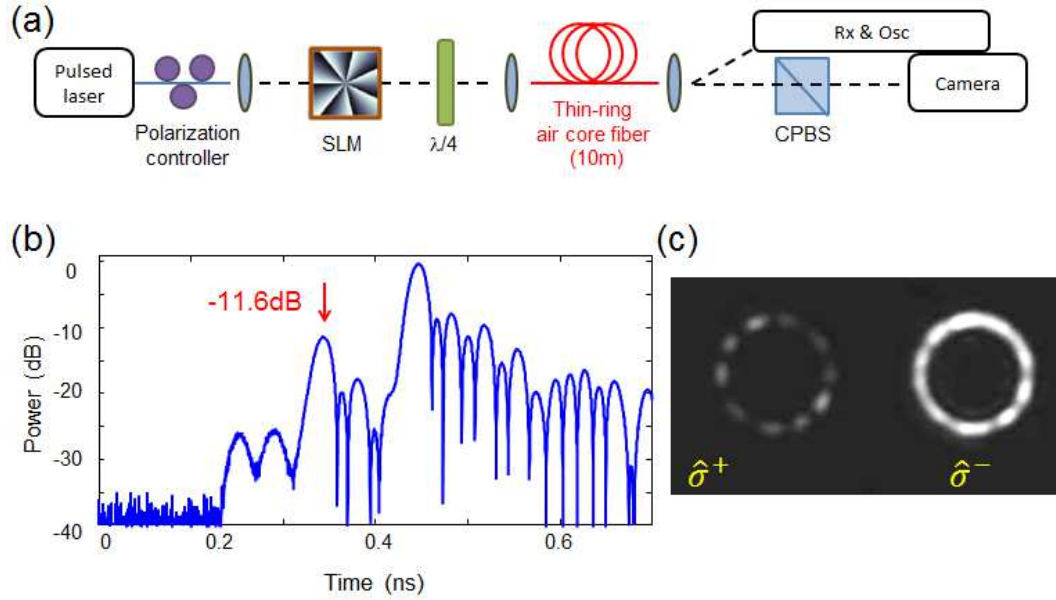


Figure 10-4: (a) Excitation and characterization system for “standard” OAM modes in the gen2 fibers (b) time of flight response for $E_{6,aa}$ (c) Output mode image projected into RCP and LCP

of l guided by the fiber, and the aspect ratio of the gen2-1 fiber. The fiber features a thin ($3\mu\text{m}$) ring far away ($9\mu\text{m}$) from the geometric center of the fiber. Both SLMs display a lens and an axicon phase, in addition to a helical phase. A similar system was proposed by (Vaity et al., 2014) to excite modes in an air core fiber, although the authors of that paper never quantitatively determined mode purity. Additionally, we find that we can increase the coupling efficiency with the choice of helical phases. For instance, in attempting to create $l = 6$ at the fiber facet, we can choose to have the two SLMs display, in series, $l = 1$ and $l = 5$, $l = 2$ and $l = 4$, or $l = 3$ and $l = 3$. This choice impacts the radial overlap at the fiber end facet slightly, and can be optimized for coupling efficiency.

The input coupling to the fiber under test is optimized using time of flight to extinguish parasitic peaks in the nearest-neighbor mode orders. It is observed that the $\Delta l = 2$ peak, as in Fig. 10-4 (b), cannot be minimized by changing fiber position. The output coupling is aligned first by power into the SMF, and optimized by observing the

time of flight spectrum into the SMF. The fiber input is then changed to an adjacent mode order, such that the input and output are set for different mode orders, and the signal corresponding to power in the undesired mode which was transmitted through the fiber under test is minimized. For each input state, power is measured in all fiber modes using all possible projection settings. The degenerate states are then summed together in power to study relative powers in different mode groups. The input is then varied to excite one mode from each of the 2-fold degenerate modal subspaces, and the fiber transmission matrix is thus mapped. The results are shown in Fig. 10-5 (b) and (c). The mode orders with $l \leq 3$ strongly couple within the test fiber because

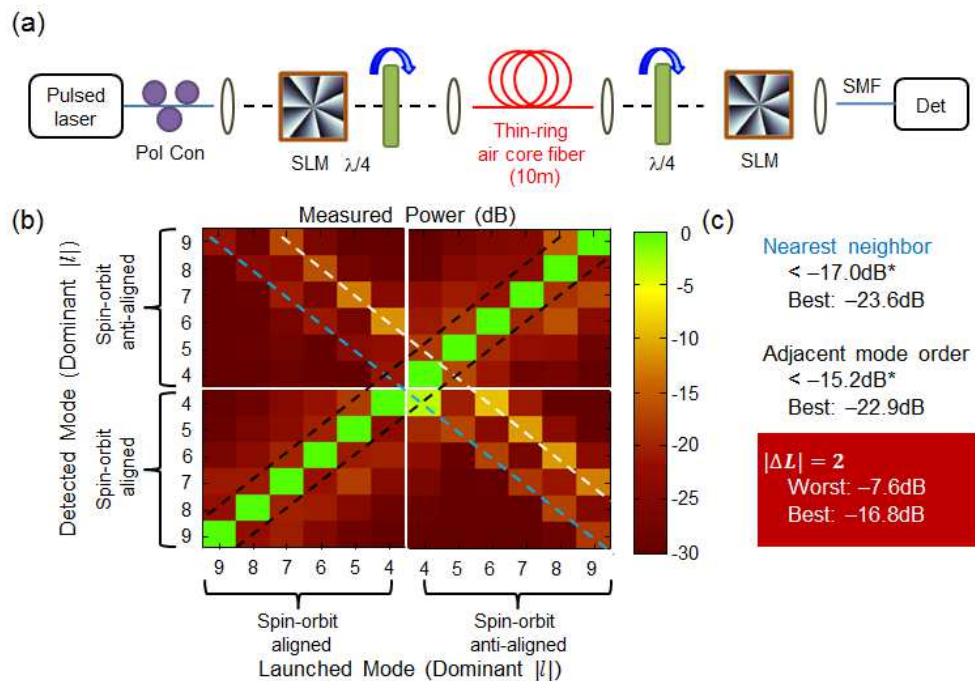


Figure 10-5: (a) Experimental setup for measuring the extent of the SOC effect by output projection (b) Output projection measurement - each column is independently normalized to itself. Blue negative slope diagonal indicates coupling to in-fiber nearest neighbor, black off-diagonals indicate coupling to nearest different mode order, which could be due to imperfect mode excitation or in fiber coupling, and the white, negative slope off-diagonal indicates parasitic input coupling due to the SOC effect (c) Summary of the performance along the three trend lines from (b)

the difference in effective index between mode orders (which could be coupled by bend perturbations) is small, and these mode orders are not shown. The in-fiber nearest neighbors are suppressed to 17dB or better, indicating that in-fiber mode coupling between nearly degenerate vector modes is suppressed, as desired. There is an exceptional measurement for $E_{4,aa}$ which we believe to be due to alignment error in the system, confirmed by later measurements. Adjacent mode orders are suppressed to at least 15dB. However, coupling between mode orders separated by $\Delta l = 2$, those mode orders connected by SOC, are only suppressed by -7.6dB in the worst case. Although some of the higher order states are better, with up to about -17dB of suppression, it is critical to note that this is a fundamental effect which will occur in these fibers, and which will intrinsically limit mode purity and thereby data rate/system performance if the source of error (input coupling) is not addressed.

We repeat the measurement with the system including q -plates for SOC mode excitation as discussed in Sec. 10.1. The mode excitation system is shown in Fig. 10-6. The SLMs are chosen for a given mode order, and the lens/axicon parameters optimized for maximum coupling. The QWP and HWP are aligned *in-situ*, using the time of flight response of the test fiber to optimize for mode purity. The $\Delta l = 2$ parasitic peak, as in Fig. 10-4, is here suppressed below 20dB. At the output, the fiber is imaged with an axicon, which maps diffraction angles to different radial positions in the far field. Since the fiber mode is made up of two different free space OAM modes of different order, and thus different diffraction angle, they are mapped onto rings of different size in the far field, as shown experimentally in Fig. 10-6 (c).

As before, we map out the fiber transmission matrix using output projection. The system is depicted in Fig. 10-7. Light from a pulsed laser at 1550nm with pulse width appx 5ps is passed through the SLM and q -plate combination to create the correct combination of free space OAM states to match the SOC modes in the fiber under

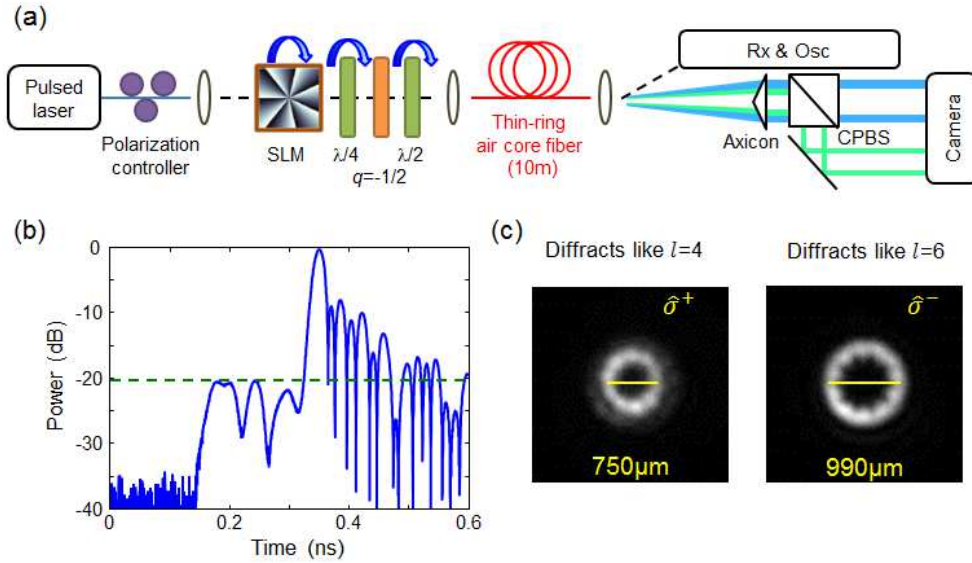


Figure 10.6: (a) Experimental setup for exciting SOC modes and analyzing beam content (b) Time of flight response for $E_{6,aa}$; note the lack of content in $E_{4,a}$. (c) Free space images of $E_{6,aa}$ after being passed through a CPBS and imaged with an axicon. The laser power has been changed between images to avoid camera saturation

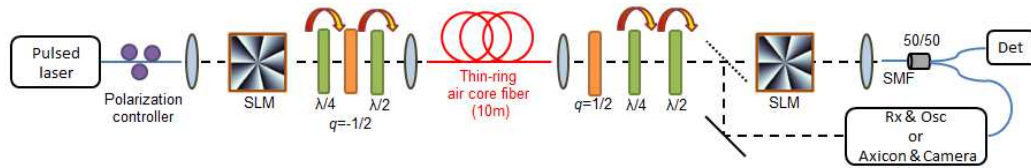


Figure 10.7: Experimental apparatus for SOC mode output projection experiment

test. The input QWP and HWP are aligned using time of flight as feedback, in order to suppress undesired parasitic peaks. Similarly, the QWP and HWP at the output are aligned to suppress undesired peaks in the detection (i.e. peaks which are identifiable as modes other than the mode we are attempting to detect). This is achieved via performing time of flight on the SMF output. For each mode order launched, the axicon and lens parameters are optimized on the SLMs at input and output. It is observed that changing the parameters alters the input coupling by 1-2 dB between $l = 4$ and $l = 9$. Significant changes in input coupling loss appear for

$l \leq 2$.

We again map out the fiber transmission matrix by launching one state from each degenerate subspace, and measuring output projections into all guided modes of interest in the fiber. The modes are propagated 10m in fiber, while the fiber is laid out in loops of radius appx 0.25m. The results are shown in Fig. 10-8. Unlike Fig. 10-5

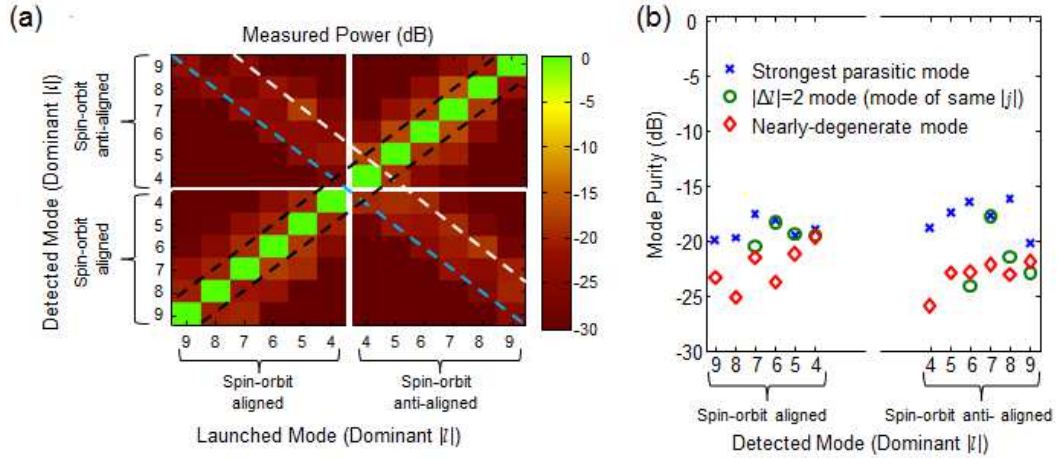


Figure 10-8: (a) Transmission matrix using SLMs and qplates to excite SOC fiber modes (b) Numerical results corresponding to the diagonals and off-diagonals of interest in (a)

which shows a strong off-diagonal due to SOC $\Delta l = 2$ content, the transmission matrix in Fig. 10-8 is predominantly diagonal, with a plot of the subset of mode groups of interest in Fig. 10-8 (b). Each desired mode of interest is separated from its in-fiber nearest neighbors by $> 19.7 \pm 0.5dB$, and all modes are separated from other modes of the same j by $> 17.6 \pm 0.5dB$, with an average suppression of 20.6dB. The strongest parasitic mode in each case is typically a mode of $\Delta l = 1$, arising from imperfect coupling at the input/output. We expect the system to be very alignment sensitive, as the incident beam will need to strike 5 optical elements at their centers of symmetry: SLM1, SLM2, the q -plate, the coupling lens, and the fiber itself. We have seen in experiments with q -plates that if a beam strikes the short-focal length aspheric lenses typically used in these experiments off-center, polarization-dependent

crosstalk can result. Similarly, at the output, the beam needs to strike 4 optical elements at their center of symmetry: the q -plate, the SLM, the output coupling lens, and the SMF. There are thus several sources of possible $\Delta l = 1$ in both the input and output coupling systems. Distributed coupling along the fiber length could also result in $\Delta l = 1$ mode content; however, at fiber lengths of 10m, we expect this coupling to be smaller than 20dB.

We have thus demonstrated that the SOC phenomenon can be overcome by intelligent mode excitation; moreover, we do not see strong distributed mode coupling between SOC modes of the same j despite the fact that the modes share an OAM component. Likely this coupling is weak because the modes are strongly dephased, being different by two scalar mode orders. This implies that the SOC modes can indeed be used as a possible basis for data transmission or fiber devices. The fiber demonstrated supports 24 stable modes, a $12\times$ increase in capacity over standard SMF. This design class of fiber has two novel features: (1) it reveals a novel eigenbasis of fiber modes shown to be stable over device lengths and which have no counterparts in free space or weakly guiding fibers and (2) unlike previous OAM fiber designs in which long-length propagation has been demonstrated, the elimination of higher radial orders actually increases fabrication tolerances, especially for maintaining air hole size during draw. We expect that even at lengths of 10m, such fibers may find application in low differential modal gain amplifiers (Jung et al., 2016), or intermodal nonlinear optics (Demas et al., 2015b).

10.3 Limitations

There are two limitations to the measurements in Sec. 10.2, which prevented transmission at longer lengths, and transmission of more modes.

The first limitation is the high loss of the fiber under test. Loss was measured by

cutback from 1100m to a few m, and found to be between 18.3 and 18.6dB/km for $l = 4$ through $l = 8$, and 20.6dB/km for $l = 9$. This loss could have three contributors: scattering off of the air glass interface due to surface roughness, absorption due to water in the fiber (Keiser, 2011), and scattering due to the high-index ring to glass cladding interface (Lines, 1984). We can detect loss due to the presence of water by performing cutback using a wide bandwidth source. These data are shown in Fig. 10-9. Compared with SMF, all of the fabricated air core fibers have a noticeable

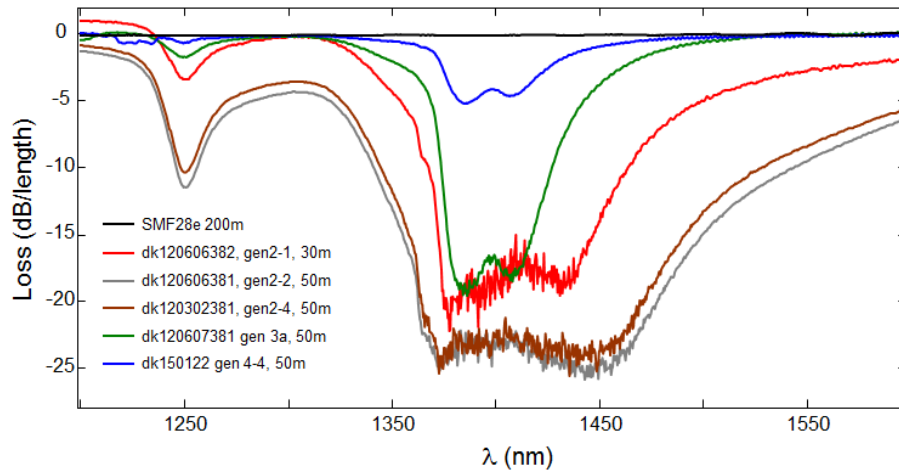


Figure 10-9: Transmission loss for several different generations of air core fiber and SMF. Sample length specified in the legend.

loss around 1380nm due to an OH absorption bond (Stone and Walrafen, 1982). This is likely due to a stage in the manufacturing process where the preform is appended to a glass rod to aid in the draw process, but the two are fused together in the presence of hydrogen and oxygen, such that water can impregnate the preform. The fusing was performed in the presence of nitrogen for the gen4 fiber, and in addition the preform was purged before the draw, resulting in a significantly reduced water concentration. However, there is also the possibility that water diffuses into the fiber from the end facet as the fiber is exposed to the laboratory atmosphere, which would be worse for the gen2 fibers, which have larger air holes.

We may expect interfacial scattering due to surface roughness to be worse for gen2 compared with gen3 and gen4, because the surface area of the inside of the air hole is significantly larger. We expect that interfacial scattering between the guiding ring and the cladding to be commensurate with that in the earlier fibers, which we know can be as low as 0.8dB/km (assuming that the *entirety* of loss in gen4 is due to this scattering).

One future experiment to be performed is to place the gen2 fiber in an oven to purge it of its parasitic water concentration, before repeating cutback and transmission measurements. This would distinguish between contributions to its loss from water and those from interfacial scattering, which we do not expect to be changed due to exposure to heating at a few hundred degrees.

The second limitation encountered in these experiments is mode coupling between mode orders separated by $\Delta l = 1$. From previous fibers, we could expect that the

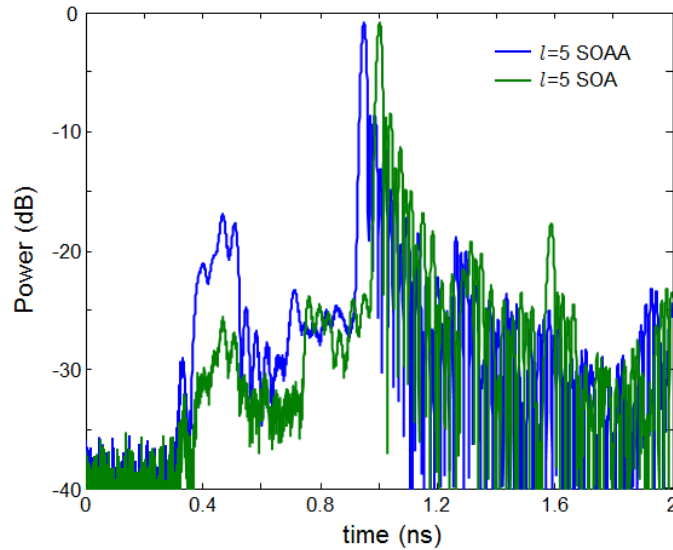


Figure 10-10: Time of flight response for $E_{5,a}$ and $E_{5,aa}$ in after 50m of gen2-1. Excitation is performed without a q-plate, thus the parasitic $\Delta l = 2$ content

$l = 0$ through perhaps $l = 2$ mode orders would be badly corrupted by such coupling

because their vector splittings were large relative to the scalar mode order splittings. However, in experiments using longer lengths of gen2 fibers, $\Delta l = 1$ cross coupling was found to be much stronger than anticipated. For instance, consider the time of flight responses for the $|l| = 5$ modes in Fig. 10-10 over 50m of gen2-1 (excited without a q -plate, resulting in $\Delta l = 2$ content). The shelf at approximately -25dB between the dominant peaks and a time of 0.8ns represents distributed coupling in the fiber to $|l| = 4$, while the next shelf represents coupling either secondary coupling from $l = 4$ to $l = 3$, or direct coupling from $l = 5$ to $l = 3$. The blob between 0.4 and 0.6ns contains mode coupling among the $l = 0$ through $l = 3$ modes. When integrated, the mode coupling between $l = 5$ and $l = 4$ is only -13dB suppressed from that in the main peak. Such coupling is weaker for higher orders since Δn_{eff} between mode orders increases as l increases. It is worse for comparable mode orders for the gen2-2 and gen2-3 fibers, as the ring volume is larger, thus supporting more modes and compressing them in n_{eff} . Moreover, the lower order modes show a continuous response in time domain up to $l = 4$, indicative of complete mode coupling. Gen2-4 shows worse performance for the same mode orders, likely because, although the n_{eff} performance is nearly identical to gen2-1, the fiber is OD105 instead of OD125, thus making it less resilient to bend perturbations. The measured coupling between adjacent mode orders, for the SOaa modes, is shown in Table 10.1 in dB scale, for a sample length of 50m. We cannot measure the coupling between $l = 5$ and $l = 4$

Table 10.1: Inter-mode-order coupling in gen2 fibers over 50m (in dB).

Fiber	$l = 9$ to $l = 8$	8 to 7	7 to 6	6 to 5	5 to 4
gen2-1	-15	-15	-12.8	-14.3	-13.1
gen2-3	-12	-11.2	-12	-10.3	??
gen2-4	-12.1	-11.9	-10.1	-9	-7.2

in gen2-3 due to the fact that $l = 4$ is strongly coupled in a distributed fashion to lower order modes. Switching from 50m to 10m, we expect the in-fiber crosstalk to decrease by about 7dB. (Thus, our assertion that the mode purity numbers specified in Sec. 10.2 are likely due to imperfect input coupling.)

However, the mode coupling is not solely a function of n_{eff} . The n_{eff} difference between $l = 8$ and $l = 9$ in gen2-1 is 3×10^{-3} . We may make a direct comparison to the $l = 3$ and $l = 2$ modes in the gen3a fiber, which are separated by 3.1×10^{-3} in n_{eff} . Both the gen2 and gen3 fibers are hard coated with $OD \approx 125\mu m$, and have nominally the same mechanical properties. Although $l = 3$ and $l = 2$ are not stable in gen3, we should be able to directly compare the mode coupling between adjacent mode orders. The time of flight response, shown in Fig. 10-11 is drastically different,

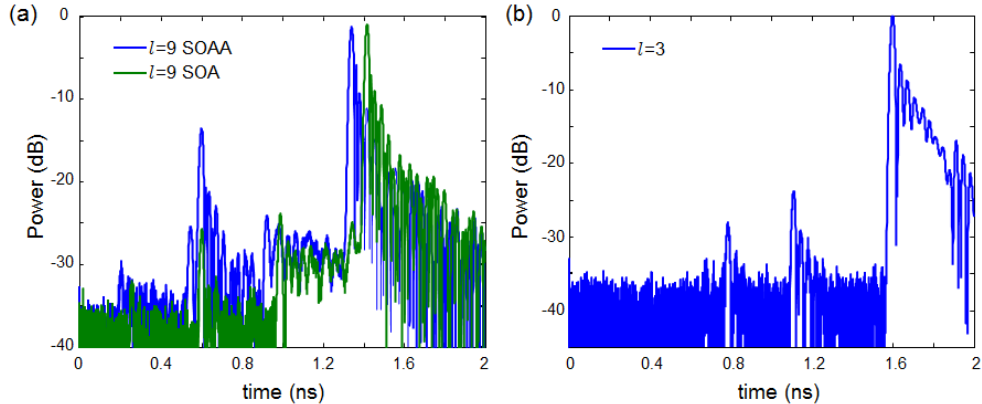


Figure 10-11: (a) Time domain response when $E_{9,aa}$ and $E_{9,a}$ are launched and transmitted through 50m of gen2-1 (b) time domain response when $l = 3$ is launched and transmitted through 50m of gen3a

with the $l = 8$ and $l = 9$ modes showing -15dB of distributed coupling between them, while no mode coupling between $l = 3$ and $l = 2$ in gen3a is visible above the noise floor of the oscilloscope, with a worst case crosstalk of approximately -25dB.

This behavior is not (immediately) explainable by perturbation theory, which indicates that, to first order, the coupling induced by a bend between modes 1 and 2,

separated in l by $\Delta l = 1$, from Eq. (3.12) and Eq. (3.13) should be proportional to:

$$\kappa_{1,2} \propto \int F_1(r)F_2(r)J_1(Kr\theta)rdrd\phi \quad (10.8)$$

Where F_j are the mode envelopes, K is a constant depending on material parameters and the wavelength of light, which should not be substantially different for gen2 and gen3, and θ is the bend angle. Although J_1 is oscillatory, for small bend angles, such as a fiber wrapped around a 16cm diameter spool coated in foam, we can approximate that θ is small, and thus Eq. (10.8) approximately reduces to:

$$\kappa_{1,2} \propto \theta \int r \times F_1(r)F_2(r)rdrd\phi \quad (10.9)$$

That is, the coupling is proportional to the radial center of mass of the modes. Approximating using the center of the ring guiding regions, this radial center of mass should be approximately $5.5\mu m$ for gen3a and $10.5\mu m$ for gen2-1, an increase by a factor of 2. Thus, we might reasonably expect that bend-induced coupling between adjacent mode orders to be about 3dB worse in gen2-1. Instead, it is worse by at least an order of magnitude.

Comparisons with gen2-2 and gen2-3 do not enable additional information, as both the ring radius and Δn_{eff} have changed. One possibility for the higher-than-expected mode coupling is that the fiber preform itself was misshapen and slightly asymmetric, resulting in higher intrinsic coupling. However, the only way of testing this is with a new fiber. Understanding this mode coupling is critical, not only because it limits the length we can propagate SOC states in gen2-1, but also because it will inform the ultimate limit to the number of modes supported by the thin-ring class of fibers.

10.4 Future Fiber Design Considerations

One of the questions this thesis seeks to answer is: what is the ultimate limitation in the number of states supportable by the class of air core fibers? We specifically consider only one guiding region (without invoking multiple ring-cores, etc), although if the ring guiding region could be replicated in a multi-core fashion, it would increase the transmission capacity linearly with the number of cores. We have demonstrated propagation of 24 SOC states, stable over 10m. Previous work has claimed 36 states over very short lengths and without quantified mode purities (Brunet et al., 2014b). Likely, the fiber in the work by Brunet *et. al.* has modal characteristics similar to the fiber we have shown, given the similarity in refractive index structure.

One could imagine a very thin ring waveguide, with sharp enough index gradients to achieve a $\Delta n_{eff} > 10^{-4}$ for a multitude of states, perhaps with even more states than gen2 by increasing the mode volume of the guiding ring. However, the ultimate limitation will be provided by the refractive index contrast of the fiber. As all of the guided modes have to fall in n_{eff} between the refractive index of the guiding ring and the refractive index of the cladding, having more guided mode orders implies that the mode orders will fall closer together in n_{eff} if the index contrast is unchanged. Supposing that we are only interested in device length fibers (10m) and that the results from gen2-1 are not indicative of an issue with the preform, but, for reasons as-yet not understood, imply that $\Delta l = 1$ coupling is stronger than anticipated in thin ring fibers. Thus we need a separation of approximately 3×10^{-3} between mode orders for stable modes. A refractive index step of $\Delta n = 50 \times 10^{-3}$ is technically challenging but feasible with the MCVD process. The best case, which itself may not be possible, is for each mode order to be equally spaced in n_{eff} , which would allow for 16 stable mode orders, or 62 stable modes, including TE, TM, and the two $l = 0$ OAM modes. We have seen, repeatedly, that the lower l mode orders tend to

bunch together, and stronger confinement will lead to more near-degeneracies due to stronger polarization splitting, meaning that the limit for a thin ring fiber made in an MCVD process is likely smaller; we conjecture that the limit is closer to 40 stable modes.

Increasing the number of modes beyond this would require increasing the refractive index contrast. One method would be to draw the fiber from other glasses. For instance, SF57 (Dense flint glass from Schott) can achieve a refractive index of approximately 1.8 at 1550nm (see Schott glass catalog; or refractiveindex.info). However, the loss is also substantial, at around 30% /m. Alternatively, an air cladding could be added, as in photonic crystal fiber (Wadsworth et al., 2003). One such fiber supporting 26 modes has been proposed (Hu et al., 2016). It is conceivable that using such enormous index contrast could lead to waveguides supporting 50 or 100 stable modes.

An alternative strategy would be to aim for a fiber with a higher density of states for the same index contrast, but only use half of the mode orders, effectively leaving OAM “guardbands” around the desired channels. This would have the advantage of requiring a less-precise MUX, and may make fiber design easier. But, it would have a higher effective loss for the desired channels, since power would leak out of the desired channels and into neighboring modes at a higher rate due to a small Δn_{eff} . It may also, for the same reason, have significantly worse MPI than a fiber in which mode coupling is suppressed, since second-coupling instances will be more likely, and will still cause the data-carrying channel to deteriorate.

10.5 Summary

Using a combination of SLMs and q -plates we have excited SOC modes in gen2-1 air core fiber. By means of output projection measurements, the fiber’s transmission

matrix has been measured at 24m. We have demonstrated stable transmission of 24 modes, to approximately -18dB in crosstalk, with the dominant source of impurity typically being neighboring mode orders, which we expect were parasitically excited due to imperfect input coupling. Although there is distributed coupling in the fiber, we expect that, based on the measured crosstalk level compared with results at 50m, the dominant source of crosstalk is from impure excitation. The mode purity for both in-fiber nearest neighbors and modes of the same total angular momentum was approximately 20dB.

We have demonstrated, for the first time, stable propagation of SOC eigenstates in an optical fiber. These modes have no counterpart in paraxial free space optics or weakly guiding fibers, and are a physically distinct mode type bridging the space between the weakly-guided OAM states, which have spatially invariant polarization, and the TE and TM modes, which are the polarization eigenstates of the cylindrical interface comprising the waveguide.

We were limited in both distance and mode number by in-fiber coupling between mode orders with $\Delta l = 1$. This coupling was stronger than expected, given the n_{eff} difference between mode orders (Maruyama et al., 2015) and is a serious concern for fiber design going forward. We were also limited by high fiber loss, which we at least partially attribute to a high water concentration in the fiber. We also note that the earlier air core fibers (gen1 and gen3) are lossier than gen4, indicating that further fabrication improvements are likely.

It is also worth considering what we have gained by going to the SOC regime, and at what cost. Assuming the loss issue is solvable and that the increased mode coupling is due to fiber imperfections which can be solved, we have gained a factor of 2 in mode count and a more reliable fabrication, due to the lack of $m = 2$ modes, meaning that the fiber's performance is less sensitive to the radius of the air core.

The cost is a more complicated experiment setup, greater difficulty cleaving the fiber (due to a larger inner ring radius), and, if multicore OAM fibers are of interest one day, a larger waveguide footprint. The difficulty in input coupling could be overcome with either photonic lanterns or a tree of fused fiber couplers, but both technologies are at present immature. The cleaving issue is entirely practical, but could prove challenging to overcome in bulk. The issue of arranging SOC or OAM fibers for multicore transmission is an interesting one; it may be that the optimum strategy is to shrink the individual waveguides to allow for more waveguides to fit into the core lattice. This topic, to my knowledge, has not been studied in detail, and may be of interest to scientists attempting to leverage the advantages of OAM and SOC modes for telecommunications.

Chapter 11

Summary and Outlook

In this chapter, we summarize significant results obtained in this thesis, and consider future directions for OAM and SOC fiber research.

11.1 Summary of Results

We have studied the problem of OAM states in air core optical fibers. Several fibers have been designed and fabricated (Chap. 6), and input coupling (Chap. 5) and characterization (Chap. 4) methods have been described. We find that OAM modes in the weakly guided regime can be supported by well designed fibers, and can propagate over km length scales with low intermodal crosstalk (Chap. 8). We have also shown, both mathematically (Chap. 2) and by experiment (Chap. 7), that such modes are carriers of photonic angular momentum, and are not simply an alternative basis set for fiber vector modes constructed for convenience. High- l states are of particular interest; just as spinning tops become more stable in the face of small perturbations as the tops spin faster, higher order OAM states are observed to become more stable as their l increases.

We have performed transmission experiments using a record number (12) of OAM modes in a single fiber (Chap. 9), and shown that all states, across multiple wavelengths, can be transmitted under the SD-FEC threshold using QPSK modulation at 10GBaud/s. Although the we were prevented from testing the full WDM compatibility of our system due to alignment drift, pessimistic approximations indicate

that our system could transmit at 10.56 Tbit/s, with a spectral efficiency of approximately 7.04bits/s/Hz, within a factor of two of the current record holder for SMF transmission spectral efficiency.

We have found that as the waveguide confinement becomes stronger due to a thin ring and an air core, second order polarization effects transform the guided fiber modes from weakly guided OAM states to Spin-Orbit Coupled modes of well-defined total angular momentum, which have no analog in free space paraxial beams. We have demonstrated excitation and transmission of 24 such modes over 10m, a suitable length for devices, and shown suppression both of modes of the same j and in-fiber nearest neighbors in n_{eff} to approximately 20dB. This is the first demonstration of controlled excitation and transmission of SOC fiber modes, and enables further study of the class of thin-ring air core fiber.

11.2 Outlook

Here we consider possible applications of OAM or SOC modes.

11.2.1 OAM in Telecommunications

It is not yet clear that SDM will be adopted in any form for long-haul communications. When fiber optics supplanted coaxial cable for long haul communications, the advantages were enormous and apparent (Miller et al., 1973):

1. Fiber (and its associated source and detector technology) had the potential for at least an order of magnitude improvement in data rate. “In the longer range future, it seems clear that gigabit rates on individual fibers will soon become technically feasible...”
2. Fiber had lower, and less frequency-dependent, loss.

3. Fiber allowed for smaller cables, smaller bends, and its performance was not temperature dependent.
4. Fiber had the potential for “graceful growth”: “the electronics can be changed on an installed fiber to increase its communication capacity.” Thus, improvements in sources and modulation/demodulation electronics could be applied to existing fibers, unlike in the electrical domain where an increased modulation frequency might necessitate a new coaxial cable design.

Moving from SMF to SDM in any form offers an improvement only in point # 1, and the improvement is multiplicative in the number of modes. Consider the current record holders for capacity within SMF (Qian et al., 2012) and any fiber (Puttnam et al., 2015) - both “hero” experiments made use of incredibly large wavelength bandwidths (9.25THz for Qian and 10THz for Puttnam), higher order modulation formats (128-ary PD-QAM for Qian, 64-ary PD-QAM for Puttnam), and the difference in data rate is essentially the number of cores (a gain of $21.2\times$ with 22 cores). Increasing the number of channels by N requires N more transmitters and receivers, regardless of whether SMF is used. The question becomes whether it is cost effective to invest in multi-core fibers and SMF to multi-core fan-outs, rather than just lay more SMF.

The cost of implementing large-scale MIMO is more onerous, as the MIMO complexity scales as the number of channels squared, increasing system cost and latency (Saridis et al., 2015). Simply increasing the number of channels in a single core and expecting more advanced DSP to unwind the entire coupling matrix is not an efficient way to increase capacity.

At current, it is not foreseeable that OAM or SOC modes will be used for long haul communications due to the high (compared to SMF) fiber loss, and 10dB lengths on the order of 5.5km (Chap. 8). For data center applications, the utility of such modes will depend on the cost and ease of implementation of MUX/DEMUX devices (Lam

et al., 2014), which is yet to be determined.

(Uncoupled) Multi-core fibers ignore one fundamental degree of freedom for increasing capacity: β , and are not intrinsically different from using N SMFs. In this way, they are inefficient, as they utilize the degree of “space” but do not utilize the degree of “modes” and thus do not increase capacity per “active” area of the fiber. The most efficient SDM transmission modality may be few-mode multi-core fibers - fibers with multiple cores, such that each core has multiple, but few, modes (Saridis et al., 2015; Soma et al., 2016). This leverages the capacity gains in both multi-core and MIMO modalities, including a less fabrication-sensitive MUX within each few-mode core, without intractably large MIMO. Even this will likely remain in the laboratory domain unless significant transmission gains are proved possible.

11.2.2 OAM-based Fiber Devices

One arena which could employ OAM or SOC modes is fiber devices. We have already demonstrated theoretically that manufacturing a low (0.5dB) differential modal gain (DMG) fiber amplifier using 12 OAM modes is possible (Kang et al., 2015), and a proof of concept supporting only one mode order has been fabricated (Jung et al., 2016). Although the MUX remains challenging, a core-pumped (or cladding pumped) amplifier based on SOC fiber, supporting 24 (or so) modes with lower differential mode gain, could yield savings in equipment cost and power efficiency (Krummrich and Akhtari, 2016).

A second possibility is the deployment of OAM fibers for fiber sensing. OAM fibers provide the only known framework for co-propagation of multiple, stable modes (as opposed to LP mode groups), which could allow for measurement of the effects of physical phenomena (stress, strain, temperature) on several modes at once (Weng et al., 2016). For instance, consider the discussion in Sec. 7.4. In a system composed of q -plate - OAM fiber - q -plate, torsion could be sensed through polarization rotation.

Moreover, the system would be j -times more sensitive than SMF, up to $j = 8$, and the ability to measure the effect of torsion on multiple modes simultaneously could resolve ambiguities present in a system where a measurement is made only on one mode. For example, if the output polarization from an SMF is observed to rotate by 80 degrees, it is not clear whether the polarization in the fiber has actually rotated by 80 degrees or 260 degrees, unless multiple measurements are taken as the polarization rotates. If, however, a $j = 8$ mode is observed to rotate by 80 degrees, observation of a $j = 6$ mode, which could be performed simply by rotating a waveplate as in Sec. 5.4, would distinguish the two, since the second mode would be rotated by 60 degrees, or 195 degrees. Ideally the OAM modes in question would be non-integer multiples of each other, to avoid rotation ambiguities.

11.2.3 OAM and Nonlinear Optics

Intermodal nonlinear optics is emerging as a field of interest for creating lasers at novel colors, or enabling wideband frequency conversion (Demas et al., 2015b). Multimode waveguides offer more paths for momentum conservation (phase matching) within a fiber due to the variety of available wave vectors. In addition, conservation of angular momentum provides a selection rule for available pathways (Vaziri et al., 2002).

In fibers, OAM supercontinuum generation has been demonstrated experimentally (Prabhakar et al., 2016), and wideband frequency conversion via Bragg scattering has been shown in theory (Tai et al., 2016). However, the role and utility of OAM in fiber nonlinear optics remains largely unexplored, and may be an area of considerable future research.

11.2.4 Quantum Key Distribution and Entanglement Preservation

OAM beams have received attention for high-dimensional entanglement (Vaziri et al., 2002) and rotation-invariant Quantum Key Distribution (Vallone et al., 2014). For

these reasons, fibers which can transmit OAM states and OAM states pairs are useful for long range quantum communications. Typically, quantum communications involve the ability to send entangled states of the form $|1\rangle$, $|0\rangle$, $|1\rangle + |0\rangle$, and $|1\rangle - |0\rangle$ to complete a set of two mutually unbiased bases (Barnett, 2009). For OAM states, $|1\rangle$ and $|0\rangle$ can be sent using the two degenerate states of a given l , which we know are preserved under many perturbations, but being able to send their combination involves maintaining a phase relationship between the two degenerate states, which is more easily scrambled, at least for high- l , due both to fiber twist and to geometric effects (Sec. 3.2.3, Sec. 7.4).

SMF preserves entanglement, but is extremely sensitive to external perturbations in terms of maintaining polarization. PM fiber maintains two polarizations (but not their combinations), but breaks entanglement since it does not preserve indistinguishability. Preliminary results with high- l states in the air core fiber indicate that fiber transmission over 10m preserves entanglement, preserves $|1\rangle$ and $|0\rangle$ (i.e. the two SOa or SOaa modes of a given l), but is extremely sensitive to external perturbations for the combined states.

It is possible that some mid-low l state, such as $l = 2$ and $l = 3$, may be high enough in l to avoid degenerate state coupling, but low enough to avoid significant phase walk off due to geometric effects. If such a fiber is successful, we envision quantum key distribution experiments with such fibers.

11.3 Conclusion

We have observed experimentally both advantages and disadvantages of OAM modes. Whether or not OAM modes are implemented for an SDM strategy, the design freedom afforded by the restructuring of a fiber's density of states, the ability to excite and propagate stable modes, and the resilience of OAM modes to many perturba-

tions will likely result in their use in some form, whether that be sensing, multimode amplification, or nonlinear frequency conversion. We expect to see many interesting results utilizing OAM or SOC states in the years to come.

Appendix A

Perturbation Theory Derivation of Spin-Orbit Coupled States

The full vector wave equation for the transverse part of the electric field of guided fiber modes, derived from Maxwell's Equations assuming no free charges or currents and a non-magnetic material, is given by:

$$[\nabla_{\mathbf{t}}^2 + n^2 k^2] \mathbf{E}_{\mathbf{t}} + \nabla_{\mathbf{t}} [\mathbf{E}_{\mathbf{t}} \cdot \nabla_{\mathbf{t}} \ln(n^2)] = \beta^2 \mathbf{E}_{\mathbf{t}} \quad (\text{A.1})$$

Meanwhile, the equation describing the scalar (LP) fiber modes is given by:

$$(\nabla_{\mathbf{t}}^2 + n^2 k^2) \Psi = \tilde{\beta}^2 \Psi \quad (\text{A.2})$$

Here we use a $\tilde{\beta}$ to denote the value of β in the scalar picture as opposed to the vector picture.

The vector mode can be approximately obtained from the LP modes by treating the term $\nabla_{\mathbf{t}} [\mathbf{E}_{\mathbf{t}} \cdot \nabla_{\mathbf{t}} \ln(n^2)]$ perturbatively. The first order correction, found via degenerate perturbation theory, breaks the four-fold LP degeneracy (Snyder and Love, 1983).

$$LP_L \rightarrow \begin{pmatrix} HE_{L+1}^o \\ HE_{L+1}^e \\ EH_{L-1}^o \\ EH_{L-1}^e \end{pmatrix} = F_L(r) \begin{pmatrix} \hat{\mathbf{x}} \cos(L\phi) - \hat{\mathbf{y}} \sin(L\phi) \\ \hat{\mathbf{x}} \sin(L\phi) + \hat{\mathbf{y}} \cos(L\phi) \\ \hat{\mathbf{x}} \cos(L\phi) + \hat{\mathbf{y}} \sin(L\phi) \\ \hat{\mathbf{x}} \sin(L\phi) - \hat{\mathbf{y}} \cos(L\phi) \end{pmatrix} \quad (\text{A.3})$$

We drop radial subscripts for brevity. At this point, the HE/EH modes are not degenerate. Note that, explicitly, L denotes LP mode order, and would be the OAM

carried by each of these modes if they were weakly-guided (sufficiently described by first order perturbation theory) and written as OAM modes instead of HE/EH . It is *not* the HE/EH mode order.

The second order correction requires calculating the overlap between these vector modes and the vector modes of a different L . In order to compute these overlaps, we write the perturbative operator acting on a state \mathbf{a} as:

$$P|a\rangle \equiv \nabla_t [\mathbf{a} \cdot \nabla_t \ln(n^2)] \quad (\text{A.4})$$

It can be shown by using Green's Theorem that the inner product of a second state, \mathbf{b} , with the above can be written as (Snyder and Love, 1983):

$$\langle b|P|a\rangle = - \int dA (\nabla_t \cdot \mathbf{b}) [\mathbf{a} \cdot \nabla_t \ln(n^2)] \quad (\text{A.5})$$

For a circularly symmetric waveguide, only the radial component of \mathbf{a} is captured by Eq. (A.5). This can be computed for each HE/EH mode as:

$$HE/EH_L \cdot \nabla_t \ln(n^2) = \frac{\partial \ln(n^2)}{\partial r} F_L(r) \begin{pmatrix} \cos[(L+1)\phi] \\ \sin[(L+1)\phi] \\ \cos[(L-1)\phi] \\ \sin[(L-1)\phi] \end{pmatrix} \quad (\text{A.6})$$

The transverse divergence of each mode must also be calculated. Using

$$\frac{\partial}{\partial x} = \cos(\phi) \frac{\partial}{\partial r} - \frac{1}{r} \sin(\phi) \frac{\partial}{\partial \phi} \quad (\text{A.7a})$$

$$\frac{\partial}{\partial y} = \sin(\phi) \frac{\partial}{\partial r} + \frac{1}{r} \cos(\phi) \frac{\partial}{\partial \phi} \quad (\text{A.7b})$$

We find that the divergences are:

$$\nabla_t \cdot HE/EH_L = \begin{pmatrix} [F'_L(r) - F_L(r)\frac{L}{r}] \cos[(L+1)\phi] \\ [F'_L(r) - F_L(r)\frac{L}{r}] \sin[(L+1)\phi] \\ [F'_L(r) + F_L(r)\frac{L}{r}] \cos[(L-1)\phi] \\ [F'_L(r) + F_L(r)\frac{L}{r}] \sin[(L-1)\phi] \end{pmatrix} \quad (\text{A.8})$$

Investigation of Eq. (A.6) and Eq. (A.8) reveals that the overlap between an even and an odd mode will always be zero, as expected, and between modes of the same L , the only nonzero overlap is between a mode and itself. However, there is a nonzero overlap between the HE_L^e mode and the EH_{L+2}^e mode, that is, between the EH and HE modes of the same cylindrical mode order. Using the abbreviations:

$$R_1(L, L-2) = \pi \int r dr F_L(r) F'_{L-2}(r) \frac{\partial \ln(n^2)}{\partial r} \quad (\text{A.9a})$$

$$R_2(L, L-2) = \pi(L-2) \int dr F_L(r) F_{L-2}(r) \frac{\partial \ln(n^2)}{\partial r} \quad (\text{A.9b})$$

and using second order (nondegenerate) perturbation theory (Das, 2012), the new fiber modes are:

$$HE_L^{e/o} = |HE_L^{e/o}\rangle_{WG} - \frac{R_1(L, L+2) + R_2(L, L+2)}{\tilde{\beta}_{L+2}^2 - \tilde{\beta}_L^2} |EH_{L+2}^{e/o}\rangle_{WG} \quad (\text{A.10a})$$

$$EH_L^{e/o} = |EH_L^{e/o}\rangle_{WG} - \frac{R_1(L, L-2) - R_2(L, L-2)}{\tilde{\beta}_{L-2}^2 - \tilde{\beta}_L^2} |HE_{L-2}^{e/o}\rangle_{WG} \quad (\text{A.10b})$$

that is, the new vector modes are combinations of the old vector modes of the same cylindrical mode order, but different Cartesian mode order. Since each of these, when written as a combination to create the OAM basis, carries a different OAM, it is evident that the modes in Eq. (A.10a) and Eq. (A.10b), when written as angular momentum states, will be in an OAM superposition state. ■

Appendix B

Full Derivation of Angular Momentum of Fiber Modes

Starting from the definition:

$$\langle \Phi_{AM} \rangle = \frac{1}{2c^2} \int \int dA \mathbf{r} \times \text{Re}(\mathbf{E} \times \mathbf{H}^*) \quad (\text{B.1})$$

noting that

$$\mathbf{r} = x\hat{\mathbf{x}} + y\hat{\mathbf{y}} + z\hat{\mathbf{z}} = r\hat{\mathbf{r}} + z\hat{\mathbf{z}} \quad (\text{B.2})$$

and using the abbreviation

$$f_k = \epsilon_{klm} \text{Re}(\hat{\mathbf{x}}_k E_l H_m^*) \quad (\text{B.3})$$

where $\hat{\mathbf{x}}_k$ are cylindrical unit vectors with subscripts denoting (r, ϕ, z) and ϵ_{klm} is the Levi-Civita tensor, the function inside the integral in Eq. (B.1) can be written as:

$$\hat{\mathbf{r}}(-zf_2) - \hat{\phi}(rf_3 - zf_1) + \hat{\mathbf{z}}(rf_2) \quad (\text{B.4})$$

Using the rotationally symmetric basis of Eq. (2.7), it is clear that f_k has no azimuthal dependence, since the only azimuthal dependence on all parts of \mathbf{E} and \mathbf{H} is $e^{ij\phi}$. The integral in Eq. (B.1) is performed over the transverse plane, where:

$$\int \int dA \hat{\mathbf{r}} = \int \int dA \hat{\phi} = 0 \quad (\text{B.5})$$

by parity. If the basis set of Eq. (2.6) is chosen, the non- $\hat{\mathbf{z}}$ components also vanish by parity, as the E_r, E_z, H_ϕ and E_ϕ, H_r, H_z field components all have the same azimuthal function (Snyder and Love, 1983), either $\sin(j\phi)$ or $\cos(j\phi)$, meaning when multiplied by $\hat{\mathbf{r}}$, their azimuthal dependence will integrate to zero by cosine/sine orthogonality relations for differing frequency arguments. Thus, the only remaining component is $\hat{\mathbf{z}}r f_2$, which, when written out in terms of \mathbf{E} and \mathbf{H} components, is Eq. (2.22):

$$\langle \Phi_{AM} \rangle_z = -\frac{1}{2c^2} \int \int dA r \text{Re} (E_r H_z^* - E_z H_r^*) \quad (\text{B.6})$$

Using the relations in equations Eq. (2.23) through Eq. (2.26):

$$H_z = \frac{1}{i\omega\mu r} \left[\frac{\partial(rE_\phi)}{\partial r} - \frac{\partial E_r}{\partial \phi} \right] \quad (\text{B.7a})$$

$$i\omega\mu \mathbf{H}_t = [\nabla_t \times (\hat{\mathbf{z}}E_z) + i\beta \hat{\mathbf{z}} \times \mathbf{E}_t] \quad (\text{B.7b})$$

$$E_z = \frac{i}{\beta} [\nabla_t \cdot \mathbf{E}_t + (\mathbf{E}_t \cdot \nabla_t) \ln(n^2)] \quad (\text{B.7c})$$

and assuming that $|E_z| \ll |\mathbf{E}_t|$, which allows us to drop terms which scale as E_z^2 , we arrive at Eq. (2.27):

$$\langle \Phi_{AM} \rangle_z = -\frac{1}{2c^2} \int \int dA \text{Re} \left[\frac{-(\pm j)}{\omega\mu} (E_r E_r^* + E_\phi E_\phi^*) + \frac{i}{\omega\mu} \left(E_r \frac{\partial(rE_\phi^*)}{\partial r} + E_\phi^* \frac{\partial(rE_r)}{\partial r} \right) + \frac{ir}{\omega\mu} E_\phi^* (\mathbf{E}_t \cdot \nabla_t) \ln(n^2) \right] \quad (\text{B.8})$$

Consider the integral of the middle term in equation Eq. (B.8):

$$\frac{i}{\omega\mu} \int \int dA \left(E_r \frac{\partial(rE_\phi^*)}{\partial r} + E_\phi^* \frac{\partial(rE_r)}{\partial r} \right) \quad (\text{B.9})$$

Substituting from the basis functions in Eq. (2.7) OR Eq. (2.6), the radial part of

this integral becomes:

$$\int dr \left(r\psi_r \frac{\partial(r\psi_\phi)}{\partial r} + r\psi_\phi \frac{\partial(r\psi_r)}{\partial r} \right) \quad (\text{B.10})$$

We cannot directly use integration by parts, since ψ_r is not continuous. The function $\Xi = n^2\psi_r$, however, is continuous. We can rewrite:

$$\int dr \left(\frac{r\Xi}{n^2} \frac{\partial(r\psi_\phi)}{\partial r} + r\psi_\phi \frac{\partial(r\Xi/n^2)}{\partial r} \right) \quad (\text{B.11})$$

Expanding the second derivative term:

$$\int dr \left(\frac{r\Xi}{n^2} \frac{\partial(r\psi_\phi)}{\partial r} + \frac{r\psi_\phi}{n^2} \frac{\partial(r\Xi)}{\partial r} + r^2\psi_\phi\Xi \frac{\partial(1/n^2)}{\partial r} \right) \quad (\text{B.12})$$

The last term in Eq. (B.12) can be rewritten as:

$$r^2\psi_\phi\Xi \frac{\partial(1/n^2)}{\partial r} = -r^2\psi_\phi \frac{\Xi}{n^2} \frac{1}{n^2} \frac{\partial n^2}{\partial r} = -r^2\psi_\phi\psi_r \frac{\partial \ln(n^2)}{\partial r} \quad (\text{B.13})$$

Which exactly cancels the last term in Eq. (B.9)

The function n^2 is not continuous. However, to a good approximation, the function $1/n^2$ is continuous, since $\frac{1}{x+\delta} \approx \frac{1}{x}$. Thus, we make the approximation that:

$$\int dr \left(\frac{r\Xi}{n^2} \frac{\partial(r\psi_\phi)}{\partial r} + \frac{r\psi_\phi}{n^2} \frac{\partial(r\Xi)}{\partial r} \right) \approx \frac{1}{n^2} \int dr \left(r\Xi \frac{\partial(r\psi_\phi)}{\partial r} + r\psi_\phi \frac{\partial(r\Xi)}{\partial r} \right) \quad (\text{B.14})$$

Using integration by parts, and the fact that ψ_ϕ and Ξ are continuous:

$$\int dr r\psi_\phi \frac{\partial}{\partial r}(r\Xi) = r^2\Xi\psi_\phi \Big|_0^\infty - \int r\Xi \frac{\partial}{\partial r}(r\psi_\phi) \quad (\text{B.15})$$

The middle term in Eq. (B.11) is zero, because both ψ_r (Ξ) and ψ_ϕ are finite at the origin, and must decay to zero faster than $1/r$ as $r \rightarrow \infty$. Thus:

$$\int dr r\psi_\phi \frac{\partial}{\partial r}(r\Xi) = - \int r\Xi \frac{\partial}{\partial r}(r\psi_\phi) \quad (\text{B.16})$$

and Eq. (B.14) is strictly zero, reducing Eq. (B.8) directly to Eq. (2.28).

The $\hat{\mathbf{r}}$ and $\hat{\phi}$ components of the linear momentum flux are equal to zero for the same reason as the $\hat{\mathbf{r}}$ and $\hat{\phi}$ components of the angular momentum flux. To simplify the $\hat{\mathbf{z}}$ component of the linear momentum flux (Eq. (2.29)):

$$\langle \Phi_p \rangle_z = \frac{1}{2c^2} \int \int dA \operatorname{Re} (E_r H_\phi^* - E_\phi H_r^*) \quad (\text{B.17})$$

Using Eq. (B.7b), Eq. (B.17) becomes:

$$\langle \Phi_p \rangle_z = \frac{1}{2c^2} \int \int dA \operatorname{Re} \left[\frac{\beta}{\omega\mu} (|E_r|^2 + |E_\phi|^2) - \frac{1}{\omega\mu} \left(E_r \frac{\partial E_z^*}{\partial r} + \frac{ij}{r} E_\phi E_z^* \right) \right] \quad (\text{B.18})$$

We now show that the right hand two terms are zero. They can be rewritten as:

$$E_r \frac{\partial E_z^*}{\partial r} + \frac{ij}{r} E_\phi E_z^* = E_t \cdot \nabla_t E_z^* = \nabla_t \cdot (E_t E_z^*) - E_z^* (\nabla_t \cdot E_t) \quad (\text{B.19})$$

Using Eq. (B.7c), and dropping terms which scale as E_z^2 , we find Eq. (B.19) simplifies to:

$$\nabla_t \cdot (E_t E_z^*) + E_z^* E_t \cdot \nabla \ln(n^2) \quad (\text{B.20})$$

Using linearity of the divergence operator, and inserting the angular momentum basis functions, this becomes:

$$\nabla_t \cdot (\hat{\mathbf{r}} \psi_r \psi_z) + \nabla_t \cdot (\hat{\phi} \psi_\phi \psi_z) + \psi_z \psi_r \frac{\partial \ln(n^2)}{\partial r} \quad (\text{B.21})$$

The integral over dA of the middle term in Eq. (B.21) is zero; since the arguments are continuous and have continuous partial derivatives, the area integral can be transformed into a contour integral around the fiber, with the curve a large distance away from the fiber, such that the field values are zero along the curve. The first term can

be transformed using the same change of variables as in Eq. (B.14), $\Xi = E_r n^2$, into:

$$\nabla_t \cdot (\hat{\mathbf{r}}\psi_r\psi_z) = -\psi_z\psi_r \frac{\partial \ln(n^2)}{\partial r} + \frac{1}{n^2} \nabla \cdot (\hat{\mathbf{r}}\Xi\psi_z) \quad (\text{B.22})$$

The first term here evidently cancels the final term in Eq. (B.21). The second term is also zero by Green's theorem - the transverse plane can be broken into smaller regions where n is continuous, i.e. the core and the cladding of a step index fiber. For the core, the normal vector of the curve everywhere will be $\hat{\phi}$, so the line integral there is zero by orthogonality. For the cladding (or any other annulus), the majority of the curve also has the $\hat{\phi}$ as a normal vector. There will be two segments of the curve 'closing' the annulus, which will be a small angular distance $\delta\phi$ separated from each other. Since Ξ and ψ_z are not a function of angle, the line integral over the outgoing and incoming parts of the integral will exactly cancel. Thus, Eq. (B.22) is exactly zero, reducing the linear momentum flux to Eq. (2.30):

$$\langle \Phi_p \rangle_z = \frac{\beta}{2c^2\omega\mu} \int \int dA \psi_r^2 + \psi_\phi^2 \quad (\text{B.23})$$

■

Appendix C

Air Core to Air Core Splice Program

In order for air core fibers to be practically useful, they should be spliceable. Fiber breaks are bound to happen, and the ability to combine two distinct fibers with low loss is critical. This presents a problem, since at a high enough temperature the air core itself will collapse (in the same way that a preform is collapsed before a conventional fiber is drawn). Thus, to successfully splice two air core fibers, the splice must be made “cold,” that is, at lower currents than usual. A splicer program to splice two air core fibers is iteratively designed using microscope images of the spliced fibers as feed back for whether the air hole has partially collapsed, totally collapsed, or remains intact.

Additionally, the fibers need to be coaligned very well during the splice. We have seen in Chap. 5 that for pure mode excitation, the incident OAM beams need to be aligned into the fiber with precision of $\sim 100nm$. The fibers need to be aligned to similar precision or else Δl crosstalk can easily occur at the splice point.

The following is a splice program used with an Ericsson FSU 995 FA to splice gen4 air core fibers. The fibers should be cleaved with angles 0.3 degrees or less and mounted into the splicer. Fiber alignment should be performed by hand with purity measured by time of flight, as the splicer does not have necessary precision to center the two fibers to low crosstalk; allowing the machine to freely splice often results in inter- l crosstalk worse than -6dB. Moreover the splice yield is low, no better than 1/4 if crosstalk of $-15dB$ is tolerated, since the splicer will still pull the two fibers

back before splicing them together - the motion of pulling back and pushing forward can cause lateral misalignment. Higher precision splicers could alleviate this issue, and there is no reason that, in principle, the entire process could not be automated.

Prefusion Current	$5mA$
Gap	$30\mu m$
Overlap	$5\mu m$
Fuse Time 1	$0.3s$
Current 1	$10mA$
Fuse Time 2	$0.6s$
Current 2	$10.5mA$
Fuse Time 3	$0.8s$
Current 3	$10.5mA$
Left MFD	$15\mu m$
Right MFD	$15\mu m$
Set Center	+255
AoA Current	0
Early Prefuse	0
Align Accuracy	$0.01\mu m$
Loss Shift	0
Auto Arc Center	No

Appendix D

Publications List

Journal articles

1. **P. Gregg**, P. Kristensen, A. Rubano, S. Golowich, L. Marrucci, and S. Ramachandran, “Spin-Orbit Coupled, Non-Integer OAM Fibers,” *in preparation*.
2. D. L. P. Vitullo, C. C. Leary, **P. Gregg**, R. A. Smith, D. V. Reddy, S. Ramachandran, and M. G. Raymer, “Observation of Interaction of Spin and Intrinsic Orbital Angular Momentum of Light,” *accepted to Phys. Rev. Lett.*
3. Y. Jung, Q. Kang, S. Yoo, R. Sidharthan, D. Ho, **P. Gregg**, S. Ramachandran, S. Alam, and D.J. Richardson, “Optical Orbital Angular Momentum Amplifier based on an Air-Hole Erbium Doped Fiber,” *accepted to J. Lightwave Technol.*
4. **P. Gregg**, P. Kristensen, and S. Ramachandran, “13.4km OAM State Propagation by Circulating Fiber Loop,” *Optics Express* Vol. 24, No. 17, 18938 (2016).
5. L. Rishøj, M. Jones, J. Demas, G. Prabhakar, **P. Gregg**, L. Yan, T. Hawkins, J. Ballato, and S. Ramachandran, “Polymer-clad silica fibers for tailoring modal area and dispersion,” *Optics Letters* Vol. 41, No. 15, 3587 (2016).
6. **P. Gregg**, P. Kristensen, and S. Ramachandran, “Conservation of orbital angular momentum in air-core optical fibers,” *Optica* Vol. 2, No. 3, 267 (2015).
7. **P. Gregg**, M. Mirhosseini, A. Rubano, L. Marrucci, E. Karimi, R.W. Boyd, and S. Ramachandran, “Q-plates as higher order polarization controllers for orbital angular momentum modes of fiber,” *Opt. Lett.* Vol. 40, No. 8, 1729 (2015).

8. S. Ramachandran, **P. Gregg**, P. Kristensen, and S.E. Golowich, “On the scalability of ring fiber designs for OAM multiplexing,” *Opt. Expr.* Vol. 23, No. 3, 3721 (2015).
9. Q. Kang, **P. Gregg**, Y. Jung, E.L. Lim, A. Alam, S. Ramachandran, and D. J. Richardson, “Amplification of 12 OAM Modes in an air-core erbium doped fiber,” *Opt. Expr.* Vol. 23, No. 22, 28341 (2015).
10. L. Yan, **P. Gregg**, E. Karimi, A. Rubano, L. Marrucci, R.W. Boyd, and S. Ramachandran, “Q-plate enabled spectrally diverse orbital-angular-momentum conversion for stimulated emission depletion microscopy,” *Optica* Vol. 2, No. 3, 900 (2015).

Conference presentations and invited talks

10. K. Ingerslev, **P. Gregg**, M. Galili, F. Da Ros, H. Hu, F. Bao, M. Usaga Castaneda, P. Kristensen, A. Rubano, L. Marrucci, S. Ramachandran, K. Rottwitt, T. Morioka, L. Oxenlowe, “12 Mode, MIMO-Free OAM Transmission”, *to be presented at OFC 2017*, M2D.1.
11. **P. Gregg**, P. Kristensen, A. Rubano, S. Golowich, L. Marrucci, and S. Ramachandran, “Spin-Orbit Coupled, Non-Integer OAM Fibers: Unlocking a New Eigenbasis for Transmission of 24 Uncoupled Modes,” **Post-Deadline Paper**, in *CLEO: 2016*, OSA Technical Digest (online) (Optical Society of America, 2016), paper JTh4C.7.
12. **P. Gregg**, P. Kristensen, and S. Ramachandran, “Record Length (13.4km) Pulse Propagation in OAM States,” in *CLEO: 2016*, OSA Technical Digest (online) (Optical Society of America, 2016), paper SW4F.1.
13. **P. Gregg**, P. Kristensen, S. Golowich, and S. Ramachandran, “Demonstration of a Thin-Ring Air Core Fiber Supporting 22 Stable Angular Momentum Modes,” *European Conference and Exhibition on Optical Communication: 2016*, OSA Technical Digest (online) (Optical Society of America, 2016) paper W3B.5.
14. G. Prabhakar, **P. Gregg**, L. Rishøj, and S. Ramachandran, “In-Fiber Monomode

Octave-Spanning OAM Supercontinuum,” in CLEO: 2016, OSA Technical Digest (online) (Optical Society of America, 2016), paper Am4J.3.

15. B. Tai, **P. Gregg**, L. Rishøj, and S. Ramachandran, “Wideband nonlinear frequency conversion with OAM fiber,” in CLEO: 2016, OSA Technical Digest (online) (Optical Society of America, 2016), paper FTh3C.6.

16. S. Pidishety, M.I.M. Abdul Khudus, **P. Gregg**, S. Ramachandran, B. Srinivasan, and G. Brambilla, “OAM Beam Generation using All-fiber Fused Couplers,” in CLEO: 2016, OSA Technical Digest (online) (Optical Society of America, 2016), paper STu1F.2.

17. Y. Jung, Q. Kang, S. Yoo, S. Raghuraman, D. Ho, **P. Gregg**, S. Ramachandran, S. Alam, and D. J. Richardson, “Optical OAM Amplifier based on an Air-Core Erbium Doped Fiber, ” **Post-Deadline Paper**, in Optical Fiber Communication Conference: 2016, OSA Technical Digest (online) (Optical Society of America, 2016), paper Th5A.5.

18. **P. Gregg**, M. Mirhosseini, A. Rubano, L. Marrucci, E. Karimi, R.W. Boyd, and S. Ramachandran, “Q-plates for Switchable Excitation of Fiber OAM Modes,” in CLEO: 2015, OSA Technical Digest (online) (Optical Society of America, 2015), paper SW4M.3

19. Q. Kang, **P. Gregg**, Y. Jung, E.L. Lim, S. Alam, S. Ramachandran, and D. J. Richardson, “Amplification of 12 OAM states in an Air-Core EDF,” in Optical Fiber Communication Conference: 2015, OSA Technical Digest (online) (Optical Society of America, 2015), paper Tu3C.2.

20. L. Yan, E. Karimi, **P. Gregg**, R.W. Boyd, and S. Ramachandran, “Single-aperture STED illumination using a q-plate and fiber,” in CLEO: 2015, OSA Technical Digest (online) (Optical Society of America, 2015), paper STu1L.5

21. **P. Gregg**, P. Kristensen, and S. Ramachandran, “OAM Stability in Fiber due to Angular Momentum Conservation,” in CLEO: 2014, OSA Technical Digest (online) (Optical Society of America, 2014), paper SM2N.2.

22. **P. Gregg**, P. Kristensen, S. Golowich, J. Olsen, P. Steinvurzel, and S. Ramachandran, “Stable transmission of 12 OAM states in air-core fiber,” in CLEO: 2013, OSA Technical Digest (online) (Optical Society of America, 2013), paper CTu2K.2.
23. Y. Chen, **P. Gregg**, and S. Ramachandran, “Fiber Mode Excitation via Free-Space Beam Shaping,” in CLEO: 2013, OSA Technical Digest (online) (Optical Society of America, 2013), paper CTu3K.4.
24. S. Ramachandran, L. Yan, **P. Gregg**, and P. Kristensen, “Light that Spins Inside Fibers: Applications from Microscopy to Telecommunications,” Invited Talk, Frontiers in Optics: 2013, OSA Technical Digest (online) (Optical Society of America, 2013), paper FM3F.2.
25. S. Ramachandran and **P. Gregg**, “Looking inside a fiber: Measuring mode content and properties,” Invited Talk, Photonics Society Summer Topical Meeting Series: 2013 (IEEE 2013) MC4.1.
26. S. Golowich, N. Bozinovic, P. Kristensen, **P. Gregg**, and S. Ramachandran, “Orbital angular momentum states for mode division multiplexing in optical fiber,” Invited Talk, Photonics Society Summer Topical Meeting Series: 2013 (IEEE 2013)
27. S. Golowich, P. Kristensen, N. Bozinovic, **P. Gregg**, and S. Ramachandran, “Fibers supporting orbital angular momentum states for information capacity scaling,” Invited Talk, Frontiers in Optics: 2012, OSA Technical Digest (online) (Optical Society of America, 2012) paper FW2D.2.
28. S. Ramachandran, N. Bozinovic, **P. Gregg**, S. Golowich, and P. Kristensen, “Optical vortices in fibers: a new degree of freedom for mode multiplexing,” Invited Talk, European Conference and Exhibition on Optical Communication: 2012, OSA Technical Digest (online) (Optical Society of America, 2012) paper Tu3F.3.

References

- Abraham, M. (1909). On the Electrodynamics of Moving Bodies. *Rendiconti del Circolo Matematico di Palermo*, 28(1):1–28.
- Abramowitz, M. and Stegun, I. A., editors (1972). *Handbook of Mathematical Functions with Formulas, Graphs, and Mathematical Tables*. Dover, New York.
- Agrawal, G. P. (2008). *Nonlinear Fiber Optics*. Academic Press.
- Aiello, A., Banzer, P., Neugebauer, M., and Leuchs, G. (2015). From transverse angular momentum to photonic wheels. *Nature Photonics*, 9(12):789–795.
- Alam, M. Z. and Albert, J. (2013). Selective excitation of radially and azimuthally polarized optical fiber cladding modes. *Journal of Lightwave Technology*, 31(19):3167–3175.
- Alekseev, K. N., Volyar, a. V., and Fadeeva, T. a. (2002). Spin-orbit interaction and evolution of optical eddies in perturbed weakly directing optical fibers. *Optics and Spectroscopy*, 93(4):588–597.
- Alekseev, K. N. and Yavorskii, M. a. (2005). Twisted optical fibers sustaining propagation of optical vortices. *Optics and Spectroscopy*, 98(1):53–60.
- Alexeyev, A. and Fadeyeva, T. (1998). Optical vortices and the flow of their angular momentum in a multimode fiber. *Semiconductor Physics, Quantum Electronics & Optoelectronics*, 1(1):82–89.
- Alexeyev, C. N., Borshak, E. V., Volyar, a. V., and Yavorsky, M. a. (2009). Angular momentum conservation and coupled vortex modes in twisted optical fibres with torsional stress. *Journal of Optics A: Pure and Applied Optics*, 11(9):094011.
- Alexeyev, C. N., Volyar, a. V., and Yavorsky, M. a. (2004). Vortex-preserving weakly guiding anisotropic twisted fibres. *Journal of Optics A: Pure and Applied Optics*, 6(5):S162–S165.
- Alexeyev, C. N., Volyar, a. V., and Yavorsky, M. a. (2008). Optical vortices in twisted optical fibres with torsional stress. *Journal of Optics A: Pure and Applied Optics*, 10(9):095007.

- Alexeyev, C. N. and Yavorsky, M. A. (2004). Optical vortices and the higher order modes of twisted strongly elliptical optical fibres. *Journal of Optics A: Pure and Applied Optics*, 6(9):824.
- Allen, L., Beijersbergen, M., Spreeuw, R., and Woerdman, J. (1992). Orbital angular momentum of light and the transformation of Laguerre-Gaussian laser modes. *Physical Review A*, 45(11):8185–8188.
- Ando, T., Ohtake, Y., Matsumoto, N., Inoue, T., and Fukuchi, N. (2009). Mode purities of Laguerre-Gaussian beams generated via complex-amplitude modulation using phase-only spatial light modulators. *Optics letters*, 34(1):34–36.
- Andrews, D. L. (2013). *The Angular Momentum of Light*. Cambridge University Press, Cambridge.
- Arlt, J. and Dholakia, K. (2000). Generation of high-order Bessel beams by use of an axicon. *Optics Communications*, 177(1):297–301.
- Arlt, J., Dholakia, K., Allen, L., and Padgett, M. J. (1998). The production of multiringed Laguerre Gaussian modes by computer-generated holograms. *Journal of Modern Optics*, 45(April 2013):1231.
- Barlow, a. J., Ramskov-Hansen, J. J., and Payne, D. N. (1981). Birefringence and polarization mode-dispersion in spun single-mode fibers. *Applied optics*, 20(17):2962–2968.
- Barnett, S. M. (2009). *Quantum Information*. Oxford University Press.
- Barnett, S. M. (2010). Resolution of the Abraham-Minkowski Dilemma. *Physical Review Letters*, 104(7):070401.
- Baumeister, M., Dickmann, K., and Hoult, T. (2006). Fiber laser micro-cutting of stainless steel sheets. *Applied Physics A*, 85(2):121–124.
- Beijersbergen, M., Coerwinkel, R., Kristensen, M., and Woerdman, J. (1994). Helical-wavefront laser beams produced with a spiral phaseplate. *Optics Communications*, 112(5-6):321–327.
- Beresna, M., Gecevicius, M., Kazansky, P. G., and Gertus, T. (2011). Radially polarized optical vortex converter created by femtosecond laser nanostructuring of glass. *Applied Physics Letters*, 98(20):201101.
- Bergano, N. S. and Davidson, C. R. (1995). Circulating Loop Transmission Experiments for the Study of Long-Haul Transmission Systems Using Erbium-Doped Fiber Amplifiers. *Journal of Lightwave Technology*, 13(5):879–888.

- Berkhout, G. C. G., Lavery, M. P. J., Courtial, J., Beijersbergen, M. W., and Padgett, M. J. (2010). Efficient sorting of orbital angular momentum states of light. *Physical Review Letters*, 105(15):8–11.
- Berkhout, G. C. G., Lavery, M. P. J., Padgett, M. J., and Beijersbergen, M. W. (2011). Measuring orbital angular momentum superpositions of light by mode transformation. *Optics letters*, 36(10):1863–1865.
- Berry, M. V. (1987). The Adiabatic Phase and Pancharatnam 's Phase for Polarized Light. *Journal of Modern Optics*, 34(11):1401–1407.
- Bjarklev, A. (1986). Microdeformation losses of single-mode fibers with step-index profiles. *Journal of Lightwave Technology*, 4(3).
- Blake, J. N., Kim, B. Y., Engan, H. E., and Shaw, H. J. (1987). Analysis of intermodal coupling in a two-mode fiber with periodic microbends. *Optics letters*, 12(4):281–283.
- Blake, J. N., Kim, B. Y., and Shaw, H. J. (1986). Fiber-optic modal coupler using periodic microbending. *Optics letters*, 11(3):177–179.
- Bland-Hawthorn, J., Ellis, S. C., Leon-Saval, S. G., Haynes, R., Roth, M. M., Löhmansröben, H. G., Horton, a. J., Cuby, J. G., Birks, T. a., Lawrence, J. S., Gillingham, P., Ryder, S. D., and Trinh, C. (2011). A complex multi-notch astronomical filter to suppress the bright infrared sky. *Nature Communications*, 2(581):1–7.
- Bliokh, K., Rodríguez-Fortuño, F., Nori, F., and Zayats, A. (2015). Spin-orbit interactions of light. *Nature Photonics*, 27(December):796–808.
- Bliokh, K. Y., Alonso, M. a., Ostrovskaya, E. a., and Aiello, A. (2010). Angular momenta and spin-orbit interaction of nonparaxial light in free space. *Physical Review A - Atomic, Molecular, and Optical Physics*, 82(6):4–10.
- Bolduc, E., Bent, N., Santamato, E., Karimi, E., and Boyd, R. W. (2013). Exact solution to simultaneous intensity and phase encryption with a single phase-only hologram. *Optics Letters*, 38(18):3546–9.
- Bornstein, A. and Croitoru, N. (1985). Chalcogenide Hollow Fibers. *Journal of Non-Crystalline Solids*, 77(1):1277–1280.
- Bozinovic, N., Golowich, S., Kristensen, P., and Ramachandran, S. (2012). Control of orbital angular momentum of light with optical fibers. *Optics Letters*, 37(13):2451.
- Bozinovic, N., Kristensen, P., and Ramachandran, S. (2011). Are Orbital Angular Momentum (OAM / Vortex) States of Light Long-Lived in Fibers ? *Frontiers in Optics*, LWL3:9–11.

- Bozinovic, N., Yue, Y., Ren, Y., Tur, M., Kristensen, P., Huang, H., Willner, A. E., and Ramachandran, S. (2013). Terabit-scale orbital angular momentum mode division multiplexing in fibers. *Science*, 340(6140):1545–8.
- Brunet, C., Ung, B., Messaddeq, Y., LaRochelle, S., Bernier, E., and Rusch, L. (2014a). Design of an Optical Fiber Supporting 16 OAM Modes. *Optical Fiber Communication Conference*, 45:Th2A.24.
- Brunet, C., Vaity, P., and Rusch, L. a. (2014b). Design , fabrication and validation of an OAM fiber supporting 36 modes. *Optics Express*, 22(21):26117–26127.
- Brüning, R., Gelszinnis, P., Schulze, C., Flamm, D., and Duparré, M. (2013). Comparative analysis of numerical methods for the mode analysis of laser beams. *Applied optics*, 52(32):7769–77.
- Bryngdahl, O. (1974). Geometrical transformations in optics. *Journal of the Optical Society of America*, 64(8):1092.
- Burns, W. K. (1993). *Optical Fiber Rotation Sensing*. Academic Press.
- Carpenter, J., Thomsen, B. C., and Wilkinson, T. D. (2012). Degenerate Mode-Group Division Multiplexing. *Journal of Lightwave Technology*, 30(24):3946–3952.
- Chang, D., Yu, F., Xiao, Z., Li, Y., Stojanovic, N., Xie, C., and Shi, X. (2011). FPGA Verification of a Single QC-LDPC Code for 100 Gb / s Optical Systems without Error Floor down to BER of 10^{-15} . In *Optical Fiber Communication Conference*, pages 10–12.
- Chiao, R. Y. and Wu, Y. S. (1986). Manifestations of Berry’s topological phase for the photon. *Physical Review Letters*, 57(8):933–936.
- Chimento, P. F., Alkemade, P. F. a., ’t Hooft, G. W., and Eliel, E. R. (2012). Optical angular momentum conversion in a nanoslit. *Optics Letters*, 37(23):4946–4948.
- Cho, J., Xie, C., and Winzer, P. J. (2012). Analysis of soft-decision FEC on non-AWGN channels. *Optics Express*, 20(7):7915–7928.
- Chuang, S. L. (2009). *Physics of Photonic Devices*. Wiley & Sons, Hoboken, NJ, 2 edition.
- Čižmár, T. and Dholakia, K. (2011). Shaping the light transmission through a multimode optical fibre: complex transformation analysis and applications in biophotonics. *Optics Express*, 19(20):18871.
- Čižmár, T. and Dholakia, K. (2012). Exploiting multimode waveguides for pure fibre-based imaging. *Nature Communications*, 3(May):1027.

- Collins, Jr., S. A. (1970). Lens-System Diffraction Integral Written in Terms of Matrix Optics. *Journal of the Optical Society of America*, 60(9):1168–1177.
- Corral, C. a. and Lindquist, C. S. (1998). On implementing Kasa’s circle fit procedure. *IEEE Transactions on Instrumentation and Measurement*, 47(3):789–795.
- Courtial, J., Dholakia, K., Allen, L., and Padgett, M. (1997). Second-Harmonic Generation And The Conservation Of Orbital Angular Momentum With High-Order Laguerre-Gaussian Modes. *Physical Review A*, 56(5):4193–4196.
- Das, A. (2012). *Lectures of Quantum Mechanics*. Hindustan Book Agency, New Delhi, 2 edition.
- Dashti, P. Z., Alhassen, F., and Lee, H. P. (2006). Observation of orbital angular momentum transfer between acoustic and optical vortices in optical fiber. *Physical Review Letters*, 96(4):1–4.
- Davis, J. a., Cottrell, D. M., Campos, J., Yzuel, M. J., and Moreno, I. (1999). Encoding amplitude information onto phase-only filters. *Applied Optics*, 38(23):5004–5013.
- Davis, J. a., Valadéz, K. O., and Cottrell, D. M. (2003). Encoding amplitude and phase information onto a binary phase-only spatial light modulator. *Applied Optics*, 42(11):2003–2008.
- Demas, J. and Ramachandran, S. (2014). Sub-second mode measurement of fibers using C^2 imaging. *Optics Express*, 22(19):23043.
- Demas, J., Rishøj, L., and Ramachandran, S. (2015a). Free-space beam shaping for precise control and conversion of modes in optical fiber. *Optics Express*, 23(22):28531.
- Demas, J., Steinvurzel, P., Tai, B., Rishøj, L., and Chen, Y. (2015b). Intermodal nonlinear mixing with Bessel beams in optical fiber. *Optica*, 2(1):14–17.
- Dong, P., Chen, X., Kim, K., Chandrasekhar, S., Chen, Y.-k., Sinsky, J. H., Laboratories, B., Avenue, M., and Hill, M. (2016). 128-Gb / s 100-km transmission with direct detection using silicon photonic Stokes vector receiver and I / Q modulator. *Optics Express*, 24(13):14208–14214.
- Dudley, A., Mhlanga, T., Lavery, M., McDonald, A., Roux, F., Padgett, M., and Forbes, A. (2013). Efficient sorting of Bessel beams. *Optics Express*, 21(1):165–171.
- Dudley, A., Vasilyeu, R., Belyi, V., Khilo, N., Ropot, P., and Forbes, A. (2012). Controlling the evolution of nondiffracting speckle by complex amplitude modulation on a phase-only spatial light modulator. *Optics Communications*, 285(1):5–12.

- Endean, V. and Allen, J. (1970). General 3-Dimensional Solution of Eddy-Current And Laplacian Fields in Cylindrical Structures. *Proceedings of the Institution of Electrical Engineers*, 117(10):2059–2060.
- Erdogan, T. (1997). Fiber grating spectra. *Journal of Lightwave Technology*, 15(8):1277–1294.
- Erdogan, T. (2000). Cladding-mode resonances in short- and long-period fiber grating filters: errata. *Journal of the Optical Society of America A*, 17(11):2113.
- Essiambre, R.-J., Kramer, G., Winzer, P., Foschini, G., and Goebel, B. (2010). Capacity Limits of Optical Fiber Networks. *Journal of Lightwave Technology*, 28(4):662–701.
- Essiambre, R. J. and Tkach, R. W. (2012). Capacity trends and limits of optical communication networks. *Proceedings of the IEEE*, 100(5):1035–1055.
- Fienup, J. R. (1982). Phase retrieval algorithms: a comparison. *Applied Optics*, 21(15):2758–2769.
- Fini, J. M. (2006). Bend-resistant design of conventional and microstructure fibers with very large mode area. *Optics Express*, 14(1):69–81.
- Fini, J. M. and Ramachandran, S. (2007). Natural bend-distortion immunity of higher-order-mode large-mode-area fibers. *Optics Letters*, 32(7):748–750.
- Fontaine, N. K., Ryf, R., Chen, H., Benitez, A. V., Guan, B., Scott, R., Ercan, B., Yoo, S. J. B., Grüner-Nielsen, L. E., Sun, Y., Lingle, R., Antonio-Lopez, E., and Amezcua-Correa, R. (2015). 3030 MIMO Transmission over 15 Spatial Modes. In *Optical Fiber Communication Conference Post Deadline Papers*, number 1, page Th5C.1.
- Freeman, R. (2007). Forward error correction and advanced digital waveforms 4.1. In *Radio System Design for Telecommunications, Third Edition*, pages 175–218.
- Freund, I. (1999). Critical point explosions in two-dimensional wave fields. *Optics Communications*, 159(1):99–117.
- Freund, R., Bunge, C.-a., Ledentsov, N., Molin, D., and Caspar, C. (2010). High-Speed Transmission in Multimode Fibers. *Journal of Lightwave Technology*, 28(4):569–586.
- Genevaux, P., Simonneau, C., Labroille, G., Denolle, B., Pinel, O., Jian, P., Morizur, J.-f., and Charlet, G. (2015). 6-mode Spatial Multiplexer with Low Loss and High Selectivity for Transmission over Few Mode Fiber. *Optical Fiber Communications Conference*, 1(W1A.5):11–13.

- Ghatak, A. and Thyagarajan, K. (1998). *Introduction to Fiber Optics*. Cambridge University Press.
- Gibson, G., Courtial, J., Padgett, M., Vasnetsov, M., Pas'ko, V., Barnett, S., and Franke-Arnold, S. (2004). Free-space information transfer using light beams carrying orbital angular momentum. *Optics Express*, 12(22):5448–5456.
- Gisin, N., Weid, J.-P. V. D., and Pellaux, J.-P. (1991). Polarization mode dispersion of short and long single-mode fibers. *Journal of Lightwave Technology*, 9(7):821–827.
- Gloge, D. (1972). Optical power flow in multimode fibers. *Bell System Technical Journal*, 51(8):1767–1783.
- Golowich, S. (2014). Asymptotic theory of strong spin-orbit coupling in optical fiber. *Optics Letters*, 39(1):92–5.
- Golowich, S., Bozinovic, N., Kristensen, P., and Ramachandran, S. (2013). Complex mode amplitude measurement for a six-mode optical fiber. *Optics Express*, 21(4):4931–44.
- Golowich, S. and Ramachandran, S. (2005). Impact of fiber design on polarization dependence in microbend gratings. *Optics Express*, 13(18):6870–6877.
- Golowich, S. E., Kristensen, P., Bozinovic, N., Gregg, P., and Ramachandran, S. (2012). Fibers Supporting Orbital Angular Momentum States for Information Capacity Scaling. In *Frontiers in Optics*, volume FW2D.2, pages 1–2.
- Goodman, J. W. (2005). *Introduction to Fourier Optics*. Roberts and Company, Greenwood Village.
- Gregg, P., Kristensen, P., Golowich, S., Olsen, J., Steinvurzel, P., and Ramachandran, S. (2013). Stable Transmission of 12 OAM States in Air-Core Fiber. In *Conference on Lasers and Electro-Optics*, page CTu2K.2.
- Gregg, P., Kristensen, P., and Ramachandran, S. (2015a). Conservation of orbital angular momentum in air-core optical fibers. *Optica*, 2(3):267–270.
- Gregg, P., Mirhosseini, M., Rubano, A., Marrucci, L., Karimi, E., Boyd, R. W., and Ramachandran, S. (2015b). Q-plates as higher order polarization controllers for orbital angular momentum modes of fiber. *Optics Letters*, 40(8):1729–1732.
- Grüner-Nielsen, L., Sun, Y., Jensen, R. V., Nicholson, J. W., and Lingle, R. J. (2015). Recent advances in low DGD few mode fiber design , fabrication , characterization and experiments. *Optical Fiber Communication Conference*, page M2C.3.

- Grüner-Nielsen, L., Sun, Y., Nicholson, J. W., Jakobsen, D., Jespersen, K. G., Lingle, R., and Pálsdóttir, B. (2012). Few mode transmission fiber with low DGD, low mode coupling, and low loss. *Journal of Lightwave Technology*, 30(23):3693–3698.
- Guo, C. S., Xue, D. M., Han, Y. J., and Ding, J. (2006). Optimal phase steps of multi-level spiral phase plates. *Optics Communications*, 267(3):235–239.
- Haberman, R. (2004). *Applied Partial Differential Equations with Fourier Series and Boundary Value Problems*. Pearson.
- Hamming, R. (1950). Hamming_ErrorCorrectionCoding_1950.pdf. *Bell System Technical Journal*, XXIX(2).
- Han, I.-k., Ko, J., and Kim, B. Y. (2015). All-fiber Variable Polarization Rotator Based on Geometric Effects. In *Conference on Lasers and Electro-Optics/Pacific Rim*, volume 28F2.4, pages 1–2.
- Hecht, J. (2004). *City of light and the story of fiber optics*. Oxford University Press, New York.
- Hocker, G. B. (1979). Fiber-optic sensing of pressure and temperature. *Applied Optics*, 18(9):1445–1448.
- Hu, Z.-A., Huang, Y.-Q., Luo, A.-P., Cui, H., Luo, Z.-C., and Xu, W.-C. (2016). Photonic crystal fiber for supporting 26 orbital angular momentum modes. *Optics Express*, 24(15):17285–17291.
- Huang, B., Fontaine, N. K., Ryf, R., Guan, B., Leon-saval, S. G., Shubochkin, R., Sun, Y., Jr, R. L., and Li, G. (2015). All-fiber mode-group-selective photonic lantern using graded-index multimode fibers. *Optics Express*, 23(1):224–234.
- Huang, H., Xie, G., Yan, Y., Ahmed, N., Ren, Y., Yue, Y., Rogawski, D., Willner, M. J., Erkmen, B. I., Birnbaum, K. M., Dolinar, S. J., Lavery, M. P. J., Padgett, M. J., Tur, M., and Willner, A. E. (2014). 100 Tbit/s free-space data link enabled by three-dimensional multiplexing of orbital angular momentum, polarization, and wavelength. *Optics Letters*, 39(2):197–200.
- Hwang, I. K., Yun, S. H., and Kim, B. Y. (1999). Long-period fiber gratings based on periodic microbends. *Optics Letters*, 24(18):1263–1265.
- Igarashi, K., Soma, D., Wakayama, Y., Takeshima, K., Kawaguchi, Y., Yoshikane, N., Tsuritani, T., Morita, I., and Suzuki, M. (2016). Ultra-dense spatial-division-multiplexed optical fiber transmission over 6-mode 19-core fibers. *Optics Express*, 24(10):10213–10231.

- Ishii, K., Kurumida, J., and Sato, K.-i. (2015). Unifying Top-Down and Bottom-Up Approaches to Evaluate Network Energy Consumption. *Journal of Lightwave Technology*, 33(21):4395–4405.
- Israelsen, S. M., Rishøj, L. S., and Rottwitt, K. (2014). Break up of the azimuthal symmetry of higher order fiber modes. *Optics Express*, 22(10):488–490.
- Ivanov, O. V., Nikitov, S. a., and Gulyaev, Y. V. (2006). Cladding modes of optical fibers: properties and applications. *Physics-Uspekhi*, 49(2):167.
- Jack, B., Padgett, M. J., and Franke-Arnold, S. (2008). Angular diffraction. *New Journal of Physics*, 10.
- Jackson, J. D. (1999). *Classical Electrodynamics*. Wiley & Sons.
- Jung, Y., Kang, Q., Yoo, S., Sidharthan, R., Ho, D., Gregg, P., Ramachandran, S., Alam, S. U., and Richardson, D. (2016). Optical Orbital Angular Momentum Amplifier based on an Air-Core Erbium Doped Fiber. In *Optical Fiber Communications Conference Postdeadline papers*, number Th5A.5, pages 21–23.
- Kaminow, I. (1981). Polarization in optical fibers. *IEEE Journal of Quantum Electronics*, QE-17(1):15–22.
- Kang, Q., Gregg, P., Jung, Y., Lim, E. L., Alam, S.-u., Ramachandran, S., and Richardson, D. J. (2015). Amplification of 12 OAM states in an air-core erbium doped fiber. *Optics Express*, 23(22):28341–28348.
- Kao, K. and Hockham, G. (1966). Dielectric-fibre surface waveguides for optical frequencies. *Proceedings of the Institution of Electrical Engineers*, 113(7):1151.
- Kapron, F. P., Keck, D. B., and Maurer, R. D. (1970). Radiation losses in glass optical waveguides. *Applied Physics Letters*, 17(10):423–425.
- Kawakami, S. and Ikeda, M. (1978). Transmission characteristics of a two-mode optical waveguide. *IEEE Journal of Quantum Electronics*, 14(8):608–614.
- Keiser, G. (2011). *Optical Fiber Communications*. McGraw Hill.
- Kien, F. L., Balykin, V. I., and Hakuta, K. (2006). Angular momentum of light in an optical nanofiber. *Physical Review A - Atomic, Molecular, and Optical Physics*, 73(5):1–7.
- Kogelnik, H. and Li, T. (1966). Laser beams and resonators. *Applied Optics*, 5(10):1550–1567.
- Kostovski, G., Stoddart, P. R., and Mitchell, A. (2014). The optical fiber tip: An inherently light-coupled microscopic platform for micro- and nanotechnologies. *Advanced Materials*, 26(23):3798–3820.

- Krenn, M., Fickler, R., Fink, M., Handsteiner, J., Malik, M., Scheidl, T., Ursin, R., and Zeilinger, A. (2014). Communication with spatially modulated light through turbulent air across Vienna. *New Journal of Physics*, 16(11):113028.
- Krummrich, P. M. and Akhtari, S. (2016). Design of efficient few mode optical amplifiers for fiber capacity increase. In *Conference on Lasers and Electro-Optics*, pages 1–2.
- Labroille, G., Denolle, B., Jian, P., Genevaux, P., Treppe, N., and Morizur, J.-F. (2014). Efficient and mode selective spatial mode multiplexer based on multi-plane light conversion. *Optics Express*, 22(13):15599–15607.
- Lai, K., Leon-Saval, S. G., Witkowska, A., Wadsworth, W. J., and Birks, T. a. (2007). Wavelength-independent all-fiber mode converters. *Optics Letters*, 32(4):328–330.
- Lam, C. F., Liu, H., and Urata, R. (2014). What devices do data centers need? *Optical Fiber Communication Conference*, page M2K.5.
- Lavery, M., Robertson, D., Berkhout, G., Love, G., Padgett, M., and Courtial, J. (2012a). Refractive elements for the measurement of the orbital angular momentum of a single photon. *Optics Express*, 20(3).
- Lavery, M. P. J., Robertson, D., Malik, M., Robenburg, B., Courtial, J., Boyd, R. W., and Padgett, M. J. (2012b). The efficient sorting of light’s orbital angular momentum for optical communications. In *Proceedings of SPIE*, volume 8542, page 85421R.
- Lavery, M. P. J., Robertson, D. J., Sponselli, A., Courtial, J., Steinhoff, N. K., Tyler, G. a., Wilner, A. E., and Padgett, M. J. (2013). Efficient measurement of an optical orbital-angular-momentum spectrum comprising more than 50 states. *New Journal of Physics*, 15(013024):1–7.
- Leon-Saval, S. G., Birks, T. a., Bland-Hawthorn, J., and Englund, M. (2005). Multimode fiber devices with single-mode performance. *Optics Letters*, 30(19):2545–2547.
- Li, Y., Zeng, X., Mo, Q., Li, W., Liu, Z., and Wu, J. (2016). Mode evolution in polarization maintain few mode fibers and applications in mode-division-multiplexing systems. In *Proceedings of SPIE*, volume 10019, pages 1–6.
- Lines, M. E. (1984). Scattering losses in optic fiber materials. I. A new parametrization. *Journal of Applied Physics*, 55(11):4052–4057.
- Litvin, I. a., Mhlanga, T., and Forbes, A. (2015). Digital generation of shape-invariant Bessel-like beams. *Optics Express*, 23(6):7312.

- Lu, I.-c., Wei, C.-c., Chen, H.-y., Chen, K.-z., Huang, C.-h., Chi, K.-l., Shi, J.-w., Lai, F.-i., Hsieh, D.-h., Kuo, H.-c., Lin, W., Chiu, S.-w., and Chen, J. (2015). High-Speed and Duo-Mode 850 nm VCSELs for 47 Gbps Optical Interconnect over 1 km OM4 Fiber. *Optical Fiber Communication Conference*, pages 17–19.
- Ma, Y. Z., Sych, Y., Onishchukov, G., Ramachandran, S., Peschel, U., Schmauss, B., and Leuchs, G. (2009). Fiber-modes and fiber-anisotropy characterization using low-coherence interferometry. *Applied Physics B: Lasers and Optics*, 96:345–353.
- Machavariani, G., Davidson, N., Hasman, E., Blit, S., Ishaaya, A. a., and Friesem, A. a. (2002). Efficient conversion of a Gaussian beam to a high purity helical beam. *Optics Communications*, 209(4-6):265–271.
- Maine, P., Strickland, D., Bado, P., Pessot, M., and Mourou, G. (1988). Generation of Ultrahigh Peak Power Pulses by Chirped Pulse Amplification. *IEEE Journal of Quantum Electronics*, 24(2):398–403.
- Mair, A., Vaziri, A., Weihs, G., and Zeilinger, A. (2001). Entanglement of the orbital angular momentum states of photons. *Nature*, 412(6844):313–316.
- Malik, M., O’Sullivan, M., Rodenburg, B., Mirhosseini, M., Leach, J., Lavery, M., Padgett, M., and Boyd, R. (2012). Influence of atmospheric turbulence on optical communications using orbital angular momentum for encoding. *Optics Express*, 20(12):225–230.
- Marcuse, D. (1972). Derivation of coupled power equations. *Bell System Technical Journal*, 51(1):229–237.
- Marcuse, D. (1974). *Theory of Dielectric Optical Waveguides*. Academic Press, New York.
- Marcuse, D. (1975). Coupled-Mode Theory for Anisotropic Optical Waveguides. *Bell System Technical Journal*, 54(6):985–995.
- Marcuse, D. (1982). Influence of curvature on the losses of doubly clad fibers. *Applied Optics*, 21(23):4208–4213.
- Marrucci, L., Karimi, E., Slussarenko, S., Piccirillo, B., Santamato, E., Nagali, E., and Sciarrino, F. (2011). Spin-to-orbital conversion of the angular momentum of light and its classical and quantum applications. *Journal of Optics*, 13(6):064001.
- Marrucci, L., Manzo, C., and Paparo, D. (2006). Optical spin-to-orbital angular momentum conversion in inhomogeneous anisotropic media. *Physical Review Letters*, 96(16):1–4.

- Martinelli, M., Huguenin, J. a. O., Nussenzevig, P., and Khoury, a. Z. (2004). Orbital angular momentum exchange in an optical parametric oscillator. *Physical Review*, 70(013812):1–11.
- Maruyama, R., Kuwaki, N., Matsuo, S., and Ohashi, M. (2015). Experimental investigation of relation between mode-coupling and fiber characteristics in few-mode fibers. In *Optical Fiber Communication Conference*, number 1, page M2C.1.
- Matsumoto, N., Ando, T., Inoue, T., Ohtake, Y., Fukuchi, N., and Hara, T. (2008). Generation of high-quality higher-order Laguerre-Gaussian beams using liquid-crystal-on-silicon spatial light modulators. *Journal of the Optical Society of America, A*, 25(7):1642–1651.
- Maurer, C., Jesacher, A., Fürhapter, S., Bernet, S., and Ritsch-Marte, M. (2007). Tailoring of arbitrary optical vector beams. *New Journal of Physics*, 9(78):1–20.
- McGloin, D., Simpson, N. B., and Padgett, M. J. (1998). Transfer of orbital angular momentum from a stressed fiber-optic waveguide to a light beam. *Applied Optics*, 37(3):469–472.
- McLeod, J. H. (1954). The Axicon: A New Type of Optical Element. *Journal of the Optical Society of America*, 44(8):592.
- Mears, R., Reekie, L., Jauncey, I., and Payne, D. N. (1987). Low-Noise Erbium-Doped Fibre Amplifier Operating at 1.54 μ m. *Electronics Letters*, 23(19):1026–1028.
- Miller, S. E., Li, T., and Marcatali, E. A. J. (1973). Research Toward Optical-Fiber Transmission Systems Part II : Devices and Systems Considerations. *Proceedings of the IEEE*, 61(12):1726–1751.
- Minkowski, H. (1908). Die Grundgleichungen für die elektromagnetischen Vorgänge in bewegten Körper. *Mathematische Annalen*, 68(1):472–525.
- Morizur, J.-F., Nicholls, L., Jian, P., Armstrong, S., Treps, N., Hage, B., Hsu, M., Bowen, W., Janousek, J., and Bachor, H.-A. (2010). Programmable unitary spatial mode manipulation. *Journal of the Optical Society of America, A*, 27(11):2524–2531.
- Nejad, R. M., Allahverdyan, K., Vaity, P., Amiralizadeh, S., Brunet, C., Messaddeq, Y., and LaRochelle, S. (2016). Mode Division Multiplexing Using Orbital Angular Momentum Modes Over 1 . 4-km Ring Core Fiber. *Journal of Lightwave Technology*, 34(18):4252–4258.

- Nicholson, J. W., Headley, C., Phillips, J., Desantolo, A., Gonzalos, E., Ghalmi, S., Yan, M. F., Wisk, P. W., Trevor, D., Fleming, J., Monberg, E., Dimarcello, F., Windeler, R. S., Fini, J. M., and Digiovanni, D. J. (2010). Higher-Order-Mode Fiber Amplifiers. In *Applications of Lasers for Sensing and Free Space Communication*, volume 2, pages 2–4.
- Nicholson, J. W., Yablon, a. D., Ramachandran, S., and Ghalmi, S. (2008). Spatially and spectrally resolved imaging of modal content in large-mode-area fibers. *Optics Express*, 16(10):7233–7243.
- Noda, J., Okamoto, K., and Sasaki, Y. (1986). Polarization-maintaining fibers and their applications. *Journal of Lightwave Technology*, 4(8):1071–1089.
- Noordegraaf, D., Skovgaard, P. M. W., Nielsen, M. D., and Bland-Hawthorn, J. (2009). Efficient multi-mode to single-mode coupling in a photonic lantern. *Optics Express*, 17(3):1988–1994.
- Oh, K., Choi, S., Jung, Y., and Lee, J. W. (2005). Novel hollow optical fibers and their applications in photonic devices for optical communications. *Journal of Lightwave Technology*, 23(2):524–532.
- Olshansky, R. (1975). Mode Coupling Effects in Graded-index Optical Fibers. *Applied Optics*, 14(4):935–945.
- O’Sullivan, M. N., Mirhosseini, M., Malik, M., and Boyd, R. W. (2012). Near-perfect sorting of orbital angular momentum and angular position states of light. *Optics Express*, 20(22):24444.
- Padgett, M. J. and Courtial, J. (1999). Poincaré-sphere equivalent for light beams containing orbital angular momentum. *Optics Letters*, 24(7):430–432.
- Pedersen, M. E. V., Kristensen, P., Gruner-Nielsen, L., and Rottwitt, K. (2011). Impact of the scalar approximation on the prediction of the group velocity dispersion. *Journal of Lightwave Technology*, 29(21):3129–3134.
- Petermann, K. (1976). Microbending loss in monomode fibres. *Electronics Letters*, 12(4):107–109.
- Phillips, R. L. and Andrews, L. C. (1983). Spot size and divergence for Laguerre Gaussian beams of any order. *Applied Optics*, 22(5):643–644.
- Pidishety, S., Khudus, M. I. M. A., Gregg, P., Ramachandran, S., Srinivasan, B., and Brambilla, G. (2016). OAM Beam Generation using All-fiber Fused Couplers. In *Conference on Lasers and Electro-Optics*, page STu1F.2.
- Poole, C. D. (1988). Statistical treatment of polarization dispersion in single-mode fiber. *Optics Letters*, 13(8):687.

- Poole, C. D. (1989). Measurement of polarization-mode dispersion in single-mode fibers with random mode coupling. *Optics Letters*, 14(10):523–525.
- Poole, C. D., Tkach, R. W., Chraplyvy, a. R., and Fishman, D. a. (1991). Fading in lightwave systems due to polarization-mode dispersion. *IEEE Photonics Technology Letters*, 3(1):68–70.
- Poole, C. D., Wiesenfeld, J. M., DiGiovanni, D. J., and Vengsarkar, A. M. (1994). Optical fiber-based dispersion compensation using higher order modes near cutoff. *Journal of Lightwave Technology*, 12(10):1746–1758.
- Poynting, J. H. (1909). The Wave Motion of a Revolving Shaft, and a Suggestion as to the Angular Momentum in a Beam of Circularly Polarised Light. *Proceedings of the Royal Society A: Mathematical, Physical and Engineering Sciences*, 82(557):560–567.
- Prabhakar, G., Gregg, P., Rishøj, L., and Ramachandran, S. (2016). In-Fiber Monomode Octave-Spanning OAM Supercontinuum. In *Conference on Lasers and Electro-Optics*, number Am4J.3, pages 1–2.
- Puttnam, B. J., Luís, R. S., Klaus, W., Sakaguchi, J., Mendinueta, J. D., Awaji, Y., Wada, N., Tamura, Y., Hayashi, T., Hirano, M., and Marciante, J. (2015). 2 . 15 Pb / s Transmission Using a 22 Core Homogeneous Single- Mode Multi-Core Fiber and Wideband Optical Comb. In *European Conference on Optical Communications*, number PDP.3.1, pages 1–2.
- Qian, D., Huang, M., Ip, E., Huang, Y., Shao, Y., Hu, J., and Wang, T. (2012). High Capacity / Spectral Efficiency 101 . 7-Tb / s WDM Transmission Using PDM-128QAM-OFDM Over 165-km SSMF Within C- and L-Bands. *Journal of Lightwave Technology*, 30(10):1540–1548.
- Ramachandran, S. (2005). Dispersion-tailored few-mode fibers: A versatile platform for in-fiber photonic devices. *Journal of Lightwave Technology*, 23(11):3426–3443.
- Ramachandran, S., Ghalmi, S., Bromage, J., Chandrasekhar, S., and Buhl, L. L. (2005a). Evolution and systems impact of coherent distributed multipath interference. *IEEE Photonics Technology Letters*, 17(1):238–240.
- Ramachandran, S., Golowich, S., Yan, M. F., Monberg, E., Dimarcello, F. V., Fleming, J., Ghalmi, S., and Wisk, P. (2005b). Lifting polarization degeneracy of modes by fiber design: a platform for polarization-insensitive microbend fiber gratings. *Optics Letters*, 30(21):2864–2866.
- Ramachandran, S., Gregg, P., Kristensen, P., and Golowich, S. E. (2015). On the scalability of ring fiber designs for OAM multiplexing. *Optics Express*, 23(3):3721.

- Ramachandran, S. and Kristensen, P. (2013). Optical vortices in fiber. *Nanophotonics*, 2(5-6):455–474.
- Ramachandran, S., Kristensen, P., and Yan, M. F. (2009). Generation and propagation of radially polarized beams in optical fibers. *Optics Letters*, 34(16):2525–2527.
- Ramachandran, S., Mikkelsen, B., Cowsar, L. C., Yan, M. F., Raybon, G., Boivin, L., Fishteyn, M., Reed, W. A., Wisk, P., Brownlow, D., Huff, R. G., and Gruner-Nielsen, L. (2001). All-fiber grating-based higher order mode dispersion compensator for broad-band compensation and 1000-km transmission at 40 Gb/s. *IEEE Photonics Technology Letters*, 13(6):632–634.
- Ramachandran, S., Nicholson, J. W., Ghalimi, S., and Yan, M. F. (2003). Measurement of multipath interference in the coherent crosstalk regime. *IEEE Photonics Technology Letters*, 15(8):1171–1173.
- Ramachandran, S., Nicholson, J. W., Ghalimi, S., Yan, M. F., Wisk, P., Monberg, E., and Dimarcello, F. V. (2006). Light propagation with ultralarge modal areas in optical fibers. *Optics Letters*, 31(12):1797–1799.
- Rashleigh, S. (1983). Origins and control of polarization effects in single-mode fibers. *Journal of Lightwave Technology*, 1(2):312–331.
- Ren, Y., Wang, Z., Liao, P., Li, L., Xie, G., Huang, H., Zhao, Z., Yan, Y., Ahmed, N., Lavery, M., Ashrai, N., Ashrafi, S., Linquist, R., Tur, M., Djordjevic, I. B., Neifeld, M. A., and Willner, A. E. (2015). 400-Gbit/s free-space optical communications link over 120-meter using multiplexing of 4 collocated orbital-angular-momentum beams. *Optical Fiber Communication Conference*, page M2F.1.
- Ricci, F., Loffler, W., and Van Exter, M. (2012). Instability of higher-order optical vortices analyzed with a multi-pinhole interferometer. *Optics Express*, 20(20):22961–22975.
- Rishøj, L., Jones, M., Demas, J., Gregg, P., Prabhakar, G., Yan, L., Hawkins, T., Ballato, J., and Ramachandran, S. (2016). Polymer-clad silica fibers for tailoring modal area and dispersion. *Optics Letters*, 41(15):3587–3590.
- Rodenburg, B., Lavery, M. P. J., Malik, M., O’Sullivan, M. N., Mirhosseini, M., Robertson, D. J., Padgett, M., and Boyd, R. W. (2012). Influence of atmospheric turbulence on states of light carrying orbital angular momentum. *Optics Letters*, 37(17):3735.
- Ross, J. (1984). The rotation of the polarization in low birefringence monomode optical fibres due to geometric effects. *Optical and Quantum Electronics*, 16:455–461.

- Sab, O. A. and Lemaire, V. (2000). Block turbo code performances for long-haul DWDM optical transmission systems. *Optical Fiber Communication Conference. Technical Digest Postconference Edition. Trends in Optics and Photonics Vol.37 (IEEE Cat. No. 00CH37079)*, 3:280–282.
- Sakaguchi, J., Klaus, W., Puttnam, B. J., Mendinueta, J. M. D., Awaji, Y., Wada, N., Tsuchida, Y., Maeda, K., Tadakuma, M., Imamura, K., Sugizaki, R., Kobayashi, T., Tottori, Y., Watanabe, M., and Jensen, R. V. (2014). 19-core MCF transmission system using EDFA with shared core pumping coupled via free-space optics. *Optics Express*, 22(1):90–5.
- Sakaguchi, J., Puttnam, B. J., Klaus, W., Awaji, Y., Wada, N., Kanno, A., Kawanishi, T., Member, S., Imamura, K., Inaba, H., Mukasa, K., Sugizaki, R., Kobayashi, T., and Watanabe, M. (2013). 305 Tb / s Space Division Multiplexed Transmission Using Homogeneous 19-Core Fiber. *Journal of Lightwave Technology*, 31(4):554–562.
- Saleh, B. and Teich, M. (2007). *Fundamentals of Photonics*. Wiley & Sons, Hoboken, NJ.
- Saridis, G., Alexandropoulos, D., Zervas, G., and Simeonidou, D. (2015). Survey and Evaluation of Space Division Multiplexing: From Technologies to Optical Networks. *IEEE Communications Surveys & Tutorials*, 17(September):2136–2156.
- Schimpf, D. N., Barankov, R. a., and Ramachandran, S. (2011). Cross-correlated (C²) imaging of fiber and waveguide modes. *Optics Express*, 19(14):13008–13019.
- Schulze, C., Dudley, A., Flamm, D., Duparré, M., and Forbes, A. (2013). Measurement of the orbital angular momentum density of light by modal decomposition. *New Journal of Physics*, 15.
- Shahraam Afshar, V., Lohe, M. A., Zhang, W. Q., and Monroe, T. M. (2012). Full vectorial analysis of polarization effects in optical nanowires. *Optics Express*, 20(13):14514–14533.
- Shapira, O., Abouraddy, A. F., Joannopoulos, J. D., and Fink, Y. (2005). Complete modal decomposition for optical waveguides. *Physical Review Letters*, 94(April):1–4.
- Sheem, S. K. and Giallorenzi, T. G. (1979). Single-mode fiber-optical power divider: encapsulated etching technique. *Optics Letters*, 4(1):29–31.
- Siegman, A. (1986). *Lasers*. University Science Books, Mill Valley, CA.

- Sleiffer, V. a. J. M., Chen, H., Jung, Y., Kuschnerov, M., Richardson, D. J., Alam, S. U., Sun, Y., Gruner-Nielsen, L., Pavarelli, N., Snyder, B., O'Brien, P., Ellis, a. D., Koonen, a. M. J., and De Waardt, H. (2013). 480 km transmission of MDM 576-Gb/s 8QAM using a few-mode re-circulating loop. *2013 IEEE Photonics Conference, IPC 2013*, pages 1–2.
- Slussarenko, S., Karimi, E., Piccirillo, B., Marrucci, L., and Santamato, E. (2011a). Efficient generation and control of different-order orbital angular momentum states for communication links. *Journal of the Optical Society of America. A, Optics, image science, and vision*, 28(1):61–65.
- Slussarenko, S., Murauski, A., Du, T., Chigrinov, V., Marrucci, L., and Santamato, E. (2011b). Tunable liquid crystal q-plates with arbitrary topological charge. *Optics Express*, 19(5):4085–4090.
- Smith, a. M. (1980). Birefringence induced by bends and twists in single-mode optical fiber. *Applied Optics*, 19(15):2606–2611.
- Snitzer, E. (1961). Cylindrical Dielectric Waveguide Modes. *Journal of the Optical Society of America*, 51(5):491.
- Snyder, A. W. and Love, J. D. (1983). *Optical Waveguide Theory*. Chapman and Hall.
- Soma, D., Igarashi, K., Wakayama, Y., Takeshima, K., and Kawaguchi, Y. (2015). 2.05 Peta-bit/s Super-Nyquist-WDM SDM Transmission Using 9 . 8-km 6-mode 19-core Fiber in Full C band. In *European Conference on Optical Communication*, number 1, pages 195–197.
- Soma, D., Wakayama, Y., Beppu, S., Igarashi, K., Tsuritani, T., Taga, H., Morita, I., and Suzuki, M. (2016). 665 and 947b / s / Hz Ultra-highly Aggregate-Spectral-Efficient SDM / WDM Transmission over 6-Mode 19-Core Fibre Using DP-16QAM / 64QAM Signals. In *European Conference on Optical Communication*, pages 1–2.
- Sorin, W. V., Kim, B. Y., and Shaw, H. J. (1986). Highly selective evanescent modal filter for two-mode optical fibers. *Optics Letters*, 11(9):581–3.
- Soskin, M., Gorshkov, V., Vasnetsov, M., Malos, J., and Heckenberg, N. (1997). Topological charge and angular momentum of light beams carrying optical vortices. *Physical Review A*, 56(5):4064–4075.
- Sridharan, A., Pax, P. H., Heebner, J. E., Drachenberg, D. R., Armstrong, P. J., and Dawson, J. W. (2012). Mode-converters for rectangular-core fiber amplifiers to achieve diffraction-limited power scaling. *Optics Express*, 20(27):28792–28800.

- Stepniak, G., Maksymiuk, L., and Siuzdak, J. (2011). Binary-phase spatial light filters for mode-selective excitation of multimode fibers. *Journal of Lightwave Technology*, 29(13):1980–1987.
- Stolen, R. H., Bjorkholm, J. E., and Ashkin, a. (1974). Phase-Matched Three-Wave Mixing in Silica Fiber Optical Waveguides. *Applied Physics Letters*, 24(7):308–310.
- Stone, J. and Walrafen, G. E. (1982). Overtone vibrations of OH groups in fused silica optical fibers Overtone vibrations of OH groups in fused silica optical fibers. *The Journal of Chemical Physics*, 76(4):1712–1722.
- Su, T., Scott, R. P., Djordjevic, S. S., Fontaine, N. K., Geisler, D. J., Cai, X., and Yoo, S. J. B. (2012). Demonstration of free space coherent optical communication using integrated silicon photonic orbital angular momentum devices. *Optics Express*, 20(9):9396.
- Sun, J., Moresco, M., Leake, G., Coolbaugh, D., and Watts, M. R. (2014). Generating and Identifying Optical Orbital Angular Momentum with Silicon Photonic Circuits. *Optics Letters*, 39(20):5977–5980.
- Tai, B., Gregg, P., Rishøj, L., and Ramachandran, S. (2016). Wideband nonlinear frequency conversion with OAM fiber. In *Conference on Lasers and Electro-Optics*, number FTh3.6, pages 1–2.
- Taylor, H. (1984). Bending effects in optical fibers. *Lightwave Technology, Journal of*, 2(5):617–628.
- Temelkuran, B., Hart, S. D., Benoit, G., Joannopoulos, J. D., and Fink, Y. (2002). Wavelength-scalable hollow optical fibres with large photonic bandgaps for CO₂ laser transmission. *Nature*, 420(6916):650–653.
- Thomas, J., Jovanovic, N., Becker, R. G., Marshall, G. D., Withford, M. J., Tünnermann, A., Nolte, S., and Steel, M. J. (2011). Cladding mode coupling in highly localized fiber Bragg gratings: modal properties and transmission spectra. *Optics Express*, 19(1):325–341.
- Tkach, R. and Chraplyvy, a. (1986). Phase noise and linewidth in an InGaAsP DFB laser. *Journal of Lightwave Technology*, 4(11).
- Tomita, A. and Chiao, R. (1986). Observation of Berry’s Topological Phase by Use of an Optical Fiber. *Physical Review Letters*, 57(8):937–940.
- Tsao, C. (1992). *Optical Fibre Waveguide Analysis*. Oxford Science Publications.
- Tsubokawa, M., Higashi, T., and Negishi, Y. (1988). Mode couplings due to external forces distributed along a polarization-maintaining fiber: an evaluation. *Applied Optics*, 27(1):166–173.

- Turnbull, G., Robertson, D., Smith, G., Allen, L., and Padgett, M. (1996). Generation Of Free-Space Laguerre-Gaussian Modes At Millimetre-Wave Frequencies By Use Of A Spiral Phaseplate. *Optics Communications*, 127:183–188.
- Ulrich, R., Rashleigh, S. C., and Eickhoff, W. (1980). Bending-induced birefringence in single-mode fibers. *Optics Letters*, 5(6):273–275.
- Ulrich, R. and Simon, A. (1979). Polarization optics of twisted single-mode fibers. *Applied Optics*, 18(13):2241–2251.
- Ung, B., Vaity, P., Wang, L., Messaddeq, Y., Rusch, L. a., and LaRochelle, S. (2014). Few-mode fiber with inverse-parabolic graded-index profile for transmission of OAM-carrying modes. *Optics Express*, 22(15):18044–18055.
- Vaity, P., Banerji, J., and Singh, R. P. (2013). Measuring the topological charge of an optical vortex by using a tilted convex lens. *Physics Letters A*, 377(15):1154–1156.
- Vaity, P., Brunet, C., Messaddeq, Y., Larochelle, S., and Rusch, L. A. (2014). Exciting OAM Modes in Annular-core Fibers via Perfect OAM Beams. In *European Conference on Optical Communication*, pages 1–3.
- Vallone, G., D’Ambrosio, V., Sponselli, A., Slussarenko, S., Marrucci, L., Sciarrino, F., and Villoresi, P. (2014). Free-space quantum key distribution by rotation-invariant twisted photons. *Physical Review Letters*, 113(6):1–5.
- Van Enk, S. and Nienhuis, G. (1994). Commutation Rules and Eigenvalues of Spin and Orbital Angular Momentum of Radiation Fields. *Journal of Modern Optics*, 41(5):963–977.
- Varnham, M. P., Payne, D. N., Birch, R. D., and Barlow, A. J. (1983). Analytic Solution for the Birefringence Produced by Thermal Stress in Polarization-Maintaining Optical Fibers. *Journal of Lightwave Technology*, 1(2):332–339.
- Vasilyeu, R., Dudley, A., Khilo, N., and Forbes, A. (2009). Generating superpositions of higher-order Bessel beams. *Optics Express*, 17(26):23389–23395.
- Vaziri, A., Weihs, G., and Zeilinger, A. (2001). Superpositions of the Orbital Angular Momentum for Applications in Quantum Experiments. *Journal of Optics B: Quantum and Semiclassical Optics*, 4:47–51.
- Vaziri, A., Weihs, G., and Zeilinger, A. (2002). Experimental two-photon, three-dimensional entanglement for quantum communication. *Physical Review Letters*, 89(24):240401.
- Vengsarkar, A. A. M., Lemaire, P. J. P., Judkins, J. B. J., Bhatia, V., Erdogan, T., and Sipe, J. E. J. (1996). Long-period fiber gratings as band-rejection filters. *Journal of Lightwave Technology*, 14(1):58–65.

- Wadsworth, W., Percival, R., Bouwmans, G., Knight, J., and Russell, P. (2003). High power air-clad photonic crystal fibre laser. *Optics Express*, 11(1):48–53.
- Wang, A., Zhu, L., Chen, S., Du, C., Mo, Q., and Wang, J. (2016). Characterization of LDPC-coded orbital angular momentum modes transmission and multiplexing over a 50-km fiber. *Optics Express*, 24(11):11716–11726.
- Wang, J., Yang, J.-Y., Fazal, I. M., Ahmed, N., Yan, Y., Huang, H., Ren, Y., Yue, Y., Dolinar, S., Tur, M., and Willner, A. E. (2012). Terabit free-space data transmission employing orbital angular momentum multiplexing. *Nature Photonics*, 6(7):488–496.
- Wang, L. and LaRochelle, S. (2015). Design of eight-mode polarization-maintaining few-mode fiber for multiple-input multiple-output-free spatial division multiplexing. *Optics Letters*, 40(24):5846–5849.
- Wang, L., Vaity, P., Messaddeq, Y., Rusch, L., and LaRochelle, S. (2015). Orbital-Angular-Momentum Polarization Mode Dispersion in Optical Fibers and Its Measurement Technique. In *European Conference on Optical Communication*, number 0035, pages 1–4.
- Wassmann, F. and Ankiewicz, A. (1998). Berry 's phase analysis of polarization rotation in helicoidal fibers. *Applied Optics*, 37(18):3902–3911.
- Weber, W. J. (1978). Differential Encoding for Multiple Amplitude and Phase Shift Keying Systems. *IEEE Transactions on Communications*, COM-26(3):385–391.
- Weng, Y., Ip, E., Pan, Z., and Want, T. (2016). Advanced Spatial-Division Multiplexed Measurement Systems Propositions From Telecommunication to Sensing Applications : A Review. *Sensors*, 16(1387):1–35.
- Wyant, J. C. and Creath, K. (1992). Basic Wavefront Aberration Theory for Optical Metrology. In *Applied Optics and Optical Engineering*, volume XI, pages 1–53.
- Xu, C., Liu, X., and Wei, X. (2004). Differential Phase-Shift Keying for High Spectral Efficiency Optical Transmissions. *IEEE Journal of Selected Topics in Quantum Electronics*, 10(2):281–293.
- Yan, L., Auksoorius, E., Bozinovic, N., Tearney, G. J., and Ramachandran, S. (2013). Optical Fiber Vortices for STED Nanoscopy. In *Conference on Lasers and Electro-Optics*, volume CTu3N.2.
- Yan, L., Barankov, R., Steinvurzel, P., and Ramachandran, S. (2015). Modal-weight measurements with fiber gratings. *Journal of Lightwave Technology*, 33(13):1–1.
- Yao, A. and Padgett, M. (2011). Orbital angular momentum: origins, behavior and applications. *Advances in Optics and Photonics*, 204:161–204.

- Youngworth, K. and Brown, T. (2000). Focusing of high numerical aperture cylindrical-vector beams. *Optics Express*, 7(2):77–87.
- Yu, F., Stojanovic, N., Hauske, F., Chang, D., Xiao, Z., Bauch, G., Pflueger, D., Xie, C., Zhao, Y., Jin, L., Li, Y., Li, L., Xu, X., and Xiong, Q. (2011). Soft-Decision LDPC Turbo Decoding for DQPSK Modulation in Coherent Optical Receivers. In *European Conference on Optical Communication*, pages 1–3.
- Zhang, W., Wang, H., and Bergman, K. (2012). Next-generation optically-interconnected high-performance data centers. *Journal of Lightwave Technology*, 30(24):3836–3844.

CURRICULUM VITAE

Patrick C. Gregg

410 Memorial Drive, Cambridge, MA, 02139

+1-443-841-5882

pgregg@bu.edu

Biographical Data

- Full name: Patrick Clayton Gregg
- Born April, 1989 in Baltimore, MD, USA
- Nationality: US Citizen

Education

- January 2017 (*expected*), Ph.D. in Electrical and Computer Engineering, Boston University, Boston, MA, USA
- May 2011, B.S. in Optics, B.A. in Physics and Japanese Language, University of Rochester, Rochester, NY, USA. GPA 4.0/4.0
- June 2007, Diploma, Calvert Hall College High School, Baltimore, MD, USA

Research and Work Experience

01/2012 - Present: Graduate Research Assistant, Boston University, Nanostructured Fibers and Nonlinear Optics Lab, Prof. Ramachandran Group

- Theoretically and experimentally studied orbital angular momentum (OAM) carrying fiber modes. Designed waveguides and measured fiber properties, developed and characterized mode excitation techniques, and performed transmission experiments using 12 OAM modes, 3x more than previous demonstrated.
- 27 published journal and conference publications, additional 4 in preparation. Presented 6 conference papers, including post-deadline paper at CLEO 2016.

09/2011 - 01/2012: Graduate Research Assistant, Boston University, Prof. Dal Negro Group

- Fabricated chemically-etched nanowires and studied enhancement of photoluminescence.

- 1 published journal paper and 1 conference paper.

06/2011 - 08/2011: Research Assistant, Johns Hopkins University Applied Physics Lab, Dr. Michael Dennis

- Investigated phase noise performance of 3GHz opto-electronic oscillator.
- Studied oven-based fiber tapering.

06/2010 - 08/2010: Research Assistant, ENSTA-École Polytechnique, Dr. Gerard Mourou and Dr. J. Bianca Jackson

- Researched ultrafast optical techniques for cleaning historically significant artifacts. Performed characterization experiments at the C2RMF at the Musée du Louvre.

06/2009 - 08/2009: Research Assistant, Johns Hopkins University Applied Physics Lab, Dr. Michael Dennis

- Design and test of ditherless low-bias regime Mach-Zehnder interferometer bias controller.

01/2009 - 06/2009: Research Assistant, Laboratory for Laser Energetics, Dr. Drew Maywar

- Modeling of vertical cavity semiconductor optical amplifiers.

Honors, Awards, and Fellowships

- Recipient National Science Foundation Graduate Student Fellowship 2013 (17% accepted nationwide).
- Maiman student paper competition semifinalist, Conference on Lasers and Electro-Optics (CLEO 2013 & 2015).
- Tingye Li Innovation Prize semifinalist, CLEO 2016.
- Best Student Paper Award, Runner Up, ECOC 2016.
- Recipient Boston University Dean's Fellowship.
- Chief Student Marshal at University of Rochester Commencement 2011.

Teaching and Outreach Activities

- STEM outreach demo targeting local area middle and high schools for Boston University's Technology Innovation Scholars Program featuring Orbital Angular Momentum in fiber.
- Received Outstanding Graduate Teaching Assistant Award for 2015/2016 for course "Electrodynamical Systems."
- Volunteer tutor for Society of Physics Students at University of Rochester.
- Undergraduate teaching assistant at University of Rochester for eight courses in mathematics and engineering.